OPTOELECTRONIC PROPERTIES OF NANO-STRUCTURED SILICON CARBIDE PREPARED BY ANODIC ELECTROCHEMICAL ETCHING

MOHD MARZAINI BIN MOHD RASHID

NEWCASTLE UNIVERSITY

OPTOELECTRONIC PROPERTIES OF NANO-STRUCTURED SILICON CARBIDE PREPARED BY ANODIC ELECTROCHEMICAL ETCHING

MOHD MARZAINI BIN MOHD RASHID

A thesis submitted to the Faculty of Science, Agriculture and Engineering
for the degree of Doctor of Philosophy

NEWCASTLE UNIVERSITY
SCHOOL OF ELECTRICAL AND ELECTRONIC ENGINEERING

JUNE 2017

To

my beloved wife

children

bapa and mama

ABSTRACT

Silicon carbide (SiC) nanostructures are appealing as non-toxic, water-stable and oxidation resistant nanomaterials. Owing to these unique properties, 3-dimensionally confined SiC nanostructures, namely SiC quantum dots (QDs) have found applications in bioimaging of living cells. Photoluminescence (PL) investigations however revealed that across the polytypes: 3C-, 4H- and 6H-SiC, excitation wavelength dependent PL is observed for larger sizes but deviate for sizes smaller than approximately 3 nm, thus exhibiting a dual-feature in the PL spectra. Additionally, nanostructures of varying polytypes and bandgaps exhibit strikingly similar PL emission centred at approximately 450 nm. At this wavelength, 3C-SiC emission is above bulk bandgap as expected of quantum size effects, but for 4H-SiC and 6H-SiC the emissions are below bandgap. 4H-SiC is a suitable polytype to study these effects. In this thesis, the hypotheses that mixed phases of polytypes or surface related defects obscuring the quantum confinement of 4H-SiC based nanostructure were investigated.

Density functional theory (DFT) calculations within the *Ab initio* Modelling Programme (AIMPRO) were performed on OH-, F- and H-terminated 4H-SiC QDs with diameters in the range of 10 to 20 Å. The chosen surface terminations relate to the HF/ethanol electrolyte used in preparation of SiC QDs and the choice of size coincide with where deviation was observed in experiments. It was found that the absorption onset energies deviated from quantum confinement with -OH and -F terminations, but conform to the prediction when terminated with -H. The weak size-dependent absorption onsets for -OH and -F is due to surface states arising from lone pair orbitals that are spatially localised to the quantum dot surface where these terminations reside. On the other hand -H termination show strong size-dependent absorption onsets due to delocalisation of the electron wavefunction towards the quantum dot core assisting quantum confinement. It is predicted that the surface related states dominate up to sizes 25 and 27 Å for -F and -OH terminations respectively. As a result, the recombination mechanism would involve the interplay between quantum confinement and surface states affecting the resultant energy gap and the resulting PL. The PL would exhibit

a dual-feature: excitation-wavelength independence for small sizes and excitation-wavelength dependence for diameters larger than 3 nm as observed in the experiments.

Mesoporous 4H-SiC was fabricated by anodic electrochemical etching in ethanoic HF electrolyte. The porous SiC suspended in ethanol exhibited three PL bands, those at wavelengths of 303 nm and 345 nm were rarely reported, above bulk bandgap and indicative of quantum confinement. The usually observed emission at 455 nm was below bulk bandgap. Dual-feature and below bandgap PL observed for wavelengths around 450 nm indicate that mesoporous 4H-SiC exhibited optical properties dictated by both quantum confinement (red-shifting with longer excitation wavelengths) and surface states (below bandgap). X-ray photoelectron spectroscopy provided evidence of -F, C=O and -COOH surface terminations that may contribute to these surface states. Raman scattering data exhibited a red-shift of 12.2 cm^{-1} and broadening in the lower frequency side of the longitudinal optical (LO) mode peak indicative of carrier depletion, surface phonons or phonon confinement as dimensions were reduced. The following ultrasonication process produced dimensions ranging from 16.9$\pm$5.5 down to 2.9$\pm$1.0 nm. The data from high resolution transmission electron microscopy (HRTEM) and X-ray diffraction (XRD) showed lattice spacing of 0.267 nm and peaks corresponding to the 4H-SiC polytype. No evidence of polytypic transformation from 4H-SiC to 3C-SiC resulting from ultrasonication was found in this work. Instead high crystallinity of 4H-SiC lattice was retained which suggested that the obscured quantum confinement may arise from surface effects rather than mixed polytypes.

Thermal oxidation and subsequent HF dip of mesoporous 4H-SiC resulting in pore wall thinning and surface removal was undertaken. Cross sectional SEM analysis showed reductions in average pore wall thickness to (20.5$\pm$2.8) nm, (18.2$\pm$2.9) nm, (17.0$\pm$1.8) nm and (15.9$\pm$1.4) nm for 1, 3, 6 and 9 hours of oxidation respectively. Following ultrasonication, the PL and PL excitation (PLE) characterisation showed absorption/emission band centred at 290/325 nm which were above bandgap. The below bandgap emission centred at 455 nm was removed and is a significant finding. Surface removal by thermal oxidation and HF dip resulted in suppressed below bandgap PL but retained the above bandgap PL. The evidence strongly indicate that the dual-feature PL and below bandgap emission in 4H-SiC seen in experiments are surface related rather than due to polytypic transformation during ultrasonication.

ACKNOWLEDGEMENTS

I am thankful to the Almighty for the PhD journey He has bestowed upon me. I would like to express my gratitude to those who have extended their help, support and companionship throughout my studies and towards the completion of this thesis.

Foremost, I am grateful and indebted to my dedicated supervisors, Dr. Alton Horsfall, Dr. Jonathan Goss and Dr. Noel Healy who were always there, providing guidance, support and motivation. Words alone cannot express my gratitude for all that they have done. I would like to thank Dr. Benjamin Horrocks for his kindness in helping me with the optical measurements.

I am thankful to my colleagues, Dr. Amit Tiwari, Dr. Hua Khee Chan, Idzdihar Idris, Faiz Arith, Syazwina Mohamed, Hector Oyem, Andres Aldana, Sandip Roy, Neal Wood, Chloe Peaker, Oras Al-Ani, Fatimah Bahrani, Hind Alsnani, Tiago Marinheiro, Luke Bradley, Johan Gausden, Enrique Escobedo-Cousin, Sami Ramadan, Srinivas Ganti, Paolo Comaron and many more who have contributed and made my years in pursuing PhD interesting as it was challenging. I would like to express my heartfelt gratitude to Abdul Muiz, Ahmad Marwan, Idzdihar Idris and their families for extending their generous hospitality and kindness in time of need.

I would like to thank for the services provided by Dr Budhika Mendes at Durham University for HRTEM imaging, Tracey Davey at the Medical School for TEM imaging, Dr. Jose Portoles at NEXUS for XPS and Dr. Isabel Arce Garcia at NACMA for the SEM imaging. I am indebted to both Universiti Sains Malaysia and the Ministry of Higher Education (MOHE) for sponsoring my study through the ASTS scholarship.

To my wife Azhana, my children Haziq, Damia, Umair and Hakim, my parents and family members, thank you for your great patience and unwavering support.

LIST OF PUBLICATIONS

1. Rashid, M., Horrocks, B.R., Healy, N., Goss, J.P. and Horsfall, A.B., 2016. 'Optical properties of mesoporous 4H-SiC prepared by anodic electrochemical etching'. *Journal of Applied Physics*, 120(19), p.194303.
2. Rashid, M., Tiwari, A.K., Goss, J.P., Rayson, M.J., Briddon, P.R. and Horsfall, A.B., 2016. 'Surface-state dependent optical properties of OH-, F-, and H-terminated 4H-SiC quantum dots'. *Physical Chemistry Chemical Physics*, 18(31), pp.21676-21685.
3. Rashid, M., Tiwari, A.K., Wood, N., Briddon, P., Goss, J.P., Rayson, M.J., Wright, N. and Horsfall, A.B., 2015. 'Tuning Optoelectronic Properties of 4H-SiC QDs Using-H,-OH and-F Surface Functionalisation'. In *Materials Science Forum* (Vol. 821, pp. 375-378). Trans Tech Publications.

LIST OF CONFERENCES

1. Rashid, M., Tiwari, A.K., Goss, J.P., Rayson, M.J., Briddon, P.R., Wright, N. and Horsfall, A.B., 'Tuning Optoelectronic Properties of 4H-SiC QDs Using H, -OH and F Surface Functionalisation', in European Conference on Silicon Carbide Related Materials (ECSCRM 2014), Grenoble, France, 21-25 September, 2014.

   (Poster presentation)
2. Rashid, M., Tiwari, A.K., Goss, J.P., Rayson, M.J., Briddon, P.R. and Horsfall, A.B., 'Effect of H, -F and OH Surface Terminations on Optical Absorption Onset of 4H-SiC Quantum Dots', in 42nd Conference on the Physics Chemistry of Surfaces interfaces, Salt Lake City, Utah, USA, 18-22 January, 2015.

   (Poster presentation)
3. Rashid, M., Tiwari, A.K., Goss, J.P., Rayson, M.J., Briddon, P.R. and Horsfall,

A.B.,'DFT Study on the Effect of H, -OH and F Surface Terminations Upon Optical Absorption Onset of 4H-SiC Quantum Dots' in Solid State Quantum Photonics 2016, The Edge, Sheffield, UK, 22 March, 2016.

(Poster presentation)

4. Rashid, M., Horrocks, B.R., Healy, N., Goss, J.P. and Horsfall, A.B., 'Quantum Confinement in Mesoporous 4H-SiC For Solution Based Processing of Optoelectronic Devices.' Symposium O, E-MRS 2016 Spring Meeting, Lille Grand Palais, Lille, France, 3 May, 2016.

   (Oral presentation)

5. Rashid, M., Horrocks, B.R., Healy, N., Goss, J.P. and Horsfall, A.B., 'Nanostructuring of 4H-SiC by Electrochemical Etching and Oxidation.' in UK Quantum Dot Day 2017, Dynamic Earth, Edinburgh, UK, 13 January, 2017.

   (Poster presentation)

Table of Contents

List of Figures

List of Tables

Chapter 1

Introduction

This chapter provides the background to quantum dots (QDs). This is followed by discussions on SiC as a promising non toxic and oxidation resistant nanomaterial, the experimentally observed optical properties of SiC quantum dots (QDs), description on SiC material properties and quantum confinement. The objectives and scope of the remainder of the thesis are then defined.

SiC QDs' biocompatibility and robustness in retaining their optical properties have been shown to surpass both II-VI and Si materials. However, the expected quantum size effects occur for diameters larger than approximately 3 nm, whilst smaller sizes deviate from the prediction of quantum confinement. The deviation is observed as a dual-feature in the photoluminescence (PL) spectra for the different polytypes of SiC despite the differences in bandgap, along with an unexpected similar emission peak at approximately 450 nm. This 450 nm emission peak is above bandgap for 3C-SiC but below bandgap for 4H-SiC and 6H-SiC, the latter being counterintuitive to quantum confinement. These observations have been attributed to phase transformation into 3C-SiC during ultrasonication or due to surface states, but to date the origin of the dual-feature PL has not been unequivocally determined or explained and is still under investigation.

The thesis describes the effect of surface termination (-OH, -F and -H) upon the optoelectronic properties of 4H-SiC QDs to elucidate the origin of the features observed in the PL spectra. Simulations using density functional theory (DFT) within the AIMPRO code was used to initially identify the charge distribution in the quantum dot and the optical energy gap. This was followed by experimental characterisation of mesoporous 4H-SiC manufactured by anodic electrochemical etching in HF/ethanol. The effect of ultrasonication on polytype change was investigated and found that phase transformation was highly unlikely. Pore wall thinning and surface removal by thermal

oxidation/HF etch was explored as a means of reducing the dimensions of quantum structures. Models were proposed to explain:

- The dual-feature PL in chapter 3.
- The above and below bandgap PL found for mesoporous 4H-SiC as described in chapter 4.
- The suppressed below bandgap PL (455 nm) after surface removal in as described in chapter 5.

1.1 Background to Quantum Dots

The use of quantum dots is not recent in human history. Historically, the ancient Egyptians have exploited the formation of PbS nanoparticles over 4000 years ago for cosmetics to dye their hair or wool black [1]. Precipitates of CdS and CdSe have been used in silicate glasses as one of the oldest and frequently used techniques to control the colour of glass. In 1981, size effects in terms of the blue-shifted optical properties was reported by Ekimov for nanometer sized CuCl in silicate glass [2]. In 1982, Efros [3] advanced the postulate of quantum size effects: that the change of optical and optoelectronic properties with size, can be utilised to control the colour of glass by either changing the size or stoichiometry of CdS_xSe_{1-x} in the glass matrix. In 1991, Rosetti and Brus [4] discussed the change in colour of colloidal solutions of semiconductor, after which various synthesis methods were developed for semiconductor nanocrystals.

Semiconductor nanocrystals or quantum dots (QDs) are crystalline inorganic particles that are spherically shaped with diameters ranging from 2 to 50 nm. QDs resemble molecules in the distribution of energy levels. Figure 1.1 is a schematic illustration of the formation of energy bands from atomic orbitals towards molecular and bulk crystal states. Splitting of the energy levels occurs when the the number of atoms increases as a consequence of the Pauli exclusion principle. For molecular sized crystals, the energy levels are discrete and the edges of the occupied and unoccupied energy levels are termed as the highest occupied molecular orbital (HOMO) and the lowest unoccupied molecular orbital (LUMO) respectively. For bulk crystals, the energy differences

between levels are small, forming bands that are quasi-continuous. The band edges are termed the valence band edge, E_V and the conduction band edge, E_C respectively, separated by the bulk bandgap, E_g. The net energy gap (E_g or HOMO-LUMO) increases with decreasing size of the crystal. While the energy levels of molecules are discrete, solids have continuous bands of energy levels and nanoparticles are in the intermediate and can be regarded as large molecules.

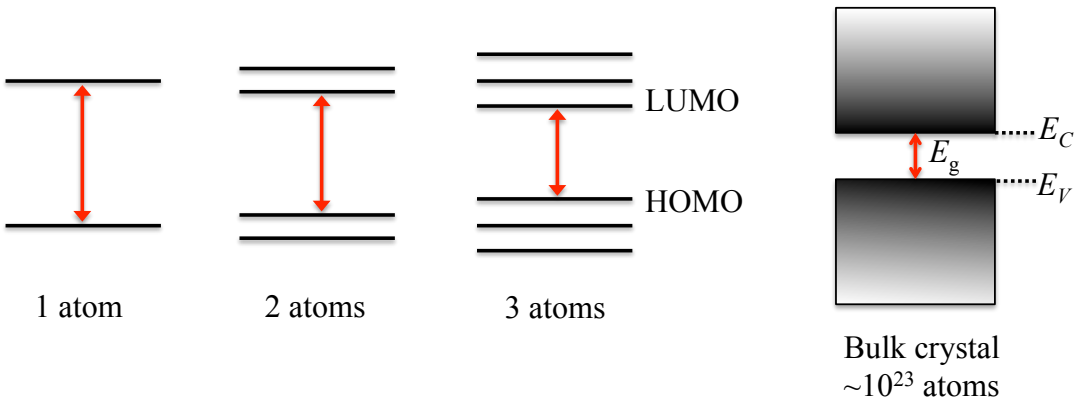

Figure 1.1: Schematic to illustrate the transition in the formation of energy bands from atoms and molecules towards the bulk state.

Consequently, for QDs, the decrease in size corresponds to increase in HOMO-LUMO gap (equivalent to the bulk, E_g), thereby increasing the photon energies required for absorption from the infrared towards the ultraviolet spectrum of the QDs. Additionally, the color of luminescence is dependent on the HOMO-LUMO gap. This attribute provides the means to fine tune the optical properties of the QDs and allow energy gap engineering for access to a specified wavelength. Fig. 1.2 shows how the constituent bands of the solar spectrum can be absorbed sequentially, from the UV by smaller QDs toward the infrared by larger QDs. In this example, energy loss due to thermalisation in a single junction solar cell can be overcome in a QD based multijunction solar cell by reducing the energy discrepancy between the absorbed photon (blue line) and the E_g or HOMO-LUMO gap (dashed black line) [5].

Table 1.1 show a comparison of bandgaps, dielectric constants and exciton Bohr radii of selected semiconductors. It can be observed that there is a general trend of reducing exciton Bohr radius and dielectric constant with increasing bandgap of the material.

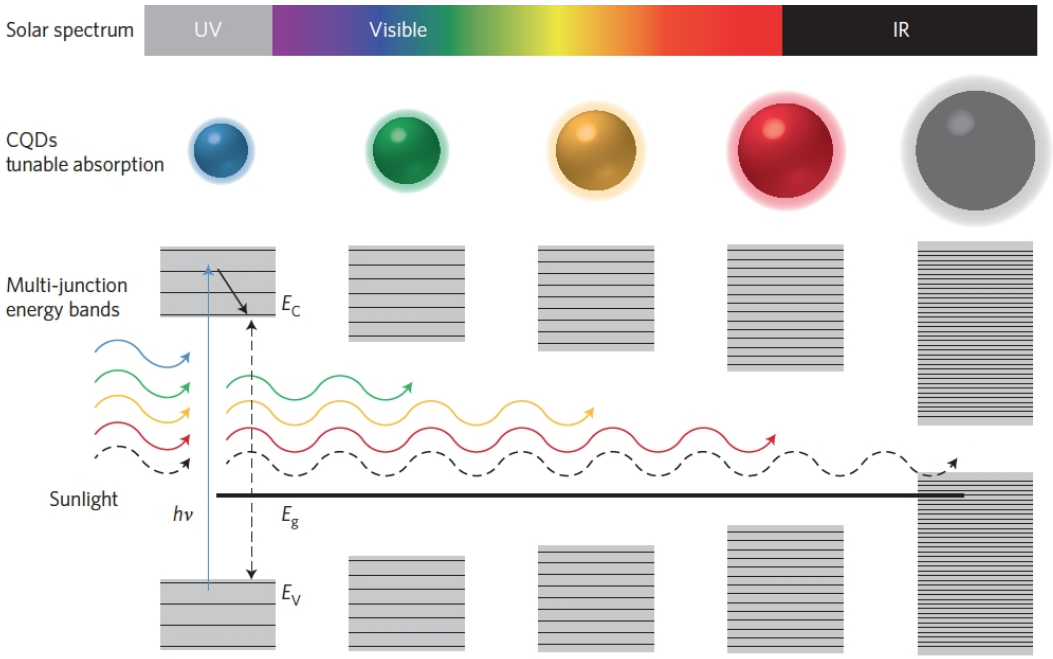

Figure 1.2: Size dependent absorption whereby decreasing QD size corresponds to increase in energy gap, E_g, absorbing increasing energies from infrared towards the ultraviolet spectrum. [5]

Figure 1.3(a) shows a HRTEM image of a CdSe QD (diameter less than the exciton Bohr radius: 6.1 nm) which may result in the delocalisation of the exciton across all the atoms within the QD core and consequently strong quantum confinement.

Figure 1.3(b) shows the emission spectra for CdTe, CdSe and ZnSe QDs for which emission energies are blue-shifted (above bandgap) due to quantum size effects. It follows then that with quantum confinement effect, 4H-SiC is expected to show PL emission at higher energies than ZnSe due to its wider bandgap as shown in Table 1.1, with expected PL emission peaks appearing at wavelengths shorter than 383 nm. As PL emission for 4H-SiC QDs predominantly appear at approximately 450 nm (below bandgap), further investigation is required in order to benefit from quantum confinement which would allow further access into the UV spectrum.

Table 1.1: Comparison table of bandgaps, dielectric constants and exciton Bohr radii of selected semiconductors [6, 7]. There is a trend of reducing exciton Bohr radius and dielectric constant with increasing bandgap.

Material	Bandgap (eV)	Dielectric constant	Exciton Bohr radius (nm)
CdSe	1.73	10.2	6.1
CdTe	1.48	10.2	6.5
CdS	2.48	9.4	3.1
ZnSe	2.67	7.1	2.8
4H-SiC	3.23	9.6	1.2

(a) (b)

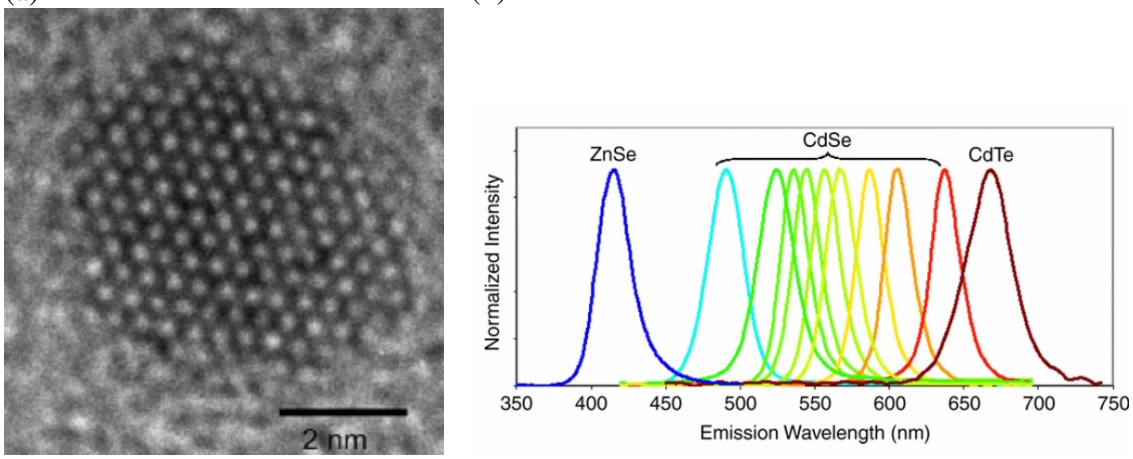

Figure 1.3: (a) A HRTEM image of a CdSe QD (b) Emission spectra for a series of different QD materials. The PL emission are blue-shifted with respect to the bulk bandgap due to quantum confinement.[8]

1.2 SiC as a Non Toxic and Oxidation Resistant Nanomaterial

There has a been significant amount of interest in nanomaterials, in which controlling matter at the molecular level allows the tailoring of fundamental properties at the scale at which these basic properties are determined [9].

Nanotechnology is defined by the National Nanotechnology Initiative in the United States [10] as the application of science that enable the control and restructuring of matter at the atomic and molecular levels in the size range of approximately 1-100 nm. The fundamental properties of nanostructures that distinguish them from their bulk counterparts include increased energy (blue-shift and above bandgap) in the optical properties [5] as a result of quantum confinement effects. The quantum size effects

occur at length scales close to the exciton Bohr radius, where the energy gap widens with decreasing particle size [11].

The energy onset in the optical absorption of 3-dimensionally confined nanostructures, namely quantum dots (QDs) is size-tuneable, a trait that has no equivalence in the bulk material. This unique property has been employed for *in vivo* bio imaging of living cells. In this application, fluorescent nanoparticles or QDs are internalised into cells in order that they can be imaged. Lead (Pb) and cadmium (Cd) chalcogenides have been dominating the field of bioimaging due to the well understood optical properties in these direct energy gap materials despite the fact that they are highly toxic [12] and highly sensitive to oxidation in ambient air. These materials require specialised capping in a core-shell structure with ZnS to render the Pb/Cd chalcogenides QDs stable in air and aqueous environments. New safer QDs, such as those manufactured from Si [13] and SiC [14] are required, however Si nanoparticles are prone to oxidation in air and water.

In contrast, silicon carbide (SiC) is a promising material that is both non-toxic and oxidation resistant. 3C-SiC QDs with an average size of 3.9 nm [14] showed robust photoluminescence (PL) emission centred at 450 nm with a quantum yield of 17%, comparable to that observed in Si nanoparticles. SiC QDs were shown to be water stable and oxidation resistant for months without any surface passivation [15]. The properties of SiC such as biocompatibility, chemical inertness, photostability, stability in aqueous environment and resistance to oxidation is highly attractive for a range of applications.

Nonetheless, researchers have observed that the optical properties of SiC QDs only follow the prediction of quantum confinement for diameters larger than approximately 3 nm but deviate for smaller sizes. Thus the expected and required size-tuneable optical properties below 3 nm was not achieved. In theory, with the exciton Bohr radii of 2.0, 0.7 and 1.2 nm for 3C-, 6H- and 4H-SiC [15] respectively, strong quantum size effects are expected to occur for diameters smaller than 4 nm in 3C- and 2.4 nm in 4H-SiC based QDs.

The deviation from quantum confinement was observed as a dual-feature in the photoluminescence (PL) spectra in which the PL emission peak position was constant

for short excitation wavelengths but red-shifting for longer excitation wavelengths. The dual-feature PL and strikingly similar PL emission peak at approximately 450 nm across all polytypes despite the varying bandgaps (3C: 2.36 eV, 6H: 3.00 eV, 4H-SiC: 3.23 eV) [16] have been attributed to phase transformation from 4H- or 6H-SiC into 3C-SiC polytype during processing (ultrasonication/laser ablation) in some studies [7, 17, 18] or due to surface chemistry in others [19–22].

1.3 The Dual-feature and Below Bandgap Photoluminescence Spectra in SiC Nanostructures

Generally, in order to verify the existence of quantum confinement effects, the red-shifting in PL peak position with increasing excitation wavelengths can be used [15, 17, 23]. As the excitation energy is systematically decreased with longer excitation wavelengths, only larger QDs are excited and smaller ones are excluded. Therefore the PL energy is expected to decrease (red-shift towards longer wavelengths). The majority of studies on PL spectra of SiC nanoparticles suspended in solvents reported that quantum size effects are observed for larger particles (diameter greater than $\sim$ 3 nm) but not for smaller diameters [7, 22, 24]. In these studies, PL peak position generally red-shifts with increasing excitation wavelengths for large sized SiC QDs, as expected from quantum size effects. In contrast, the PL peak position remained constant (not dependent on excitation wavelength) for small sized QDs (smaller than 3 nm), which contradicts the predictions from quantum confinement. Mixed results are reported in the literature, but in general the PL emission peak is shown to be insensitive to excitation wavelengths up to around 320 nm. The 'dual-feature' observation is schematically illustrated in Fig. 1.4(a) where region A depicts the constant PL peak position for excitation wavelengths shorter than 320 nm and region B where the PL peak position red-shifts for excitation wavelengths longer than 320 nm. For brevity, the associated regions A and B are referred to as 'constant PL' and 'red-shifting PL' and the combination of both trends are referred to as 'dual-feature'.

The dual-feature trend in the PL peak position with respect to excitation wavelength in experiment is clearly evident in Fig. 1.4(b) where deviation from the expected size-dependent PL emission (straight dotted line) occurs at approximately 320 nm [18].

The QD's size distribution in [18] was 2 to 5.5 nm and has been associated with the excitation of QDs smaller than 3 nm.

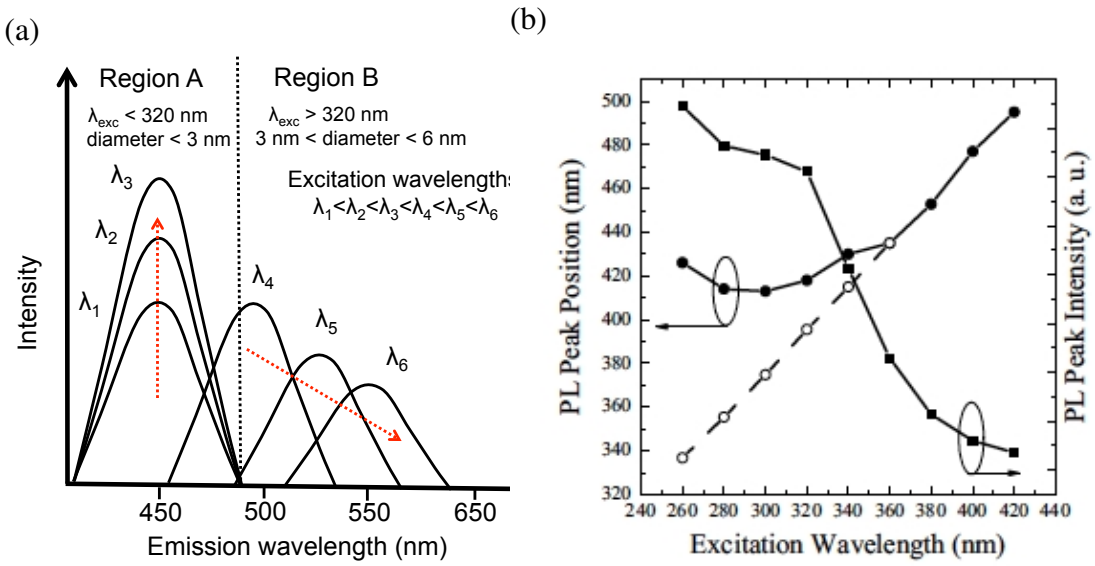

Figure 1.4: (a) Schematic illustrating the dual-feature PL spectra of SiC QDs characterised by the constant PL emission peak in region A and red-shifting PL peak in region B for excitation wavelengths shorter than or longer than 320 nm. (b) The experimentally observed deviation from quantum confinement (deviate from dotted line) in the PL peak position for excitation wavelengths shorter than 320 nm [18].

Table 1.2: Comparison of results in the literature and this work for characterisation of nanostructured SiC: showing polytype, constant PL emission and its excitation wavelength range, red-shifting PL emission and its excitation wavelength range, the PL emission energy relative to bulk bandgap, photoluminescence excitation (PLE) associated with absorption peaks, TEM, and XPS results. Dual-feature PL across polytypes and predominantly below bandgap emission in 4H-SiC and 6H-SiC are observed, being counterintuitive to quantum confinement. The above bandgap emissions (303, 345 nm) and corresponding absorptions (235, 280 nm) for 4H-SiC is a significant finding in this work.

Reference	Polytype	Constant PL emission (nm)	Excitation λ (nm) for constant PL	Red-shifting PL emission (nm)	Excitation λ (nm) for red-shifting PL	PL emission energy relative to bandgap	PLE (nm)	TEM (nm)	XPS
This work in [25]	4H-SiC	455 303, 345	320-340 250-279	455-470 -	320-400 -	below bandgap above bandgap	365 235, 280	Size: $16.9\pm5.5, 2.9 \pm 1.0$ lattice spacing: 0.267 [(100 / $10\bar{1}0$) 4H]	OH, F, C=O/COOH
[7]	3C-SiC 4H-SiC 6H-SiC	452	260-320	452-563	320-520	above bandgap below bandgap below bandgap	324, 348 ,368 297, 323, 365 288, 314, 365	Size: 1.0-8.0 lattice spacing: 0.217 [(200) 3C]	-
[26]	3C-SiC	375	240-345	-	-	above bandgap	258, 302, 326	Size: 0.2-1.8	C=O, C=C, COOH
[21]	3C-SiC	438	260-340	470-560	340-440	above bandgap	267, 326, 365	Size: 0.5-8.5 lattice spacing: 0.195 [(210) 3C]	OH, C=O, COOH
[22]	3C-SiC	435	310-340	435-510	350-410	above bandgap	-	Size: 1.5-6.5	OH
[17]	6H-SiC	434	280-360	450-550	360-540	below bandgap	-	Size: 1.0-10.0 lattice spacing: 0.195 [(210) 3C], 0.199 [(105) 6H]	-
[18]	6H-SiC	410	260-320	420-500	340-360	below bandgap	-	Size: 2.0-5.0 lattice spacing: 0.25 [(111) 3C, (102) 6H]	-
[27]	6H-SiC	430	325	-	-	below bandgap	-	25	-
[28]	6H-SiC	323	255	-	-	above bandgap	-	1.8-10	- -

Data summarised in Table 1.2 show that the reported PL results indeed exhibit the dual-feature illustrated in Fig. 1.4. Additionally, in the case of 6H- and 4H-SiC, the PL emissions were predominantly below the bulk bandgap energy. Sub bandgap emission do not concur with quantum confinement effects; as blue-shift and above bandgap emission is expected as a result of the HOMO-LUMO gap widening with decreasing size.

It is instructive to note an example of the unexpected similar PL properties observed in SiC polytypes regardless of the large bandgap difference such as 4H-SiC (E_g: 3.23 eV) and 3C-SiC (E_g 2.36 eV). In [7], SiC QDs were manufactured by the electrochemical etching/ultrasonication route. For QDs subjected to quantum size effects, the PL emissions are expected to be above bandgap in energy, which corresponds to emission wavelengths shorter than 383 nm for 4H-SiC and shorter than 525 nm for 3C-SiC. Figs. 1.5(a) and (b) however show strikingly similar PL emission centred at 452 nm as a function of excitation wavelength (260-560 nm) for both 3C-SiC and 4H-SiC QDs. Thus, 3C-SiC exhibited above bandgap emission whereas 4H-SiC in contrast, exhibited below bandgap emission. In TEM measurements, lattice spacings of 0.217 nm indexed to (200) planes of 3C-SiC was found in both 4H-SiC and 6H-SiC samples. This led to the hypothesis [7] that ultrasonic waves during sample preparation drove polytypic transformations of the QDs from hexagonal to cubic resulting in mixed phases of 3C and 6H, rendering similar PL spectra (centred at 452 nm) as shown in Fig.1.5(a) and (b).

Both polytypes exhibited a 'dual-feature' in the PL spectra (Figs. 1.5(a) and (b)) as denoted by the fixed and slanting black lines that distinguish the two regions. The constant PL under high excitation energies was attributed to the existence of defects including vacancies and interstitials. In contrast, the red-shifting PL under lower excitation energies was attributed to quantum confinement effects [7].

Fig. 1.5(c) and (d)[7] show the photoluminescence excitation spectra (PLE) under different monitoring emission wavelengths for 3C and 4H-SiC respectively. Each PLE peak corresponds to a particular absorption process. For 3C-SiC, the absorption peaks at 324 and 348 nm (Fig. 1.5(c)) were associated with defect related constant PL, whilst the 368 nm PLE peak was associated with quantum confined related states.

In the case of 4H-SiC, PLE peaks at 297 and 323 nm were said to be defect related, whilst the absorption at 365 nm was assigned to quantum confinement. The similar absorption band centred near 365 nm in both 3C and 4H-SiC were associated to the absorption line of the cubic SiC QDs. This follows the hypothesis that the QDs derived from different polytypes consist of both cubic and hexagonal QDs as a result of phase transformation during ultrasonication.

In another study [17], SiC QDs were produced by chemically etching 6H-SiC powder in HF-HNO_3 (3:1 by volume) at 100°C followed by ultrasonication. QDs suspended in ethanol with a mean size of 5 nm exhibited below bandgap PL emission band centred at 434 nm. Similar to the previous example, the observed sub bandgap emission of QDs was ascribed to α to β (hexagonal to cubic) phase transformation. TEM data showed both (210) planes of 3C-SiC and (105) planes of 6H-SiC were present [17]. A PL study on size segregated QDs showed that quantum confinement was dominant in the larger sized QDs whereas surface-defect luminescence dominate in the ultrasmall QDs (below 3 nm).

X-ray photoelectron spectroscopy (XPS) studies probed the surface chemistry of SiC QDs and showed that -COOH, C=O (carboxyl/carbonyl) [21, 26], and -OH (hydroxyl) [21, 22] groups or defects, reside on the surfaces. The data indicate that a second hypothesis to explain the origin of the dual feature PL and below bandgap emission is plausible: that surface terminations and surface defects are likely contributors; in which they introduce surface states within the energy gap obscuring quantum confinement.

Work on surface passivation have been done for applying SiC-QDs in solid thin films, including the encapsulation of 3C-SiC QDs with poly acrylic acid (PAA) [29]. Strong room temperature PL in the emission range 400-540 nm was achieved for excitation wavelengths between 300 and 500 nm. Wang *et al.* [30] fabricated glycerol-bonded 3C-SiC QDs, resulting in a PL peak emission centred at about 480 nm from solid films. In both cases, the data show PL emission associated with the dual-feature PL.

Interestingly, Beke *et al.* [19] has demonstrated in experiment that the PL emission of the QDs can be modulated by changing the surface chemistry, from as prepared 3C-SiC QDs (PL emission: 455 nm) to H-terminated QDs (PL emission: 410 nm) by

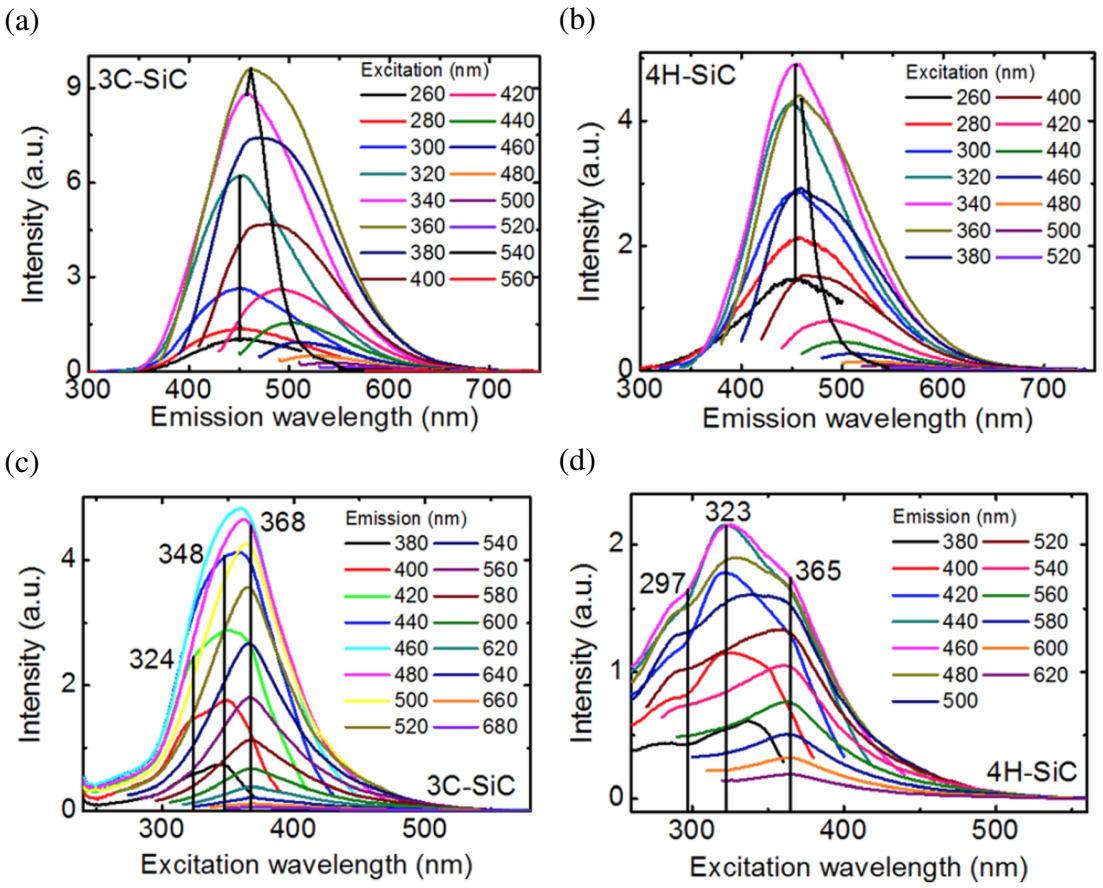

Figure 1.5: Similar PL spectra of aqueous solutions of SiC QDs derived from electrochemical etching of bulk with different bandgaps: (a) 3C-SiC and (b) 4H-SiC. Both polytypes exhibited a 'dual-feature' in the PL spectra as denoted by the fixed and slanting black lines that distinguishes the two regions in (a) and (b). PL emission centred at 452 nm is above bandgap for 3C- whereas 4H-SiC in contrast, is below bandgap. PLE spectra under different monitoring emission wavelengths are shown for (c) 3C-SiC and (d) 4H-SiC. Absorption peaks at 324, 348 nm for 3C and 297, 323 nm for 4H were associated with defect related constant PL. The 368 and 365 nm absorption peaks were associated with quantum confined related states for 3C and 4H respectively[7].

reduction with Zn/H^+. This strongly suggests that the luminescence of SiC QDs can be surface and environment-dependent when QD core properties are maintained.

Hence, there are two hypotheses in the literature that may explain the dual feature PL and below bandgap emission in experiments: firstly, they are consequences of mixed phases of 3C with other polytypes within the QD structures after polytypic transformation during ultrasonication and secondly, surface termination and surface defects on the QDs may introduce surface states within the HOMO-LUMO gap, obscuring quantum confinement effect. Whilst surface passivation has been attempted in experiments, surface removal after anodic electrochemical etching has not been reported.

In this thesis, sacrificial oxidation was performed on the mesoporous 4H-SiC through the pore wall thinning technique that resulted in the suppression of the below bandgap PL. This indicated that surface states within the energy gap originated from the surface as opposed to the bulk (polytype) which can be removed via sacrificial oxidation. The removal of the sub bandgap PL after surface removal is in support of the second hypothesis that surface termination and surface defects on the QDs may introduce surface states within the HOMO-LUMO gap, obscuring the quantum confinement effect. Additionally, DFT simulations showed that the interplay between the QD core related states and surface states would give rise to the observed dual-feature PL as observed in the experiment.

1.4 Ab Initio Calculations on SiC Nanostructures

Density functional theory (DFT) simulations have shown that apart from size, other factors including surface passivation, surface reconstruction and surface defects influence the optical properties of SiC nanostructures. Bandgap variation in spherical SiC nanoclusters was studied using DFT [31], based on the generalised gradient approximation (GGA), for dimensions in the range of 0.5 nm to 2 nm obtained from bulk 2H, 3C and 4H polytype crystals. The dangling bonds of the surface atoms were passivated using hydrogen atoms. It was found that the energy gap was not polytype dependent for sizes smaller than 1 nm as shown by the data in Fig. 1.6. The energy gaps

for nanocrystals larger than 1 nm exhibited size dependence with different polytypes and approach the respective bulk gaps as size increased. It was observed that the critical diameter at which 4H and 3C QDs become indistinguishable was 0.75 nm equivalent to ∼three Si-C bilayers. In other words, from the fourth layers (∼1 nm) onwards, the structural changes defining the polytypes were obtained giving rise to different energy gaps. The calculated size-dependent energy gaps for the different polytypes: 3C, 4H and 2H as shown in Fig. 1.6 is an assertion that quantum confinement for SiC QDs should be expected in the size range below 2 nm which however is not observed in the experiment for sizes smaller than 3 nm.

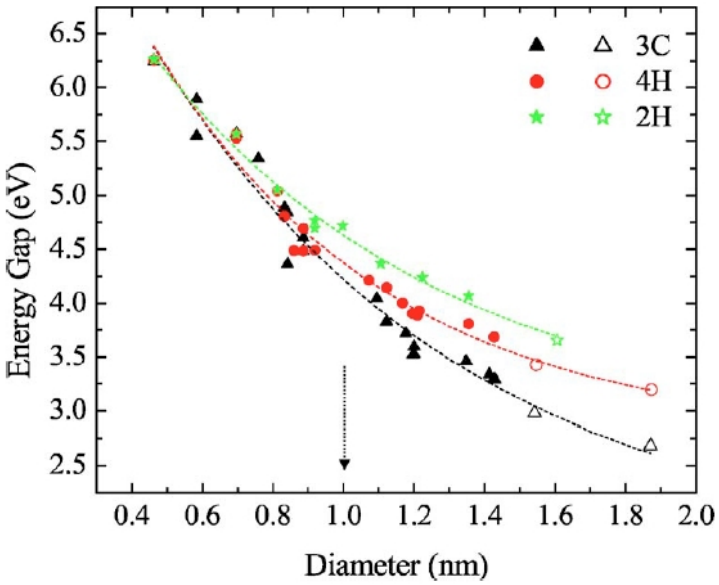

Figure 1.6: Variation of DFT calculated HOMO-LUMO gap with size for 3C- (black triangles), 4H- (red circles) and 2H-SiC, H-terminated QDs (green stars) [31]. The calculated size-dependent energy gap exhibiting quantum size effects for diameters less than 2 nm is an assertion that similar results should be expected in experiment, which is however not the case for QDs smaller than 3 nm in PL measurements.

The effect of surface reconstruction was investigated on H-terminated 3C-SiC QDs [32] for diameters between 0.9 and 3.2 nm using time-dependent DFT with the hybrid functional, PBE0 (Perdew, Burke, and Ernzerholf 0). It was found that long Si-Si dimers cause narrowing of the energy gap and surface reconstruction show higher

absorption intensity than nonreconstructed QDs, due to the enhanced dipole transition strength between the localised states and increased states near the HOMO and LUMO.

Fluorinated 3C-SiC nanowires [33] with hexagonal cross sections were studied by DFT via GGA with the Perdew, Burke, and Ernzerholf, (PBE) exchange-correlation functional. A fully fluorinated surface always results in a lower energy gap in comparison to a fully hydrogenated surface, this can be attributed to the difference in the electronegativity between H and F atoms and tuning of the bandgap was possible by varying the surface fraction of H and F atoms.

The effect of OH-termination and oxygenated surface of 3C-SiC nanoparticles [34] with diameters 0.9-1.4 nm was investigated by time-dependent DFT with the PBE0 functional. The presence of the Si-OH bond did not alter the optical gap whereas C-OH bonds may result in the lowering of the optical gap by $\sim$0.6 eV for a 8% coverage. C=O bonds resulted in significant narrowing of the optical gap indicating that sub bandgap emission may occur (red emission). Si=O bonds narrowed the optical gap slightly resulting in a blue emission. In contrast, single bonded Si-O and C-O bonds did not modify the optical gap and the emission was thus maintained in the ultraviolet region.

Surface structure and composition play a role in the investigated 3C-SiC QDs with diameters between 1 and 3 nm in a study using DFT within GGA and PBE exchange-correlation functional [35]. C-terminated and H-rich QDs were shown to have the largest energy gap. Conversely, when the surfaces are Si-terminated or H-deficient, the energy gaps of SiC QDs decreases. Surface C-C dimers were found to not only reduce the energy gap, but rendered the QDs almost size independent in the 1-3 nm range. The smallest gaps was shown by Si-terminated and Si rich QDs.

The electronic structure of 3C-SiC QDs in the size range 0.9-1.4 nm surface passivated by -H, -OH and -NH_2 was calculated by the density functional tight-binding (DFTB) method [36]. The -H passivated QDs exhibited the largest HOMO-LUMO gap followed by -OH and -NH_2 (Fig. 1.7). The optoelectronic properties of the nanoparticles are largely governed by the orbitals closest to the gap, being near the HOMO and LUMO. Inspection of the spatial distribution of HOMO and LUMO energies revealed that with surface passivation, the wavefunctions were delocalised

and fewer contributions were from the surface atoms. The HOMO was mainly centred on C atoms whilst the LUMO was centred on Si atoms.

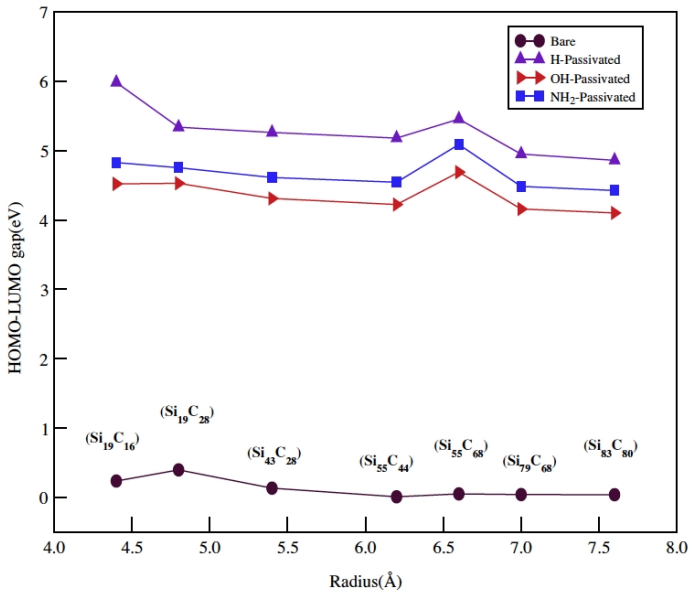

Figure 1.7: Variation of HOMO-LUMO gap of bare, -OH, -H and -NH_2 passivated 3C-SiC QDs [36].

Ab initio calculations revealed the effects of varying surface chemistry upon the optical gap of the SiC nanostructures. In general, H-termination resulted in optical properties governed by quantum confinement, whilst other termination species such as C=O bonds and -OH reduces the optical gap. Much focus have been given on the study of composition, surface termination, and surface reconstruction on 3C-SiC based nanostructures with some simulation results able to relate and explain the observed measurements in experiments. However, studies on polytypes other than 3C-SiC, such as 4H-SiC, which exhibit the unexpected below bandgap emission, is lacking and thus far the 'dual-feature' in the observed PL spectra of SiC QDs has yet to be fully understood and supported by DFT calculations.

1.5 Process Routes for the Preparation of Nanostructured SiC

The potential routes to the production of SiC nanoparticles with sizes sufficiently small to exhibit strong quantum confinement and efficient emissions are the vapor phase route, the solution route and the electrochemical etching route.

Table 1.3: Comparison table among different SiC nanostructure synthesis methods, highlighting the anodic electrochemical etch as the preferred route owing to its low cost, simplicity and ambient conditions processing.

Process considerations	Plasma assisted deposition	Solvothermal	Acid etch	Laser ablation	Anodic electrochemical etch
Temperature (°C)	170-575	600	100	20 (room)	20 (room)
Pressure (Torr)	10^{-7} to 2 (vacuum)	$\sim 750 \times 10^3$ (in Ti alloy autoclave)	760 (atmospheric)	760 (atmospheric)	760 (atmospheric)
Particle size (nm)	< 20	< 25	< 10	< 10	< 10
Crystallinity	mixed amorphous and crystalline	crystalline	crystalline	crystalline	crystalline
Hazardous material	SiH_4 (ignite in air)	$SiCl_4$ (corrosive)	HF/HNO_3 (toxic and corrosive)	-	HF (toxic and corrosive)
Cost	high	medium	low	medium	low
Route	vapor phase	solution	solution	solution	electrochemical etching

As summarised in Table 1.3, in comparison to the vapor phase and solution routes, the anodic electrochemical etching route has been the preferred process in combination with ultrasonication due to the lower cost and simplicity in experimental set up allowing for room temperature and ambient atmospheric pressure processing.

In the vapor phase route, laser pyrolysis of gaseous silane (SiH_4) and acetylene (C_2H_2) can produce SiC nanoparticles with a size distribution centred around 10 nm diameter [37] and red PL was observed which was ascribed to the inclusion of amorphous material and the presence of Si-O bonds.

In hypersonic plasma particle deposition (HPPD) [38], vapor phase precursors such as tetrachlorosilane ($SiCl_4$) and hydrocarbon (methane, CH_4 and acetylene, C_2H_2) were injected into an Ar-H_2 plasma generated by a DC arc. The plasma underwent a supersonic expansion and ultrafine particles nucleated and deposited on a temperature controlled substrate (170°C). Amorphous SiC with grain sizes of the order of 20 nm

was obtained.

Plasma enhanced chemical vapor deposition (PECVD) techniques [39] employing temperatures ranging from 80°C to 575°C using diethylsilane ($(C_2H_5)_2SiH_2$) diluted in H_2, Ar or He, can produce nanocrystallites in the size range of 2 to 10 nm in an amorphous matrix. The onset temperature of crystallisation was found to be 300°C. The crystallisation factor improved to 65% when the temperature was increased to 575°C.

The solution route includes several techniques. β-SiC was synthesised by the solvothermal method at 600°C based on reduction-carbonisation [40], where Na served as the reductant and carbon and $SiCl_4$ were the source materials. Spherical particles with average diameters of 25 nm can be produced.

β-SiC QDs have been produced with average 3.5 nm size by laser ablation [41] from Si wafer immersed in pure ethanol using a Nd:YAG laser operated at 1064 nm (10 ns pulses, 10 Hz). The liquid was stirred during irradiation for 2 hours. The resulting QDs suspended in ethanol showed PL peak position that red-shifted from 417 nm to 451 nm with increasing excitation wavelengths from 340 nm to 400 nm. The observed excitation-wavelength dependent red-shift was attributed to quantum confinement.

To improve yield, work has been performed on chemical etching of 3C-SiC powders with grain sizes of several micrometers [42]. Nitric acid (HNO_3) and hydrofluoric acid (HF) was used to etch 3C-SiC powder at 100°C for 1 hour. The resulting 3C-SiC nanocrystals were ultrasonicated and dispersed in ethanol, resulting in QDs with sizes smaller than 6.5 nm and an average of $\sim$3.6 nm.

The electrochemical etching route of crystalline substrate, is the favoured method in producing SiC nanocrystals with ultrasmall sizes due to the simplicity in experimental setup, room temperature processing and high crystallinity of the obtained nanocrystals. Pioneering work by Shor *et al.* [43] first reported on porous SiC formation by anodizing *n*-type 6H-SiC in HF under UV illumination in a Teflon electrochemical cell. Mesoporous structures with pore sizes of 10-30 nm with interpore spacings 5-150 nm were reported. Ke *et al.* [44] performed anodic electrochemical etch on n-type 6H-SiC and showed that nano-columnar pores of $\sim$20 nm diameter can be achieved by using a voltage bias of 20 V.

QDs and ultrasmall nanocrystals can be derived from porous structures via a two step process - anodic electrochemical etching followed by ultrasonication. Anodic electrochemical etching and ultrasonication of polycrystalline 3C-SiC in HF/ethanol (HF/C_2H_5OH, 2:1 ratio) was performed [23]. The process included etching of 1 hour at a current density of 60 mA/cm^2 followed by ultrasonication. The resulting 3C-SiC nanocrystals were in the size range of 1-6 nm. The PL emission peak maximum, ranged from 440 nm to 560 nm for excitation wavelengths of 320 nm to 490 nm.

In summary, the electrochemical etching route of crystalline substrate in HF, is the favoured method in producing SiC nanocrystals in order to obtain ultrasmall sizes using a low cost and simple experimental setup for processing at room temperature. Particle diameters of less than 10 nm can be produced.

1.6 Material Properties of SiC

SiC forms over a hundred different crystal structures which describe over a hundred different polytypes. Fig. 1.8 show the schematic cross sections of the atomic crystal structures for four of the most technologically relevant SiC polytypes [45]. Polytypes differ in the sequences that SiC bilayers (or SiC double layers) are stacked. A SiC bilayer is as highlighted in the dashed boxes in Fig. 1.8(a) and labelled using a letter notation. Each atom in a bilayer is covalently bonded to 3 other atoms within the same bilayer while the fourth atom is covalently bonded to an adjacent bilayer. In ABC notation, the top most bilayer serves as the reference and is denoted A. The next bilayer is denoted B and its upper atoms are directly below the lower atoms of bilayer A. Further bilayers are denoted A: if the upper atoms are directly below the upper atoms of the reference or B: if the upper atoms are below the lower atoms of the reference bilayer respectively. Otherwise, when the upper atoms are below the hexagonal hollow of the reference layer it is then denoted as C. A sequence of 3 different letters (ABC) indicates cubic type stacking whereas a letter (for example B) being in between the same 2 letters (ABA) indicate a hexagonal site. Local cubic sites consist of translations of subsequent layers whereas hexagonal sites consist of both translations and rotations of subsequent layers. In Ramsdell notation, 4H-SiC refers to 4 SiC bilayers (ABCB) to define a unit repeat cell in its hexagonal (H) crystal

structure along the c-axis (often labelled as [0001] using Miller indices, indicating the direction of growth) while 6H-SiC requires 6 SiC bilayers (ABCACB) in its hexagonal structure. Fig. 1.9(a) illustrates the hexagonal unit cell of 4H-SiC consisting of the crystallographic faces: $(1\bar{1}00)$, $(11\bar{2}0)$, $(1\bar{1}02)$ and the c-axis along $<0001>$ direction whilst Fig. 1.9(b) indicate the $(11\bar{2}0)$ and $(1\bar{1}02)$ as black and grey lines within the 4H-SiC structure [46]. The cubic polytype 3C-SiC has a zinc blende crystal structure and is also known as beta-SiC, β-SiC, whereas hexagonal polytypes such as 4H and 6H-SiC with hexagonal crystal structure (wurtzite) are referred to as alpha-SiC, α-SiC.

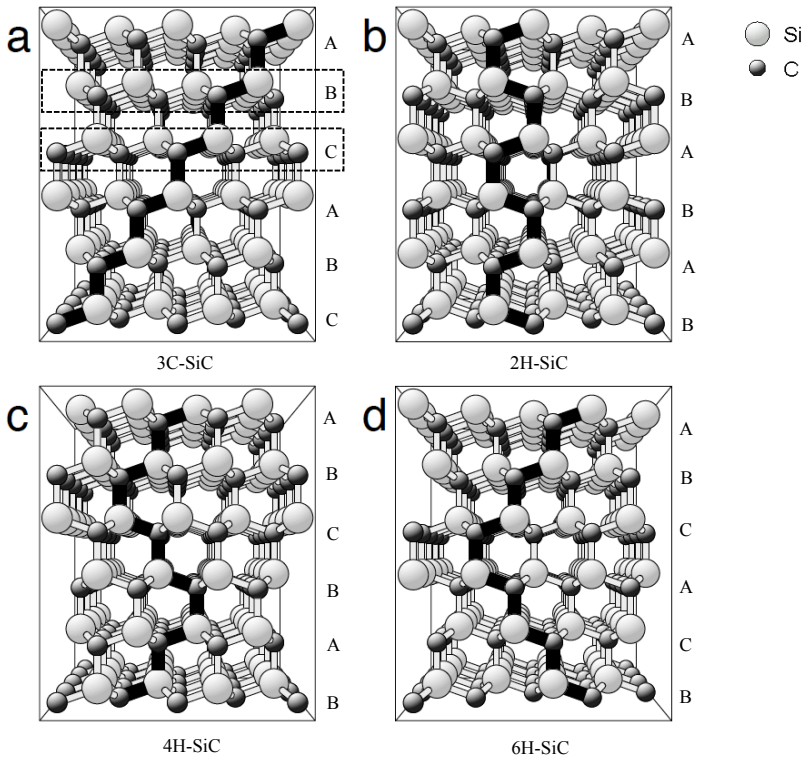

Figure 1.8: Schematic atomic structures along with Ramsdell and ABC notations for (a) 3C-SiC, (b) 2H-SiC, (c) 4H-SiC and (d) 6H-SiC in a side view in [1120] direction [45].

Due to these different Si and C atom arrangements, SiC crystals exhibit differing electrical and optical properties as shown in Table 1.4 [16]. SiC has an advantage in comparison to Si, for applications requiring material robustness and chemical inertness, as evident in its higher melting point at 2820 °C (in comparison to Si is

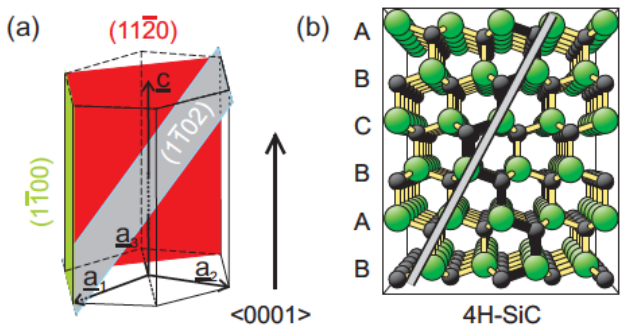

Figure 1.9: Schematic orientation of 4H-SiC for (a) (1$\bar{1}$00) face, (11$\bar{2}$0) face, (1$\bar{1}$02) face and the c-axis along the <0001> direction. (b) Side view of 4H-SiC polytype structure with bonds within the (11$\bar{2}$0) plane indicated by a black line and (1$\bar{1}$02) plane as the grey line [46].

at 1412 °C). The higher melting point corresponds to the higher dissociation bonding energy of Si-C (318 kJ/mol) in comparison to the Si-Si bond (222 kJ/mol) [47]. The high melting point (high bond strength) and wide energy gap contribute to SiC being oxidation resistant and suitable for applications at extreme temperatures [48] and in the higher energy range (UV-blue) of the electromagnetic spectrum.

Fig. 1.10 shows the band structure of 4H-SiC depicting the important minima of the conduction bands and maximum of the valence band. The energy gaps between the top of the valence band and M, Γ, L valleys are shown. The bandgap range of 2.36-3.23 eV in SiC are wide in comparison to 1.12 eV for Si. The wide bandgap for SiC allow optoelectronics applications in the ultraviolet range which otherwise would not be readily accessible in Si or Ge.

1.7 Quantum confinement

One of the unique properties found in nanostructures is quantum confinement. When the length scale is near or smaller than the exciton Bohr radius, a_B of charge carriers in a semiconductor (21 nm in PbS, 5 nm in Si, and 1.2 nm in 4H-SiC)[7, 11], quantum confinement occurs as depicted schematically in Fig. 1.11(a).

During optical absorption in a bulk semiconductor, an electron is excited across the bandgap to an excited state in the conduction band leaving a hole in the valence band,

Table 1.4: Properties of SiC and Si [16]. SiC is a robust material to operate in the UV/blue range and chemically stable as evident in its wider energy gap and twice as high in melting point in comparison to Si.

Property	3C-SiC	4H-SiC	6H-SiC	Si
Energy gap (eV)	2.36	3.23	3.00	1.12
Dielectric constant	9.72	9.66	9.66	11.90
Lattice constant (Å)	4.3596	a=3.0730 c=10.053	a=3.0806 c=15.1173	5.431
Direct gap (eV)	6	5-6	5-6	3.3
Melting point (°C)	2826	2826	2826	1412
Breakdown field (V cm^{-1})	$\sim 10^6$	$3X10^6$	$3X10^6$	$0.6X10^6$
Intrinsic carrier concentration (cm^{-3})	~10	$\sim 10^{-7}$	$\sim 10^{-5}$	$\sim 10^{10}$

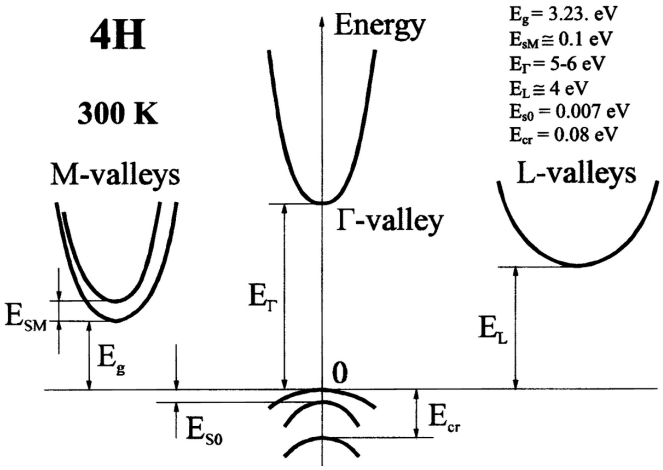

Figure 1.10: Band structure of 4H-SiC [16].

creating an electron-hole pair (EHP) known as an exciton. The distance between the electron and hole is called the exciton Bohr radius, a_B. The exciton can be considered to be the lowest excited state of the semiconductor solid consisting of an electron orbiting a hole, analogous to an electron orbiting a proton in a hydrogen atom in the Bohr model.

The binding energy of an exciton can be expressed as [49]:

$$E = \frac{\mu e^4}{2\hbar^2 \epsilon_r^2} \tag{1.1}$$

where μ is the reduced effective mass of the EHP ($\mu = m_e m_h/(m_e + m_h)$), $\hbar$ is

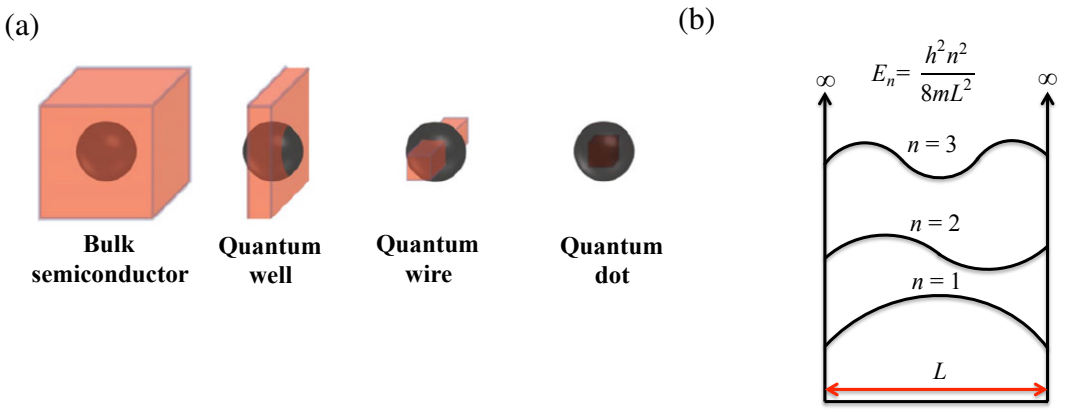

Figure 1.11: (a) Schematic illustration of quantum confinement from reduced semiconductor dimensionality with respect to the exciton Bohr diameter, $2a_B$. The Bohr diameter is represented by the sphere. (b) Representation of the wavefunctions for the first three states of a 'particle in a box', confined in a 1-D infinite square well potential with length L.

the reduced Planck constant, ϵ_r is the dielectric constant of the semiconductor and e is the electron charge. The binding energy of an exciton is typically 100 to 1000 times smaller than that of a hydrogen atom (13.6 eV). This is contributed by two factors: firstly, the free electron in a crystal lattice sees an effective charge of the hole that is reduced from the electron charge e by the dielectric constant, ϵ_r of the medium. In other words, the Coulomb interaction between the EHP are screened by the intermediate atoms within the solid. Secondly, the effective masses of the electron and hole, m_e and m_h in semiconductors are typically smaller than the electron rest mass, m_o.

As formalised in the Bohr model, the Bohr radius, a_o is the mean radius of the orbit of an electron around the nucleus of a hydrogen atom at its ground state which can be calculated as:

$$a_o = \frac{4\pi\epsilon_o\hbar^2}{e^2 m_o} = 0.053\ nm \tag{1.2}$$

where $\hbar$ is the reduced Planck constant, ϵ_o is the permittivity of free space, e is the electron charge and m_o is the electron rest mass.

By analogy, the exciton Bohr radius, a_B for a semiconductor, can be calculated by scaling the hydrogen atom Bohr radius, a_o (0.053 nm) from the Bohr model, by the

ratio of the semiconductor dielectric constant, ϵ_r, and reduced effective mass of the electron-hole pair (EHP), μ [7]:

$$a_B = \frac{4\pi\epsilon_o\epsilon_r\hbar^2}{e^2\mu} = \epsilon_r\frac{m_o}{\mu}\,0.053\;(nm) \tag{1.3}$$

The combined effects of smaller effective masses and electrostatic interaction screening results in the exciton Bohr radius, a_B of semiconductors, being significantly larger than the Bohr radius, a_o of the hydrogen atom (0.053 nm) [50].

In quantum mechanics, the particle in a box model with infinitely high walls is used to describe quantum systems. The electron wavefunction does not propagate freely beyond the physical dimensions of the dot, but form standing waves (stationary states) within the confinement of the nanoparticles.

For an electron in a 1-dimensional infinite square well potential (as depicted in Fig. 1.11(b)), the condition to satisfy a standing wave that consists of *n* half-waves of wavelength λ, in a box with size L (corresponding to the particle diameter, *d*) can be described using:

$$L = \frac{n\lambda}{2} \tag{1.4}$$

Equation 1.4 is substituted into the De Broglie equation that describes the wave properties of matter (electrons in this case), which then leads to:

$$p = mv = \frac{h}{\lambda} = \frac{nh}{2L} \tag{1.5}$$

where *p* is the momentum, *m* is the mass, and *v* is the velocity of the electron.

Calculating the energy of the electron, E_n, in the quantum state denoted by *n*, gives:

$$E_n = \frac{mv^2}{2} = \frac{p^2}{2m} = \frac{h^2}{2m\lambda^2} = \frac{h^2n^2}{8mL^2} \propto \frac{n^2}{L^2} \tag{1.6}$$

The value of λ from equation 1.5 is substituted into equation 1.6 to express E_n in terms of L, which corresponds to the particle diameter, *d*. The important fundamental characteristics of quantum confined systems can be identified from equation 1.6 are

that the confinement energies of the electron are discrete and scale as $1/d^2$ (inversely quadratic to the nanoparticle diameter). The direct consequence on the optical properties of the nanoparticle is that as the particle size decreases, its energy gap increases, resulting in the increase of its absorption onset in energy. In optical measurements, the absorption edge will blue-shift in energy with decreasing particle size.

Quantum confinement is related to the number of degrees of freedom of the carriers within the boundaries of the particles [51]. Figure 1.12(a) shows a 2D system (quantum well): where carriers are confined in 1 dimension with 2 degrees of freedom, a 1D system (quantum wire): where carriers are confined in 2 dimensions with 1 degree of freedom and a 0D system (quantum dot): where carriers are confined in 3 dimensions with 0 degrees of freedom. The change in the confinement dimension directly alters the allowed energies of the occupation levels as shown by the density of states (DoS) in Fig.1.12(b). With stronger confinement (fewer degrees of freedom) the energy onset of the DoS increases whilst becoming more discrete. The modified DoS as a result of the change in dimension allows for band gap engineering, where the absorption or emission of a material can be engineered to a specific wavelength by reduction in the size of the material to length scales close to the exciton Bohr radius.

Apart from modification of the DoS, an alternative route to band gap engineering is through the breaking of rules for the conservation of momentum. Si, Ge and SiC are indirect gap semiconductors in the bulk state that require the aid of a phonon in order to have optical emission. This is a consequence of the Heisenberg uncertainty principle: localisation of carriers in a confined volume spreads the electron and hole wave functions in reciprocal space [51–53]. The tails of both electron and hole distributions overlap (as depicted in the dashed circle of Fig. 1.13(a)) resulting in the breaking of the usual crystal momentum selection rules. Consequently, zero phonon vertical transitions (denoted by the dotted arrow line) become allowed in accordance to the overlap of the carriers' wave functions, instead of the usual phonon assisted optical transition (solid arrow line). The effect of lowering the dimension of a crystallite results in an increased coupling between the transition matrix elements of the electron and hole states. Reduction of particle size result in increased coupling between hole and electron wavefunctions at different Brillouin zone locations as shown

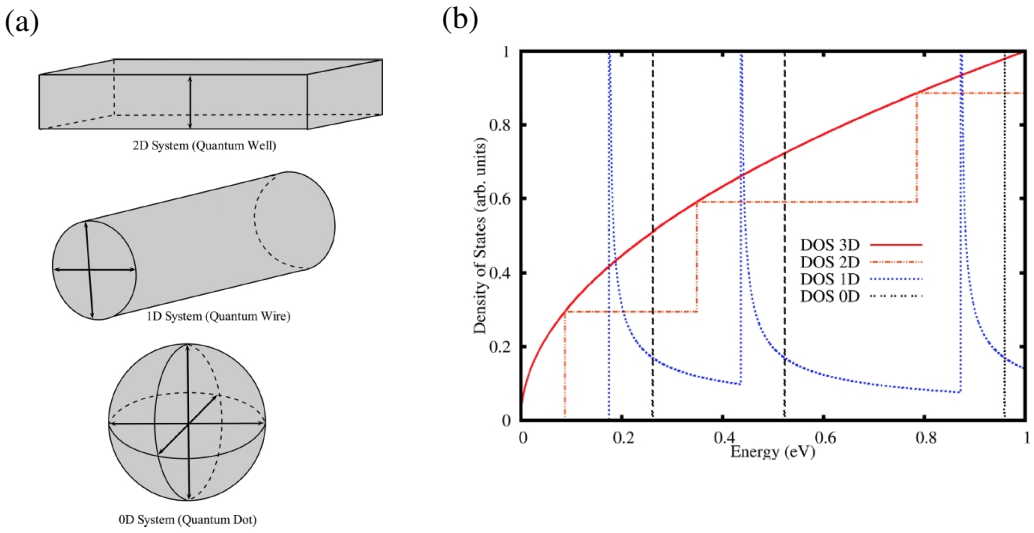

Figure 1.12: The different degrees of freedom in quantum systems (a) and the corresponding density of states (DoS) with the bulk (3D) shown for comparison. [51]

in Fig.1.13(b) [51]. Consequently, the transition probability increases and hence optical transitions across the bandgap can occur at different locations of the Brillouin zone without phonon assistance (Fig. 1.13(a)). This effect is meaningful for indirect bandgap materials as the luminescence rate [51–53] may be increased by the breaking of the *k*-conservation rules. Additionally, a disorder or break in the translational symmetry of the crystal lattice may relax the *k*-conservation rules.

1.8 Scope of Thesis

Following the literature review in this chapter, there are two hypotheses in the literature that may explain the dual feature PL, below bandgap emission and deviation from quantum confinement for diameters smaller than 3 nm: firstly, they may be consequences of mixed phases of 3C with other polytypes within the QD structures after polytypic transformation during ultrasonication and secondly, surface termination and surface defects on the QDs may introduce surface states within the HOMO-LUMO gap, obscuring quantum confinement effect. The objectives of this study are laid out to address these hypotheses. The objectives are to :

(a) (b)

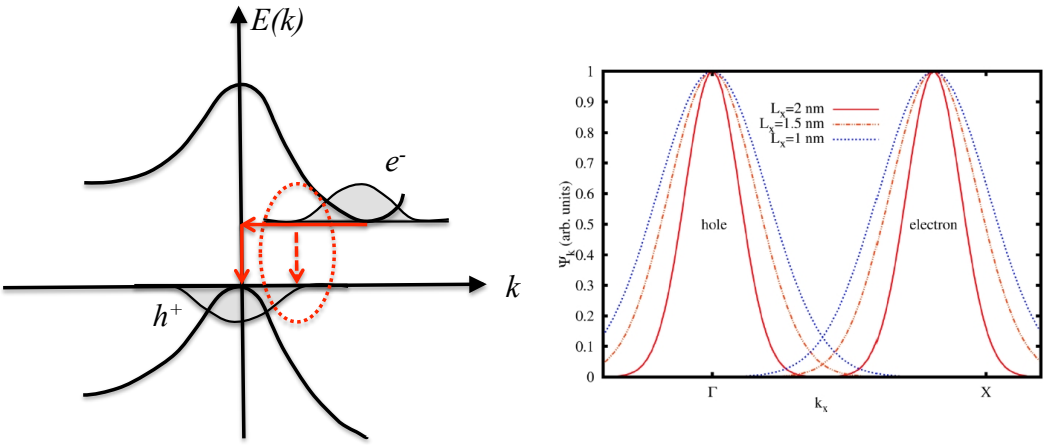

Figure 1.13: Breakdown of the momentum conservation rules where (a) electron and hole wavefunctions spread in reciprocal space allowing zero phonon transition and (b) increase of the overlap between hole and electron wavefunction with decreasing size.[51]

- utilise DFT simulation to identify the effect of surface chemistry on the optical properties of 4H-SiC QDs for a range of sizes (1 to 2 nm) which coincide with the size range affected by the deviation from quantum confinement (less than 3 nm) in experiments and explain the dual-feature PL spectra that have been observed,
- manufacture mesoporous 4H-SiC via anodic electrochemical etching and ultrasonication processes followed by structural and optical characterisations to determine polytype, crystallinity, size and PL characteristics,
- evaluate a new pore wall thinning technique by sacrificial oxidation (post electrochemical etch treatment) on mesoporous 4H-SiC. The surface removal by thermal oxidation/HF etch followed by optical characterisation serve two purposes which are to reduce dimensions and to distinguish whether the below bandgap emission was contributed by mixed phases within the core or contributed by surface related defects of the nanostructure.

Chapter 2 describe the methodology and techniques used in the subsequent thesis chapters 3, 4 and 5. Density functional theory (DFT) within *ab initio* Modelling

Program (AIMPRO) was applied to study the effect of surface chemistry on 4H-SiC quantum dots' (QDs) optoelectronic properties. The specifics for structural construction of OH-, F- and H-terminated 4H-SiC QDs of varying diameters from 10 Å to 20 Å are given and the calculated absorption cross section and joint density of states are discussed. The details of the experiment on the manufactured mesoporous 4H-SiC by anodic electrochemical etching in HF/ethanol electrolyte and the various optical and surface characterisation techniques of the material such as photoluminescence (PL), Raman scattering, X-ray photoelectron spectroscopy (XPS), transmission electron microscopy (TEM), and X-ray diffraction (XRD) are outlined. The experimental approach by thermal oxidation that resulted in the pore wall thinning of mesoporous 4H-SiC and its subsequent characterisation to understand the effect on optical properties are explained.

Chapter 3 presents a DFT study implemented within the $Ab\,Initio$ Modelling Programme (AIMPRO) code. In order to understand the effect of surface chemistry upon the optical properties of 4H-SiC QDs: different surface composition, surface reconstructions and surface termination groups (OH, F and H) were compared for QDs with diameters ranging from 10 Å to 20 Å. The impact on onset energies for absorption cross section (ACS), and joint density of states (JDoS); and spatial distribution in the electron probability density were assessed. A novel model to account for and explain the dual-feature PL spectra as observed in the experiments for SiC nanostructures was developed.

Chapter 4 shows the manufacturing of mesoporous 4H-SiC by anodic electrochemical etching in ethanoic HF electrolyte. In order to ascertain polytype, crystallinity and crystallite size, the delaminated porous layer was characterised by Raman scattering, X-ray diffraction (XRD) and atomic force microscopy (AFM). The delaminated layer was subjected to ultrasonication and subsequently dispersed in ethanol. To measure the optoelectronic properties and chemical composition; characterisation by UV-Visible absorbance, photoluminescence (PL), photoluminescence excitation (PLE), X-ray photoelectron spectroscopy (XPS), high resolution transmission electron microscopy (HRTEM) and current-voltage (I-V) was performed. A model based on the findings in chapter 3 was developed to explain the observed optical characteristics for mesoporous 4H-SiC.

Chapter 5 demonstrates a new sacrificial oxidation treatment on porous SiC wherein the as-etched mesoporous 4H-SiC was oxidised at 1100°C for durations of 1, 3, 6 and 9 hours. The oxidised mesoporous structure was then dipped in HF to remove the oxide layer. The reduction in the pore wall thickness was evaluated by cross sectional scanning electron microscopy (SEM). The effect of the treatment was assessed by Raman scattering spectroscopy. Following ultrasonication and dispersion in ethanol, characterisation by PL and PLE was undertaken. The observed changes in the optical characteristics including the important suppression of below bandgap emission after surface removal are discussed in relation to the model developed in chapter 4.

Chapter 6 summarises and concludes the work. Suggestions for future work are included.

Chapter 2

Methodology

This chapter is intended to describe the methodology used in the subsequent thesis chapters 3, 4 and 5. For chapter 3, density functional theory (DFT) calculations within *ab initio* Modelling Program (AIMPRO)[54–56] were performed to study the effect of surface chemistry on the optoelectronic properties of 4H-SiC quantum dots (QDs). The underlying theory and specifics for structural construction of OH-, F- and H-terminated 4H-SiC QDs of varying diameters from 10 Å to 20 Å are given and the calculated absorption cross section and joint density of states are discussed. In relation to chapters 4 and 5, the details of the experiment on the manufactured mesoporous 4H-SiC by anodic electrochemical etching in HF/ethanol electrolyte and the experimental approach by thermal oxidation that resulted in the pore wall thinning of mesoporous 4H-SiC are described. This is followed by discussion on the optical and surface characterisation techniques of the material such as Raman scattering, photoluminescence (PL), photoluminescence excitation (PLE), X-ray diffraction (XRD), X-ray photoelectron spectroscopy (XPS), atomic force microscopy (AFM) and high resolution transmission electron microscopy (TEM).

2.1 DFT Background and Implementation

A wave equation to explain the observed wave-like behaviour of atomic particles was developed by Schrödinger. The stationary Schrödinger equation can be solved for a single particle:

$$\frac{-\hbar^2}{2m}\nabla^2\Psi + V(\boldsymbol{r})\Psi = E\Psi \tag{2.1}$$

where m is the reduced mass, $\boldsymbol{r}$ is the relative coordinate and V the effective potential.

The wavefunction of the equation can be used to determine the probability distribution, the probability of finding the particle at a certain position. The solution is a wave describing the quantum aspects of a system from which the allowed energy levels can be determined. The stationary Schrödinger equation can be solved for simpler cases such as the free particle and hydrogen atom.

In order to calculate the electronic properties of molecules and solids using *ab initio* (from first principles) methods based only on atomic constants and coordinates, requires a solution to the Schrödinger equation:

$$\hat{H}\Psi = E\Psi \tag{2.2}$$

where $\hat{H}$ is the many body Hamiltonian, Ψ the many body wavefunction and E corresponds to the energy eigenvalue. Ψ is a function of electron spatial spin coordinates and nuclear positions, and can be expressed as

$$\Psi = \Psi(\boldsymbol{r}_1, \boldsymbol{r}_2, ...; \boldsymbol{R}_1, \boldsymbol{R}_2, ...) \tag{2.3}$$

where $(\boldsymbol{r}_1, \boldsymbol{r}_2, ...\boldsymbol{r}_N)$ are the electrons' coordinates and $(\boldsymbol{R}_1, \boldsymbol{R}_2, ...\boldsymbol{R}_M)$ are the coordinates of the nuclei, each of mass $(M_1, M_2, ...M_M)$.

In real systems, there would be many interacting particles for which precise calculations would be resource prohibitive. In these cases approximations in the calculations are required.

2.1.0.1 The Born-Oppenheimer Approximation

Born-Oppenheimer approximation allow the wavefunction of a molecule to be divided into its electronic and nuclear wavefunction components. The assumption that the motion of atomic nuclei and electrons can be divided is based on the fact that the heavy nuclei move slowly in comparison to the lighter electrons. Therefore this method lead to a Hamiltonian for electrons in a field generated by a static nuclei such that,

$$\hat{H}_{electronic}\Psi_{electronic} = E\Psi_{electronic} \tag{2.4}$$

The decoupling between the nuclei and electron wavefunctions in this approximation allow the electron problem to be solved separately and is computationally less demanding.

2.1.1 The Hartree-Fock Scheme

The problem of many electrons moving in a potential field remains to be tackled. In computational quantum mechanical modelling in physics and chemistry, the Hartree-Fock (HF) and density functional theory (DFT) methods are widely used as simplifications of the many electrons problem. Hartree-Fock theory relies on simplification of the wavefunction, whereas DFT relies on the use of the spin-charge density. Two important interactions between electrons need to be considered which are the correlation and exchange interactions. Electronic correlation affects the position of each electron, since when one electron moves, its electrostatic field influences the position of other electrons. This effect (exchange correlation) is included in DFT but not accounted for in HF theory which underlines another advantage of DFT in addition to its lower computational demands. The exchange effect is related to the Pauli exclusion principle where electron wavefunctions are antisymmetric under particle interchange. In effect electrons of parallel spins are not allowed in pair states.

The Hartree-Fock method assumes that many-electron wavefunctions can be incorporated into a determinant of single-electron wavefunctions, called a Slater determinant. However, a many-electron wavefunction cannot be expressed as a single determinant. For this reason, the electronic correlation is neglected in Hartree-Fock theory resulting in the predicted energies being higher than the experimental values, and require post-Hartree-Fock techniques in order to include electron correlation.

2.1.2 The Hohenberg-Kohn Theorem

In DFT, the many-electron wavefunction is avoided by adopting electron density based on the first Hohenberg-Kohn (H-K) theorem which states that for a system

consisting of electrons under the influence of an external potential, the total energy is a unique functional of the electron density. The functional of the electron density depends only on 3 spatial coordinates. It postulates a one-to-one mapping between the ground state electron density and the ground state wavefunction. If two systems of electrons, one trapped in a potential $\upsilon_1(\boldsymbol{r})$ and the other in $\upsilon_2(\boldsymbol{r})$ are assumed to have the same ground state density $n(\boldsymbol{r})$, then necessarily $\upsilon_1(\boldsymbol{r}) - \upsilon_2(\boldsymbol{r})$ = constant, which means that it is not possible for both systems to have the same $n(\boldsymbol{r})$. Thus, the ground state density uniquely determines the potential and consequently all properties of the system. Additionally, the many-body problem of N electrons with 3N spatial coordinates is reduced to 3 spatial coordinates through the use of functionals of the electron density.

The external potential affecting a number of electrons, *N*, is a function of the electronic density in the ground state, plus an additive constant, where the electronic density is,

$$n(\boldsymbol{r}) = N \int \left|\Psi(\boldsymbol{r})\right|^2 d^3r \tag{2.5}$$

A universal functional (system independent) of the density, *F* is defined for all electronic structure problems as,

$$F[n(\mathbf{r})] = \langle \Psi | \, T + U \, | \Psi \rangle \tag{2.6}$$

where *T* and *U* are operators of the kinetic energy and electron-electron interaction energy respectively.

The second H-K theorem states that the ground state density would minimise the total electronic energy of the system if and only if the input density is the true ground state density. The ground state energy of the system is defined by,

$$E_{(r,N)}[n(\boldsymbol{r})] = F[n(\boldsymbol{r})] + \int \upsilon(\boldsymbol{r}) n(\boldsymbol{r}) d^3r \tag{2.7}$$

For a system with *N* electrons in a potential $\upsilon(\boldsymbol{r})$, a density functional $F[n(\boldsymbol{r})]$ exists so that $E_{(r,N)}[n(\boldsymbol{r})]$ obtains its minimal value at the ground state density $n(\boldsymbol{r})$. This minimal value of $E_{(r,N)}[n(\boldsymbol{r})]$ is then the ground state energy of the system.

2.1.3 The Kohn-Sham Equations

Kohn and Sham [57] developed a concept of a non-interacting system of particles that generate the same charge density as any given system of interacting particles. The Kohn-Sham equations consist of a set of eigenvalue equations for which the wavefunction of the non-interacting particles can be found.

The total energy of a system is expressed as a functional of the charge density as,

$$E[n(\boldsymbol{r})] = E_{\text{kin}} + \int V_{\text{ext}}(\boldsymbol{r}) n(\boldsymbol{r}) d^3r + U_{\text{H}}[n] + E_{\text{XC}}[n] \tag{2.8}$$

where E_{kin} is the kinetic energy of the system, V_{ext} the external potential acting on the system, $U_{\text{H}}[n]$ the Hartree energy and $E_{\text{XC}}[n]$ is the exchange-correlation energy. A straightforward application of this formula presents two obstacles: firstly, the exchange-correlation energy is not known exactly, and secondly, the kinetic energy term must be formulated in terms of the charge density.

In the Kohn-Sham approach, the exact, interacting electron density is made up of the molecular orbitals of the non-interacting electrons. The wavefunctions are solutions to the Schrödinger equation for N non-interacting electrons in the effective potential, or Kohn-Sham potential, $V_{\text{KS}}(\boldsymbol{r})$:

$$-\nabla^2 \Psi_i(\boldsymbol{r}) + V_{\text{KS}} \Psi_i(\boldsymbol{r}) = \epsilon_i \Psi_i \tag{2.9}$$

where the Kohn-Sham potential is defined to be,

$$V_{\text{KS}}(\boldsymbol{r}) = V_{\text{ext}}(\boldsymbol{r}) + \int \frac{n(\boldsymbol{r'})}{|\boldsymbol{r} - \boldsymbol{r'}|} d^3r' + \frac{\delta E_{\text{XC}}}{\delta n(\boldsymbol{r})} \tag{2.10}$$

The Kohn-Sham potential generate a system of non-interacting electrons with density equal to the density of the interacting electrons.

2.1.4 Local Density and Generalised Gradient Approximations

The common approximations for the exchange-correlation energy implemented in DFT are the local density approximation (LDA) and generalised gradient

approximation (GGA). Within LDA, the energy of the true density is approximated by the energy of a local constant density. For a local density $n(\boldsymbol{r})$, the actual exchange-correlation energy density is replaced with that of a homogeneous electron gas at each point $\boldsymbol{r}$ in space. On the other hand, GGA considers the gradient of the electron density which is useful for systems where density undergoes rapid spatial changes.

DFT has become the choice for large scale calculations where the total energy of a system is described by a functional of the electronic density and the exact ground state energy is solved from a system of N one-particle equations. In this thesis, DFT calculations based on electronic charge density was implemented in AIMPRO within the local density approximation (LDA) following the methods described in Perdew Wang[58].

2.1.5 Structure Optimisation

The minimisation of the energy is attained by the optimisation of the structure. The lowest total energy of the system can be found by minimising the force on each atom. AIMPRO employs the *conjugate gradient* algorithm where each atom is moved a small distance inducing energy change, after which new forces are calculated. The atoms are then moved in accordance to these forces. The algorithm utilises knowledge of the previous search direction in combination with the latest forces to determine the next direction to move atoms. The process is repeated iteratively until the total energy is minimised and the resulting forces are considered insignificant.

In this thesis, the SiC-QDs were geometrically optimised until atomic forces were smaller than 0.06 eV/Å. In the literature, the reported maximum force threshold range from 0.02 eV/Å in the DFT-GGA simulation for SiC QDs [31] to 0.05 eV/Å in DFT-GGA study of H- and OH-terminated 3C-SiC nanoparticles [22]. The reported trend in the energy gap from 4.5 eV to 3.5 eV for H-terminated 4H-SiC QDs for diameters of 1 to 2 nm in [31] is comparable with that reported in this thesis suggesting that the chosen atomic forces in this range do not significantly influence the calculated optoelectronic properties of the SiC nanostructures.

2.1.6 The Supercell Approach

In the supercell approach, a repeating unit cell of the crystal lattice is used to describe the structure. Periodic boundary conditions [56] simulate an infinite crystalline material. In this mode a lattice needs to be defined. In this thesis, simulation of 4H-SiC quantum dots were performed using the supercell structure as in the 'cluster in box' sense. In this arrangement, atomic systems were placed in a fictitious face-centred cubic lattice, with the vacuum spacings between quantum dots made sufficiently large (inter-dot distance of 4 times the quantum dot diameter) to ensure no significant interactions between systems and their images (larger than 1 nm spacing [59]).

2.1.7 Brillouin Zone Sampling

In order to calculate the physical properties of a material, the Kohn-Sham orbitals are integrated over the Brillouin zone. In practise, to simplify the calculation, a set of special $\boldsymbol{k}$-points can be taken, from which an average value for the integrand function $f(\boldsymbol{k})$ is calculated. A scheme was proposed by Monkhorst and Pack [60] for Brillouin zone sampling where the average $\overline{f}$ integrated over the Brillouin zone with volume $(2\pi)^3/\Omega$ is given by

$$\overline{f} = \frac{\Omega}{(2\pi)^3} \int f(\boldsymbol{k})\, d\boldsymbol{k} \;\approx \frac{1}{N_{\boldsymbol{k}}} \sum_{n=1}^{N_{\boldsymbol{k}}} f(\boldsymbol{k}_n) \tag{2.11}$$

where the Brillouin zone volume is $\frac{\Omega}{(2\pi)^3}$ and $N_{\boldsymbol{k}}$ is the number of special $\boldsymbol{k}$-points. In this thesis, calculations were performed at the Γ point of the Brillouin zone as no dispersion occurs for quantum dot structures [61, 62].

2.1.8 The Pseudopotential Approximation

As the computation of all electrons in a system is highly demanding, an approximation can be made by replacing all-electron potentials with pseudopotentials. In this approximation, the effects of the motion of the core electrons and the nuclear Coulomb

potential is replaced with an effective potential. The behaviour of the pseudopotential is constructed so that it follows the real full potential to the first order in energy. This is achieved by the use of a *norm-conserving* pseudopotential. Norm-conserving pseudopotentials enforce 2 conditions. Firstly, inside the cut-off radius r_c the norm of each pseudo-wavefunction is identical to its corresponding all-electron wavefunction. Secondly, the all-electron and pseudo wavefunctions are identical outside r_c. The approximation is relevant for solid-state systems because core electrons are not involved in bonding and chemical interactions, only the valence electrons need to be considered. In this thesis, the pseudopotentials developed by Hartwigsen, Goedecker and Hutter (HGH) [63] were used. To take advantage of the accuracy afforded by representation of the charge density in reciprocal space using a plane-wave expansion (Fourier transform), the SiC-QDs were modelled using periodic boundary conditions [56]. The number of plane waves used in the fitting were determined by the cut-off energy, E_{cut}. The plane wave energy cut-off that correspond to the largest cut-off energy of the individual species used in the expansion was 400 Ry. The chosen E_{cut} was sufficient to converge the energies to within 10 meV. In AIMPRO, the computational demands are greatly reduced as the Kohn-Sham wavefunctions are expanded as Gaussian basis sets which allows for a higher E_{cut} value of 400 Ry in this work.

2.1.9 Expansion of the Wavefunction

The expansion of rapidly varying wavefunctions for atoms such as oxygen would require a large number of plane waves per atom, leading to high computational demands. In AIMPRO, the Kohn-Sham wavefunctions are expanded in a basis set of Gaussian functions [55] which is more efficient and only weakly dependent on atom type. The basis describing the wavefunctions were constructed from Gaussian orbitals. A Gaussian basis requires only a small number of functions (20-30 functions) per atom to describe the wavefunction.

In AIMPRO the Gaussian s-orbitals take the form:

$$\Psi(r) = \sum_{n=i} c_i \exp\left[-\alpha_i(\boldsymbol{r} - R_i)^2\right] \tag{2.12}$$

where the exponent α, determines the width of the Gaussian, *R* the centre of location and c_i is the coefficient that is varied to minimise the overall energy.

In this thesis, Kohn-Sham orbitals were expanded using sets of independent real-space, atom-centred Gaussian basis-sets [55] of: for C, O, F, and Si, sets with four different widths were used, whereas for H three widths were used. In addition, d-Gaussians of 1, 2, 2, and 4 widths were included to account for polarisation for O, C, Si and F, respectively.

2.1.10 Self-Consistency Cycle

Solving the Kohn-Sham equation has to be performed in a self-consistent way (iteratively) since the last two terms (the Coulomb and exchange-correlation potentials) in equation 2.10 depend on the density, $n(\boldsymbol{r})$ and hence on the wavefunction that we seek when solving equation 2.9. The self-consistent field (SCF) procedure begins with a trial charge density to calculate the Kohn-Sham potential and solve the Kohn-Sham equation 2.9 for the wavefunction. From these, a new charge density is calculated and the process is repeated. The procedure is repeated until convergence is reached. In this thesis, when the differences between the input and output of the Hartree energies were within 0.3 meV, the self-consistency of charge densities were regarded to reach the convergence point.

2.1.11 Optical Absorption Cross Section (ACS) and Joint Density of States (JDoS)

AIMPRO has the capability to calculate measurable observables in experiments such as the optical absorption cross section (ACS). Optical absorption is modelled within AIMPRO from the calculated complex dielectric function, $-Im\epsilon(E)^{-1}$ [64, 65]. The dielectric function, ϵ, is given as $\epsilon = \epsilon_r + i\epsilon_i$ where ϵ_r is the real part, ϵ_i is the imaginary part and *E* is the energy of the incident photon. The imaginary part of the dielectric function is calculated in the long-wavelength dipole approximation by summing transition matrix elements over all the bands [65] within AIMPRO by

$$\epsilon_i(E) = \frac{4\pi e^2}{\Omega} \sum_{c,v,\boldsymbol{k}} \left|\langle \Psi_{\boldsymbol{k}}^c | \, \mathbf{r} \, | \Psi_{\boldsymbol{k}}^v \rangle\right|^2 \delta(E_{\boldsymbol{k}}^c - E_{\boldsymbol{k}}^v - E) \tag{2.13}$$

where Ω is the unit cell volume and $|\Psi_{\boldsymbol{k}}^{v,c}\rangle$ are valence and conduction states with respective energies of $E_{\boldsymbol{k}}^{v,c}$. The dielectric function is dependent on the orientation of the associated electric field of the incident photon through the orientation of **r**. The term $\left|\langle \Psi_{\boldsymbol{k}}^c | \, \mathbf{r} \, | \Psi_{\boldsymbol{k}}^v \rangle\right|^2$ is proportional to the transition probability, dependent on the dipole matrix element for the optical transition between the initial occupied Kohn-Sham state $|\Psi_{\boldsymbol{k}}^v\rangle$ and the final unoccupied Kohn-Sham state $\langle \Psi_{\boldsymbol{k}}^c|$. The term $\delta(E_{\boldsymbol{k}}^c - E_{\boldsymbol{k}}^v - E)$ is related to the joint density of states (JDoS) which represent the possible optical transitions between energy levels with energy separation equal to the energy of the absorbed photon, E. The density of states (DoS) was evaluated by calculating the Kohn-Sham spectra at the Γ point in the Brillouin zone.

In this thesis, the sum off all the bands over $\boldsymbol{k}$ in equation 2.13 was restricted to the Γ point ($\boldsymbol{k}$=0) at the zone centre as the wavefunctions do not propagate and dispersion in the Brillouin zone does not occur for nanoparticles that are spatially confined in 3-dimensions (quantum dots). The calculations accounted for *x*, *y* and *z* polarised light whereby the total sum of these contributions gave $-Im\epsilon(E)^{-1}$ with a given number of Kohn-Sham states included in the sum. This can be defined relative to the number of occupied states *G* by ρG, where ρ was 4 (four times the number of occupied states). The real part of the dielectric function, $\epsilon_{(\boldsymbol{r})}$, was then calculated by the Kramers-Kronig relation.

The optical absorption coefficient, α, is related to the complex dielectric function by

$$\alpha(\omega) = \frac{4\pi}{\lambda} \left[\frac{-\epsilon_r(\omega) + \sqrt{\epsilon_r(\omega)^2 + \epsilon_i(\omega)^2}}{2} \right] \tag{2.14}$$

The spectral shape and trends of the ACS is expected to track that of the JDoS as the optical transitions occur across available allowed energy states represented by the JDoS. The calculated ACS and JDoS in this thesis were subjected to a polynomial line broadening of 0.1 eV as previously employed in Si quantum dot study using AIMPRO [62] .

2.1.12 Computation of 4H-SiC Quantum Dots

Density-functional theory calculations, as implemented within local density approximation (LDA) in the AIMPRO code [54, 56], were performed for quasi-spherical 4H-SiC-QDs with core diameters varying from 10 to 20 Å. Apart from effects of different surface termination groups (OH-, F- and H-termination), contributions from QD composition (Si-centred versus C-centred) and surface reconstruction were investigated.

To study these effects, QD structures constructed in the thesis were divided into 6 groups. There were 11 QDs (10 to 20 Å diameters) for each of the 6 groups, namely: (1) unreconstructed C-centred H-terminated QDs, (2) reconstructed C-centred H-terminated QDs, (3) unreconstructed Si-centred H-terminated QDs, (4) reconstructed Si-centred H-terminated QDs, (5) reconstructed Si-centred OH-terminated QDs and (6) reconstructed Si-centred F-terminated QDs.

To construct the SiC-QDs, atoms within some chosen distance (10 to 20 Å) of either a Si or C atom in bulk SiC were selected (Si or C centred), and the atoms at the surface saturated by either an H atom, a F atom, or an OH group. Fig. 2.1 shows the configurations to identify the contributions of different composition in 4H-SiC QDs comprising of Si-centred QDs (Fig. 2.1(a)) and C-centred QDs (Fig. 2.1(b))

This construction generally produces surface Si and C atoms requiring two or three terminating groups. In the case that three were required, this means that there was a single Si-C bond linking the surface atom to the SiC core, and the surface atom was removed. Where there were two unsaturated bonds, two cases have been examined. The first was where two terminating atoms or groups were added generating, for example, SiH_2 and CH_2 surface groups. Fig. 2.2(a) shows the unreconstructed 20 Å core diameter 4H-SiC QD and the structure after termination with -H atoms (Fig. 2.2(b)). Where these surface sites neighbour each other, this saturation results in significant steric repulsion between the terminating species. Therefore where pairs of two-fold bonded surface sites neighbour each other as indicated in (Fig. 2.2(b)), an alternative was to first form C–C or Si–Si reconstructions (Fig. 2.2(c)), and only saturate the remaining sites Fig. 2.2(d)). For F- and OH-terminated SiC-QDs, where the terminating species would be placed within a covalent bond-length, evaluation of

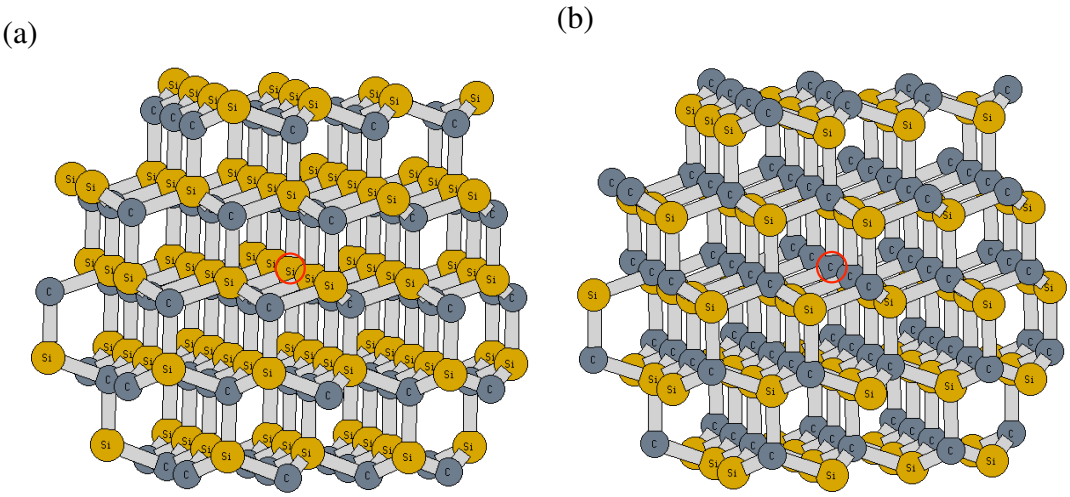

Figure 2.1: Different composition of 4H-SiC QD (Si-gold, C-gray): examples of 15 Å core diameter 4H-SiC QDs which are (a) Si-centred and (b) C-centred as indicated by the red circles. Structural constructions involved contribution from Dr. Jonathan Goss.

structures with a small fraction of H-terminating groups to reduce unrealistic steric repulsion was undertaken. Both full saturation and reconstruction have been examined in this study.

To take advantage of the accuracy afforded by the representation of the charge density in reciprocal space using a plane-wave expansion (Fourier transform), the SiC-QDs were modelled using periodic boundary conditions [56], with a cut-off in energy of 400 Ry and was sufficient to converge the energies to within 10 meV. In AIMPRO, only the charge density is represented by a plane-wave expansion whereas the Kohn-Sham wavefunctions are expanded as Gaussian basis sets in real space which greatly reduces the computational demands. The afforded capacity allow for a higher cut-off energy in AIMPRO (400 Ry in this work) and is not a limiting factor in this thesis. The SiC-QDs were placed in a periodic boundary condition within a face-centred cubic lattice. The lattice constant was chosen to be equal to four times the nominal core diameter to allow for both the surface groups and sufficient vacuum between SiC-QDs to minimise interactions.

Once the core has been prepared and the surface groups added, the SiC-QDs were geometrically optimised. For the structural optimisation or relaxation, the stable equilibrium for molecular system was obtained by applying the conjugate gradient

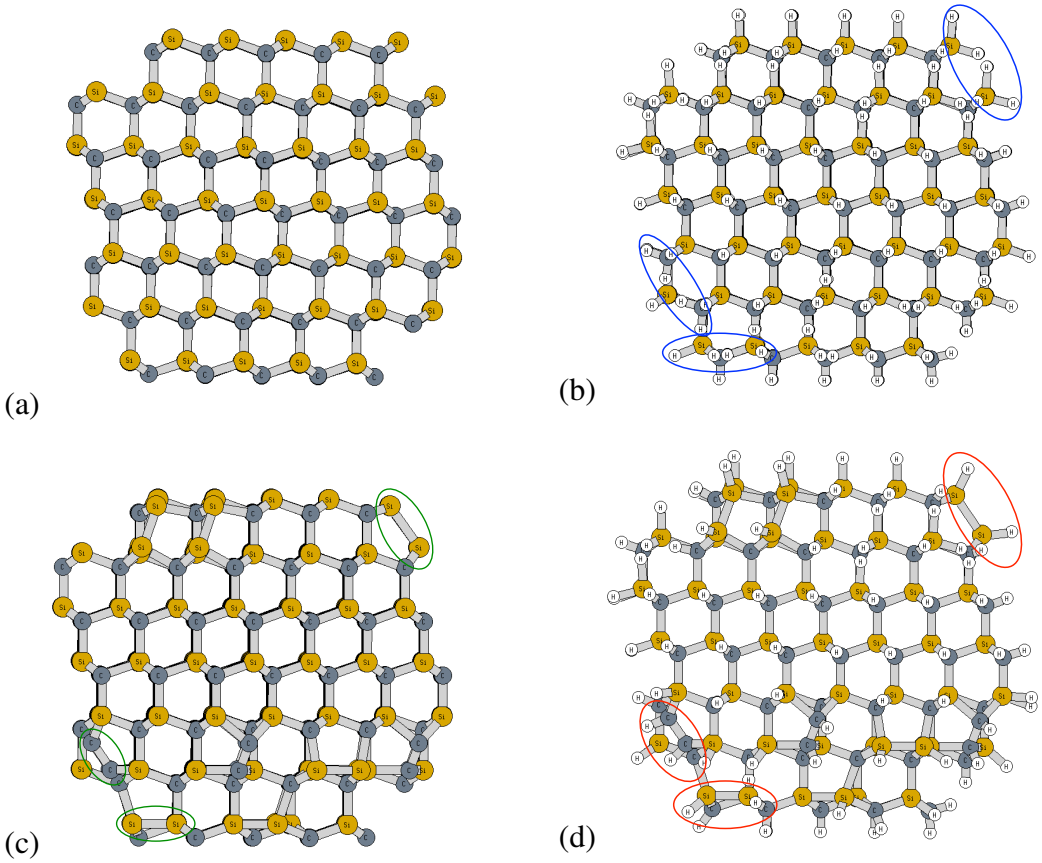

Figure 2.2: Examples of 20 Å diameter 4H-SiC QD core construction and surface termination (Si-gold, C-gray, H-white). (a) Bare Si- or C-centred 4H-SiC QD core of a chosen diameter (20 Å) without surface reconstruction. (b) Without surface reconstruction, the resulting surface termination with a terminating species (-H, -OH or -F) may consist of two-fold bonded sites neighbouring each other (such as indicated by blue ellipses) potentially causing steric repulsion. (c) Alternative was to construct bare Si- or C-centred QD with C-C or Si-Si bonds (with surface reconstruction) at these sites (such as indicated by green ellipses) to reduce steric effects. (d) Termination of surface reconstructed QDs to reduce steric repulsion (indicated by red ellipses). The influence of unreconstructed and reconstructed surfaces were compared for H-termination for all diameters between 10 Å to 20 Å for each of the C-centred and Si-centred QD groups (4 groups). Reconstructed 4H-SiC QDs in the diameter range from 10 Å up to 20 Å were constructed for each of OH- and F-terminations (2 groups). Structural constructions involved contribution from Dr. Jonathan Goss.

technique [66]. In this technique, atoms were allowed to move until the minimum of the total energy of the system was achieved, that is when the forces acting on the atoms

were smaller than 0.06 eV/ Å. The chosen maximum force within structures being below 0.06 eV/ Å has negligible impact upon the calculated ACS and onset energies in this thesis as shown in Fig. 2.3 (a) and (b). The impact of the structural forces within this range on the optical onset energies was less than 10 meV.

(a)

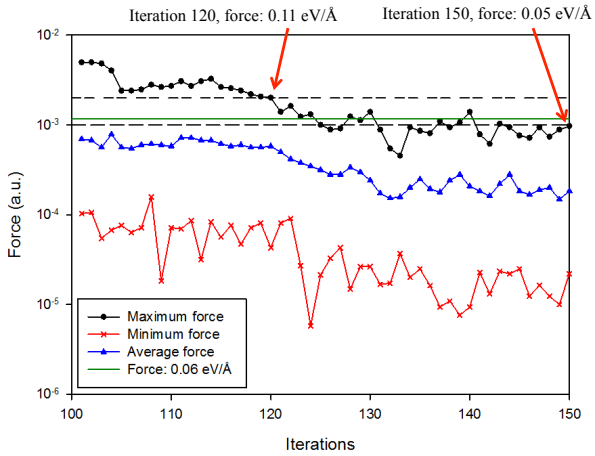

(b)

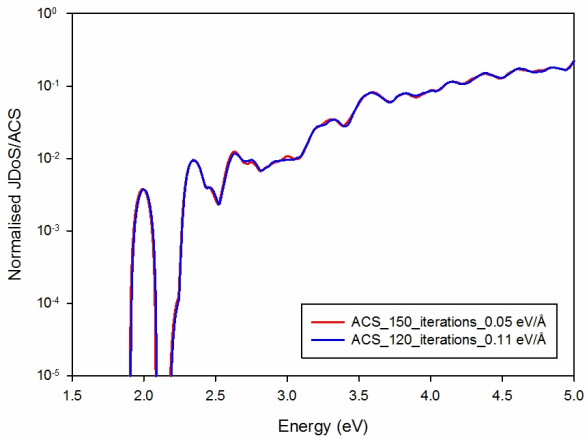

Figure 2.3: Determination of allowable maximum force in structural relaxation. (a) Comparison between maximum forces 0.11 eV/ Å and 0.05 eV/ Å at iterations 120 and 150 respectively for a reconstructed 12 Å diameter OH-terminated 4H-SiC QD. The chosen 0.06 eV/ Å threshold being within this range. (b) Comparison of absorption cross sections between maximum forces 0.11 and 0.05 eV/ Å were very similar and the energy onset difference was only 6 meV. Thus, the chosen maximum force within structures smaller than 0.06 eV/ Å has negligible impact upon the calculated ACS and onset energies in this thesis.

In the literature, the reported maximum force threshold ranges from 0.01 eV/Å in

DFT study of 1-2 nm sized 3C-SiC nanocrystals [59], 0.02 eV/Å in the DFT-GGA simulation for SiC QDs [31] to 0.05 eV/Å in DFT-GGA study of H- and OH-terminated 3C-SiC nanoparticles [22]. The trend in the energy gap from 4.5 eV to 3.5 eV for H-terminated 4H-SiC QDs for diameters of 1 to 2 nm in [31] is comparable with the trend reported in this thesis suggesting that the chosen atomic forces in this range do not significantly influence the calculated optoelectronic properties of the SiC nanostructures.

The optical absorption cross section (ACS) and joint density of states (JDoS) were calculated as described in section 2.1.11.

The energy gap (HOMO-LUMO) was obtained from the DoS. The JDoS represent the possible optical transitions between energy levels with energy separation equal to the energy of the absorbed photon. The energy onsets of JDoS were compared with the energy onsets of ACS and the calculated energy gaps of the respective OH-, F- and H-terminated 4H-SiC QDs.

Although the underestimation of the energy gap in DFT calculations is well known, the aim of this study is to establish the systematic differences between different surface terminations and DFT calculations are well placed to predict these trends [31, 67, 68].

2.2 Anodic Electrochemical Etching and Ultrasonication of 4H-SiC

Bulk, 8° off-axis, *n*-type (10^{19} cm^{-3}) 4H-SiC wafer pieces (1 cm $\times$1 cm) purchased from CREE were cleaned using an RCA process. The wafer pieces were degreased in acetone and dipped in HF prior to silver paste being applied as the back contact to allow connection to an a copper plate that is the anode connection. Por-SiC was prepared by anodic electrochemical etching in an electrochemical cell using a tungsten wire as the counter electrode.

Figure 2.4 shows the cross sections of the two parts of the electrochemical cell with the dimensions given in mm. Both assemblies were fabricated from a 40 mm diameter polytetrafluoroethylene (PTFE). PTFE was chosen as it is HF acid resistant. Assembly 1 incorporates a 10 mm external thread at the base of the PTFE structure as shown by the diagonal lines. The thread was used to firmly fix the two components

together. Within assembly 1, a cylindrical hole with a diameter of 8 mm and a height of 55 mm was designed to contain the HF/ethanol electrolyte solution. At the top end of assembly 1, a 0.5 mm deep and 1 mm wide radial groove was fabricated to place a Viton O-ring of a 10 mm outer diameter (8 mm inner diameter). Viton was chosen for its resistance against HF acid. Assembly 2 consist of a larger cylindrical hole with a diameter of 24 mm and a height of 48 mm. A 10 mm internal thread at one end of the cylindrical hole in assembly 2 matches the external thread of assembly 1. A small hole of 1 mm diameter was drilled into assembly 2 to allow a copper wire to the copper anode plate and allow connection to the external circuit.

The procedure for anodic electrochemical etch employed in this thesis was as follows:

1. A Viton O-ring was placed onto the groove of assembly 1. A good and reliable fit for the O-ring in the groove was ensured.

2. A SiC wafer piece with the clean surface was placed face down (towards the Viton O-ring) onto the Viton O-ring on assembly 1. The back contact was face up. Care was taken to ensure that the wafer piece fully covered the radial area of the O-ring underneath to avoid leakage.

3. Assembly 2 was held upright above assembly 1 and slowly brought down to enclose assembly 1. Once the inner thread of assembly 2 was in contact with the inner thread of assembly 1, assembly 2 was rotated clockwise for about 40 rotations. The torque was converted to a linear force to push the SiC wafer on the O-ring against the copper anode for contact.

4. Once contact was made between the SiC wafer with the copper anode, the enjoined assemblies were turned upside down to complete the electrochemical cell assembly as shown in Figure 2.4

5. Leakage test for 5 minutes was performed using deionised water. In the wetbench, after the electrochemical cell was confirmed leak proof, a 4 ml solution of 48 % HF/ absolute ethanol (1:1 by volume) was prepared and transferred into the electrochemical cell by the use of a plastic pippette.

6. The anode was connected to the copper wire soldered to the copper plate and the cathode directly to an acid resistant tungsten wire (immersed in HF/ethanol). A

20 V bias was applied to commence the etch at room temperature.

7. Upon completion of etch, the HF/ethanol electrolyte was replaced with ethanol, followed by deionised water to rinse the sample and the electrochemical cell.

8. The resulting mesoporous layer was delaminated (D-Por-SiC) from the surface of the wafer piece with tweezers. Care was taken in handling to avoid breakage of the brittle and fragile D-Por-SiC.

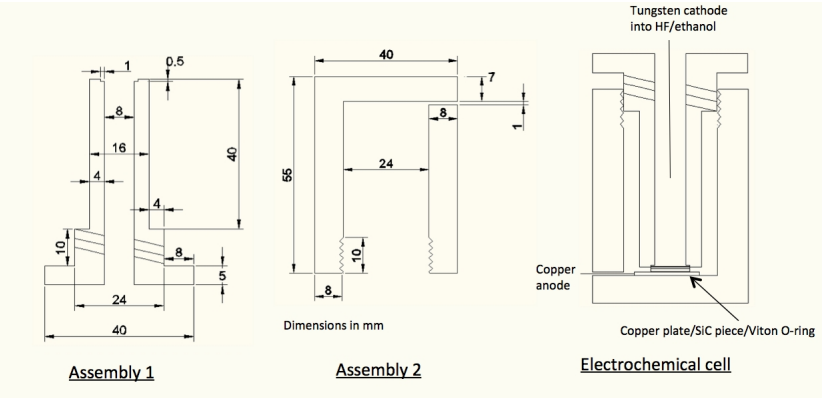

Figure 2.4: Schematic cross-section of in-house teflon electrochemical cell

The etching duration was one hour at an applied bias of 20 V. The voltage bias of 20 V was selected as it has been reported to be optimal in producing columnar walls [69] in electrochemically etched SiC. The use of ethanol with HF was important in order to reduce surface tension and ensure the electrolyte was able to penetrate into the porous structure [70, 71]. During etching, the current flow decreased commensurate with the increase in the resistance as the porous layer was formed; the current dropped from 40 mA to 10 mA during the etch corresponding to an increase in the cell resistance from 0.5 $k\Omega$ to 2 $k\Omega$.

After being allowed to dry, the free standing D-Por-SiC was characterised by Raman spectroscopy, atomic force microscopy (AFM) and cross-sectional scanning electron microscopy (SEM). Then, the D-Por-SiC was immersed in a 13 mm diameter glass vial filled with 2 ml of ethanol and subjected to ultrasonication at room temperature for 30 minutes. The sonicated D-Por-SiC (S-Por-SiC) in ethanol was allowed to settle overnight resulting in a sediment. The top portion was

decanted for further characterisation by UV-visible spectroscopy, photoluminescence (PL), photoluminescence excitation (PLE), high resolution transmission electron microscopy (HRTEM), X-ray diffraction (XRD) and X-ray photoelectron spectroscopy (XPS). Current-voltage measurements for S-Por-SiC drop-casted on interdigitated electrodes were conducted on a Keithley 4200-SCS system.

2.2.1 Pore Wall Thinning and Surface Removal of Delaminated Porous 4H-SiC by Sacrificial Oxidation

Pore wall thinning and surface removal by sacrificial oxidation of the as-etched delaminated mesoporous 4H-SiC (D-Por-SiC) was performed by a two step process. After anodic electrochemical etching and drying of the D-Por-SiC in air, the material was loaded into the furnace for thermal oxidation in dry oxygen with a flow rate of 100 sccm at 1100°C. Oxidation durations of 1, 3, 6 and 9 hours were employed. After thermal oxidation, the oxidised D-Por-SiC were dipped in HF/ethanol solution (1:1 by volume) for 5 minutes to remove the thermally grown SiO_2 followed by a rinse in ethanol and deionised water. The pore wall thinned D-Por-SiC is referred to as PWT-Por-SiC. The PWT-Por-SiC was characterised by cross-sectional SEM. Subsequently, the PWT-Por-SiC was reimmersed in a 2 ml ethanol filled glass vial and sonicated for 30 minutes at room temperature. The PWT-Por-SiC suspension in ethanol was then characterised by PL and PLE.

2.3 Characterisation Techniques

Interesting changes in the properties of nanostructure materials manufactured from the bulk may be experimentally monitored through measurements such as Raman spectroscopy, photoluminescence (PL), X-ray diffraction (XRD), atomic force microscopy (AFM), X-ray photoelectron spectroscopy (XPS) and high resolution transmission electron microscopy (HRTEM) and current-voltage (I-V) characteristics. These characterisation techniques served to gain insight and complement theoretical results from DFT simulation.

2.3.1 Determination of Etch Depth

The etch depths for 1 hour duration process were 25-30 μm as determined from the underlying wafer pieces by measuring the step heights between the unetched and etched surfaces using a Tencor P-1 Long Scan Profilometer. These were direct contact measurements and were not performed for D-Por-SiC to avoid damaging the porous structures. Thus the profilometer was used only for the underlying substrates. The thickness of D-Por-SiC were determined by cross-sectional scanning electron microscopy (SEM).

2.3.2 Raman Spectroscopy

D-Por-SiC and PWT-Por-SiC films were characterised with Raman spectroscopy on a Horiba Jobin Yvon HR800UV at a wavelength of 514.5 nm in a near backscattering geometry at room temperature [72]. Care was taken to avoid local heating effects and therefore 5 mW of incident laser power was used. Initial measurements demonstrated no shift in the Raman lines occured within 1 to 10 mW of incident power. The measurements were taken at magnification of 100X. The spectral resolution of the measurements were 0.3 cm^{-1}.

Raman spectroscopy is based on inelastic scattering of monochromatic light. The incident photons interact with molecular vibrations or phonons within the sample resulting in the shifting up or down of the scattered photon's energy. This shift in energy describes the vibrational modes in the system. The conservation of momentum rule, $\Delta \boldsymbol{k} \approx 0$ is a consequence of the infinite periodicity of the crystal lattice. In nanocrystals, the absence of periodicity beyond their boundaries relaxes the zone-centre optical phonon $\Delta \boldsymbol{k} \approx 0$ selection rule. The relaxation or breaking of the translational symmetry allow contributions from phonons away from the Brillouin-zone centre. This results in peak shift of the Raman line and line-broadening which are dependent on the shape of the phonon dispersion curve.

For 4H-SiC, as shown by the solid red arrow in Fig. 2.5, the optical phonon wavenumber decreases as the dispersion moves away from the Brillouin zone centre

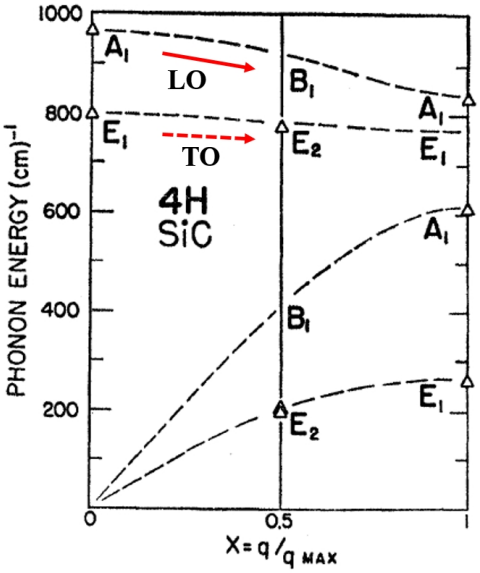

Figure 2.5: Negative phonon dispersion of the optical branches of 4H-SiC (red solid arrow: LO mode, red dotted arrow: TO mode) [73].

(**X**=0) thereby exhibiting negative dispersion. A negative phonon dispersion result in contributions of phonons from the lower side of the frequency (lower wavenumbers). Thus, as the particle size reduces, the Raman line shape exhibits an asymmetric broadening due to contributions from the low frequency side and a red-shift in the peak position towards the same lower wavenumber side. As the LO mode's negative dispersion (red solid arrow) is larger than the TO mode's (red dotted arrow) negative dispersion, the red-shift is almost exclusively observed for the LO mode peak rather than the TO mode peak.

Fr*ö*hlich modes are another source of Raman lineshape broadening where it often appears as a shoulder in between TO and LO peaks. These surface phonon modes affect polar semiconductors for particles with sizes smaller than the wavelength of the exciting laser light. Fr*ö*hlich modes are of dielectric origin occurring in heterogenous materials consisting of at least one polar substance such as SiC, GaN and InP allowing for long-range surface interaction.

The polytype phase of a SiC sample can be determined from Raman spectra by identifying the respective TO and LO mode energies (in cm^{-1}) with respect to polytype as shown in Fig. 2.6.

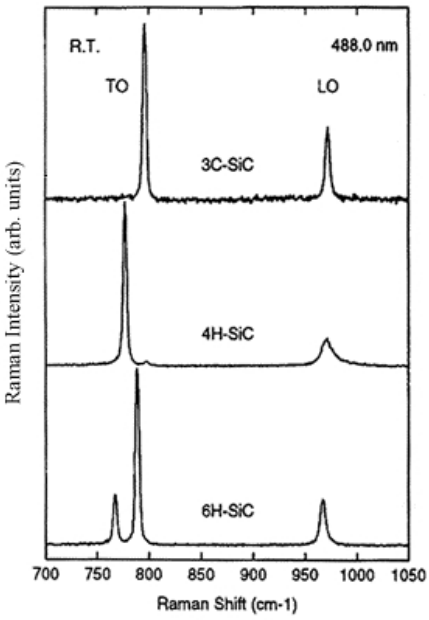

Polytype	TO (cm^{-1})	LO (cm^{-1})
3C-SiC	796	972
4H-SiC	776, 796	964
6H-SiC	767, 789	965

Figure 2.6: Raman scattering spectra for 3C-, 4H- and 6H-SiC and the respective energies (in cm^{-1}) of phonon modes [74, 75].

In-phase oscillations of neighbouring atoms are called acoustic vibrations whilst out of phase oscillations are called optical vibrations, as depicted in Fig 2.7. Additionally, phonons that move parallel to the direction of the incident light wave propagation $\vec{k}$ are longitudinal, whereas phonons that move perpendicular to the direction of the propagating wave are transversal.

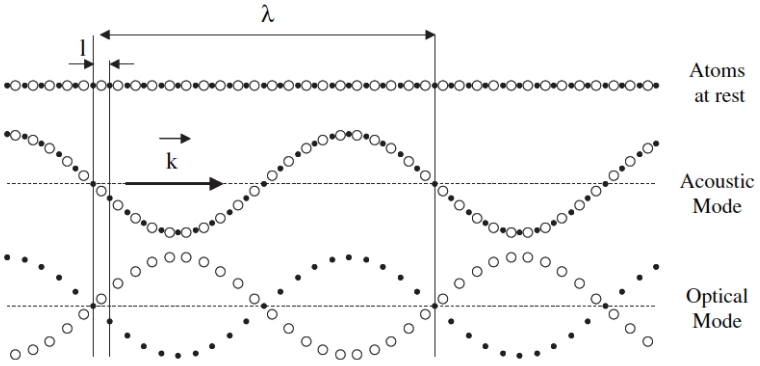

Figure 2.7: Transverse phonons of the acoustic and optical modes [76].

2.3.3 UV-Visible Spectroscopy, Photoluminescene (PL) and Photoluminescence Excitation (PLE)

Optical characterisation was undertaken using UV-visible absorption (UV-Vis) on a Hitachi U-3010 spectrophotometer for S-Por-SiC suspended in ethanol for wavelengths in the range 240 to 400 nm. A quartz cuvette was used in order to avoid absorption and luminescence from the vessel. Absorbance measures the attenuation of transmitted radiant power, is dimensionless and is a ratio of incident to transmitted radiant power through a material. Pure ethanol was first measured as a blank so that the absorbance of the solvent was known prior to S-Por-SiC. Therefore, any change in absorbance would be made just by the solute of interest.

Photoluminescence (PL) and photoluminescence excitation (PLE) were conducted for S-Por-SiC and sonicated PWT-Por-SiC suspended in ethanol on a Hitachi F-2500 fluorescence spectrophotometer. The measurements were performed at room temperature for excitation wavelengths ranging from 220 to 400 nm that coincide with the dual-feature PL observed in experiments at 320 nm [7, 17]. The photomultiplier tube (PMT) was set to 700 V. The scan speed was at 300 nm/min and slit width at 2.5 nm. Photoluminescence (PL) is the most widely used optical characterisation method in nanostructure investigation. The incident light create electron-hole pairs which later recombine, some radiatively. The radiated light is collected for analysis. The PL peaks contain information regarding electronic band structure, impurity centres and defects. The absorption process that lead to the PL emission can be probed by photoluminescence excitation (PLE). For PLE, the monitored emission wavelength is kept constant whilst the tunable laser is used to vary the excitation energy. The analysis of a broad PL peak can be resolved by selectively exciting a narrow subset of the luminescent states by tuning the excitation so that it is in resonance with the PL emission band. PLE measurement is also used to avoid scattering effects often observed in direct absorption measurements that may arise from macroscopic inhomogeneity in the nanostructured material. Quantum confinement effects in the material are usually observed in PL spectra as an increase in intensity and a blue-shift in energy in comparison to the bulk emission.

2.3.4 X-ray Diffraction (XRD) and X-ray Photoelectron Spectroscopy (XPS)

To assess whether ultrasonication resulted in polytypic transformation, D-Por-SiC (without ultrasonication) and S-Por-SiC (sonicated) samples were ground into a powder with an agate mortar and characterised by X-ray diffraction (XRD). Bruker D8 Advance diffractometer equipped with a Cu Kα source of wavelength 1.54 Å was utilised for this purpose. In XRD, measuring Bragg diffraction from the atomic lattice of a nanostructured material allows assessment of the crystallinity and determination of the lattice spacing. If the crystallites are sufficiently small the maxima of the diffraction pattern broadens and is inversely proportional to the crystallite size. The additional broadening may be measured to give an estimation of the crystallite size by Scherrer equation [77]:

$$\tau = \frac{K\lambda}{\beta cos\theta} \tag{2.15}$$

where τ is the crystallite size, λ is the wavelength of X-ray radiation, β is the additional broadening in radians, θ is the Bragg angle and K is a dimensionless shape factor close to unity (0.9).

S-Por-SiC in ethanol were drop-casted on gold foils and left to dry prior to examination by X-ray photoelectron spectoscopy (XPS) on a Thermo Theta Probe XPS spectrometer equipped with Al Kα X-rays (E_{photon}: 1486 eV). The gold foil was used as the underlying material to avoid overlapping of peaks of the binding energies with Si and C. The binding energy for gold is 546 eV. In X-ray photoelectron spectroscopy (XPS), the incident X-ray excites atomic core levels producing photoelectrons from which the kinetic energies are measured. The measured kinetic energies of the ejected electrons are used to calculate the binding energies of the related bonds within the material. XPS is sensitive to the top 10 nm of a surface and can identify all elements above lithium in the periodic table. Various studies of SiC nanostructures [21, 22, 26] have utilised XPS to ascertain the surface chemical bonds and relate to findings in PL spectra and therefore is important in this thesis.

2.3.5 Current-voltage (I-V) Characterisation

To investigate on potential photocurrent generated from mesoporous 4H-SiC, current-voltage (I-V) measurements for S-Por-SiC drop-casted on interdigitated electrodes with varying inter-electrode separations of 3, 5 and 10 μm were conducted on a Keithley 4200-SCS system. Measurements under UV illumination with nominal wavelength of 365 nm (70 mW/cm^2) and without UV illumination (dark) for both symmetric (Al-Al and Ni-Ni) and asymmetric Ni-Al interdigitated electrodes were performed with bias voltage sweeps from 10 V to -10 V.

2.3.6 Atomic Force Microscopy (AFM), High Resolution Transmission Electron Microscopy (HRTEM) and Field Emission Scanning Electron Microscopy (FESEM)

The D-Por-SiC layers were characterised by atomic force microscopy (AFM) using a XE-150 from Park Systems. The AFM utilises a micro-machined cantilever with a sharp tip to scan in very close proximity of the surface. A silicon AFM tip with aspect ratio 1.5-3.0 and radius of curvature of 6 nm was used. The measurement settings were amplitude of 1,580 nm, oscillating frequency of 284 kHz and scanning rate of 0.3 Hz in a non-contact mode.

In AFM, depending on the distance between the atoms at the tip of the cantilever and those at the sample surface, there exists a repulsive or attractive force interaction. In non-contact mode, as the distances between the probe tip and sample are relatively large, attractive forces due to dipole-dipole (van der Waals forces) interaction becomes dominant. The force can be detected by how much the cantilever deflects. The cantilever deflection is quantified by measurement of a laser beam reflected off the backside of the cantilever onto a photodetector. Non-contact AFM measure changes in the phase or vibration amplitude of the cantilever that are induced by the attractive van der Waals forces while the cantilever was mechanically oscillated near its resonant frequency. AFM provides high resolution at the nm scale but results may be influenced by the cantilever's tip shape and size if larger than the sample's feature sizes.

(S-Por-SiC) were characterised by high resolution transmission electron microscopy (HRTEM) on a JEOL-2100F FEG TEM operated at 200 kV. S-Por-SiC suspension in ethanol was drop-casted on a TEM copper grid and allowed to air dry prior to loading into the system. HRTEM employ high energy electrons accelerated in vacuum through a thin electron transparent sample (maximum thickness $\sim$100 nm). The transmitted electrons from the sample makes up the image with a 2.3 Å point resolution. The HRTEM technique is capable of providing detailed information on the structural features with resolutions down to the atomic scale.

D-Por-SiC and PWT-Por-SiC layers were fractured with a tweezer and scanned on the side in cross-sectional field emission scanning electron microscopy (FESEM) using Phillips XL30 ESEM-FEG. The scans were performed at 10 kV with magnification of up to 50,000X. In FESEM, images of samples are produced by scanning with a beam of electrons. Unlike the TEM, samples can be thicker than 100 nm as measurements are not in the transmission mode. Secondary electrons (emitted by atoms excited be electron beam) are detected to produce images with resolutions down to 1 nm.

2.4 Summary

In order to elucidate the potential causes of the observed dual-feature PL and below bandgap PL emission for 4H-SiC nanostructures in experiments, a density functional theory (DFT) study within the local density approximation was performed. The effects of QD composition, surface reconstruction and surface terminations with species most likely to occur during the preparation of SiC nanostructures (-OH, -F, -H) were studied. The underlying theory concerning DFT calculations and details of the QD structures are explained in this chapter. 10 to 20 Å diameter 4H-SiC QDs were constructed and geometrically relaxed until all atomic forces were below 0.06 eV/Å. Charge density was expanded using a plane-wave expansion in reciprocal space with plane-wave cut-off energy of 400 Ry. The Kohn-Sham orbitals were expanded by atom-centred Gaussian basis sets. Absorption cross section (ACS) and joint density of states (JDoS) were evaluated with a polynomial line broadening of 0.1 eV at the Γ point ($\boldsymbol{k}$=0) of the Brillouin zone centre as no dispersion occur for QD structures. To study 4H-SiC nanostructures, the anodic electrochemical etching route of bulk 4H-SiC in ethanoic

HF electrolyte at 20 V was performed resulting in mesoporous 4H-SiC. The details of the experimental setup for anodic electrochemical etch and procedures are outlined in this chapter. A post etch treatment on the as-etched D-Por-SiC by thermal oxidation and subsequent silicon oxide etch in HF served twofold benefits: to reduce pore wall thickness and to remove potential surface defects. The latter was to test the hypothesis that surface defects play a greater role than polytypic phase transformation. The pore wall thinning experimental details are described in this chapter. In order to determine the polytype, dimensions and effect of ultrasonication on polytype, characterisations by Raman scattering, AFM, XRD, FESEM and HRTEM were performed. Optical characterisations by PL and PLE and investigation of surface chemistry by XPS were conducted. The details and parameters concerning each technique are described.

Chapter 3

DFT Study On the Optoelectronic Properties of OH-, F- and H-Terminated 4H-SiC Quantum Dots

Results in the chapter was published in the Physical Chemistry Chemical Physics, **18**, 21676 (2016)

3.1 Introduction

This chapter presents results from DFT calculations within the *Ab Initio* Modelling Programme (AIMPRO) on the optical properties of OH-, F- and H-terminated 4H-SiC QDs in the diameter range of 10 to 20 Å. The 4H-SiC polytype serves as a good representative to study both the dual-feature and below bandgap PL emissions observed in experiments. The QD diameter range from 10 to 20 Å was chosen in order to investigate the discrepancy in quantum confinement effects between the theoretical prediction and the experimentally observed deviation for SiC QDs smaller than 30 Å. Practically, biomarkers smaller than 50 Å are required for effective renal excretion and so retaining quantum size effects within this size range is important and warrant further understanding. The deviation in the optical properties observed in 4H-SiC QDs may be contributed by surface effects as opposed to being primarily due to the bulk (polytype). In order to determine the influence of surface effects, different surface termination groups that are likely to be found in the commonly used HF/ethanol electrolyte are simulated, namely -OH, -F and -H. The effect of and contributions from these surface terminations on the onset energies of absorption cross section (ACS) and joint density of states (JDoS) are analysed and compared against those due to surface reconstructions (Si-Si and C-C dimers) and composition (C or Si centred) of the 4H-SiC QDs. A model is constructed to explain the experimentally observed dual-feature PL. The model serves as the basis to later explain the experimental findings relating to the dual-feature PL, above bandgap and below bandgap emissions reported in chapter

4; for mesoporous 4H-SiC in terms of the interplay between quantum confinement and surface states. The removal of the below bandgap emission by sacrificial oxidation as part of a pore wall thinning technique is discussed in greater detail in chapter 5.

3.2 Results

Firstly, simulations of OH-, F- and H-terminated, 10 Å diameter 4H-SiC QDs were constructed and subsequently optimised. The corresponding density of states (DoS), absorption cross section (ACS), joint density of states (JDoS), electron wavefunction isosurfaces and electron probability densities for this QD size were calculated and compared for the different terminations. Then, calculation results on larger size sets (optimised structures of 10 to 20 Å 4H-SiC QDs) were presented. Representative structures of relaxed 20 Å QDs were shown. Calculated ACSs for different 4H-SiC composition (C or Si-centred) on H-terminated QDs were shown for varying QD size in the range of 10 to 20 Å. Comparisons were made between H-terminated 4H-SiC QDs with surface reconstruction (containing Si-Si or C-C dimers on the surface) and without surface reconstruction. The difference in ACS between Si-centred OH-, F- and H-terminated 4H-SiC QDs (different surface terminations) were then compared against those with different composition and surface reconstruction to assess each of their contributions towards the observed trends in the optical properties, within the 10 to 20 Å size range. This is followed by detailed examinations of the DoS, electron wavefunction isosurfaces and electron probability densities on 20 Å QDs to explain the observed trends. A model comprising the core and surface HOMO/LUMO was constructed to explain the dual-feature PL observed in experiments. Finally, projection of the QD size range influenced by surface states was made based on the calculations.

3.2.1 Optical Properties of 10 Å Diameter 4H-SiC QD Structures

Relaxed geometries of 10 Å diameter QDs terminated with -OH ($Si_{19}C_{20}O_{40}H_{40}$), -F ($Si_{19}C_{20}F_{40}$) and -H ($Si_{19}C_{20}H_{40}$) are illustrated in Fig. 3.1. The average Si-C, O-H, Si-X, C-X (X=H, O and F in each case) bond lengths in Å are calculated to be 1.87 Å, 1.00 Å, (1.50 Å, 1.65 Å, 1.59 Å), (1.10 Å, 1.46 Å and 1.41 Å) as summarised

(a) (b) (c)

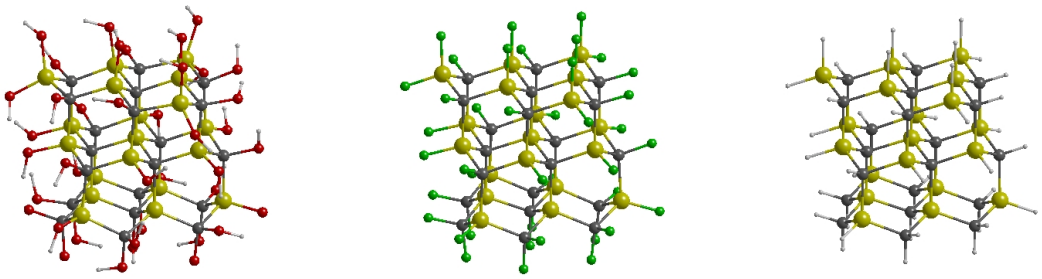

Figure 3.1: Geometrically relaxed 10 Å diameter 4H-SiC quantum dots with (a) -OH, (b) -F and (c) -H termination. Color coding: gray - C, yellow- Si, red- O, green -F, white -H. Construction of structures has been contributed by Dr. Jonathan Goss.

in Table 3.1. The bond lengths lie within the anticipated range for Si and C based single bonds [32, 78]. The standard deviation in the Si-C bond lengths across QDs with different surface terminations are within 0.01 Å.

Table 3.1: 10 Å diameter SiC-QD bond lengths.

Bond	Si-C	O-H	Si-H	Si-O	Si-F	C-H	C-O	C-F
Average bond length (Å)	1.87	1.00	1.50	1.65	1.59	1.10	1.46	1.41

Different surface functionalisation (-OH, -F and -H) on the same Si and C core atoms configuration resulted in variation in the highest occupied (HOMO) and lowest unoccupied (LUMO) energy gap as shown in Fig. 3.2(a). The HOMO-LUMO energy gap is clearly distinguishable between different surface terminations, with -H termination showing the largest energy gap (4.50 eV), followed by -F (2.27 eV) and -OH (2.14 eV) respectively.

It is instructive to examine the effects of the surface terminations upon the QDs' absorption cross section (ACS) as shown in Fig. 3.2(b). The absorption onsets correlate with the HOMO-LUMO energy gaps where H termination show a higher energy optical absorption onset (4.50 eV) compared to -F and -OH in agreement to its larger calculated energy gap. The optical absorption onset of -OH is red-shifted by (2.3 eV while -F is red-shifted by (1.7 eV) when compared to -H. For optical properties, the

joint density of states (JDoS) is important as it shows all the possible optical transitions from the valence (HOMO) to the conduction (LUMO) energy levels with energy separation equal to the energy of the absorbed photon. The resemblance in spectral shape and energies of the ACS in comparison to the JDoS indicate that the calculated optical transitions concur with the calculated allowed energies of the electronic density of states.

The difference in the HOMO-LUMO energy gap is further elaborated by examining the spatial distribution of the frontier orbitals (HOMO and LUMO). For -OH termination, Figure 3.3 (I-a) shows HOMO being primarily localised on the surface C and O atoms in the form of C *p*-orbitals and O lone-pairs, respectively. LUMO orbitals are seen primarily on O atoms (Fig. 3.3 (I-b)). As shown in Fig. 3.3 (I-c), a 2-dimensional slice confirms the electron probability density (within 1 eV of the HOMO) residing mostly on the surface of the QD. The electron probability density examined is the sum of the squared modulus of the wavefunction, $\sum_{n=i} |\psi_i|^2(r)$, where (HOMO - E_i) $\leqslant$ 1 eV.

For F-termination, lone-pairs on F atoms and p-like wave functions of the nearest neighbours (Figs. 3.3(II-a) and (II-c)) mainly contribute to the HOMO, while for the LUMO (Fig. 3.3(II-b)), similar to OH-termination, mainly the F atoms contribute. In contrast to -OH and -F terminations, the HOMO orbitals for -H termination (Figs. 3.3(III-a)) are dispersed through the whole cluster, with the electron probability density reaching towards the core of the QD. The LUMO (Figs. 3.3(III-b)) wave function is relatively delocalised to the QD core with minimal contribution from functional H atoms. Relating to the particle in a sphere model, the delocalised wave function spatial distribution towards the QD core suggests that the large HOMO-LUMO energy gap for -H termination result from the confining potential of the core of the QD (quantum confinement) whilst surface states are dominant and influences the electronic and optical properties of OH- and F-terminated QDs.

Whilst it is shown that the H-terminated 10 Å diameter QD exhibits an optical absorption onset well above that of -F and -OH for a similar cluster size it would be instructive to investigate size dependent quantum confinement effects for a range of QD diameters. In the next sections, the experimentally relevant 10-20 Å diameter range is presented. Full passivation of larger QDs' surfaces ($>$10 Å in diameter) with

(a)

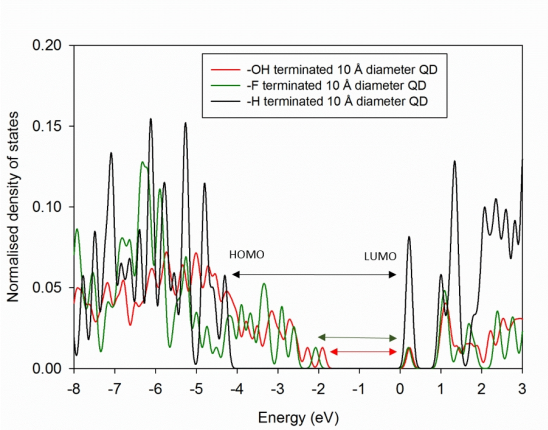

(b)

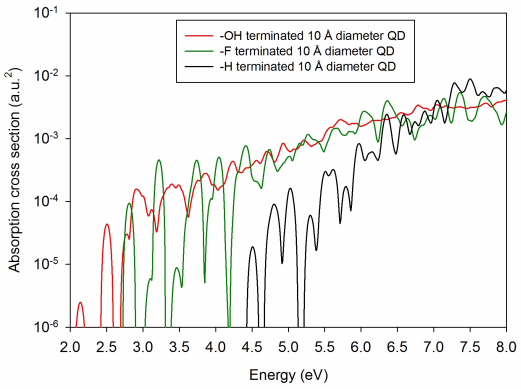

(c)

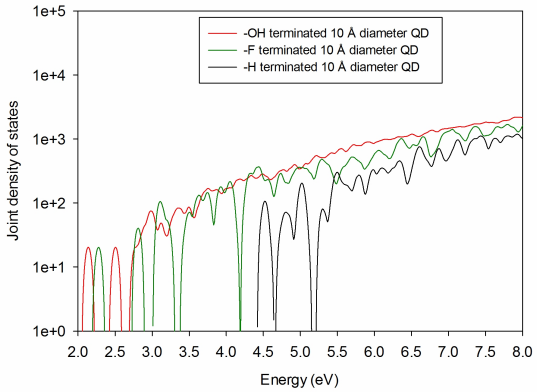

Figure 3.2: The respective (a) normalised density of states (DoS), (b) absorption cross section (ACS) and (c) joint density of states (JDoS) for 10 Å diameter -OH, -F and -H functionalised 4H-SiC QDs.

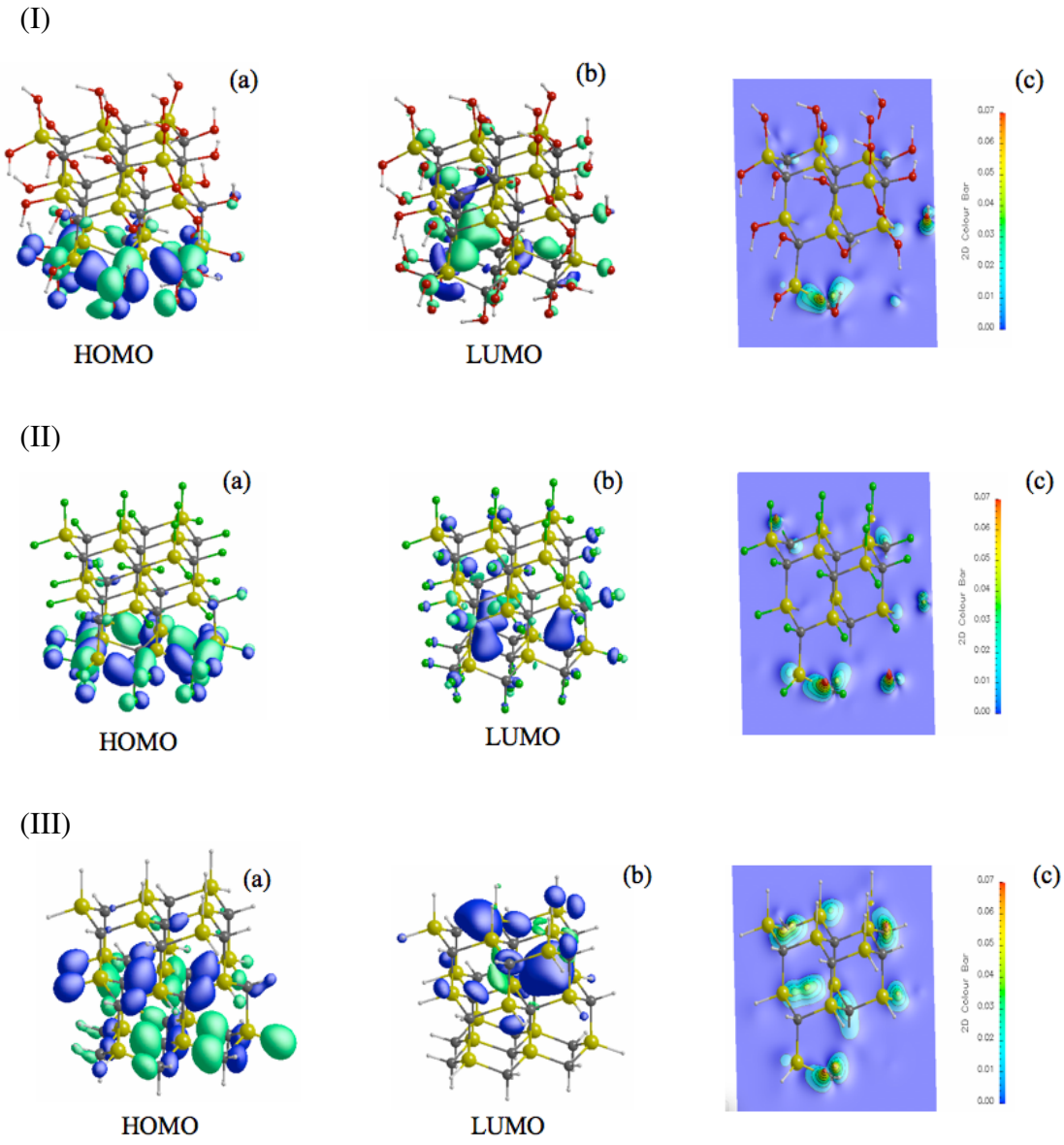

Figure 3.3: Wave functions for 10 Å diameter (I) -OH terminated, (II) -F terminated and (III) -H terminated 4H-SiC QDs with respective 3-D wave function isosurface (0.07 a.u.) for (a) HOMO, (b) LUMO and (c) 2-D slice of electron probability density within 1 eV of the HOMO. The delocalised wave function spatial distribution towards the QD core suggests that the large HOMO- LUMO energy gap for H-termination result from the confining potential of the core of the QD.

-OH, -F and -H would result in the surface termination species coming closer to each other through which steric repulsion becomes significant. By surface reconstructions with Si and C dimers, these surface species would be better accommodated for larger

QD diameters. The effect of surface reconstruction and surface composition on the QDs' electronic and optical properties is presented in the next section.

3.2.2 Effect of Surface Composition and Surface Reconstruction

Data relating to the optimised structures of the SiC-QDs is presented, in the diameter range varying between 10–20 Å, the range that exhibits quantum confinement effects in experiment [31], since the exciton Bohr radius in 4H-SiC is 12 to 8 Å [7, 23]. Table 3.2 lists the QD compositions as a function of QD diameter: N_{Si} (X) and N_C (X) being the number of Si and C atoms for X-centred QD (X for Si or C at the core centre of QD), $N_{Surface}$ represent the number of surface sites on unreconstructed clusters whereas N_{recon} (X) is the number of surface sites for reconstructed clusters with X-centre (X for Si or C). The choice of atom centre of either Si or C does not affect the total number of core atoms but the number of Si or C atoms are interchanged as shown in Table 3.2.

Table 3.2: SiC-QD cluster composition as a function of QD diameter in the range of 10 to 20 Å.

Diameter (Å)	N_{Si}(Si), N_C(C)	N_{Si}(C), N_C(Si)	$N_{surface}$	$N_{recon.}$(Si)	$N_{recon.}$(C)
10	19	20	40	40	40
11	29	29	56	44	44
12	51	41	82	70	70
13	57	62	94	76	76
14	69	74	100	88	88
15	81	83	112	100	100
16	99	96	126	114	114
17	132	118	160	130	136
18	147	151	172	130	142
19	159	175	190	160	148
20	207	199	208	166	172

The number of surface sites on the unreconstructed clusters is independent of whether the QD is Si or C centred. For the reconstructed clusters the number of surface sites is different for Si and C centred cases.

In the case of unreconstructed clusters, only the positions of Si and C atoms are interchanged without changes to bondings with surface sites. In contrast, for the reconstructed clusters, formation of dimers (Si-Si or C-C) on the surface depends on

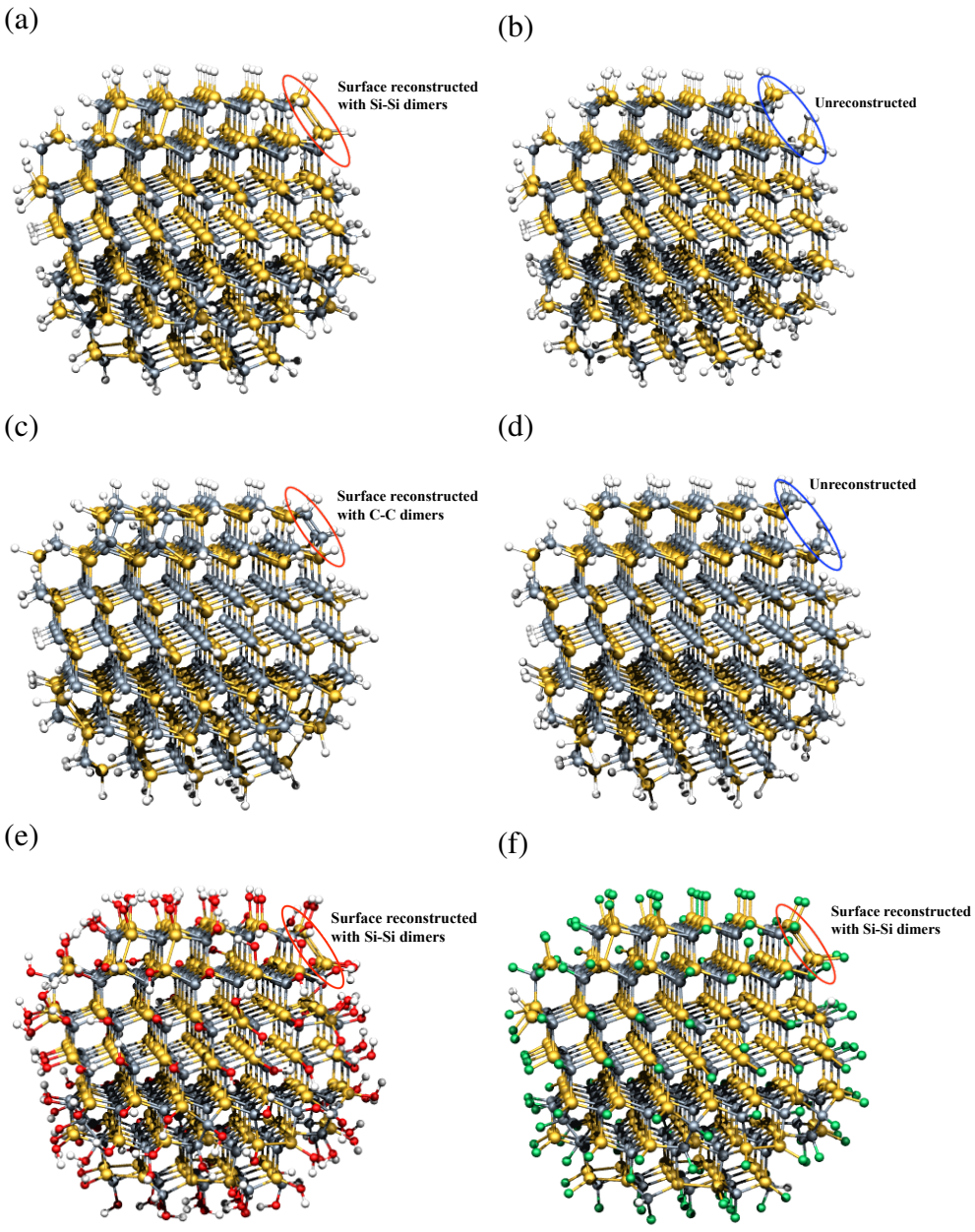

Figure 3.4: Optimised 20 Å SiC-QDs. (a) and (b) are Si-centred, H-terminated SiC-QDs with and without surface reconstructions, respectively. (c) and (d) are C-centred, H-terminated SiC-QDs with and without surface reconstructions, respectively. (e) and (f) are Si-centred SiC-QDs (with surface reconstructions) terminated with OH- and F-groups, respectively. White, red, yellow, gray, and green atoms are H, O, Si, C and F, respectively. The regions indicated by the red and blue ellipses highlight surface sites where the choice of reconstruction or two surface groups varies. Construction of structures has been contributed by Dr. Jonathan Goss and images by Dr. Amit Tiwari.

the choice of C or Si as the QD centre. Additionally, Si-Si with longer bond length may be formed at certain locations where C-C could not, due to its shorter bond length, thus the C atoms are terminated with more surface sites in comparison to Si for this case.

Figure 3.4 shows the 20 Å SiC-QDs, with different centres and surface treatments.The average Si-C, O-H, Si-X, C-X (X=H, O and F in each case), Si-Si and C-C bond lengths in Å are calculated to be 1.87, 1.00, (1.50, 1.64, and 1.59), (1.10, 1.46, and 1.42), 2.39, and 1.60, respectively, which are summarised in Table 3.3. This provide evidence that the optimised structures have reasonable geometries to represent the spherical SiC-QDs observed in experiments. The calculated bond-lengths vary only very slightly in comparison to the 10 Å diameter QDs.

In order to distinguish the effect of surface reconstructions from surface termination, two groups of Si centred H-terminated QDs for the 10 to 20 Å size are compared, where one group includes surface reconstruction.

Table 3.3: 20 Å diameter SiC-QD bond lengths.

Bond	Si-C	O-H	Si-H	Si-O	Si-F	C-H	C-O	C-F	Si-Si	C-C
Average bond length (Å)	1.87	1.00	1.50	1.64	1.59	1.10	1.46	1.42	2.39	1.60

Figure 3.5 shows the ACS for H-terminated, Si centred QDs with and without surface reconstruction. The overall appearance and variation with core diameter is similar, although the onsets, where they differ, are at lower energies where reconstructions are present: the steeper slope (contour) found in reconstructed QDs relative to non-reconstructed for sizes less than 14 Å indicate that surface reconstructions cause greater energy-gap narrowing for small QDs. Additionally, ACS magnitudes near the onsets are larger for the reconstructed QDs whilst at higher energies they are nearly size independent as quantum confinement is known to mostly affect the frontier molecular orbitals (band-edge) energy levels [79].

The ACS show the trends with core diameter, but to understand the origin of the differences it is instructive to examine the DoS. The data for the 20 Å QD are shown in Fig. 3.6 with the zero energy aligned to the Fermi energy. Of note, the reconstructed surface leads to a larger DoS near the HOMO, and this is the origin of the larger ACS.

(a) (b)

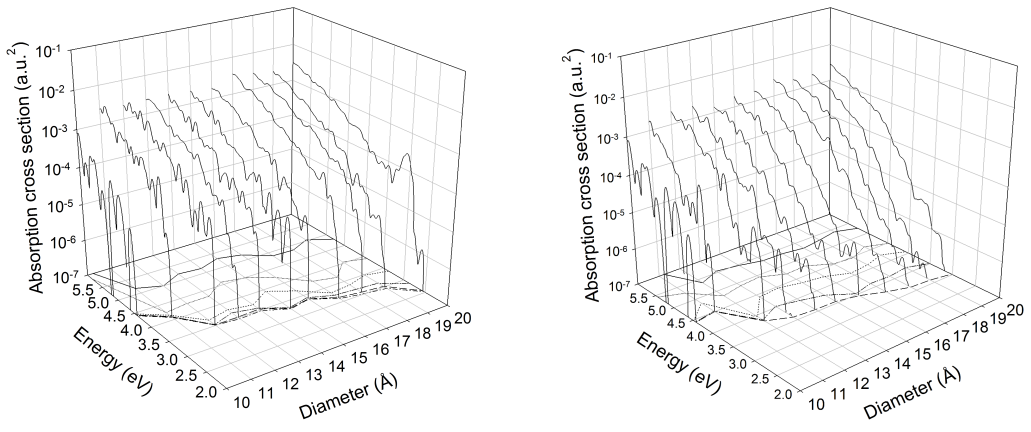

Figure 3.5: ACSs for H-terminated Si centred 4H-SiC QDs as a function of core diameter for surfaces that are (a) reconstructed, and (b) not reconstructed. The contours indicate 10^{-7}a.u.^{2} to 10^{-3}a.u.^{2}, in factors of 10.

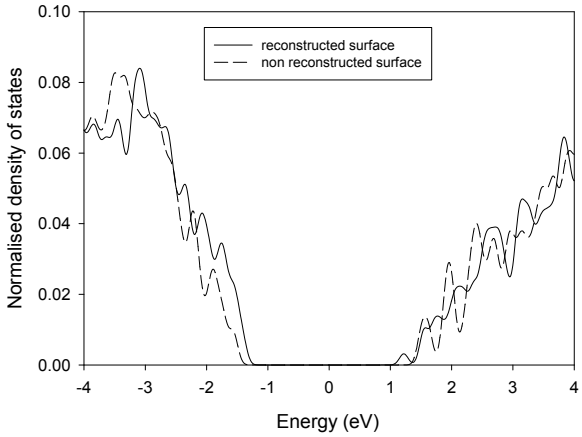

Figure 3.6: Density of states for reconstructed and unreconstructed 20 Å diameter Si centred, H-terminated QD. The zero energy is aligned to the Fermi energy.

The HOMO-LUMO gap of the unreconstructed QD is approximately 0.4 eV wider than the reconstructed case, which explains the lower energy onset in the case of the reconstructed surface. The wave functions for the two surface reconstructions are shown in Fig. 3.7. The HOMO where reconstruction has occurred (Fig. 3.7(a)) indicates some localisation around the reconstructions, with even more significant localisation in the LUMO (Fig. 3.7(b)). In contrast, the HOMO (Fig. 3.7(c)) and

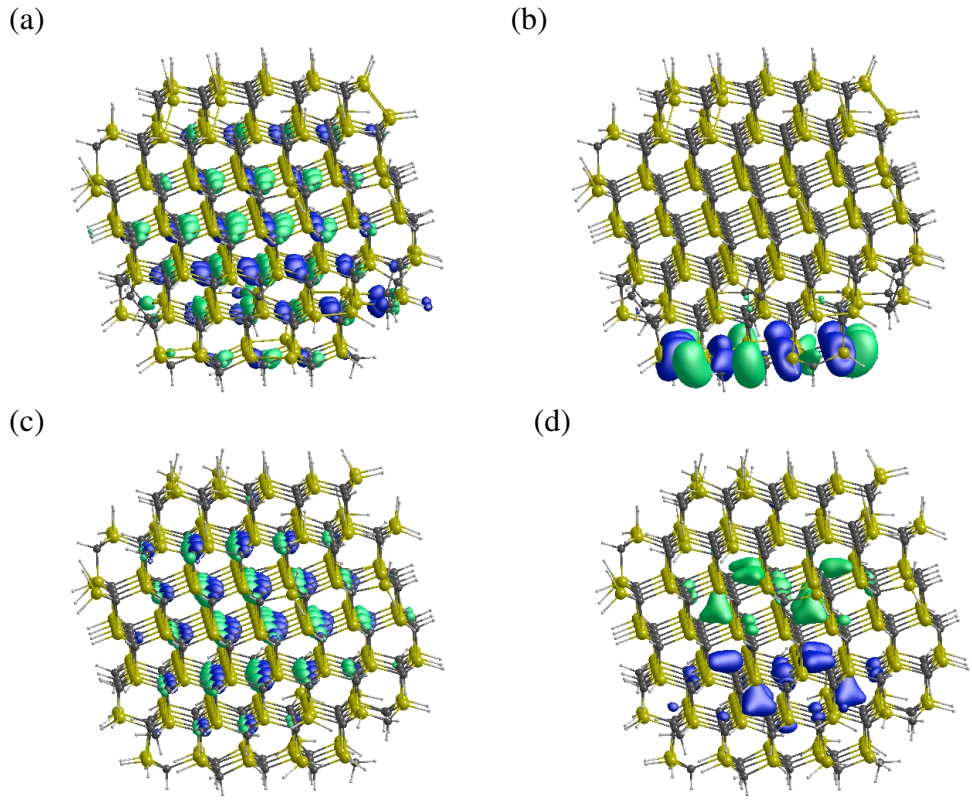

Figure 3.7: Wave function iso-surfaces for Si centred, H-terminated, 20 Å SiC-QDs. (a) and (c) are HOMOs, and (b) and (d) LUMOs, with (a) and (b) showing the reconstructed surface, and (c) and (d) the non-reconstructed surface. Yellow, gray, and white atoms are Si, C, and H, respectively. The green and blue iso-surfaces show the molecular orbitals of positive and negative phase, with amplitude of 0.04 a.u.$^{-3/2}$. The clusters are shown with the c-axis of the underlying 4H-SiC vertical. The delocalisation of electron wavefunctions towards the QD core, assist quantum confinement for H-termination.

LUMO (Fig. 3.7(d)) for the unreconstructed case are distributed throughout the core. This suggests that the homo-nuclear dimers present in reconstructions lead to surface states, narrowing the energy gap. Energy gap narrowing and an increase in absorption due to Si-Si dimers has been reported previously [32], with similar conclusions drawn as in the current study. Despite the impact reconstruction has upon the ACS, it is important to note that quantum size effects are observed across the sizes examined in this study irrespective of the reconstruction.

Previous reports [36, 80] suggested that energy-gap changes relate to a shifting HOMO

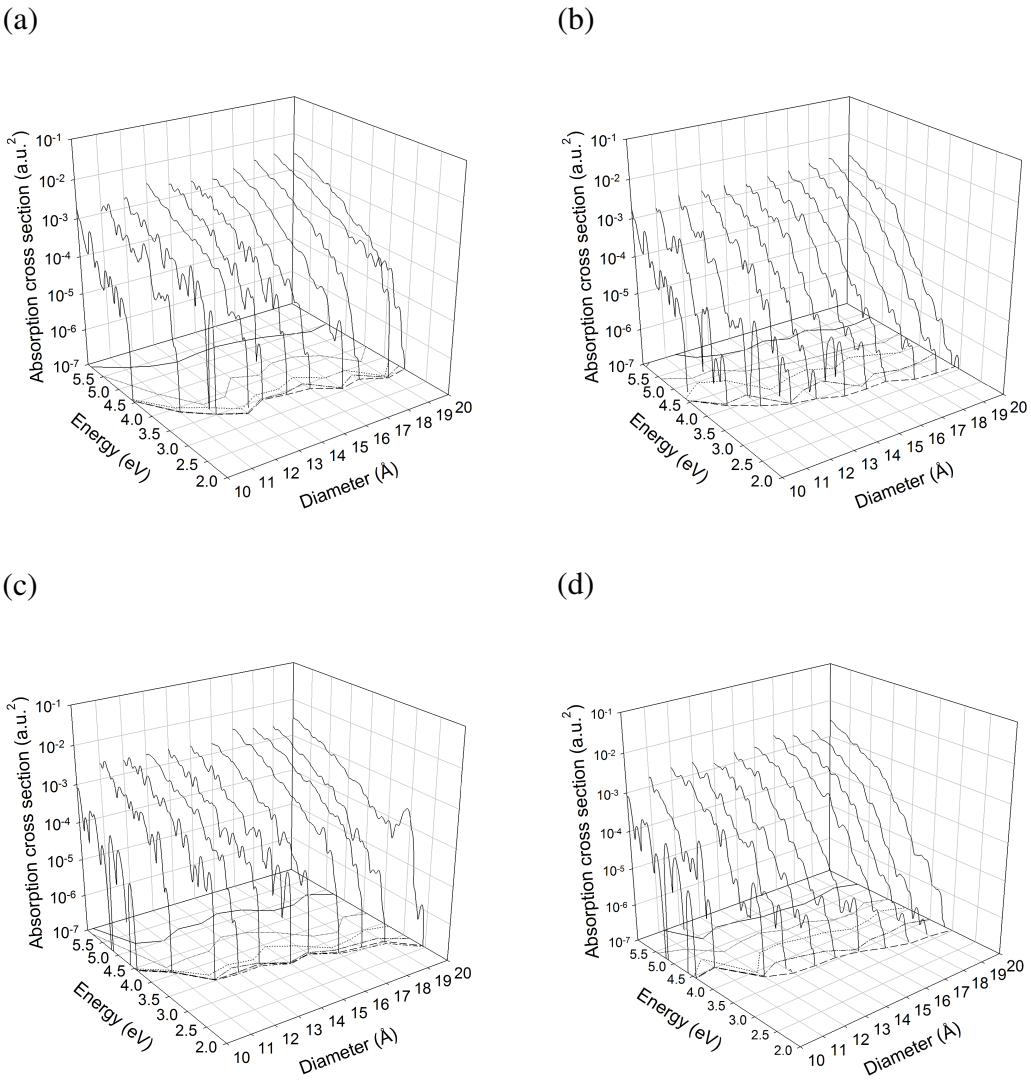

Figure 3.8: ACSs for H-terminated C-centred 4H-SiC QDs as a function of diameter for surfaces that are (a) reconstructed, and (b) not reconstructed. ACSs for H-terminated Si centred 4H-SiC QDs as a function of core diameter for surfaces that are (c) reconstructed, and (d) not reconstructed. The contours indicate 10^{-7}a.u.^{2} to 10^{-3}a.u.^{2}, in factors of 10. Overall trends are very close for C-centred and Si-centred QDs. Thus, there is no significant dependence upon the choice of centre.

while the LUMO remains constant with different surface terminations. However, the influence of dimers in the structures were not investigated in Ref. 36 while in Ref. 80 the LUMO pinning ascribed to nearest-neighbor π and σ^* orbitals may be related to the tetrahedral structures studies, in contrast with our pseudo-spherical models.

Another choice made at the point of construction of the QDs is the species upon which

the cluster is centred. Figure 3.8 show the ACS for C-centred SiC-QDs. The relatively small differences between the Si and C centred structures are most likely a consequence of the differing mixtures of C-H and Si-H bonds at the surface [31, 80], as previous studies report QDs with Si-H surface bonds exhibit smaller energy gaps compared to C-H surface [32, 34, 35, 81].

Although there are minor differences, the overall trends for C-centred SiC-QDs are very close to those of the Si-centred clusters shown in Fig. 3.8 (c) and (d), and it is concluded that so far as the optical properties are concerned there is no significant dependence upon the choice of centre. Indeed, this is what one might expect since these clusters are of the order of the exciton Bohr radius, so that the states involved in the optical transitions involve all of the Si and C atoms.

However, the role of the hydrogen chosen to terminate the clusters and remove any dangling bonds remains to be analysed. The effect of hydroxyl (OH) and fluorine (F) termination on the same cores as presented above for the hydrogen termination case is presented.

3.2.3 Effect of Surface Termination Groups on Optical Absorption

Figure 3.9(a) and (b) show the ACS for OH- and F-terminated QDs, where all clusters have been reconstructed and are Si centred, and can be compared directly with Fig. 3.9(c). The effect upon the absorption onset for OH- and F-termination (size-independent and flat along $\sim$ 2.0 eV) in comparison to H-termination (size-dependent from 4.5 to $\sim$3.0 eV) is immediately evident: the differences between, for example, Figure 3.9(a) and Fig. 3.9(c) is much larger than the effects of reconstruction or whether the cluster is centred on the Si or C (Fig. 3.9(c), (d) or (e), (f)).

In particular, the quantum confinement effect tend to increase from hydroxyl, to fluorine, to hydrogen termination, with H-termination showing the clearest size dependence. The absorption onset for the H-termination increases from 2.5 to 4.4 eV with reducing size, a net increase of $\sim$2 eV in the 10–20 Å diameter range, whereas for F- and OH-termination, almost no size-dependent change is observed. As a result, for low core diameters there is a large difference in the onset energy as a function of

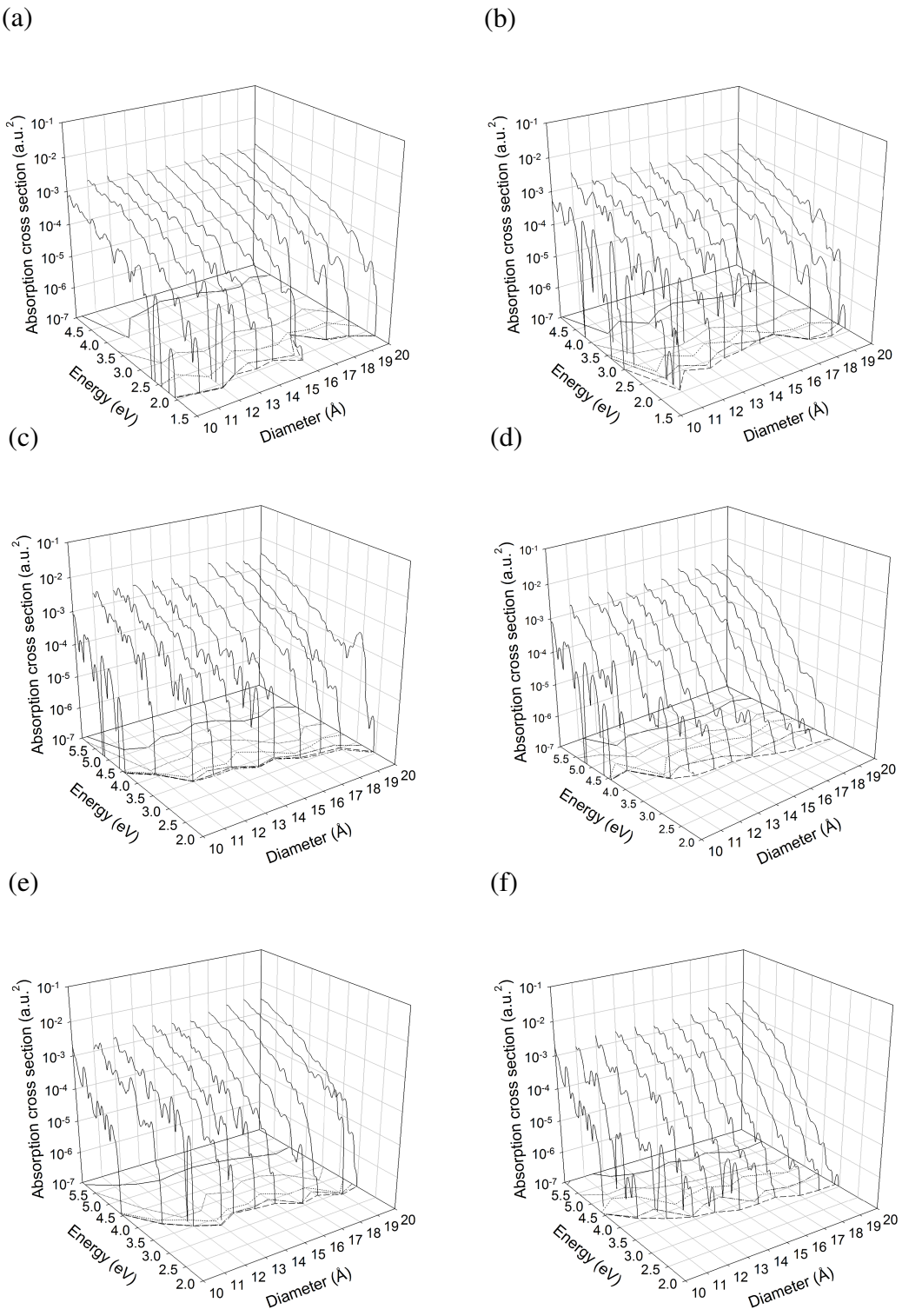

Figure 3.9: ACSs for (a) OH-terminated and (b) F-terminated 4H-SiC QDs. ACSs for Si-centred, H-terminated (c) reconstructed and (d) unreconstructed QD. ACSs for C-centred, H-terminated (e) reconstructed and (f) unreconstructed QDs. The contours indicate 10^{-7}a.u.^{2} to 10^{-3}a.u.^{2}, in factors of 10. The effect of termination species (-OH, -F, -H) outweigh the effects of composition and surface reconstruction.

termination, so that for example, in the case of 10 Å SiC-QDs, the difference in onset for the ACS for OH- and H-termination is nearly 2.5 eV.

3.2.4 Effect of Surface Termination on Density of States, HOMO/LUMO Wave Functions and Electron Probability Density

Figure 3.10 shows the DoS for Si-centred, surface-reconstructed, 20 Å-diameter SiC-QDs terminated by OH, F, and H, with zero energy aligned to the Fermi energy. The major effect of terminating species is variation in the HOMO: OH, F, and H have energies of $-0.51\ eV$, $-0.76\ eV$, and $-1.23\ eV$, respectively. In contrast, the LUMO energies are relatively constant, lying in the 1.0–1.1 eV range.

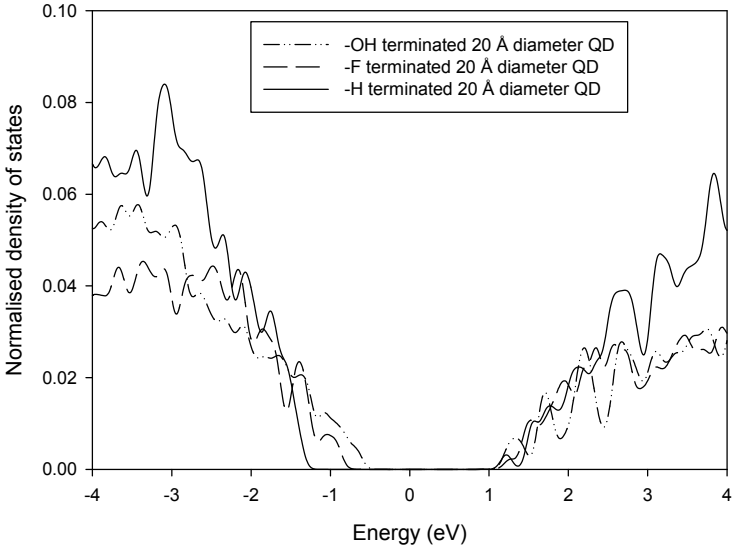

Figure 3.10: DoS of 20 Å, Si-centred QDs in the vicinity of the optical gap.

The difference in the energies of the HOMO is related to the degree of wave function localisation at the surface. Figure 3.11(a) shows the OH-termination HOMO is strongly associated with surface C p-orbitals and oxygen lone-pairs. Similarly, HOMOs of F-terminated clusters are associated with F lone-pairs (Fig. 3.11(c)), whereas H-termination (Fig. 3.7(a)) show no such localisation. The LUMOs of OH-termination (Fig. 3.11(b)) and F-termination (Fig. 3.11(d)) consist of mixtures of surface O (F) lone-pairs and core C p-orbitals for OH- (F-) terminations, respectively.

The LUMO localisation at the QD surface is more significant in OH- than F-termination. Although the HOMOs and LUMOs are localised on one part of the SiC-QD surfaces in the figure, the surface states associated with the lone-pairs in fact form a band of orbitals that when taken together cover the surfaces. The lone-pair energies are not significantly affected by the core diameter because they are localised on the surface, leading to the relatively weak size dependence in the ACS (Fig. 3.9). It is concluded that the insensitivity of optical absorption for OH- and F-terminated SiC-QDs is a reflection of surface states associated with the terminating species.

The influence of surface terminations on the electronic structure is further elucidated by examination of energy levels deeper than the frontier electronic levels. Figure 3.12 shows that for -H terminated Si centred 20 Å SiC-QDs, the electron probability density of the HOMO (Fig. 3.12(a)) is dominated by

electrons within the core of the QD while the LUMO (Fig. 3.12(b)) is surface related arising from the Si dimers. For deeper energy levels, within 0.5 eV of the HOMO (Fig. 3.12(c)), the probability density increases with more electrons populating the QD core while for the LUMO (Fig. 3.12(d)), in addition to the surface, electrons from the core start to contribute. Examining deeper still in energy (within 1 eV) from the frontier electronic levels, it is found that the electron probability density is well delocalised throughout the QD core as can be seen in Fig. 3.12(e) and Fig. 3.12(f). The delocalised electron probability density at higher energy levels (core HOMO and core LUMO) within the QD core would be influenced by the confining potential that support quantum confinement effects. In contrast, surface states near the frontal orbital of the LUMO (surface LUMO) are weakly influenced by the confining potential and would obscure quantum size effects. It is illustrated clearly that the energies in the vicinity of the HOMO for H-termination is highly dominated by electrons from the core. On the other hand, for the LUMO, the surface states dominate at lower energies but at higher energies, electrons from orbitals within the core of the QD contributes.

For F-termination, at the frontier orbitals, the HOMO (Fig. 3.13(a)) constitute electrons that are highly localised to the surface with no contribution from the core while the LUMO (Fig. 3.13(b)) show a mix of electrons occupying the surface and core of the QD. Within 0.5 eV of the HOMO (Fig. 3.13(c)), the electron occupation of surface

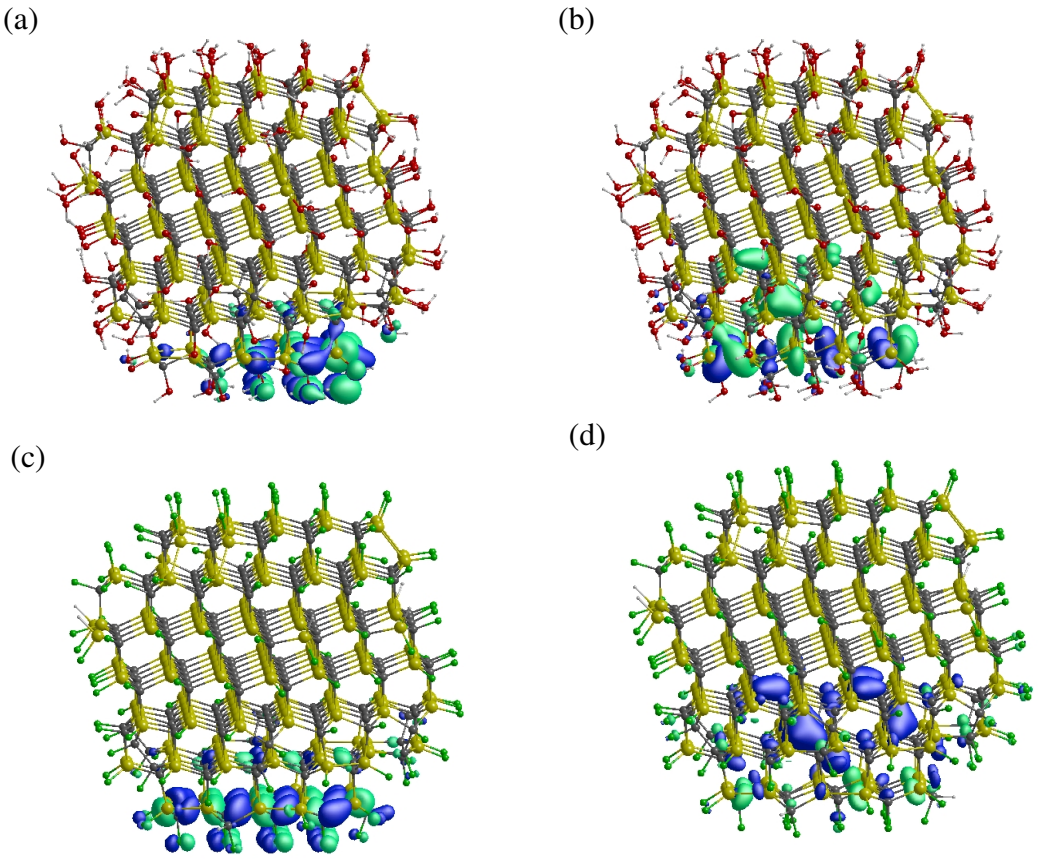

Figure 3.11: Wave function iso-surfaces for Si centred 20 Å SiC-QDs.(a) and (b) are HOMO and LUMO for -OH termination whereas (c) and (d) are HOMO and LUMO for F-termination. Choice of iso-surfaces, the atom colors, and orientation of the SiC-QDs are as indicated in Fig. 3.7. Lone-pair energies are not significantly affected by the core diameter because they are localised on the surface, leading to the relatively weak size dependence in the ACS for F- and OH-terminations.

atoms around the perimeter of the QD is further elaborated and additional contribution from core-related electrons is observed. The LUMO (Fig. 3.13(d)) in this higher energy interval involve more highly localised electrons at the surface and added contributions from electrons in the core. Higher up in energy to within 1 eV interval from the HOMO and LUMO, more electrons from the QD core participates, such that there is a mix of highly localised surface electrons and core related

electrons in the vicinity of the HOMO (Fig. 3.13(e)), whilst in the LUMO (Fig. 3.13(f)) the core related electrons start to dominate. The trends for -OH termination follows that of -F termination but surface localisation is greater for -OH as can be seen for the HOMO (Fig. 3.14(a)) due to surface C p-orbitals and oxygen lone-pairs. The LUMO

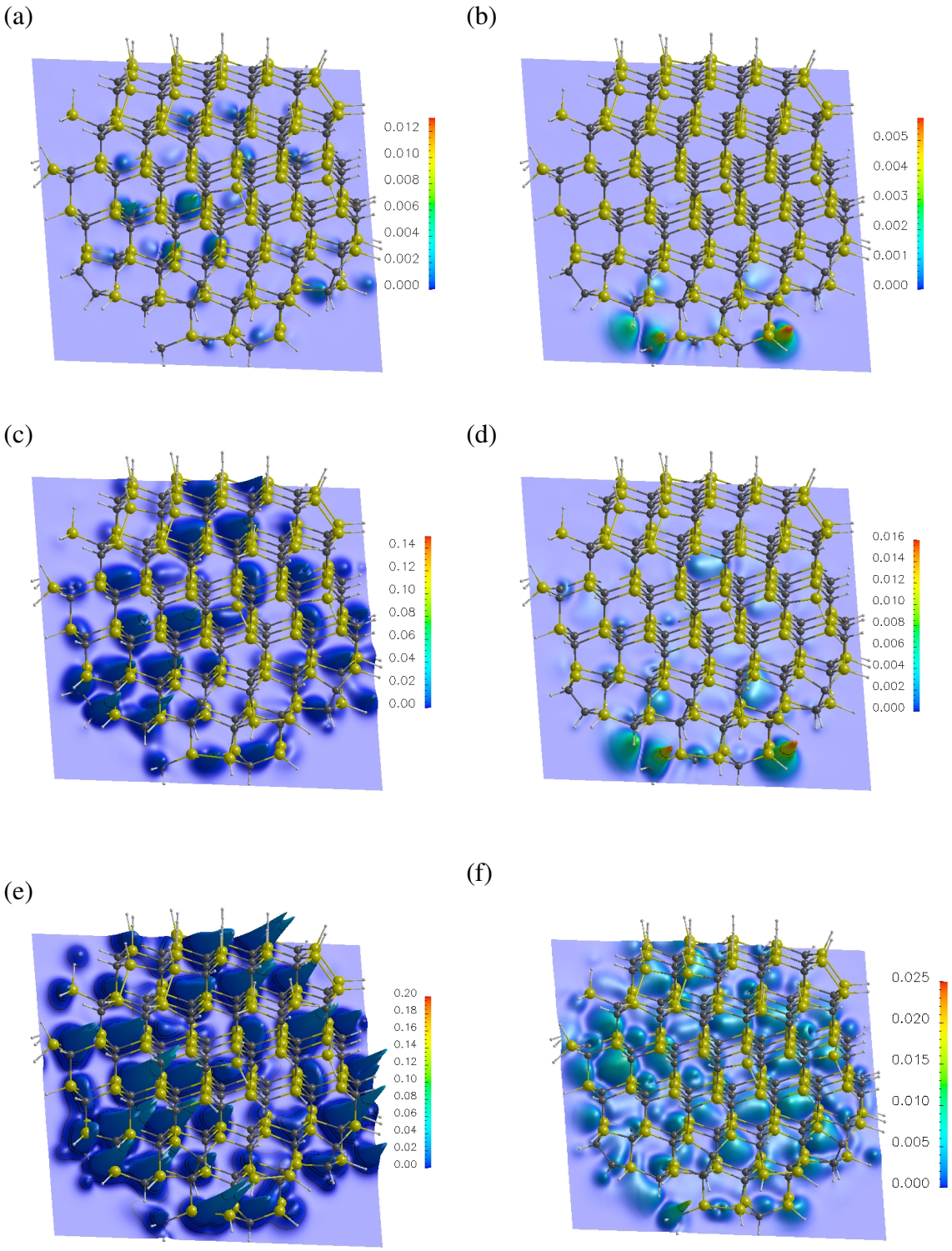

Figure 3.12: 2 dimensional slice through the centre of Si centred 20 Å SiC-QD exhibiting -H electron probability density for (a) HOMO, (b) LUMO, (c) within 0.5 eV of the HOMO, (d) within 0.5 eV of the LUMO, e) within 1 eV of the HOMO and (f) within 1 eV of the LUMO. The delocalised and localised states of the respective HOMO and LUMO are represented in Fig. 3.16(a).

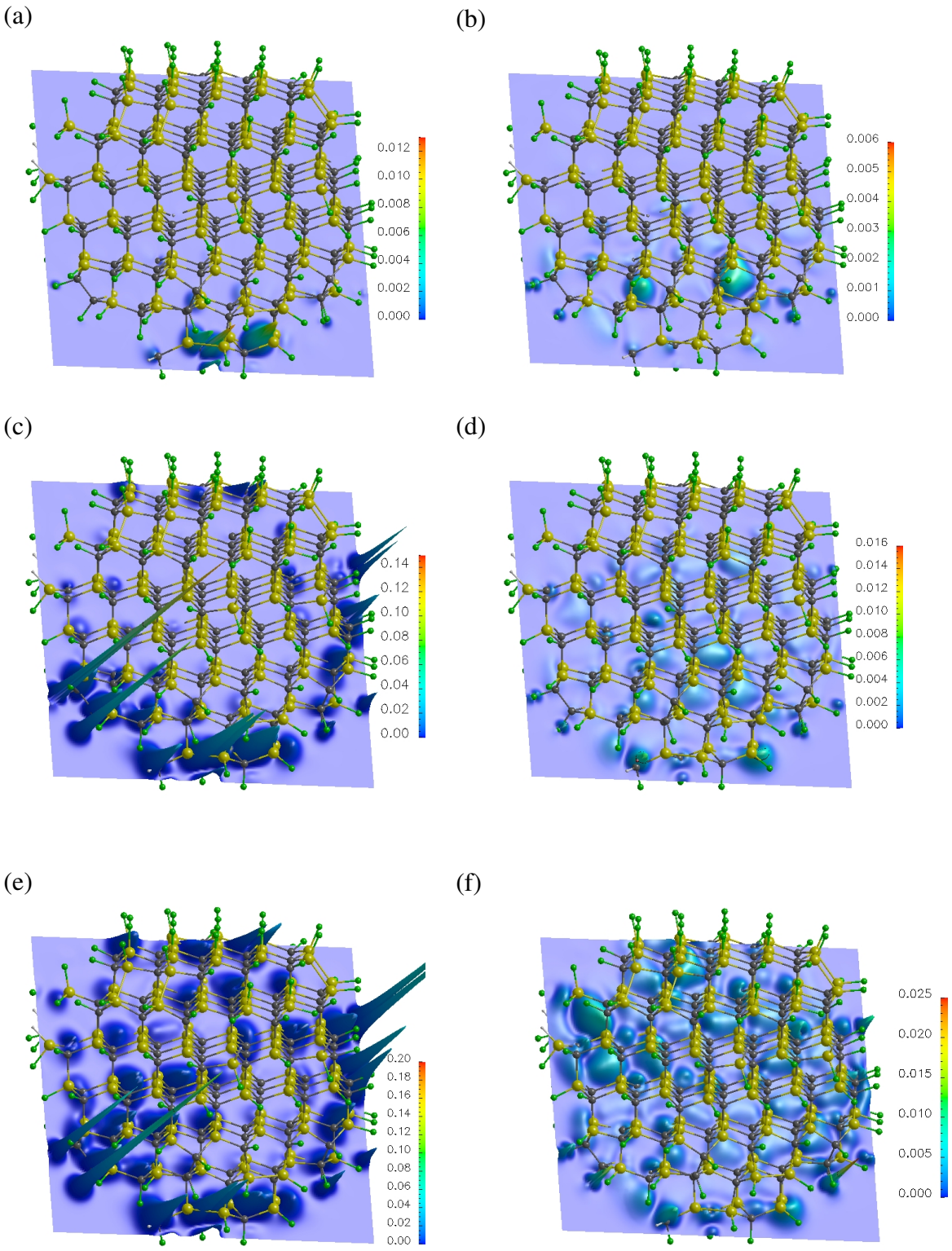

Figure 3.13: 2 dimensional slice through the centre of Si centred 20 Å SiC-QD exhibiting -F electron probability density for (a) HOMO, (b) LUMO, (c) within 0.5 eV of the HOMO, (d) within 0.5 eV of the LUMO, e) within 1 eV of the HOMO and (f) within 1 eV of the LUMO. The localised states of the respective HOMO and LUMO are represented in Fig. 3.16(b).

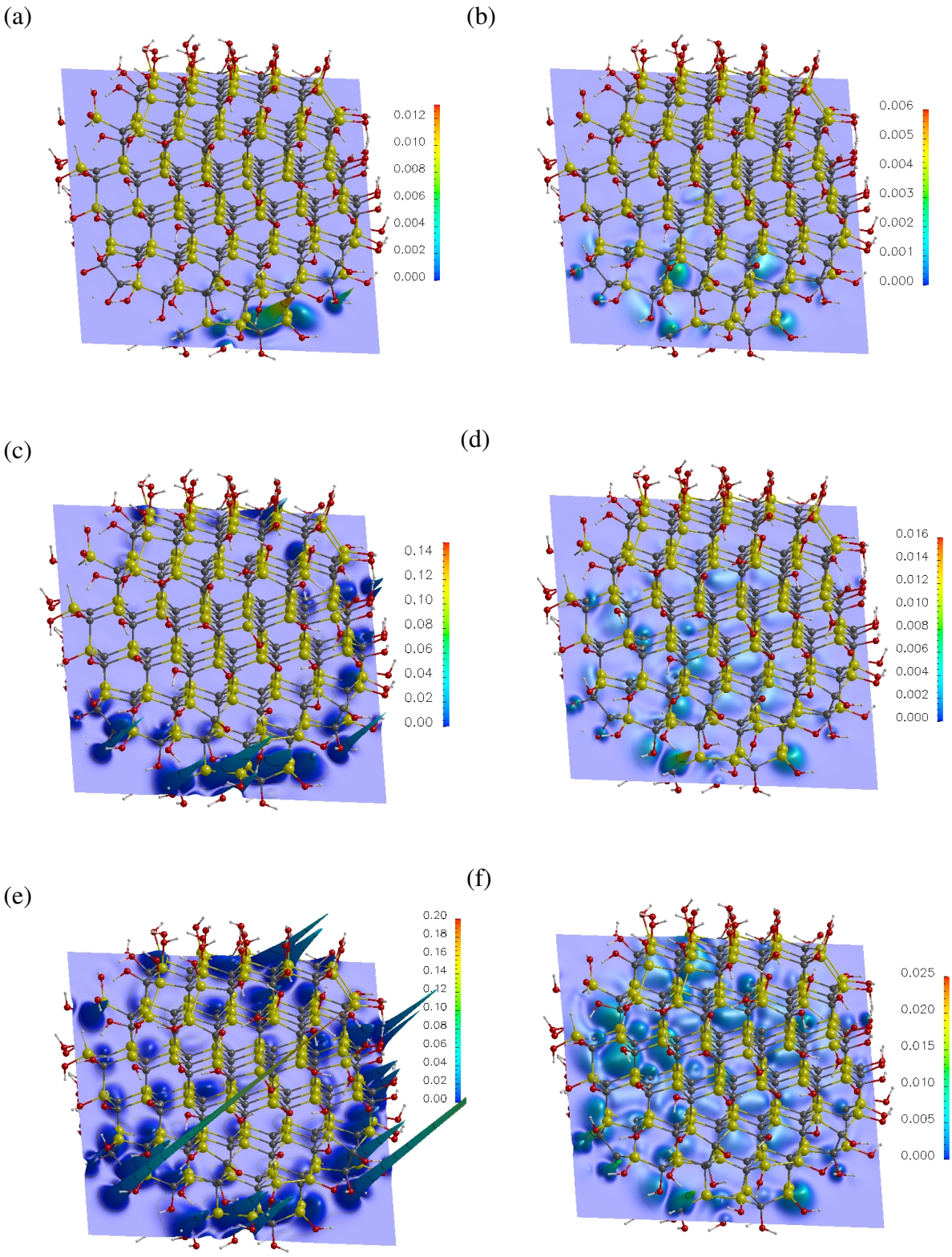

Figure 3.14: 2 dimensional slice through the centre of Si centred 20 Å SiC-QD exhibiting -OH electron probability density for (a) HOMO, (b) LUMO, (c) within 0.5 eV of the HOMO, (d) within 0.5 eV of the LUMO, e) within 1 eV of the HOMO and (f) within 1 eV of the LUMO. The localised states are represented in Fig. 3.16(b).

(Fig. 3.14(b)) is a mix of surface and core electrons. Towards higher energies of within 0.5 eV of the respective HOMO and LUMO, more electrons occupying the surface of the QD can be observed with still minimal contribution from the QD core in the vicinity of the HOMO (Fig. 3.14(c)) while the electron probability density for energies near the LUMO involve electronic states within the core (Fig. 3.14(d)). It is observed that going higher in energies, the localisation of electrons at the surface is being balanced out with electrons from within the core as shown in (Fig. 3.14(e) and (f)).

The examined electron probability density for -H, -F and -OH terminations spanning the frontier orbital energies towards higher energies indicate that the electrons at the surface and within the QD core are well coupled throughout the investigated energy range for -H. Conversely, for -F and -OH terminations, these are decoupled: the core related electrons predominantly occupy higher energies whereas surface related electrons dominate the frontal electronic levels, particularly the HOMO which causes narrowing of the optical gap. Having inspected the core and the surface electron probability density for 20 Å SiC-QD, further examination of the trends of the JDoS at high energy (core-related) versus the JDoS at onset (surface related) for the diameter range 10-20 Å was undertaken. In the next section the effect of the surface termination groups; -H-, -OH and -F upon the optical properties of 4H-SiC QDs is discussed.

3.2.5 Surface-state Dependent Optical Properties of 4H-SiC QDs

Where quantum confinement is present, energies can be predicted following a 'particle in a sphere model'[11], that predicts that they are discrete and scale with the QD diameter, d, as d^{-2}. Figure 3.15(a) summarises the energy gap of the QDs as a function of the size and terminating species. H-termination results in a large size dependence, whereas F- and OH-termination do not. The HOMO-LUMO gap increases in the case of H-termination due to the quantum mechanical 'particle in a sphere' picture, where spatial localisation of the particle within a potential well causes the oscillator energy to increase as the potential well width decreases. For F and OH termination additional surface states are present, their energy being defined by the immediate bonding to the SiC surface, and not by the size of the QD. Owing to the chemistry involved in sample

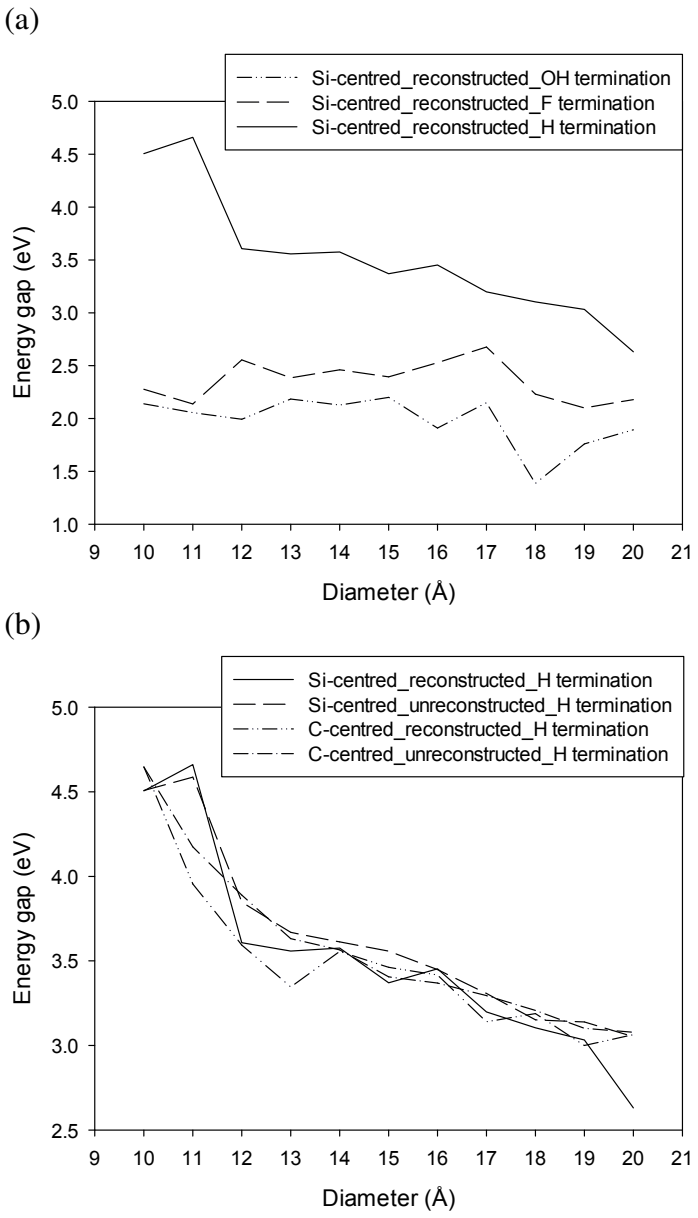

Figure 3.15: (a) Energy gap versus QD size with different surface termination groups and (b) energy gap of -H terminated QD versus QD size by surface reconstruction and surface composition. Surface termination groups (OH, F, H) play a greater influence than size and surface reconstruction.

preparation, the electronegative O and F atoms terminates on the SiC QDs, resulting in localisation of the electron wavefunctions in non-bonding lone pair orbitals on the QD surface. The effect is in contrast to H-termination that form sigma bonds and delocalisation of the electrons wavefunctions towards the QD core. This effect has been observed in DFT calculations for Si QDs where surface termination with O, F, OH and S introduce additional gap states localised to the passivant and consequently

narrowing the optical gap [82]. It is noted that in the case of Si QDs [83], an initial blue emission may red-shift to orange/red upon oxidation despite the reduction in QD core size indicating that absorption/emission at the Si-SiO_2 interface may be at play. Figure 3.15(b) allows for comparison of H-terminated clusters with different compositions, and surface reconstructions, encapsulating the conclusions above that reconstruction and choice of cluster centre have no significant impact upon the energy gap relative to the effect of the termination. Amongst quantum dots larger than 10 Å that are all surface reconstructed across the different surface group terminations, -H termination consistently exhibit stronger quantum confinement compared to -F and -OH. This indicates that the surface termination groups play a greater influence than size and surface reconstruction. The energy-gap as a function of size for H-terminated QDs agrees quantitatively with previous DFT results [31], and although those obtained using tight-binding are systematically larger [36], they exhibit the same trend.

However, to understand the size-dependence of SiC-QDs, it is required to include all possible configurations of surface states. In a simple model, two factors are considered. The states associated with the SiC core exhibiting quantum confinement will result in a narrowing of the optical gap as the core diameter increases. This is represented schematically by the solid lines in Figs. 3.16(a) and (b). The second component arises from two surface effects. The first is the introduction of states due to homo-nuclear bonds arising from reconstruction. In the case of H-termination, this introduces an unoccupied state below that of the core, as represented by the higher of the dashed lines in Fig. 3.16(a). This state is relatively independent of core diameter, as it is essentially a surface effect. For a large enough cluster, this surface state is expected to lie outside the core gap, *i.e.* reconstructions impact the optical properties of relatively small SiC-QDs. However, as noted above, at a quantitative level the impact of the reconstruction is relatively modest. For F- and OH-termination (Fig. 3.16(b)) the lone-pair orbitals mean that there are both occupied and empty surface-states within the gap arising from the core. Therefore the predicted optical properties of F- and OH-terminated SiC-QDs can be divided into two regions. In region A, the HOMO and LUMO are associated with surface states and the energy gap is approximately constant. In region B, the HOMO and LUMO originate from core states, so that quantum confinement effects become significant.

(a)

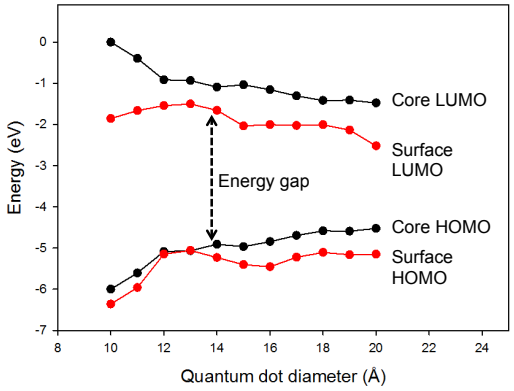

(b)

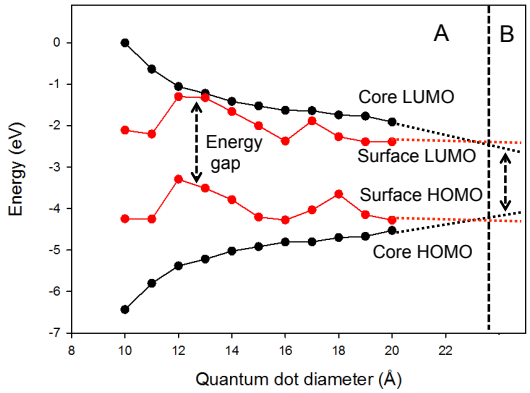

(c)

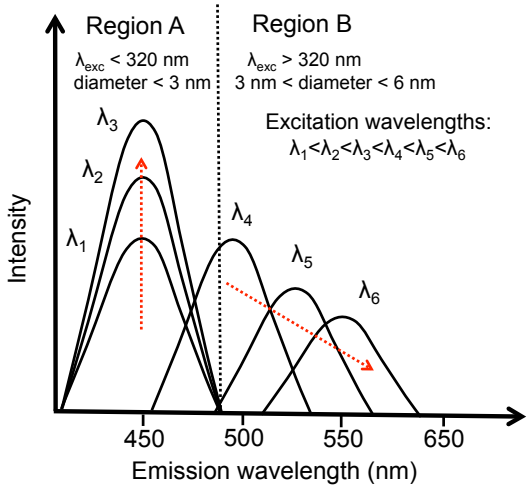

Figure 3.16: Illustration of core and surface states related HOMO and LUMO as a function of size in surface reconstructed 4H-SiC QD for (a) H-termination and (b) OH- or F-termination with the respective regions A and B. (c) Shows a simplified dual-feature photoluminescence spectrum of SiC QDs in regions A (when surface states dominates) and B (when core related states dominates).

The dual-feature PL spectra of SiC-QDs observed experimentally is represented schematically in Fig. 3.16(c). In a QD ensemble containing a range of core sizes, short wavelengths excite all QDs [7, 17, 24], whereas longer wavelengths excite only large QDs. However, 10–60 Å SiC-QDs yield PL peaks which are largely insensitive to excitation wavelength up to around 320 nm. The dual feature of the PL spectra has been discussed in terms of quantum confinement effects only being responsible for the observed size-dependence of emission in larger SiC QDs [7, 17, 21], but to-date a clear explanation regarding the size-independent features has not yet been fully established. The presence of mixed phases and defects have been reported based on measured interplanar spacings. 4H and 6H-SiC based QDs exhibited interplanar spacings of 0.217 nm for 3C $(20\overline{2}0)$ planes [7] and 0.195 nm for 3C $(21\overline{3}0)$ planes [17], attributed to the polytype changes during ultrasonication process. Mixed phases of polytypes within the QDs may explain the sub bandgap emissions observed for the 4H- and 6H-SiC derived QDs, as these may contain 3C crystallites of a lower bandgap; resulting in the low energy emission peak. However, it cannot explain the dual-feature PL which show quantum confinement (red-shifting PL) for larger sizes, but deviation for the smaller sizes (constant PL) in all polytypes. Should there be crystallites of multiple polytypes (hence multiple bandgaps) within the QDs, then quantum confinement should increase when the sizes decrease as the polytypes with larger bandgaps becomes more confined. The observation can be explained if the emission (and excitation) is not purely a core property, but rather has a contribution from surface states (Figs. 3.16(a) and (b)). Red-shifts for excitation wavelengths above around 360 nm show the onset of quantum-confinement effects, as only those SiC-QDs large enough to be in region B in Fig. 3.16 are excited.

In a previous investigation on SiC quantum ring [84], the quantum size effects is absent when the excitation wavelengths are smaller than 350 nm and spectral shifts due to quantum confinement is noted for excitation wavelengths larger than 350 nm. Experimental findings indeed validate the argument that the complex interplay between surface reconstructions and terminating species is critical below the threshold diameter of < 30 Å. In the present context, the threshold size can be defined in a similar fashion, when the QD core related joint density of states (JDoS) start to dominate over those that are surface related (Figs. 3.5(a)).

(a)

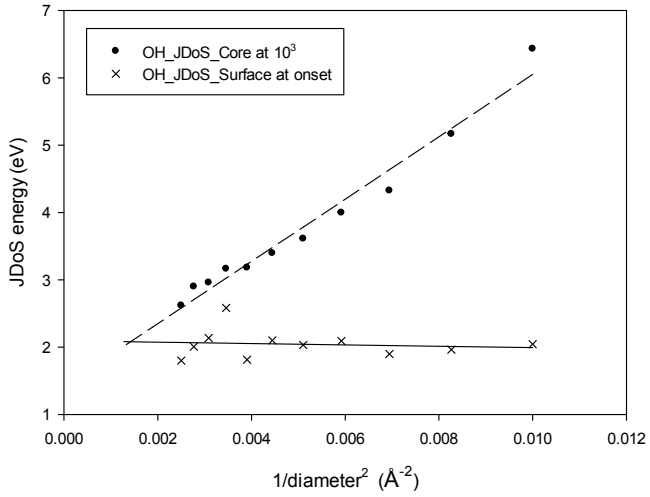

(b)

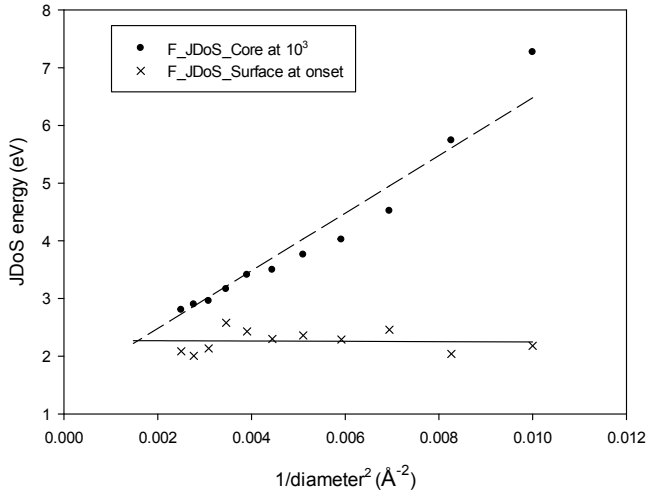

Figure 3.17: Change in energy of core related and surface related JDoS versus inverse square of diameter for (a) OH termination and (b) F termination. Based on the trend, it is predicted that the surface related states will define the emission up to between 25 and 27 Å diameter for F- and OH-terminations.

To illustrate the relative roles of the surface and core states as simulated in this study, the JDoS contours related to absorption onsets and at $10^3\,\mathrm{eV}^{-1}$ representative of the core (Fig. 3.17) are plotted. Core atoms related JDoS shows a linear correlation with diameter^{-2} for both OH and F terminating groups, consistent with the particle in a sphere model [11, 85]. However, the surface-state related JDoS do not increase. The particle in a sphere model imposes a boundary condition for the wavefunction to be zero at the QD edge resulting in the confinement energy scaling as diameter^{-2},

analogous to the energy of the free electron in a one dimensional infinite square well potential. Since the core-related JDoS originate from electron and hole wavefunctions that are spatially delocalised to the QD core, this boundary condition is satisfied resulting in energy scaling with diameter^{-2}. On the other hand, surface-related JDoS with wavefunctions localised to the QD edge do not conform to the model's boundary condition resulting in a constant or size-independent trend. Based on the trend, it is predicted that the surface related states will define the emission up to between 25 and 27 Å diameter for F- and OH-terminations (the intersections of the lines in Fig. 3.17). For other surface groups, the intersection is expected to differ from these values, but the general feature of a dual-feature optical spectrum for systems involving main-group lone-pairs is expected.

3.3 Conclusions

In conclusion, 10 to 20 Å diameter SiC-QDs with OH-, F-, and H-termination have been investigated. Although underestimation of the energy gap in DFT calculations is well known, the nature of the study is qualitative and is aimed to establish the systematic differences between different surface termination. DFT calculations are well placed to predict these trends.

In real experiments, the dual-feature PL was observed for all major polytypes comprising 3C-, 6H- and 4H-SiC. The SiC bulk bandgap increases with polytype in the order: 2.36 eV (525 nm), 3.00 eV (413 nm) and 3.23 eV (383 nm) for 3C, 6H and 4H respectively. However SiC QDs derived from these polytypes exhibit strikingly similar constant PL emission wavelength near 450 nm for sizes smaller than 3 nm, which is above bandgap for 3C but below bandgap for 6H and 4H-SiC. The role of polytypes was not observed in the optical properties of SiC QDs particularly at smaller sizes. Beyond 3 nm, increasing the excitation wavelength result in red-shifting in the PL emission from 450 towards 560 nm, exhibiting PL that is characteristic of 3C-SiC regardless of the starting material. Due to these observations, polytypic phase transformation are frequently given as the explanation.

In this work, by examining the electronic structures of a wide range of compositions and surface treatments, it is concluded that the dual-feature PL spectra observed

experimentally is best explained by considering the interplay of core and surface states, where surface states dominate at small scales (smaller than around 25 Å) and core states dominate at for larger SiC-QDs.

It is found that the chemical nature of the surface termination groups is a critical factor in controlling the quantum confinement of 4H-SiC QDs, and hence the optical properties. It is also noted that although surface reconstructions have an impact, it is generally much smaller than that arising from the choice of termination.

An important conclusion follows. If it is desirable to have a wide range of absorption energies, one might best realise this by using a suitable range of the sizes of the optically absorbing cluster. Surface states must then be avoided, and from our analysis, H-termination is favourable. Furthermore, for SiC-QDs smaller than $\sim$30 Å, surface termination with hydrogen is a highly effective, although experimentally challenging, route [86, 87] to tune the optical properties for a wide spectral range since it significantly suppresses the influence of surface states.

However, one might wish the SiC-QDs to absorb and/or emit with wavelengths only weakly dependent upon the particle size, and then one might exploit the commonality of the energies arising from the terminating species. It is predicted that over a relatively wide range of core diameters, OH- and F-terminated SiC-QDs show weak quantum confinement due to wavefunction localisation to surface atoms introducing surface states within the energy gap. Indeed, it is projected that a threshold size after which surface states lose their influence to be around 26 Å for both surface species.

The projection in threshold size at which the influence of the surface states diminishes in this work has been performed for surface termination groups, -OH and -F. Similar calculations can be performed for other reported surface groups or defects, such as carboxyl (COOH), carbonyl (C=O), silicon dioxide (SiO_2) and oxycarbide (SiO_3). Investigation into more surface groups/defects may show the different ways in which they contribute to the deviation from quantum confinement. At present, the deviation from quantum confinement at smaller diameters (less than 3 nm) is attributed to surface states introduced by localised electron wavefunctions in lone pairs of non-bonding orbitals and due to the electronegative surface atoms. The calculations made for 4H-SiC in this work which can explain the dual-feature PL in experiments may be extended

to other polytypes such as 2H-, 6H- and 3C-SiC.

Finally, it is noted that SiC-QDs are fabricated using the wet etching methods employing HF, ethanol and water, which will naturally lead to a range of chemical termination of the surfaces. It is therefore critical to understand the chemical nature of the surface termination, since control of surface states will be essential in either exploiting or eliminating the size-dependent optical characteristics.

Chapter 4

Optoelectronic Properties of Mesoporous 4H-SiC Prepared by Anodic Electrochemical Etching

Part of results in the chapter was published in the Journal of Applied Physics, **120** , 194303 (2016)

4.1 Introduction

This chapter presents the results of surface, electrical and optical characterisations performed on mesoporous 4H-SiC prepared by anodic electrochemical etching in HF/ethanol electrolyte. The experimental details and characterisation techniques used throughout this chapter such as photoluminescence (PL), photoluminescence excitation (PLE), Raman spectroscopy, X-ray diffraction (XRD), X-ray photoelectron spectroscopy (XPS), high resolution transmission electron microscopy (HRTEM) and current-voltage (I-V) measurement have been described in chapter 2. I-V characteristics under illumination were obtained to investigate the photoconduction of mesoporous 4H-SiC for potential use as a photodetector.

This chapter highlights on the observation of the rarely reported above bandgap PL emission, in addition to the usually reported below bandgap PL peak for 4H-SiC nanostructures suspended in solvents. The dual-feature PL spectra was experimentally verified and the potential origins discussed. XRD was employed to ascertain whether polytype phase transformation during ultrasonication played a role in determining the optical properties. The collected data as a whole served to elucidate as to whether the deviation from quantum confinement in the observed optical properties were polytype or surface related. A new model based on the findings from DFT calculations in chapter 3 was applied to explain the experimentally observed PL spectra discussed in this chapter in terms of the interplay between quantum confinement and surface states.

4.2 Results

Data on crystallite size, dimensions and polytype of mesoporous 4H-SiC were inferred from Raman spectroscopy, atomic force microscopy (AFM) and HRTEM. The surface chemical composition were probed by XPS and relation to the chemistry of electrochemical etch was discussed. Current-voltage characteristics were performed and analysed from two approaches: first considering an idealised surface and the other through the back-to-back Schottky model where different barrier heights and ideality factors would account for surface states. Optical characterisations comprise of UV-visible spectrosopy, PL and PLE. Effect of ultrasonication on the polytype was investigated by XRD. A model to explain the experimentally observed above bandgap, below bandgap and dual-feature PL has been included.

4.2.1 Crystallite Size

The average crystallite size can be inferred from Raman scattering measurements by analysing the Raman peak position and line shape. Figure 4.1 shows the D-Por-SiC delaminated from the bulk wafer after the electrochemical etch in HF/ethanol. This allows characterisation of the material without any contribution from the bulk. The corresponding Raman spectrum for this layer normalised to the peak intensity of the TO mode is compared against the bulk 4H-SiC substrate counterpart as shown in Fig. 4.2(a). In the bulk, the A_1 longitudinal optical (LO) mode at 980.3 cm^{-1} and transverse optical (TO) modes with respective E_1 and E_2 symmetries at 797.7 cm^{-1} and 777.1 cm^{-1} are observed. These correspond to known features of 4H-SiC [73, 75, 88]. The observed LO peak in this case is broad and at a higher wavenumber (980.3 cm^{-1} compared to reported 965 cm^{-1} [89]). The blue-shift in the A_1 LO peak corresponds to a high *n*-type doping concentration of about 5×10^{18} cm^{-3} [90]. The doping concentration is lower than the nominal concentration of 10^{19} cm^{-3} but within the process variation specified by the manufacturer.

Similarly, the D-Por-SiC Raman spectrum exhibited A_1, E_1 and E_2 phonon bands (968.1, 797.0, 776.5 cm^{-1}) indicating that 4H polytype crystallinity was preserved after the etch process. Peaks near 785 cm^{-1} for both bulk and D-Por-SiC are ascribed

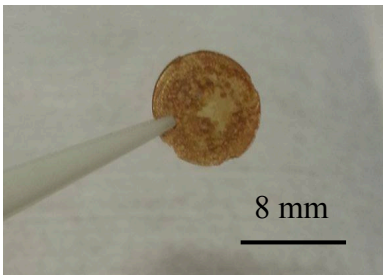

Figure 4.1: D-Por-SiC prepared by anodic electrochemical etching in HF/ethanol electrolyte

to the formally Raman forbidden A_1 (TO) [91] peak which is allowed in this case most likely due to the off-axis orientation [89] or crystal imperfection. Breaking of the crystal lattice periodicity and selection rules for D-Por-SiC resulted in enhanced intensity of the TO peaks compared to those observed for the bulk. The data show red-shifts in the TO and LO peaks in D-Por-SiC compared to the bulk.

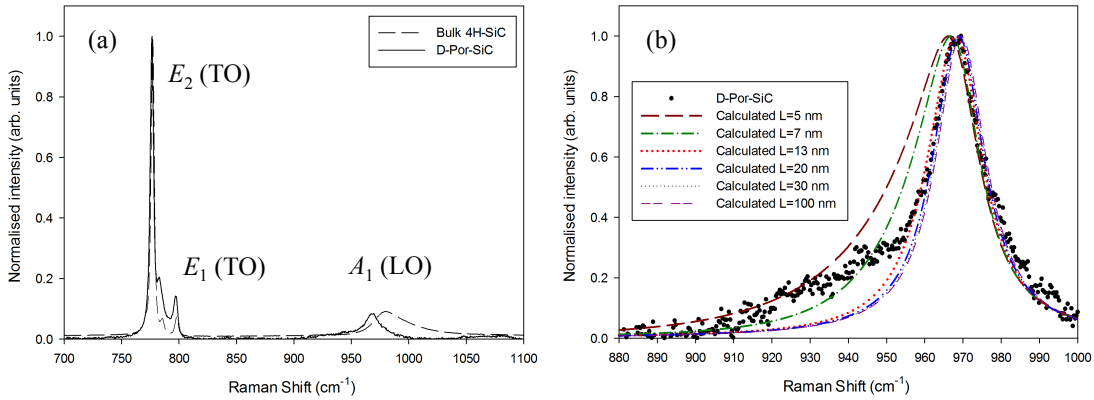

Figure 4.2: (a) Raman spectra of bulk 4H-SiC and D-Por-SiC, (b) A_1 LO mode line shape analysis based on phonon confinement model.

The red-shifts in the TO peaks are less than 1 cm^{-1}, from 797.7 cm^{-1} to 797.0 cm^{-1} (Figure 2(a)) and 777.1 cm^{-1} to 776.5 cm^{-1} for E_1 and E_2 respectively, comparable to the measurement spectral resolution of 0.3 cm^{-1}. The A_1 (TO) peak was red-shifted by 3 cm^{-1} from 785.7 cm^{-1} to 782.7 cm^{-1}. The LO peak red-shifted significantly by approximately 12.2 cm^{-1} from 980.3 cm^{-1}to 968.1 cm^{-1}. The observed 12.2 cm^{-1} red-shift and a narrower D-Por-SiC LO mode peak frequency may be the combined effects of quantum confinement of optical phonons [92] and free carrier depletion as a result of surface trapping [93]. If the latter is true then based on the red-shift, the

free carrier concentration has decreased from around 5×10^{18} cm^{-3} to 3×10^{18} cm^{-3} [90]. In addition, the LO mode peak is accompanied by an asymmetric broadening to the low frequency side (Figure 2(b)). In relation to quantum confinement, the Raman line shapes can be quantitatively described by the phonon confinement model (PCM) [27, 92] given by

$$I(\omega) \propto \int_0^1 \frac{e^{-q^2L^2/4c^2}}{[\omega - \omega(q)]^2 + \tau_o^2/2}\, \mathrm{d}^3q \tag{4.1}$$

where *I* is the Raman scattering intensity, ω is the Raman frequency, *q* is the reduced wave vector (*q*=*q'*/q_{max}) , where *q'* is in units of the reciprocal lattice vector $2\pi/c$ and q_{max}=$4\pi/c$ [73] for for 4H-SiC, lattice parameter along the c-axis, *c*=1.0053 nm [94], τ_o is the line width in the bulk crystal, *L* the diameter of the nanocrystal and $\omega(q)$ is the phonon dispersion relation for A_1 LO mode approximated by

$$\omega^2(q) = A + B\cos\left(\frac{\pi q}{2}\right) \tag{4.2}$$

where the values A=702×10^3 cm^{-2} and B=238×10^3 cm^{-2} are adapted from 4H-SiC phonon dispersion given by Feldman *et al.* [73].

PCM is not commonly applied to the acoustic modes due to their energy being zero at the Brillouin zone centre and is rarely used for TO modes because of their low phonon dispersion. It is almost exclusively applied to the LO modes [95]. To simplify the calculations, the Brillouin zone is assumed to be spherical and the dispersion curve isotropic; these assumptions are justified as only a small region centred at Γ in the Brillouin zone which contributes to the scattering [96]. According to the PCM model [27, 96], an asymmetric broadening and a red-shift in the LO peak is expected for nanostructures whose finite sizes result in relaxation of the selection rule for Raman scattering, allowing transitions with $\Delta q \neq 0$. The average crystallite size for which equation (1) was used in Ref. 27 was 25 nm, which is comparable to the $\sim$20 nm size scales in this work, as will be shown later in the text. The 12.2 cm^{-1} red-shift in frequency in the A_1 LO peak for the D-Por-SiC compared to that of the bulk in Figure 4.2(a) is relatively large in comparison to the data in [27] where red-shifting of the LO peak was not observed. Considering the average crystallite size of $\sim$20 nm,

it is possible that most of the observed red-shift of the A_1 LO mode from the peak position of the bulk may be related to free carrier depletion due to surface states in the porous material in contrast to the highly doped bulk substrate. Being heavily doped, the bulk material showed blue-shifted LO mode associated with phonon coupling with the free carrier plasma of electrons (LO phonon-plasmon coupling). In terms of line shape, Figure 4.2(b) compares the experimental A_1 LO mode for D-Por-SiC to the calculated phonon confined line shapes for different crystallite sizes based on the PCM model. The experimental LO peak is asymmetric and exhibits a shoulder at the low frequency side consistent with relaxation of selection rules allowing contributions from the negative dispersion of the optical phonon branch away from the zone centre. A comparison of the calculated line shapes with the experimental data indicates that the average crystallite diameter in the D-Por-SiC sample is approximately 13 nm. It should be noted that other factors such as surface modes of small particles smaller than the excitation wavelength (Fröhlich modes) [27] unique to porous polar semiconductors can contribute to the Raman line shape on the low frequency side. Like the LO phonon mode, the Fröhlich mode can also couple with the plasmon mode and so may further influence the position of the peak frequency. Therefore the particle size was determined from XRD and electron microscopy techniques. Both the observed asymmetric broadening at the low frequency side and red-shifting are strong indications of the existence of nanocrystallites, small enough for phonon confinement to occur in the D-Por-SiC, whilst its slight deviation from the theoretical line shape (920-950 cm^{-1} region) may be influenced by the existence of surface phonons [27]. Previous investigations for por-SiC have reported mixed results in that LO broadening was observed, but the peaks had negligible shift in comparison to the bulk or showed a blue-shift instead of a red-shift due to surface phonon-plasmon coupling [27, 97–100]. These could be the combined effects of diffuse scattering, spectral line broadening and violation of symmetry selection rules [27].

Figure 4.3 shows the XRD patterns for bulk 4H-SiC and D-Por-SiC (magnified by a factor of 100). Both show sharp peaks near the 2θ Bragg angle of 36° associated with the (0004) SiC planes. A peak near 33° for D-Por-SiC associated with the $(10\bar{1}0)$ SiC plane is visible in the D-Por-SiC data indicating disorder which was introduced during the etching process. These peaks show that the D-Por-SiC was highly crystalline and

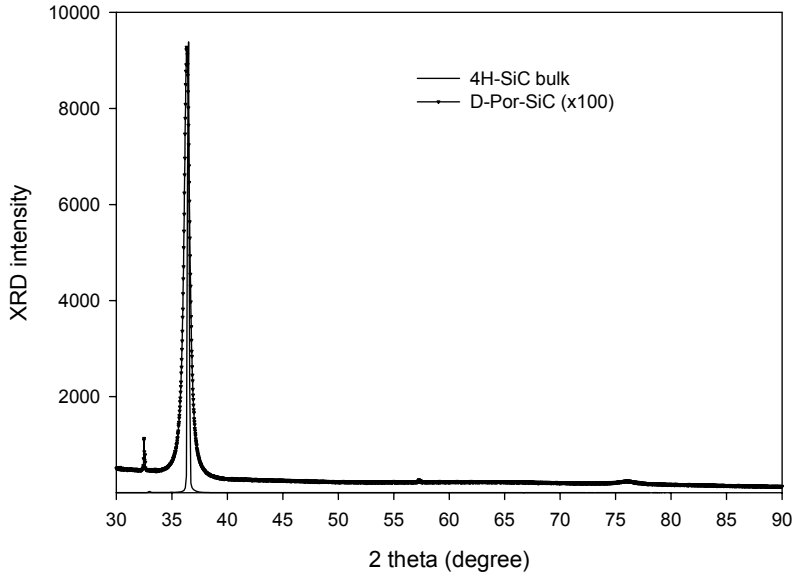

Figure 4.3: XRD pattern for bulk 4H-SiC and D-Por-SiC.

parts of the remaining etched skeletal structure retained the long range order of the bulk lattice. However, there is a broadening in the XRD peak for D-Por-SiC in comparison to the bulk, and the full width at half of maximum (FWHM) is 0.6° in comparison to the bulk of 0.1°. The peak broadening suggests a reduction of the average crystallite size in D-Por-SiC. The calculated average crystallite diameter by Scherrer's method [77] is about 13 nm for the D-Por-SiC being in close agreement with the average size of approximately 13 nm as inferred from the Raman spectrum.

Figure 4.4 shows AFM images acquired in non-contact mode (AFM tip with aspect ratio 1.5-3.0 and radius of curvature of 6 nm), depicting the surface morphologies of D-Por-SiC. Figure 4.4(a) shows that the top surface of the delaminated layer (etched substrate surface) has a lower surface roughness with a root mean square (RMS) of 0.8 nm in comparison to the bottom surface (bottom of delaminated layer) (Fig. 4.4(b)) that shows a surface roughness at a RMS of 51.4 nm within a 10×10 μm sample size. Initiation of the pores on the top surface were likely to occur at defect sites and irregularities [101] or in this case along the lines left by the chemical mechanical polishing process used in the manufacturing of the SiC substrate. In contrast, the rough morphology at the bottom of D-Por-SiC that incorporated much smaller feature sizes

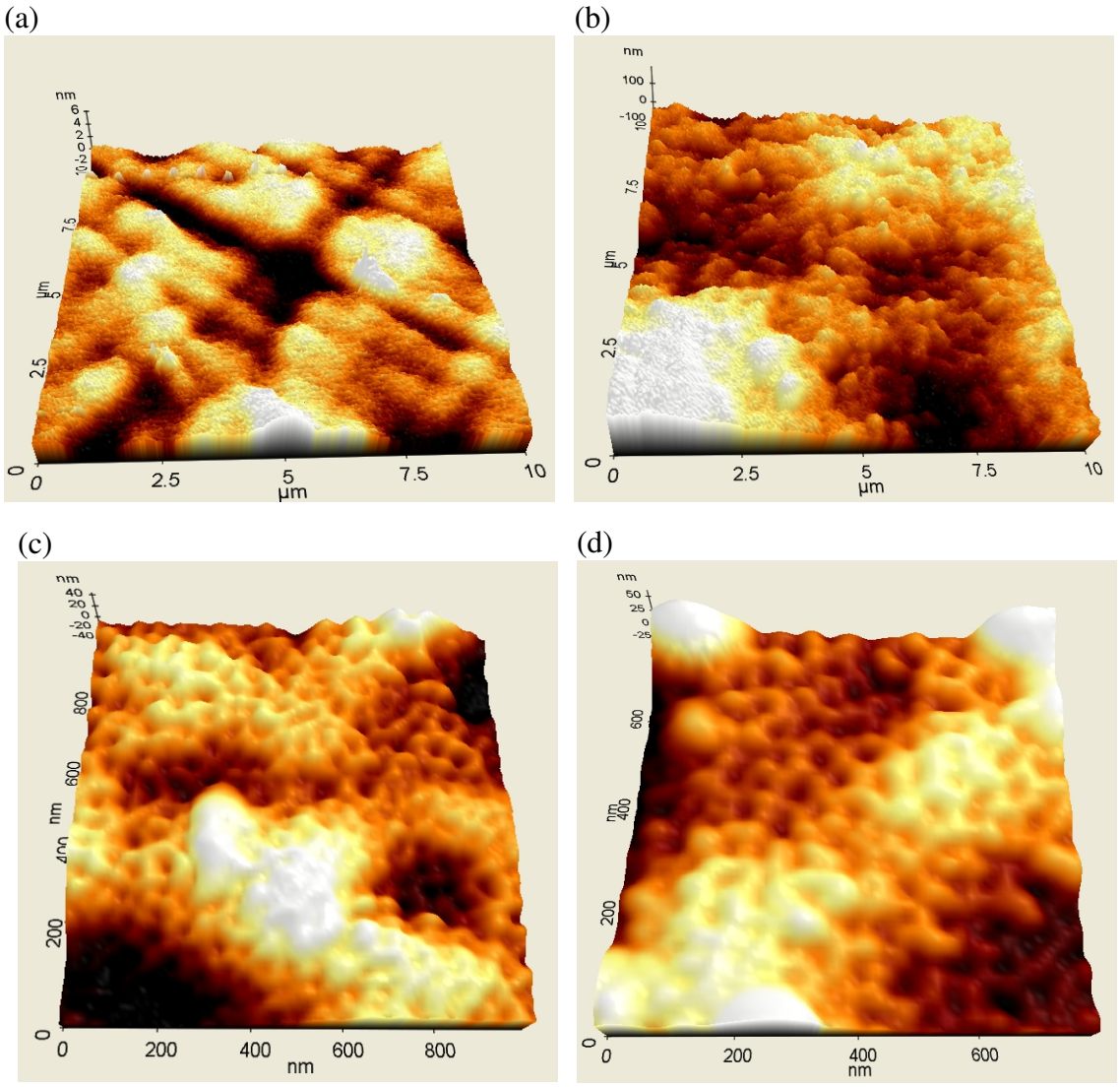

Figure 4.4: AFM images of D-Por-SiC for top and bottom surfaces: (a) 10×10 μm top morphology, (b) 10×10 μm bottom morphology, (c) 1×1 μm bottom morphology and (d) 0.8×0.8 μm bottom morphology.

was throughout the surface, indicative that a porous structure was formed. The AFM images for 1×1 μm and 0.8×0.8 μm bottom surfaces as shown in Fig. 4.4(c) and Fig. 4.4(d) respectively illustrate that numerous nanometer scale pores were evident throughout the surface, some of which makes up the structure of larger pores. The pore diameter is a metric that can be used to classify the porous material. According to the International Union of Pure and Applied Chemistry (IUPAC) classification of pore size [102], pores with diameters less than 2 nm are of the micro type, 2-50 nm are of the meso type and more than 50 nm are of the macro type. Figure 4.5(a) shows a pore diameter of approximately 33 nm and an interpore spacing of approximately

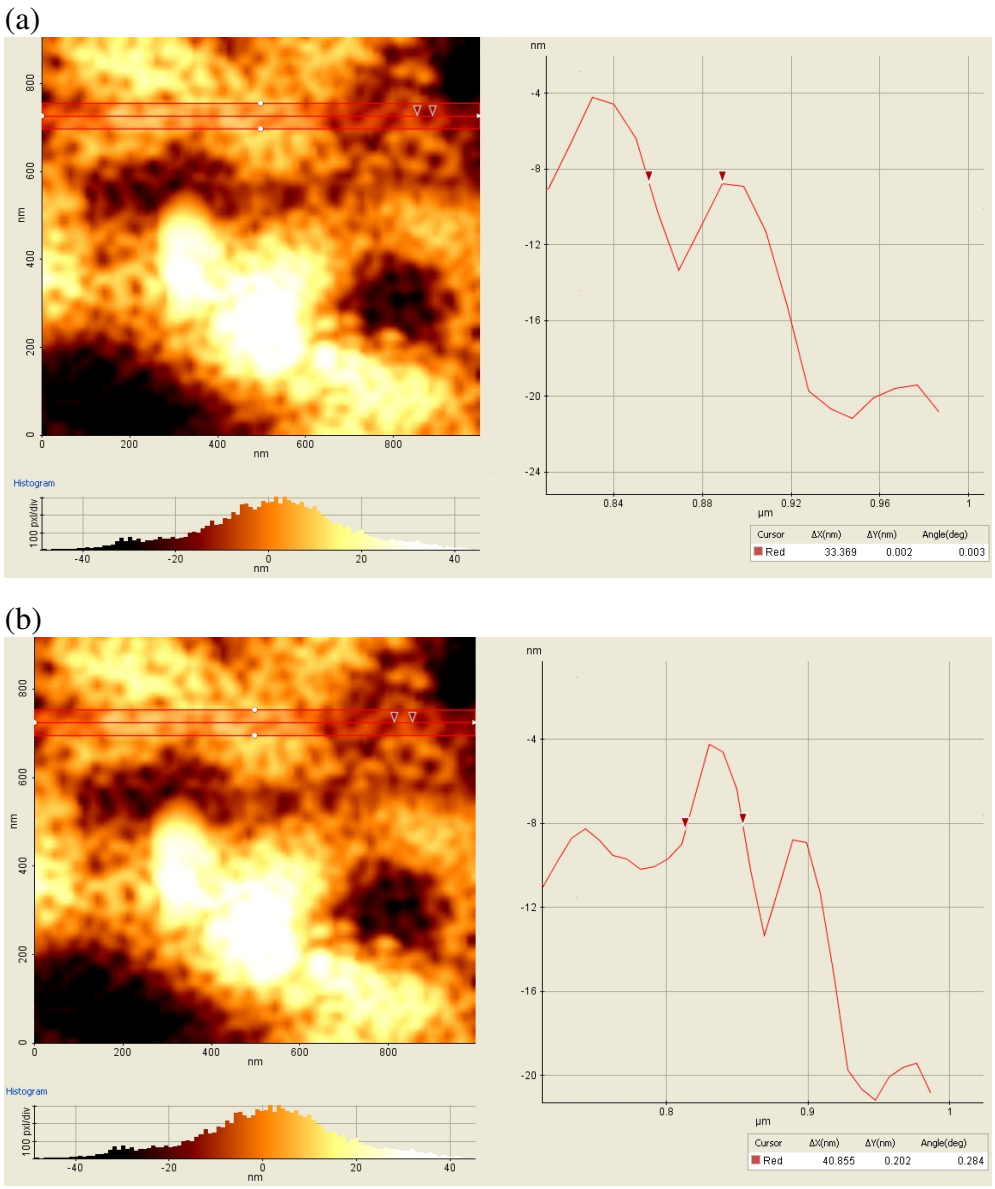

Figure 4.5: (a) Pore diameter (33 nm) and (b) interpore spacing (40 nm) as determined from AFM image.

40 nm (Figure 4.5(b)) as determined from the AFM image and this classifies the pore as a mesopore. The interpore spacing of 40 nm is however very large in comparison to the estimates inferred from Raman scattering and XRD at approximately 13 nm, indicating that the porous material may vary in dimension or consist of a distribution of sizes along the structure from top to bottom. Another possible contributor is lateral width broadening, as despite AFM having outstanding vertical resolution, its lateral resolution may be influenced by the AFM tip shape and noise [103].

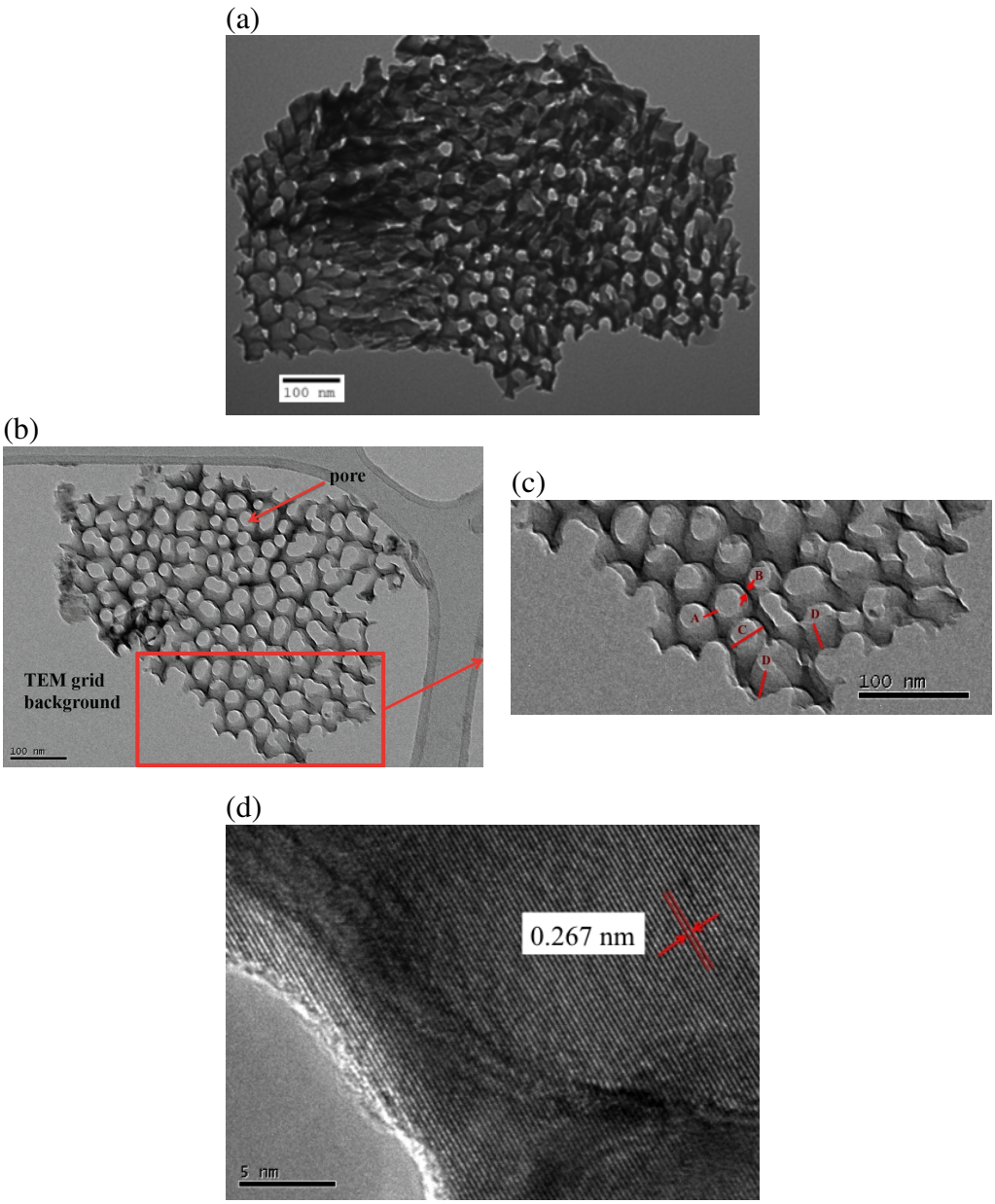

Figure 4.6: HRTEM images of (a) and (b), mesoporous S-Por-SiC particle consisting of a network of interconnected thin walls, (c) zoomed in image of S-Por-SiC showing the labelled dimensions of thin walls and pore diameter with average sizes as stated in the text, and (d) the average interplanar spacing of 0.267 nm corresponding to 4H-SiC $(10\bar{1}0)$ planes.

The D-Por-SiC layer was broken up by sonication in ethanol producing dispersed S-Por-SiC particles. Figure 4.6(a) and (b) show the HRTEM images of S-Por-SiC structure dried off from ethanol solution. The S-Por-SiC represented a skeleton of the original bulk 4H-SiC with mesopores spread throughout the structure. The interpore

spacings consist of interconnecting thin walls. Figure 4.6(c) is the high magnification image showing representative dimensions within the S-Por-SiC structure where the average interpore spacing (A) is 16.9±5.5 nm, smallest wall dimension (B) of 2.9±1.0 nm, pore diameter (C) of 30.5±6.3 nm and depth (D) of approximately 25 nm. It is noted that the value of the depth (D) is approximate as it may be distorted by the perspective of the image. The areal porosity of the structure is determined to be 0.37 by means of image analysis using ImageJ [104, 105]. The size estimates inferred from the Raman and XRD of approximately 13 nm appear to corroborate with the interpore spacing (A) of 17 nm. It is noted that for Raman scattering in a perfect backscattering configuration, the TO mode peaks (planar mode) arise from atomic vibrations perpendicular to the c-axis while the LO mode peak (axial mode) originate from vibrations that are parallel to the c-axis. Figure 4.6(d) shows that the atomic planes within the interpore spacings have an average interplanar spacing of 0.267 nm corresponding to the distance between 4H-SiC $(10\bar{1}0)$ planes. This suggests that the dimensions in the plane of the image are nearly perpendicular to the c-axis. Therefore the small interpore dimensions (A and B) relate to the TO modes while the LO mode relates to the larger dimensions of depth into the pore (D). A plausible explanation as to why the LO mode may red-shift in the case of larger dimensions is the shape effect, stemming from the long-range dipolar interactions as reported for polar semiconductor nanowires [106]. It has been observed that polar semiconductor nanowires with lengths of several microns and diameters of $\sim$20 nm exhibit red-shift and asymmetric broadening in the LO mode and the effect is enhanced for structures with a larger aspect ratio. The prominent shift in the LO mode can be attributed to its larger phonon dispersion width in comparison to other Raman lines. XRD provides a better estimate of the interpore spacing. The XRD data also indicates that the sonication process did not result in a phase change in the 4H polytype.

The average interpore spacing acquired from AFM imaging was 40 nm. Lateral width broadening may have influenced the measurement as a result of the AFM tip shape and noise. The inferred average crystallite size of 13 nm from Raman and XRD for the por-SiC structure is consistent with the average size of 17 nm observed in HRTEM. The nanoscale lengths of around 2 nm at the walls' edges may potentially support quantum size effects where spatial localisation of photogenerated carriers in the mesoporous

4H-SiC structure can increase the emission intensity and energy.

4.2.2 Chemical Composition

As not only quantum size effects govern the optical properties of nanostructures, the chemical composition, particularly at the surface needs to be investigated. XPS with probing depths of up to 10 nm of the surface is suitable for this purpose. The high resolution core level XPS spectra for S-Por-SiC drop-casted on gold foils are shown in Fig. 4.7 plotted as counts per second as a function of binding energy. The high resolution XPS spectrum of Si 2*p* for S-Por-SiC in Fig. 4.7(a) shows a peak at 100.64 eV indicating the existence of SiC bonds [22, 107, 108] in the porous structure. In addition, other chemical states for Si 2*p* in S-Por-SiC involve silicon oxycarbide (102.10 eV) [109] and SiO_2 (103.70 eV) [110], which indicate oxidation of Si as a result of the anodic etch process. As the HF solution dissolves SiO_2 during etching, it is likely that the exposed Si with dangling bonds is oxidised on contact with air after the process. The peak at 105.40 eV is attributed to SiF_x bonds in the S-Por-SiC [111, 112] which relates to the chemical interaction with HF. Figure 4.7(b) shows that C 1*s* for S-Por-SiC consists of Si-C bonds (282.65 eV) and surface reconstructions of C sp^3 dimers (284.30 eV) and C-O bonds (286.05 eV) [109]. Surface terminations as a result of chemical interaction with ethanol and HF may have resulted in C bonding in carbonyl (C=O) or carboxyl groups (COOH) (288.20 eV) [113, 114] and C-F (290.10 eV) [115]. S-Por-SiC O 1*s* peaks in Fig. 4.7(c) show SiO_2 and C-O bonds [109] which may have arisen from the interaction with water or ethanol. In the literature [116, 117] the following electrochemical reactions have been proposed for the electrochemical etching of SiC and dissolution of SiO_2 in HF/ethanol electrolyte:

$$SiC + 2H_2O + 4h^+ \rightarrow SiO + CO + 4H^+$$

$$SiC + 4H_2O + 8h^+ \rightarrow SiO_2 + CO_2 + 8H^+$$

$$SiO_2 + 6HF \rightarrow H_2SiF_6 + 2H_2O$$

where h^+ is the hole and H^+ is the proton.

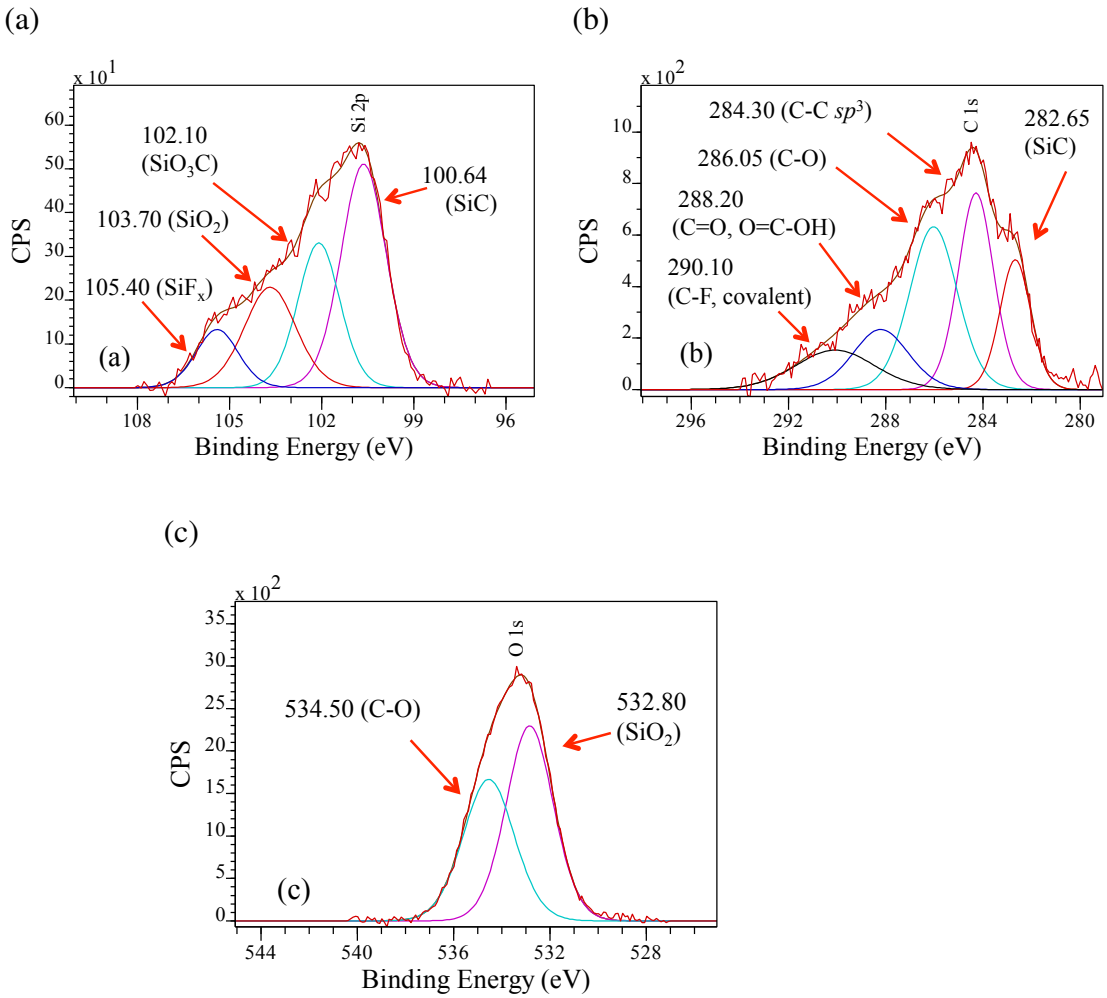

Figure 4.7: Core level Si 2p, C 1s and O 1s XPS spectra for S-Por-SiC (a), (b), (c) respectively.

The dissolution of SiC commences only when anodic currents are present whereby holes are required to be supplied at the SiC-electrolyte interface. By applying a large enough positive (reverse bias) to n-type SiC, no photoassistance is required as in our case to etch SiC. Ethanol is added to electrolytes for the formation of porous semiconductors to reduce the surface tension at the solid/electrolyte interface and allow the aqueous electrolyte to penetrate the pores [118]. The reduction in viscosity is a secondary factor. HF serves to remove the oxide. However, as F has been identified as forming bonds with Si and C in the XPS spectra, ethanol might also interact with unsatisfied dangling bonds on the surface of the porous material. Thus, the core level Si 2*p*, C 1*s* and O 1*s* spectra indicate that SiF_x, SiO_2, C-C, C=O/COOH, C-F and C-O bonds on the S-Por-SiC surface resulted from the etching process in HF/ethanol electrolyte and subsequent dispersion in ethanol [119]. These bonds comprise the

surface termination (such as fluorine) and surface defects (C=O/COOH) that result in surface states, which may influence the optical properties of S-Por-SiC. Exposure to air in addition to the etching process and subsequent dispersion in ethanol is expected to play a role in the formation of some of the surface groups, since the material must be dried before some of the characterization techniques can be applied.

4.2.3 Current-voltage Characteristic

The current-voltage (I-V) characteristics of S-Por-SiC drop-casted on $10\times400\ \mu m$ interdigitated electrodes with varying inter-electrode separation of 3, 5 and 10 μm were investigated. Both symmetric and asymmetric contact metallisation were explored. Asymmetric contact metallisation scheme has been employed in previous studies pertaining to monolayer and multilayer flakes to produce a doping effect at the semiconductor-metal interface [120] or to allow effective hole and electron injection in the device [121] by selecting suitable work-functions from different metals. In graphene QD based photodetectors, the use of asymmetric electrodes with a larger workfunction difference was found to enhance carrier separation and transportation [122]. Selective contacts to achieve preferential hole or preferential electron transfer mechanisms have been investigated for quantum dots films [123, 124]. Asymmetric Schottky barriers through different metals or different contact areas have also been shown to help suppress dark current in metal-semiconductor-metal (MSM) based photodetectors [125]. In this work, aluminium (Al) with a low work-function of 4.28 eV (ϕ_{Al}) [126] was chosen as the Fermi level is close to the conduction band edge of 4H-SiC (electron affinity, χ_{4H-SiC}: 3.6±0.2 eV) [127] to assist electron conduction, whilst nickel (Ni), a higher work-function metal of 5.15 eV (ϕ_{Ni}) [126] was selected as the Fermi level is nearer to the valence band edge for hole conduction.

Interdigitated electrodes were patterned through a standard lithography process and Al-Al, Ni-Ni and Al-Ni with thicknesses of approximately 100 nm were deposited by electron beam evaporation onto SiO_2/Si wafer pieces. Figures 4.8(a) and (b) show interdigitated electrodes on SiO_2/Si with 3 μm inter-electrode separation without S-Por-SiC for symmetric contacts (Al-Al) and asymmetric contacts (Ni-Al) respectively.

(a) (b)

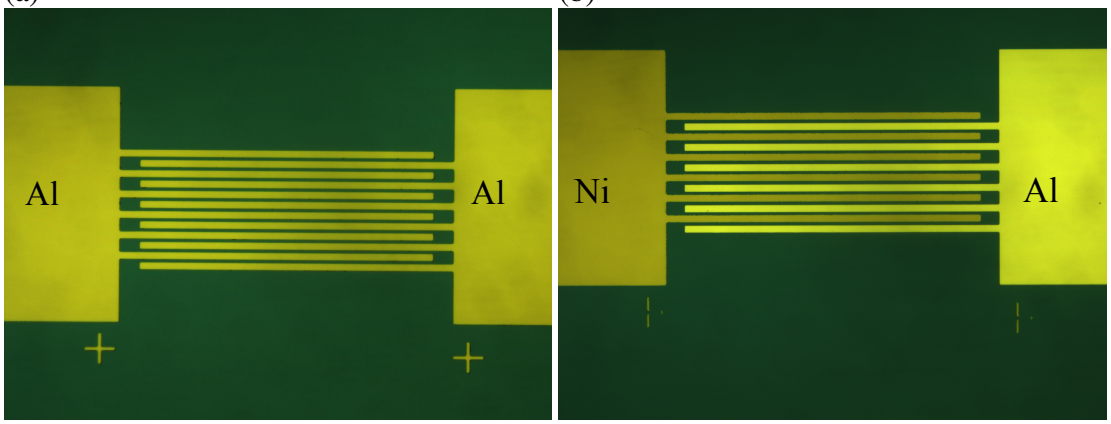

(c)

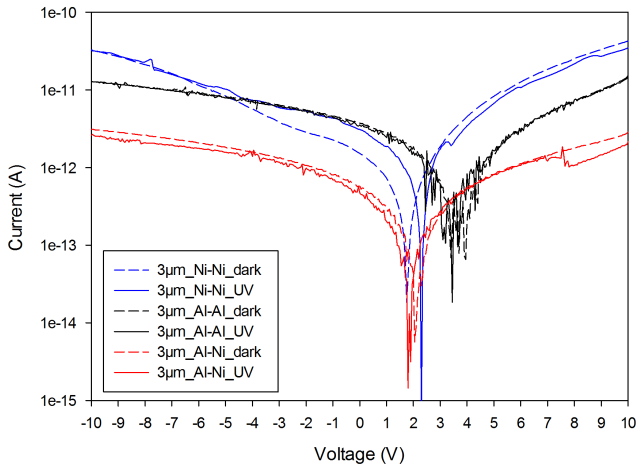

Figure 4.8: Optical images of $10\times400\ \mu m$ interdigitated electrodes having 3 μm inter-electrode separation on SiO_2/Si without S-Por-SiC for (a) symmetric electrodes (Al-Al) and (b) asymmetric electrodes (Ni-Al). The corresponding current-voltage characteristics (c), with and without UV illumination for Ni-Ni, Al-Al and Ni-Al interdigitated electrodes.

Figure 4.8(c) show the I-V characteristics under UV illumination with nominal wavelength of 365 nm (70 mW/cm^2) and without UV illumination (dark) for both symmetric (Al-Al and Ni-Ni) and asymmetric Ni-Al interdigitated electrodes. The voltage bias sweeps were from 10V to -10V. In the absence of S-Por-SiC, there was no difference in the measured current between dark and UV illuminated conditions regardless of the electrode configuration. The electrodes were then drop-casted with S-Por-SiC and dried prior to I-V measurement as shown by the optical micrographs

in Figures 4.9(a) and (b) for Al-Al and Al-Ni electrodes respectively, where the measurement probes are also visible. Figure 4.9(c) shows the I-V characteristics under dark and UV illuminated conditions.

(a) (b)

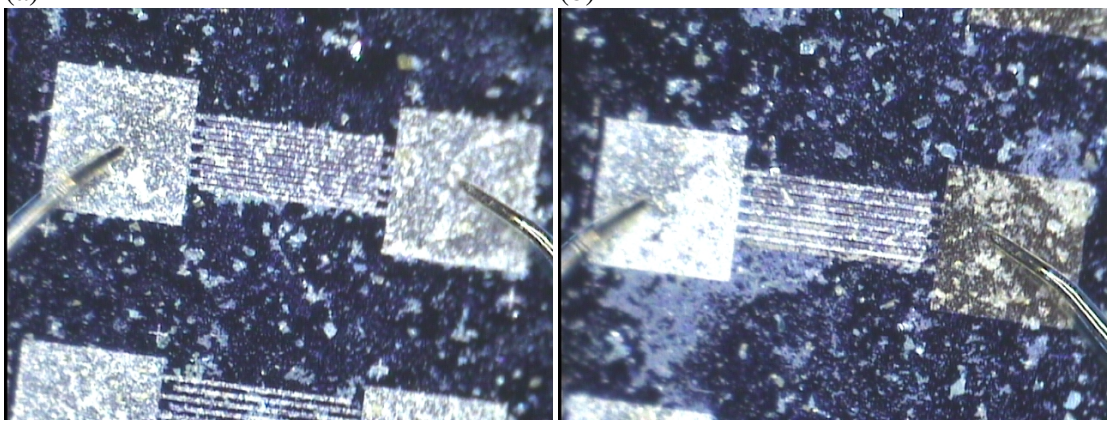

(c)

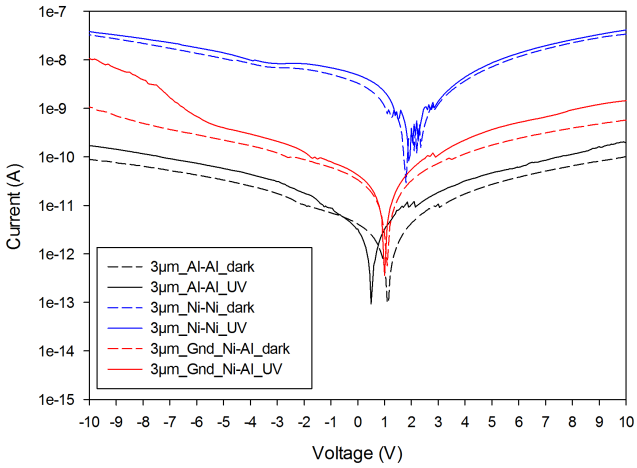

Figure 4.9: Optical images of interdigitated electrodes on SiO_2/Si with 3 μm electrode separation for (a) symmetric electrodes (Al-Al) and (b) asymmetric electrodes (Al-Ni) with S-Por-SiC drop-casted onto electrodes. The corresponding current-voltage characteristics (c), with and without UV illumination for Ni-Ni, Al-Al and Ni-Al interdigitated electrodes.

It should be noted that for the Ni-Al electrode configuration, the Ni contact was the ground and voltage sweep applied to the Al contact. It was observed that with S-Por-SiC drop-casted onto the electrodes, the current increased under UV illumination in comparison to the dark for all electrodes indicative of photogenerated current,

attributed to the presence of S-Por-SiC. Electron-hole pairs were created within the S-Por-SiC following photoexcitation which then separated and drifted towards the electrodes due to the applied electric field. The dark currents were low, in the range of 10^{-7} to 10^{-10}A as desired for photodetection [128]. The symmetric electrodes (Al-Al and Ni-Ni) exhibited photocurrents that were independent of voltage polarity unlike the asymmetric Ni-Al which showed a significant increase in current of nearly an order of magnitude at -10 V in comparison to 10 V. The significant increase occurred when Ni was the anode and Al was the cathode.

To verify the bias polarity dependence, another asymmetric, Al-Ni electrode (not the existing one) was measured in a reverse configuration in comparison to the previous measurement where the Al was set to ground and voltage sweep (10 V to -10 V) applied to the Ni contact. The result is as shown in Fig. 4.10(a) (purple curve) where now the significant increase in photocurrent occurred at 10 V instead of at -10 V (depicted by the red curve). For this reverse measurement configuration on another electrode, the significant increase of nearly an order of magnitude was again replicated when Ni was the anode and Al the cathode. For both measurements, the prominent increase in photocurrent started to occur from approximately 6 V suggesting that the increase in current was field related. Accounting for the 3 μm inter-electrode separation this translate to a relatively low electric field of 20 kV/cm. Fig. 4.10(b) shows the I-V characteristics of asymmetric electrodes with different inter-electrode separation of 3, 5 and 10 μm. It was noted that the significant photocurrent increase beyond 6 V in the asymmetric electrodes were absent for larger inter-electrode separations of 5 and 10 μm. This is most likely due to the corresponding diminishing electric field strength with increasing inter-electrode separation as shown in Fig. 4.10(c) and potential recombination of electron-hole pairs over the larger distances.

Fig. 4.11 shows the photocurrent (difference between the current under illumination and in the dark) to dark current ratios for the investigated symmetric and asymmetric electrodes at 10 V and -10 V. For the 3 μm inter-electrode separation, the photocurrent to dark current ratio was the lowest for Ni-Ni (0.16) followed by Al-Al electrodes (0.94). As the Fermi level of Al is more closely aligned to the conduction band of the n-type 4H-SiC in comparison to Ni [126, 127], the band alignment would have better facilitated electron conduction than Ni, resulting in a higher ratio for Al. Both

(a)

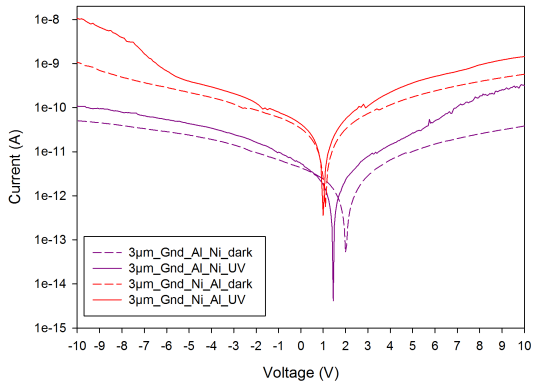

(b)

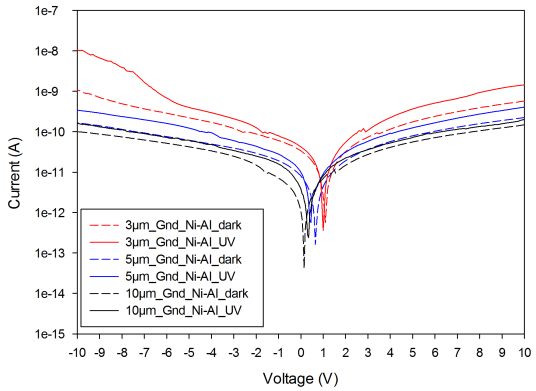

(c)

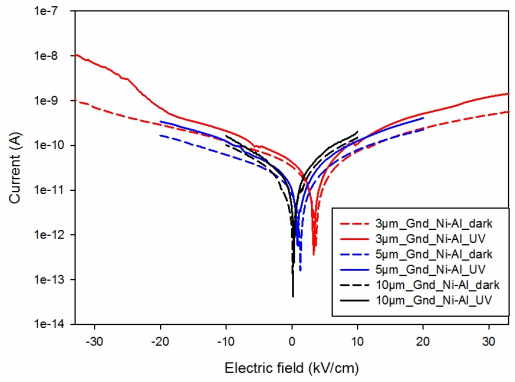

Figure 4.10: Current-voltage characteristics of S-Por-SiC on asymmetric Al-Ni electrodes (a) for different bias polarity, (b) varying inter-electrode separation and (c) corresponding electric field for the -10 to 10 V bias range. Up to one order of magnitude increase in photocurrent was observed for Ni-Al, indicative of photon absorption. 5 to 6 orders of magnitude would be required to qualify as a photodetector [129].

electrodes show relatively consistent ratios at opposite bias voltages of -10 V and 10 V. In contrast, higher ratios were shown by the Ni-Al electrode which may be ascribed to the energy band offsets of the different metals and larger band bending (larger electric field) on the Ni electrode side. Unlike the symmetric electrodes, Ni-Al photocurrent to dark current ratios were bias-polarity dependent, at 1.52 (anode: Al, cathode: Ni) and 8.96 (anode: Ni, cathode: Al). The ratios monotonically decrease with the increase in inter-electrode separation and were consistently higher when Ni was the anode in the configuration.

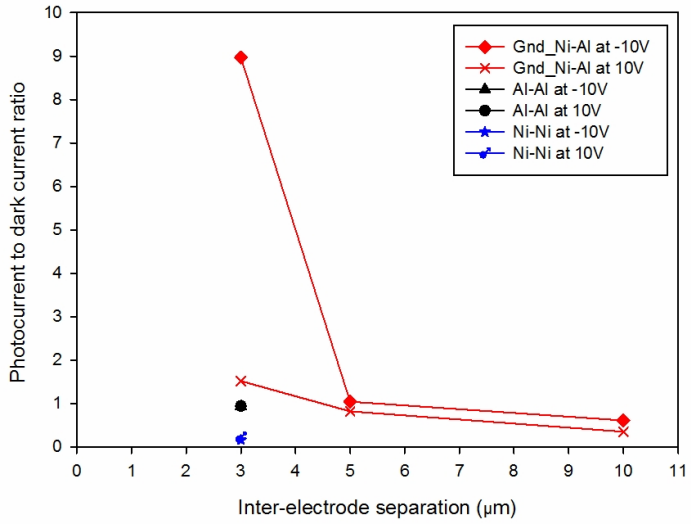

Figure 4.11: Photocurrent to dark current ratios for symmetric electrodes (Al-Al, Ni-Ni) and asymmetric electrode (Al-Ni) taken at 10 V and -10 V. Up to one order of magnitude increase in photocurrent was observed for Ni-Al, indicative of photon absorption. 5 to 6 orders of magnitude would be required to qualify as a photodetector [129].

In order to explain the observed asymmetric I-V characteristic for Ni-Al, two considerations can be made. In the first consideration, the ideal conditions of negligible surface effects and without Fermi level pinning are assumed whilst in the second treatment, surface effects are considered later in section 4.2.4 using the back-to-back Schottky diode model within the thermionic emission theory. For the first treatment, work by M. Casalino *et al.* [125] on internal photoemission effect in metal-semiconductor-metal (MSM) photodetector and current transport due to thermionic emission previously discussed by S.M. Sze *et al.* [130] are referenced. MSM structures

when sufficiently thin to be fully depleted can exhibit a wide range of high level minority carrier injection via thermionic emission [130]. Carrier injection from the metal by internal photoemission effects can also be exploited by engineering the barrier heights of the two contacts. Copper (Cu) was used as the optical absorber layer whose cut-off wavelength was determined by the Schottky barrier height at the metal-Si interface [125]. In these works [125, 130] the semiconductors were lightly doped in the range of 10^{12} to 10^{14} cm^{-3}, so that full depletion was easily achieved. However as the starting material for the creation of the porous material in this work is highly doped (5×10^{18} cm^{-3} based on the Raman LO peak position), lateral full depletion is unlikely to occur at 10 V over a 3 μm inter-electrode separation. The calculated depletion width (assuming no surface states) at the Schottky contact for 4H-SiC (dielectric constant of 9.7) with a doping concentration of 5×10^{18} cm^{-3} is approximately 50 nm at 10 V. Therefore full depletion can only be achieved vertically near the contacts as the S-Por-SiC was very thin, as shown in HRTEM where thicknesses of around 25 nm was observed. The penetration depth of UV light at a wavelength of 365 nm is around 50-100 μm for bulk 4H-SiC [89], more than sufficient to penetrate through S-Por-SiC to the underlying contact. The full carrier depletion near the contacts may have facilitated both electron and hole injection in the S-Por-SiC when Ni was the anode by thermionic emission or internal photoemission. In this work, for all electrodes, the induced photocurrent within S-Por-SiC was generated throughout the applied voltages and polarities, with the exception of the asymmetric Ni-Al electrode (Ni as anode) beyond 6 V which showed deviation in the I-V characteristics.

Figure 4.12 illustrates the mechanism which may have contributed to the observed significant increase beyond 6 V for Ni-Al electrodes [125, 130]. Fig. 4.12(a) shows the energy band alignment including the electron and hole barrier heights at zero bias for Ni [131] and Al [132] on bulk 4H-SiC. We assume that S-Por-SiC shows similar trends to those of bulk 4H-SiC, and so we neglect possible surface effects from the porous material. When Ni is the anode and positively biased as shown in Fig. 4.12(b), the hole and electron barrier heights are 1.66 eV and 0.98 eV respectively. These barriers are lower in comparison to the hole and electron barrier heights of 2.28 eV and 1.60 eV when Ni is the cathode and negatively biased as shown in Fig. 4.12(c). The significant increase beyond 6 V for Ni-Al electrodes, when Ni is positively biased may mainly

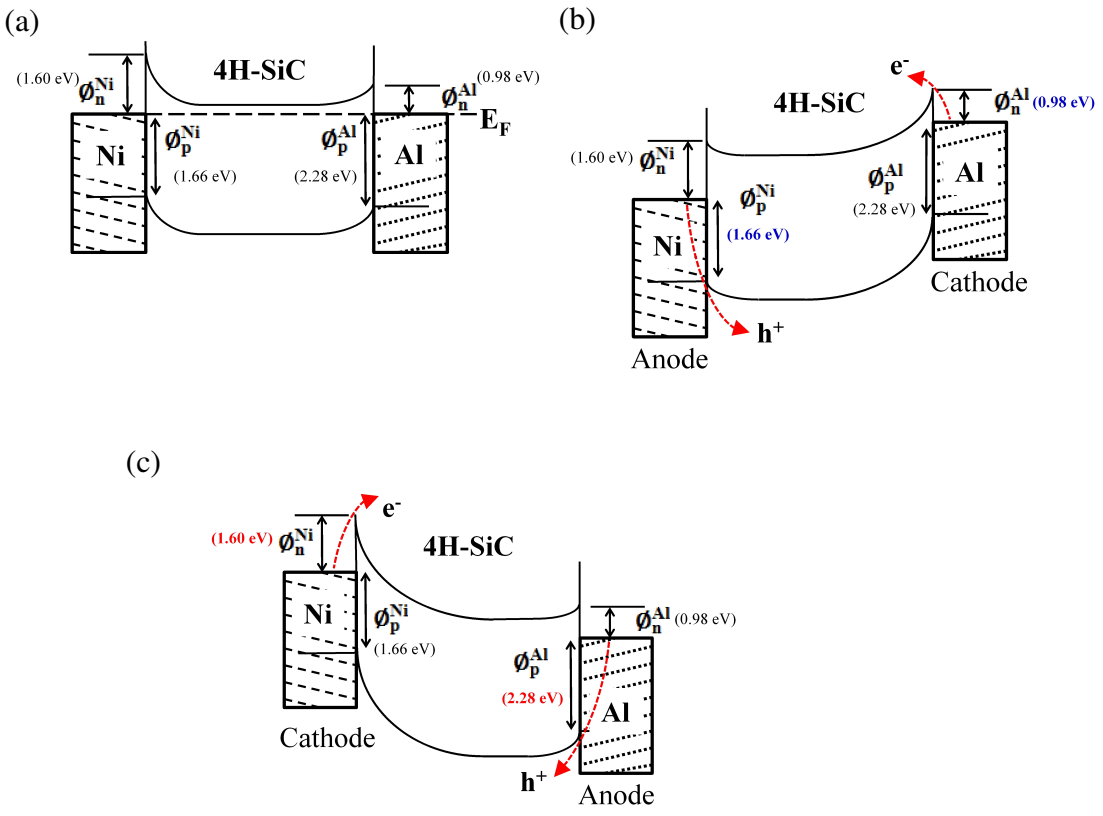

Figure 4.12: Energy band alignment diagrams for 4H-SiC with asymmetric Ni-Al electrodes for (a) without bias, (b) Ni as anode, Al as cathode and (c) Ni as cathode, Al as anode.

be the contribution of electron and hole injection from the metal contacts upon photon absorption. Thus, upon UV illumination, a higher current can be expected when Ni is positively biased relative to Al as a result of lower barrier heights facilitating both hole and electron injection from the metal.

The S-Por-SiC exhibited modest photocurrent upon UV illumination attributable to the lateral structure of the electrodes and the non-uniform coverage of S-Por-SiC on the electrodes. Utilising vertical structures instead of the current lateral electrodes would enable a higher electric field to be generated. An enhanced electric field is further afforded by the thin layer of S-Por-SiC in the vertical structure and likely to lead to the reduction in recombination of electron-hole pairs. Consequently, it would be expected that the photocurrent would be increased.

4.2.4 Comparison of J-V Characteristics with Back-to-Back Schottky Diodes Model

In nanoscale research, making reliable electrical contacts to nanostructures presents difficulties because the nature of the surfaces give rise to disordered potentials and localised charges. Metal/semiconductor contacts depend on the interfacial chemistry and surface states, resulting in electrical characteristics ranging from Schottky to ohmic behaviour. The current-voltage characteristics arising from the Ni and Al contacts to mesoporous SiC in this thesis show non-ohmic characteristics as a result of the formation of back-to-back Schottky diodes in the metal-semiconductor-metal (MSM) structures. The influence of surface states and choice of metal on the barrier height for each contact in the structure need to be considered separately. A study on tin oxide (SnO_2) nanowires in a metal/SnO_2/metal configuration [133] developed a back-to-back Schottky model based on thermionic emission theory. The model provides barrier heights and ideality factors for both diodes from a single data set.

Fig. 4.13 show two back-to-back Schottky diodes formed between Ni-Ni (Fig. 4.13(a)), Al-Al (Fig. 4.13(b)) and Ni-Al (Fig. 4.13(c)) contacts on a porous SiC film, respectively. When a positive voltage is applied, junction 1 is reverse biased and junction 2 is forward biased. Conversely, when negative voltage is applied, junction 1 becomes forward biased and junction 2 becomes reverse biased. The indicated barrier heights correspond to when the respective junctions were reverse biased as the majority of the voltage drop occur at the reverse biased junctions [134].

In a MSM structure, the barrier heights at the two contact ends and the ideality factor can be calculated by fitting the following equation [133, 135],

$$J(V) = \frac{J_1 J_2 \text{sinh}(\frac{qV}{2KT})}{J_1 \text{exp}(\frac{qV}{2n_i KT}) + J_2 \text{exp}(-\frac{qV}{2n_i KT})}, \tag{4.3}$$

where the saturation current densities $J_{1,2}$ are given by

$$J_{1,2} = A^{**} T^2 \text{exp}(-\frac{q\Phi_{B1,B2}}{KT}). \tag{4.4}$$

Here, A^{**} is the Richardson constant (146 A cm^{-2} K^{-2} for 4H-SiC) [131], $T = 300$ K,

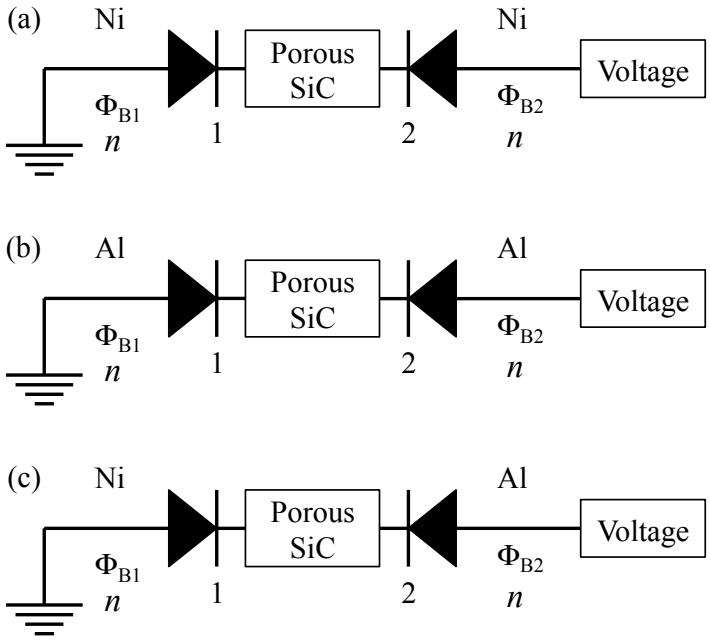

Figure 4.13: Back-to-back Schottky configurations for symmetric electrodes (a) Ni-Ni, (b) Al-Al and asymmetric electrode (c) Al-Ni for voltage sweeps from 10 V to -10 V. On account of the porous surface disorder, different barrier heights can be expected at each end of the contacts. The indicated barrier heights correspond to when the respective junctions were reverse biased.

Φ_B is the barrier height, n the ideality factor, q is the electronic charge and K is the Boltzmann constant (1.3806 $\times$ 10^{-23} J.K^{-1}). Fitting to the experimental J-V characteristics using Equation 4.3, provides both barrier heights as independently adjustable parameters.

Figure 4.14 shows the fitting of equation 4.3 to experimental data for different metallisation schemes under dark and UV illuminated conditions. It is noted that a better quality fit was achieved at higher voltages, whilst the deviation at smaller voltages arises from a result of a mathematical anomaly in the formula to separate out the barrier heights of respective diodes. The J-V curves were weakly rectifying and nearly symmetric for Ni-Ni (Fig. 4.14(a)) and Al-Al (Fig. 4.14(b)) but in contrast were highly asymmetric in the case of Ni-Al (Fig. 4.14(c)). Reported I-V characteristics on

(a) (b)

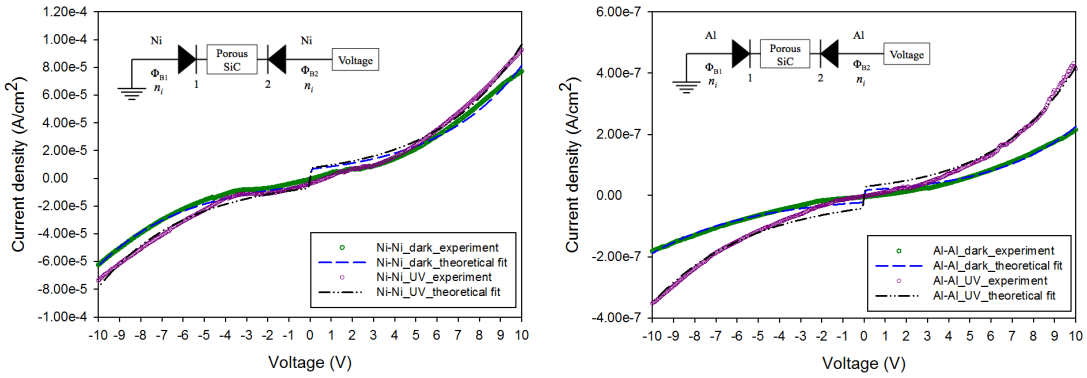

(c)

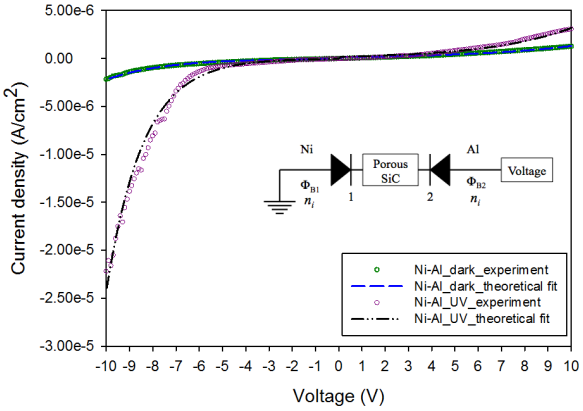

Figure 4.14: Fitting of equation 4.3 to experimental J-V characteristics of (a) Ni-Ni, (b) Al-Al and (c) Ni-Al within the thermionic emission theory. The indicated barrier heights correspond to when the respective junctions were reverse biased.

porous SiC have largely shown to be weakly rectifying and forming Schottky contacts [136, 137] as observed in this work. The photocurrent to dark current ratio was calculated as the ratio of the difference between the current under illumination and the current in the dark to the current in the dark, $(\frac{I_L - I_D}{I_D})$. The photocurrent to dark current ratios for symmetric metallisations were relatively polarity independent, being lower for for Ni-Ni at 0.16 and higher for Al-Al at 0.94. The ratios were highest for Ni-Al which were bias polarity dependent, being 1.52 under positive applied voltage (junction 1 reverse biased, junction 2 forward biased) and 8.96 under negative applied voltage (junction 1 forward biased, junction 2 reverse biased).

The observed differences may be explained by referring to the extracted barrier heights

Table 4.1: Comparison table of extracted barrier heights and ideality factors for symmetric metallisations (Ni-Ni and Al-Al) and asymmetric metallisation Ni-Al.

Condition	Barrier height (eV)		Ideality factor	
Ni-Ni	Φ_{B_1}	Φ_{B_2}	n_1	n_2
Dark	0.719	0.714	1.012	1.013
UV	0.712	0.711	1.012	1.013
Change	0.007	0.003	0.000	0.000
Al-Al	Φ_{B_1}	Φ_{B_2}	n_1	n_2
Dark	0.861	0.868	1.011	1.013
UV	0.845	0.855	1.011	1.014
Change	0.016	0.013	0.000	0.001
Ni-Al	Φ_{B_1}	Φ_{B_2}	n_1	n_2
Dark	0.815	0.845	1.011	1.020
UV	0.806	0.845	1.014	1.034
Change	0.009	0.000	0.003	0.014

and ideality factors summarised in Table 4.1. Barrier heights and ideality factors and their respective changes in the dark versus UV illumination are compared for Ni-Ni, Al-Al and Ni-Al contacts. The extracted barrier height of 0.71 eV for Ni-Ni was much lower than that reported for Ni on *n*-type 4H-SiC bulk at 1.60 eV [131]. Likewise for Al-Al, the extracted barrier height of 0.86 eV was slightly lower than the one reported for Al on bulk at 0.98 eV [131]. In the case of Ni-Al, the barrier heights Φ_{B_1} and Φ_{B_2} were associated with junctions 1 and 2 when they were reverse biased respectively. 0.815 eV (Φ_{B_1}) was the barrier height related to Ni whilst 0.845 eV (Φ_{B_2}) was related to Al. The barrier heights were polarity dependent, where it was higher at 0.845 eV under negative applied voltage (junction 1 forward biased/junction 2 reverse biased) and lower at 0.815 eV under positive applied voltage (junction 1 reverse biased/junction 2 forward biased). In general, the I-V characteristics of nanostructures are mostly influenced by the reverse biased Schottky barrier where the majority of the voltage drop occur [134].

It is also possible that an interfacial insulating oxide layer exist at the contacts. A potential drop in the oxide layer may result in the barrier height being lowered than the expected value in an ideal diode. Depending on the thickness of the oxide layer, the surface states are in equilibrium with the metal for oxide thickness of less than

30 Å and are in equilibrium with the semiconductor if the thickness is more than 30 Å [138, 139]. States in equilibrium with the metal tend to reduce the ideality factor while states in equilibrium with the semiconductor tend to increase it. Oxide thickness of the order 20 Å usually show values of n in the range 1.3 to 1.5 [138]. Since the n values in this work are relatively low, an interfacial oxide layer may not be the primary cause to the lowered barrier height.

Lowering of barrier heights in bulk 4H-SiC-metal contacts have been observed and attributed to high concentrations of localised defects such as the Z_1/Z_2 defects and stacking faults that pin the Fermi level locally [140]. The Z_1/Z_2 defect at a high enough concentration has an energy of $\sim$0.63 eV below the conduction band as determined by deep level transient spectroscopy, creating a local Schottky barrier height of $\sim$0.6 eV [140]. Another potential cause for the lowering of barrier height may be due to metal-induced gap states (MIGS) that is characterised by the density of surface states and difference in electronegativity of the metal and the semiconductor in contact [141]. MIGS may be applicable to explain the observation of much reduced Ni-Ni barrier height in comparison to Al-Al. Interfacial surface states may have formed at the Ni-por-SiC interface introducing energy levels within the energy gap. Lowering of the barrier height has been observed in ZnO nanowires with Au contacts where the obtained Φ_B of 0.6 eV was lower than the theoretically predicted 1.2 eV [142]. The presence and ionisation of surface states has been ascribed to the observed barrier height reduction.

For Ni-Ni, UV illumination appeared to cause little or no change in barrier heights as shown by the data in Table 4.1, which correlated with the low photocurrent to dark current ratio of 0.16. It was highly likely that the photogenerated carriers arising from UV illumination have recombined at surface traps at both Ni contacts. The expected effect of surface states on the ideality factor was not observed however, most likely due to the symmetric back-to-back diode configuration. In contrast, Al-Al exhibited a reduction in both barrier heights and ideality factor upon UV illumination which correlate to the higher photocurrent ratio (0.94) arising from the photogenerated carriers. In the case of Ni-Al, surface states may have played a role. Upon UV illumination, when under positive applied voltage (junction 1 reverse biased), the photocurrent to dark current ratio was 1.52. This is likely to be due to ionised

electrons from surface states and photogenerated electrons overcoming the barrier when Φ_{B_1} decreased from 0.815 to 0.806 eV. Under negative applied voltage however, junction 1 was forward biased which results in further barrier lowering of the Ni contact (Φ_{B_1}). When strongly forward biased ($\sim$6 V), under increased lateral electric field, photogenerated carriers and ionised electrons from surface states could easily overcome the barrier, resulting in significantly higher photocurrent to dark current ratio of 8.96 at -10 V.

It was observed that the ideality factors were higher for Ni-Al being 1.02 in the dark and 1.03 under UV illumination, in comparison to approximately 1.01 for Al-Al and Ni-Ni in both conditions. It is noted that the variation is small in comparison to the uncertainty. In theory, $n = 1$ when the current is determined only by thermionic emission. The increase in the ideality factor from unity suggested that in combination with thermionic emission, generation and recombination mechanisms within the depletion layer near the Ni contact had occurred. This is in agreement with carrier ionisation from surface states contributing to the observed large photocurrent when junction 1 of Ni-Al was forward biased.

In the present work, the photocurrent to dark current ratio improved with asymmetric metallisation scheme in comparison to the symmetric where Ni-Ni showed 0.16, Al-Al showed 0.94 and Ni-Al showed a ratio of 8.96. Analysis of the I-V characteristics under idealised conditions without surface states showed that employing asymmetric metallisation may result in carrier injection by internal photoemission from metal contacts when Ni was illuminated and strongly forward biased. A more realistic approach via a back-to-back Schottky diode within the thermionic emission model showed that the barrier height for Ni in particular was lower than expected, indicative of influence from surface states at the Ni-por-SiC interface. The higher ideality factor suggested generation and recombination within the depletion region as the electrons were likely ionised from these states when Ni was strongly forward biased. Whilst the increase in photocurrent of an order of magnitude is encouraging, an increase in excess of 5 to 6 orders of magnitude is required to operate as photodetectors [129]. Improvement in photocurrent is expected if the present lateral interdigitated electrode design is changed to a vertical structure that is expected to result in better contacts and an electric field dependent on the thickness of the mesoporous 4H-SiC layer rather

than lateral electrode spacing. Tuning and optimisation of the contact barrier height is a prerequisite to extending the use of mesoporous 4H-SiC as a photodetector.

4.2.5 Optical Characterisation

The effects of nanostructuring and surface termination/defects upon the optical properties of S-Por-SiC were assessed via UV-Vis absorption, PL and PLE measurements. Figure 4.15 shows UV-Vis absorbance spectra in ethanol dispersion. Pure ethanol without S-Por-SiC showed very little absorbance in comparison to the S-Por-SiC dispersion.

The 4H-SiC substrate showed a prominent below bulk bandgap absorption peak at 462.9 nm (2.67 eV) as shown in Figure 4.15(a) which was widely reported in the literature in terms of n-type N donor [143–145] assisting interconduction band transitions at the M point. It is possible that the Z_1 centre [146] located at E_C-0.63 eV where the energy of the transition between the defect and the valence band is approximately $\sim$2.6 eV is a potential contributor. The fundamental absorption occurred near 383 nm (3.23 eV) (dotted vertical line) consistent with the indirect energy gap for bulk 4H-SiC [147]. The absorption spectrum for S-Por-SiC incorporates multiple scattering mechanisms of which Rayleigh scattering is predominant but does not show evidence of free carrier absorption or a significant defect related peak. Below 380 nm, the absorption increases as smaller particles were being excited. An onset in absorption occurred around 290 nm (4.27 eV). As the shoulder was broad, the origin would be better resolved and further verified by PLE which will be discussed later in this section. The increased absorption for wavelengths shorter than 290 nm may include contributions arising from mesoporous structures with nanometric scale walls, that have energy gaps larger than those observed in the bulk. The energy gaps at the M, L and Γ points of the Brillouin zone for bulk 4H-SiC are 3.23 eV, $\sim$4.00 eV and 5-6 eV respectively [16, 148]. The energy at the onset of 290 nm (4.27 eV) for S-Por-SiC is larger than the energy gap of bulk 4H-SiC at the M and L points indicating that lowering of the lattice symmetry by size effects may have increased the indirect energy gap [52].

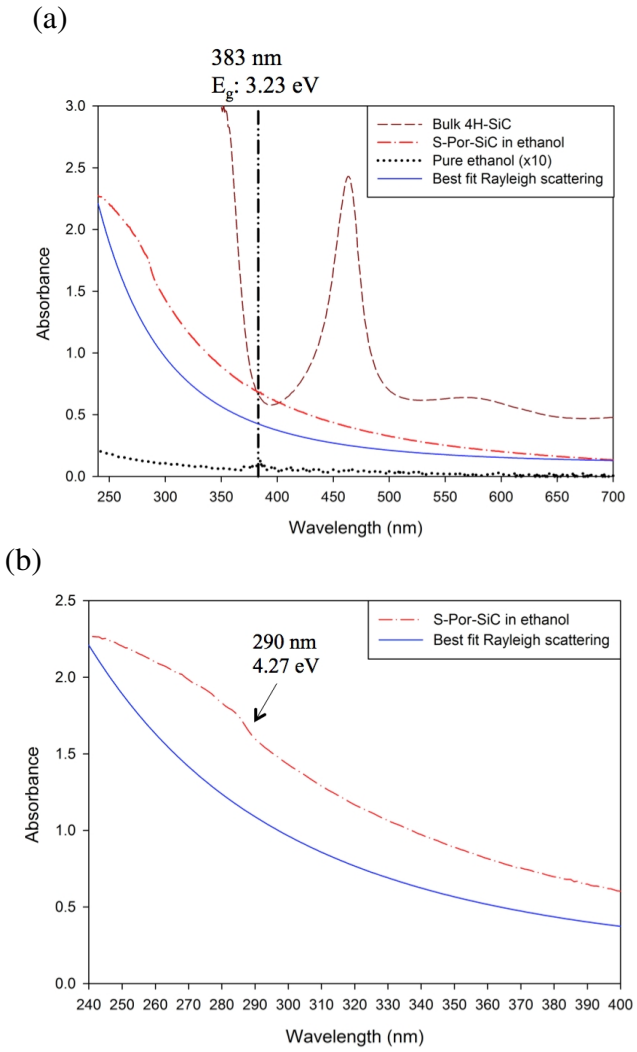

Figure 4.15: (a) UV-Vis absorption spectra of bulk 4H-SiC, S-Por-SiC and pure ethanol, (b) zoomed in absorption spectrum of S-Por-SiC showing absorption onset near 290 nm region.

In order to verify the existence of quantum confinement effects, the shift in PL peak position with respect to the change in excitation wavelength can be used. One explanation is that as the excitation energy is decreased (longer wavelengths) only larger QDs are excited and therefore the PL energy is expected to decrease (red-shift towards longer wavelengths). The red-shifting in PL peaks with increasing excitation wavelengths is another means of confirming the existence of the quantum size effects [15, 17, 23, 84, 149].

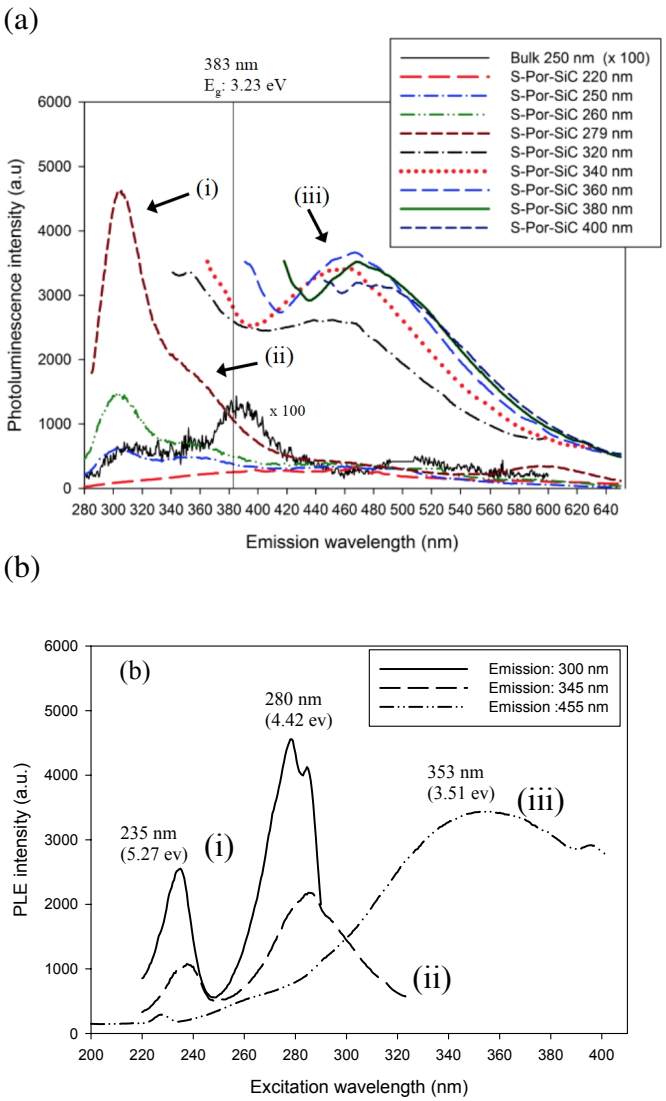

Figure 4.16: PL emission spectra of bulk 4H-SiC and S-Por-SiC suspended in ethanol at different excitation wavelengths. Numerals (i), (ii) and (iii) indicate main designated PL emission peaks at 300 nm, 345 nm and 455 nm. (b) PLE spectra under different monitoring wavelengths for designated PL peaks to probe the absorption transitions preceding emission. The above bandgap PL emissions of 303 nm / 345 nm and corresponding absorptions at 235 nm / 280 nm have rarely been reported in the literature and is a significant finding in this thesis, supporting quantum confined emission in nanostructured 4H-SiC.

Figure 4.16(a) shows the PL spectra at room temperature for bulk 4H-SiC and S-Por-SiC in ethanol for a range of excitation wavelengths. S-Por-SiC exhibited enhanced PL emission with an intensity approximately 100 times greater than that observed for the bulk. For excitation in the range 250-279 nm, above bulk bandgap PL emission peaks

and shoulders (above 4H-SiC E_g : 3.23 eV, 383 nm) that were relatively constant with excitation wavelength were produced, with the primary peaks obtained near (i) 303 nm and secondary shoulders near (ii) 345 nm. The typical FWHM values were 50 nm. Whilst the two orders of magnitude increase in intensity and above bandgap PL features (303 nm and 345 nm) are indications of quantum confinement within the thin walls of S-Por-SiC, the expected red-shifting with changing excitation energies [7, 23] was not observed. These above bandgap emission peaks (303 nm / 345 nm) have rarely been reported in the literature and is a significant finding in this thesis, supporting quantum confined emission in nanostructured 4H-SiC. For excitation wavelengths in the range 320-400 nm, PL features were mainly below the bulk bandgap and red-shifting from (iii) 455 to $\sim$470 nm whilst a contribution from above gap was possibly associated with the 345 nm feature. These peaks were broader with typical FWHM values of around 150 nm. The excitation wavelength-independent PL peaks at short excitation wavelengths and red-shifting PL peaks at longer wavelengths are counterintuitive to quantum confinement theory and have been reported previously for SiC QDs in solvents [7, 119]. In general, previous reports have ascribed excitation wavelength-independent PL peaks around 450 nm to SiC-QDs dominated by surface states (diameters smaller than 3-4 nm) whilst the red-shifting PL peaks were due to quantum confinement in the larger QDs (larger than 3 nm) that were not affected by surface states [7, 150].

In order to distinguish the origins of the constant above bandgap and the red-shifting below bandgap PL peaks, the absorption processes preceding radiative recombination were probed by photoluminescence excitation spectroscopy (PLE) [151]. Figure 4.16(b) shows the PLE spectra monitored at the PL emission wavelengths of interest; (i) 300 nm, (ii) 345 nm and (iii) 455 nm. The above bulk bandgap, excitation wavelength-independent PL emission peaks at (i) 300 nm and (ii) 345 nm in Figure 4.16(a) were preceded by absorptions at similar energies near (i) 235 nm (5.27 eV) and (ii) 280 nm (4.42 eV) as shown in Figure 4.16(b). The PLE peak at 280 nm correlates with the absorption feature observed via UV-Vis spectroscopy in Figure 4.15(b). These PLE peaks were narrow, suggesting transitions between discrete states and high above the bulk bandgap. The PLE peak at 235 nm (5.27 eV) is rarely reported and may be related to the direct optical transition at the Γ point of 4H-SiC

[148]. On the other hand, the rather broad, below bulk bandgap and red-shifting PL emission peaks (iii) from 455 nm towards ∼470 nm as shown in Figure 4.16(a) originate from a broad absorption band with a PLE peak near the band edge at (iii) 353 nm (Figure 4.16(b)). Since the red-shifting PL peaks in this work were very broad and below the bulk bandgap at around 455 nm, these peaks are ascribed to surface defects or possibly donor impurities as has been reported for 6H-SiC porous SiC [152]. It is noted that 4H-SiC QDs were shown to have sub-bandgap PL peaks around 450 nm with corresponding PLE peaks at 297 nm, 323 nm and 365 nm [7]. The sub-bandgap PL peak around 450 nm for 4H-SiC was ascribed to hexagonal to cubic phase transformation during ultrasonication resulting in similar PL emission and a common PLE peak near 365 nm for all polytypes.

4.2.6 Effect of Ultrasonication

In the literature, ultrasonication [7, 17] has been claimed to be the cause of the unexpected sub bandgap emission in 6H- and 4H-SiC derived nanostructures. The ultrasonic based process during sample preparation was thought to result in both cubic and hexagonal SiC nanocrystals. In order to assess the effect of ultrasonication on the 4H-SiC polytype in this thesis, XRD data were compared between (i) ultrasonicated, dried and mechanically ground S-Por-SiC and (ii) mechanically ground D-Por-SiC (without ultrasonication) as shown in Figure 4.17.

In powdered form, a higher number of XRD peaks relating to the randomised crystallites can be determined. These peaks were consistent with those expected for the bulk 4H polytype for both sonicated S-Por-SiC and unsonicated D-Por-SiC. It is noted however that polytype phase transformation may be preferentially induced in the smallest of crystallites. In this measurement technique, the peaks for the smallest crystallites would be significantly broadened and not noticeable when masked by those of the larger crystallites. Complementing the XRD data was the interplanar spacing of 0.267 nm measured via HRTEM for S-Por-SiC (Fig. 4.6 (d)) ascribed to 4H-SiC $(10\bar{1}0)$ planes. The data substantiated that the polytype remained to be 4H-SiC after sonication.

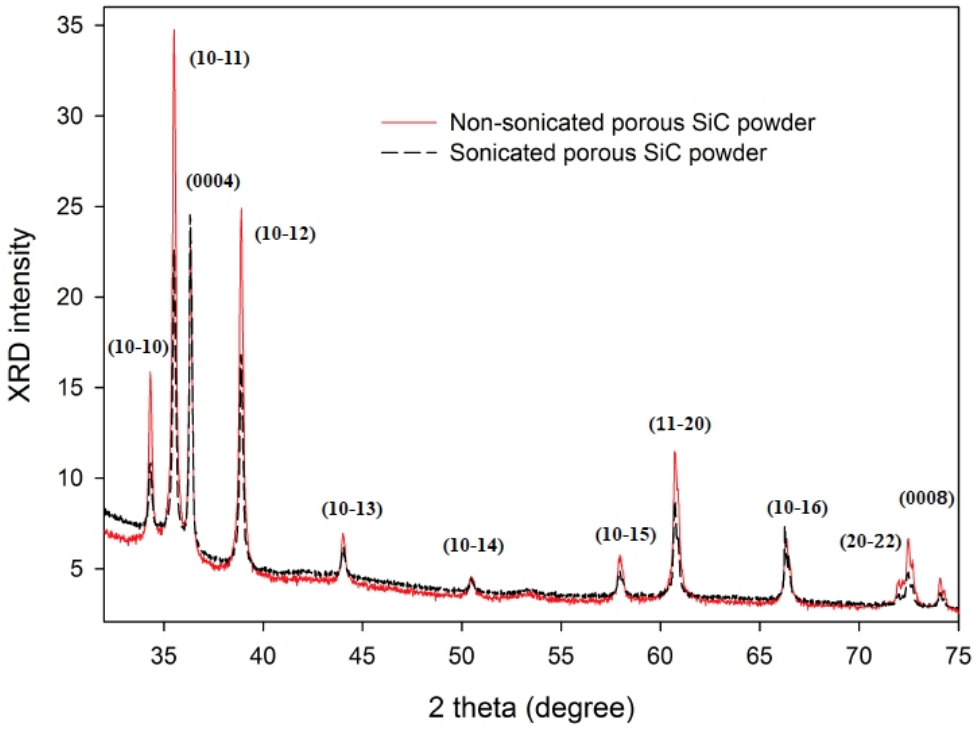

Figure 4.17: XRD pattern comparing ground S-Por-SiC and D-Por-SiC samples

Earlier studies showed that SiC polytypic transformation nucleated from dislocations under thermal stress. Gross transformation can occur for crystals with high densities of dislocations when exposed to temperatures of around 1150°C for 2.5 hours [153], indicative of the high energies required for polytypic transformation. The HRTEM data in Fig. 4.6(d) exhibited high crystallinity and retained 4H-SiC interplanar spacing after ultrasonication. The XRD pattern (Fig. 4.17) indicated that much of the crystal remained to be 4H-SiC. It is likely that ultrasonication process used in this study does not impose sufficient energy for gross polytypic transformation, thus, the link of sonication to change of phase is unlikely.

It follows then that the below bulk bandgap and red-shifting PL peaks in this work and previous works may not be solely related to polytype transformation from 4H-SiC into 3C-SiC. Rather, these can be surface related, a result of 4H-SiC band edge transitions with surface defects or donor impurities found in the larger sized crystallites. Data from XPS revealed surface termination (such as fluorine) and surface defects (C=O/COOH) on S-Por-SiC that may result in surface states. The reported excitation wavelength-independent PL emission at 450 nm and the near band edge PLE

peak at 365 nm are common amongst the different polytypes; 3C, 6H and 4H-SiC QDs [7] which suggest that both quantum confinement, surface states and defects dictate the optical properties of SiC nanostructures as will be explained in section 4.2.7.

4.2.7 Model for Quantum Confinement and Surface States Dependent Emission

The model described is shown schematically in Figure 4.18 which illustrates the observed emission processes in the porous SiC structures. The top most valence energy level and bottom most conduction energy level associated with Si and C atoms within the crystallite are referred to as core HOMO (highest occupied molecular orbital) and core LUMO (lowest unoccupied molecular orbital) respectively, while those related to surface atoms are referred to as surface HOMO and surface LUMO respectively. As the crystallite size decreases, the core HOMO-LUMO gap, related to the Si and C atoms in the interior of the crystallite (core atoms) widens due to quantum confinement. At sufficiently small sizes, the HOMO-LUMO energy difference is sufficiently large for the surface states (surface HOMO and LUMO related to atoms at the crystallite's surface) to dominate the optical gap, resulting in the excitation wavelength-independent PL emissions in region A.

These surface states may obscure the underlying quantum confinement as density functional theory (DFT) calculations and experiments have shown that surface groups such as carboxyl (-COOH), C-O, and fluorine (-F) may introduce fixed energy levels (surface atoms' HOMO and LUMO) within the energy gap of SiC nanoparticles [21, 33, 154, 155] rendering the optical properties size independent. As the core-related HOMO and LUMO (relating to the interior of the crystallite) narrow with increasing size, the surface states lose their influence allowing transitions between core HOMO and core LUMO to dominate, resulting in the observed red-shifting of the above bandgap emission PL in region B, exhibiting size dependent optical properties. As the sizes of the crystallites increase further, donor impurities become important [28] as more dopants are available in larger crystallites and on average more defects may be found. The optical transitions now constitute the core HOMO with donor impurity/defect states near the core LUMO producing below bandgap and red-shifting

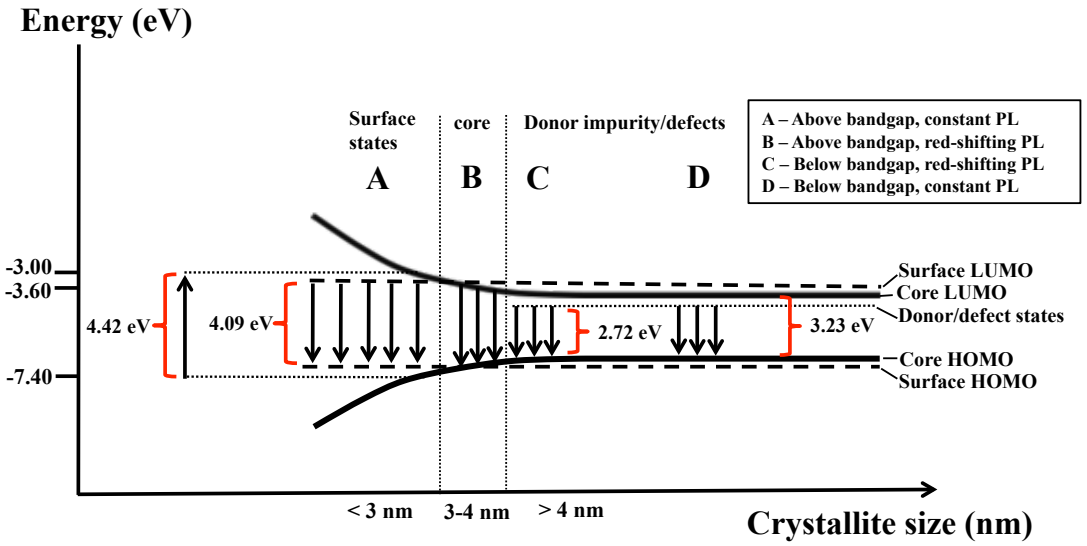

Figure 4.18: Illustration of the interplay between quantum confinement and surface states for small crystallites (<3 nm and 3-4 nm) and influence of donor impurities/defects for larger crystallites (>4 nm) on the optical transitions of por-SiC. The illustrated energy is with respect to vacuum with −3.60 eV being the electron affinity of bulk 4H-SiC. Absorption energy of 4.42 eV resulted in the subsequent above bandgap PL emission of 4.09 eV. Absorption energy of 3.51 eV (not illustrated) resulted in the below bandgap emission of 2.72 eV. The 3.23 eV energy interval represents the 4H-SiC bulk bandgap. Values of crystallite size range correspond to the observed dual-feature PL and trends in the literature [23, 24, 28]. Deviation from quantum confinement are observed in region A (sizes less than 3 nm) as a constant PL when surface HOMO/LUMO dominate whilst the quantum confined red-shifting PL occur for sizes larger than 3 nm in region B when the core HOMO/LUMO dominate. Regions C and D represent below bandgap emissions contributed by donor/defect states in the energy gap.

PL emissions as observed in region C. As the crystallite size approaches bulk-like dimensions (region D), the HOMO and LUMO represent the respective bulk valence band and conduction band edges. In the bulk, excitation wavelength-independent and below bulk bandgap PL dominates, as shown by region D. In this work, because of the surface states introduced by fluorine surface termination, upon absorption at 4.42 eV (280 nm), excitation wavelength-independent PL emissions around 4.09 eV (303 nm)

are observed in region A, while oxygen related defects in C=O/COOH bonds and N doping are ascribed to the red-shifting below bulk bandgap PL emission band (2.72 eV, 455 nm) upon absorption at 3.51 eV (353 nm) in region C [28, 34]. The PL peak then becomes independent of size with a peak wavelength of $\sim$470 nm in region D. It is difficult to assign the precise transition involved, but the energy approximately matches that of the absorption peak in Figure 4.15(a) or the energy of the Z_1 center [146]. The model presented here is in conceptual agreement with the theoretical model given by Wolkin *et al.* for Si QDs in porous Si (pristine versus oxidised porous Si) [156] and our DFT calculations on 4H-SiC quantum dots ($-$H versus $-$F and $-$OH surface terminations) [157] where both quantum confinement and surface passivation determine the electronic states of the QDs.

4.3 Conclusions

The mesoporous 4H-SiC suspended in ethanol (S-Por-SiC) exhibited three PL bands: two of which had energies that are above bandgap, showed a narrow linewidth, evidence of quantum confinement that were related to surface states, and in the UV (300 and 345 nm). The above bandgap emissions for nanostructured 4H-SiC observed in this work were rarely reported in the literature. In contrast, the third PL band was below bandgap, had a broad linewidth, were donor impurity/defect related, and in the visible spectral range (455 nm). These UV and visible range emission bands are accessible by high and low excitation energies respectively (excitation wavelengths of 235 and 280 nm for the former and 353 nm for the latter). In addition to quantum confinement of the por-SiC, surface states formed by fluorine surface termination groups as a result of etching in HF electrolyte and subsequent suspension in ethanol are ascribed to the excitation wavelength-independent emission in the UV. Donor impurity, C=O/COOH surface groups, defects and diminishing quantum confinement in larger sized crystallites are assigned to the band edge transitions that are responsible for the broad sub-bandgap emission.

It is proposed that the deviation from quantum confinement in the optical properties of nanostructured SiC are strongly surface related. Data from XRD and HRTEM indicated that ultrasonication used for sample preparation retained the 4H-SiC

polytype, although the sub bandgap emission (455 nm) usually associated with 3C-SiC was still observed. The retained polytype strongly indicates that the below bulk bandgap and red-shifting PL peaks observed in this and previous works may not be solely related to polytype transformation from 4H-SiC or 6H-SiC into 3C-SiC. Rather, these can be surface related, a result of 4H-SiC and 6H-SiC band edge transitions with surface defects or donor impurities. XPS data showed -F surface termination and oxygen related defects (C=O/COOH) on the surface of anodically etched mesoporous 4H-SiC. Should the origins be surface related rather than bulk (polytype), as shown by DFT calculations, surface terminations with -F or -OH may result in surface states lowering the energy gap whilst -H may passivate the surface states as discussed in chapter 3. As full hydrogenation of nanostructures may be challenging, an alternate route by sacrificial oxidation that removes the surface layer or surface defects may be promising to suppress below bandgap emission. Thus similar PL emissions across different polytypes may be resolved. This is a subject explored in greater detail in chapter 5.

As discussed in chapter 3, engineered surface terminations using -F, -OH or -H, in conjunction with defect control and intentional impurity doping, may be used to control electronic states in novel optoelectronic devices or biomedical applications. Por-SiC is a promising material in producing nanocrystallites having absorption and emission in the UV that may be applicable for UV photodetectors. Emission in the visible range may find applications as non-toxic biomarkers. For contact metallisation, the asymmetric metallisation scheme incorporating lateral interdigitated Ni and Al contacts was shown to provide a means of increasing the photocurrent by an order of magnitude for S-Por-SiC due to the different interfacial properties between Ni-por-SiC and Al-por-SiC. Analysis of the I-V characteristics without considering surface states showed that employing asymmetric metallisation may result in carrier injection by internal photoemission from metal contacts. Carrier injection may have occurred when Ni was illuminated and strongly forward biased. Consideration of surface states in the back-to-back Schottky diode model showed that the barrier height for Ni in particular was lower than expected, indicative of influence from surface states at the Ni-por-SiC interface. Ionisation from surface states may have resulted in increased photocurrent. An increase of 5 to 6 orders of magnitude in photocurrent is required for

applications in photodetectors. The low photocurrent to dark current ratio and possible carrier injection/surface states related conduction need to be addressed. For the former, the use of vertical structure instead of lateral electrodes may result in increased electric field and higher photocurrent, whilst barrier height engineering is required for the latter.

In summary, por-SiC from *n*-type 4H-SiC substrates was fabricated via anodic electrochemical etching in HF/ethanol solution followed by an ultrasonication process. The average crystallite size, porous structure, crystallinity and polytype have been verified by Raman scattering, HRTEM, and XRD. Using UV-Visible absorption, PL and PLE, above and below bulk bandgap absorption/emission processes related to the interplay between quantum confinement, surface states and donor impurity/defects related optical transitions were revealed. Though common PL characteristics across different SiC polytypes of dissimilar band gaps have been widely reported, no complete explanation for the effects has been previously identified. A model has been proposed in this chapter to explain the observed constant, red-shifting and below bulk bandgap PL emissions seen in SiC based nanoparticles in solvents. Finally, it is noted therefore that it is critical to understand the chemical and physical features of SiC derived nanostructures surfaces as control of surface states is a requisite to exploiting the size-dependent optical properties.

Chapter 5

Size Reduction By Pore Wall Thinning Method

5.1 Introduction

In the previous chapter, S-Por-SiC realised from the sonication of D-Por-SiC, showed a size distribution ranging from 16.9±5.5 nm to 2.9±1.0 nm as verified by transmission electron microscopy (TEM) in section 4.3.1. The motivation behind the manufacturing of SiC based QDs in the size range of 1 to 6 nm is to meet the requirement as biomarkers that can be effectively discharged from the body by renal excretion. The hydrodynamical size required for this is below 5.5 nm [24]. The dimensions of the porous structure within the as-etched D-Por-SiC may be further reduced by an additional process step prior to sonication. Recently, it was shown that nanoparticles smaller than 6 nm can be obtained from porous Si after pore-wall thinning using an oxidation step [158] which was otherwise difficult to achieve with sonication alone. It was hypothesized that the surface energy barrier to form particles increases with reducing particle size and eventually sonication would not be sufficiently powerful to further breakdown to smaller sizes. In another work, it was shown that the fracture energy to break a nanometer-sized particle is larger than a micrometer-sized one [159] during bubble collapse in ultrasonication. This follows the idea that the pore wall thickness in the porous structure determines the minimum particle size that can be achieved by sonication or mechanically driven top-down approaches. The pore wall thinning method has not been reported as a complementary process for electrochemically etched porous SiC. Additionally, the process consists of sacrificial oxidation which potentially removes potential surface defects. It is shown in this work that the dual-feature PL and sub bandgap emission in mesoporous 4H-SiC was suppressed as a result of the sacrificial oxidation.

To the author's knowledge, the pore wall thinning and suppression of sub bandgap

emission on mesoporous 4H-SiC in this work is a first and a novel approach for SiC nanostructuring. In this chapter, the effect of pore wall thinning on D-Por-SiC and the resulting optical properties are discussed.

5.2 Results

In this section, in order to further reduce the dimensions of as-etched mesoporous 4H-SiC structures, the pore wall thinning method was employed by means of sacrificial oxidation in a furnace at 1100°C with a gas flow of 100 sccm O_2 for durations of 1, 3, 6 and 9 hours followed by a 5 minutes silicon oxide removal in HF/ethanol. The effectiveness of the process was examined by cross sectional scanning electron microscopy (SEM) using Phillips XL30 ESEM-FEG, Raman scattering, photoluminescence (PL) and photoluminescence excitation (PLE).

5.2.1 As-etched Mesoporous 4H-SiC

The cross sectional SEM image of as-etched delaminated mesoporous 4H-SiC (D-Por-SiC) using the process conditions specified in section 4.2 is shown in Fig. 5.1(a). The labelled 'top' portion of D-Por-SiC represents the side near to the substrate surface while the labelled 'bottom' portion is the side of the underlying porous layer which was accessible once delaminated from the bulk substrate. It is clear from the image that within the D-Por-SiC a morphological transition occurred during the etching process as demarcated by the lateral break in the structure between the top (cap layer) and bottom (porous layer) sides. Figure 5.1 (b) is a high resolution SEM image of the circled area in Fig 5.1(a), showing that the cap layer is approximately 3.5 μm in thickness. As reported in the literature, the top region of porous SiC consists of a very thin skin layer and a thick cap layer [160–162]. The skin layer is a non-porous layer that is roughly 10-100 nm [160, 161, 163] in thickness which can be removed by reactive ion etching (RIE) [160, 161, 163] to expose the underlying porous material. Underneath the skin layer, is the cap layer, with a thickness of up to approximately 50 μm comprising a porous structure [160]. In Fig. 5.1 (b), the porous layer (13 μm in thickness) consists of

fine vertical structures with lateral dimensions of ~ 27 nm which are not well resolved at this magnification. The structure is brittle, featuring sharp and straight edges at the point of fracture. Figure 5.1 (c) show areas that were further examined, area labelled 'A' within the cap layer and area labelled 'B' within the porous layer.

Figure 5.2 show cross sectional SEM images at higher magnification for areas 'A' and 'B' with the red arrow denoting direction of etch from the substrate surface. The transition cap layer depicts the early stage of pore formation, following pore nucleation at the surface. The initial porous growth was almost featureless and did not show any regularity of pore structure or any well formed channels that follow a particular crystalline direction. Only with increasing etch depth did the structure reveal initiation of columnar channels. As the etch process progressed, a regular self-ordered nanocolumnar porous structure parallel to the c-axis was evident for depths greater than the 3.5 μm cap layer, as shown in area 'B'.

The formation of nanocolumnar porous structures was previously observed [44] for C-face samples where it was reasoned that the C-face is the preferred etching surface in a fast electrochemical oxidation process, resulting in straight downward etching. This was attributed to the C-face oxidising faster than the Si-face, as similarly observed in both wet and dry oxidation of bulk SiC [164, 165]. Slow oxidation of the Si-face promotes more rapid etching in the lateral direction, therefore branching horizontally rather than vertically. However this point may not be applicable to this work as the substrate used is 8° off-axis and therefore preferential etching on a C-face versus the Si-face is unlikely.

An alternative explanation for the observed characteristics is that under sufficient voltage bias, electrochemical etching only occurs at the pore tips, as illustrated schematically in Fig. 5.3. As etching progresses, the resistance increase from 0.5 $k\Omega$ to 2 $k\Omega$, highly likely due to the porous layer formation. The electric field is enhanced at the pore tips in comparison to the bulk of the SiC, and so holes are attracted to the SiC/electrolyte interface, away from the pore walls, resulting in vertical etching. This may explain why the pores propagate vertically, in the direction opposite to the applied field. It was found in [44] that 20 V was the optimal bias to obtain the nanocolumnar pores. The direction of applied electric field determines the direction of generated

(a)

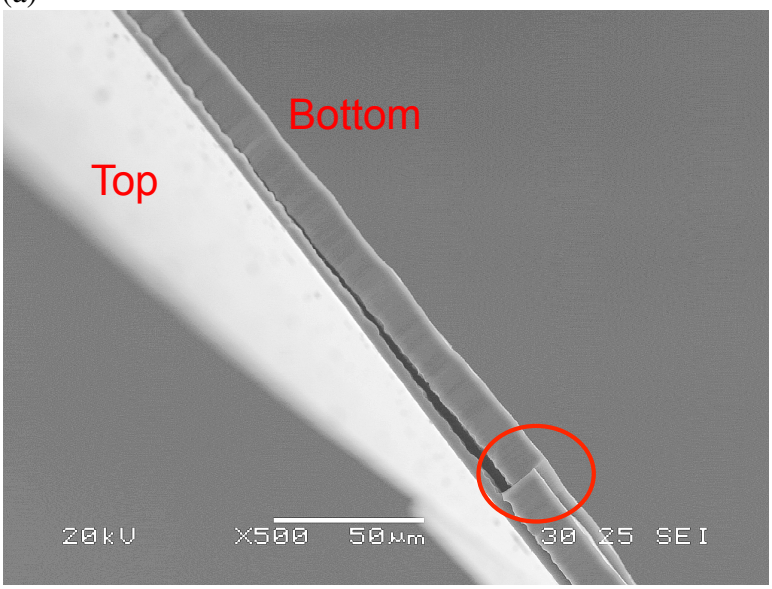

(b)

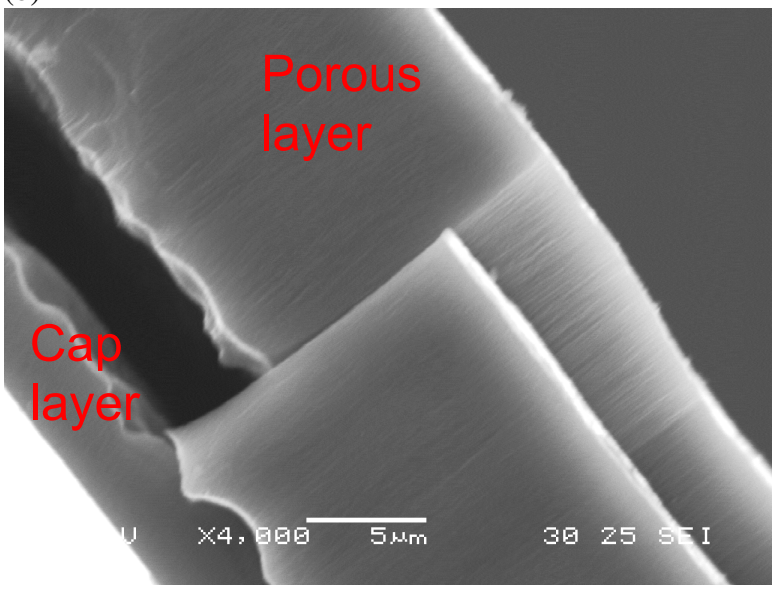

(c)

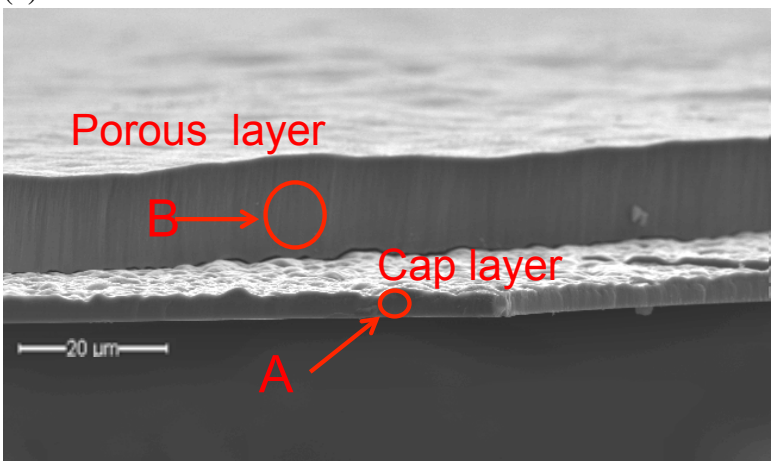

Figure 5.1: Cross-sectional SEM images of as etched D-Por-SiC showing (a) the top and bottom sides, (b) the cap layer and porous layer and (c) marked areas A and B that were examined.

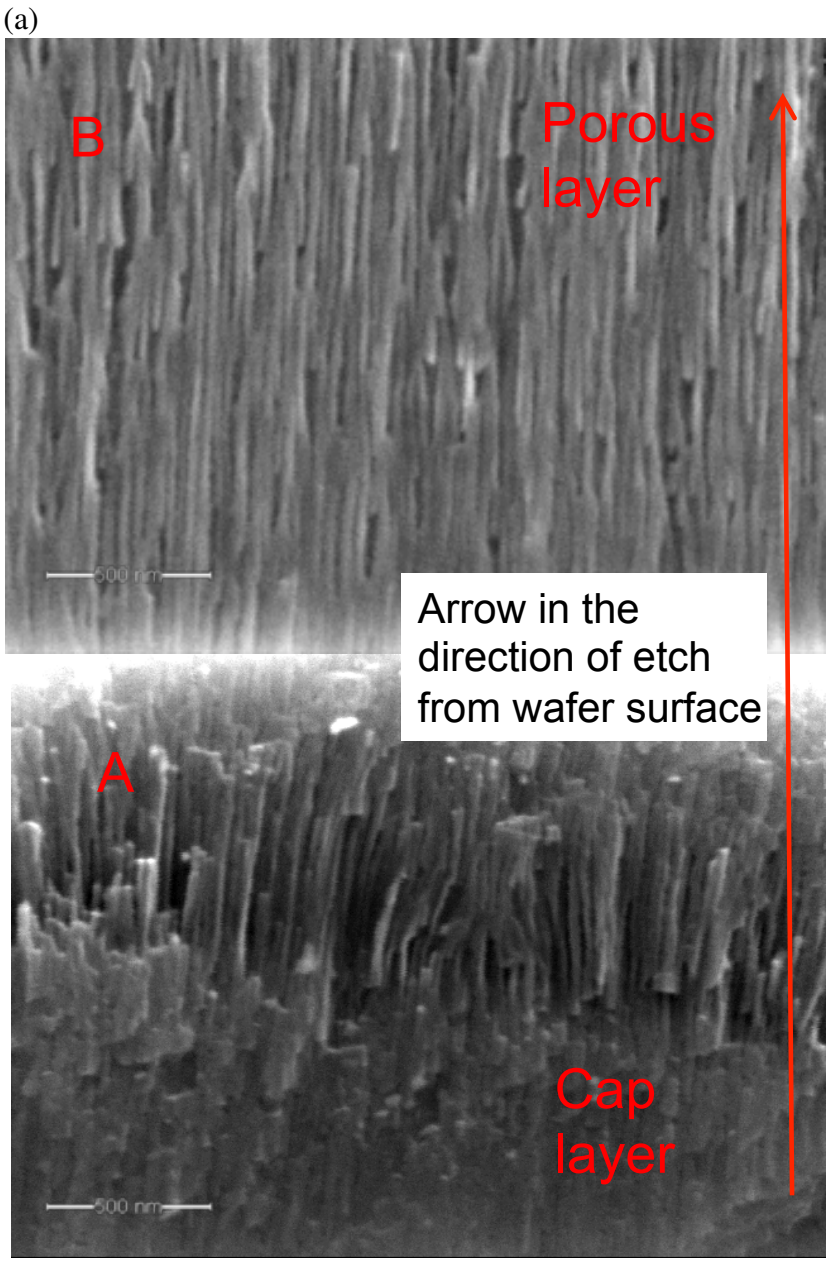

Figure 5.2: Cross-sectional SEM image showing the morphologies of the transitional porous cap layer and the regular nanocolumnar porous structure. The arrow denotes the etching direction from the surface of the substrate.

holes, thus forming vertical nanocolumnar pores. At this voltage bias, the etching of oxide by HF is faster than the electrochemical oxidation of the SiC due to the high concentration of HF used, (48% HF/ethanol in a 1:1 ratio by volume). This resulted in the observed vertical preferential etching direction.

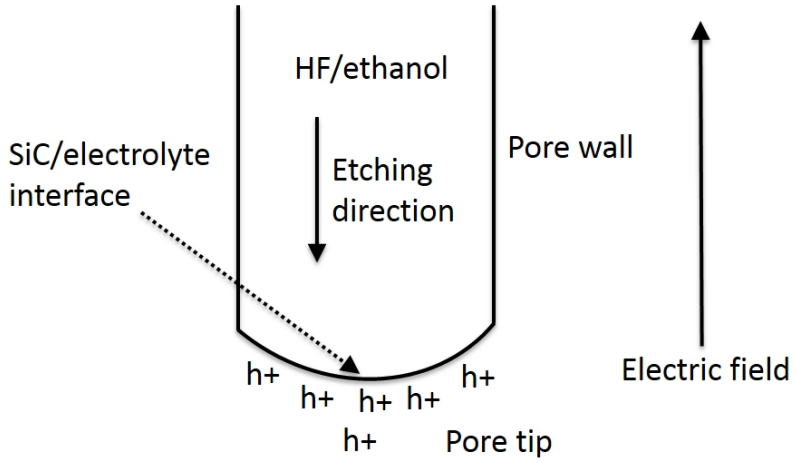

Figure 5.3: Illustration of accumulated holes at the pore tip under the influence of an applied electric field. The direction of the electric field determines the flow direction of holes, thereby influencing the electrochemical oxidation direction. Fast removal of the oxide by using concentrated HF ensures continuous vertical pore etching.

5.2.2 Pore Wall Thinning of Mesoporous 4H-SiC

In this work, the as-etched mesoporous structure shows regularity in shape and orientation which are desirable traits for achieving monodisperse nanoparticles. However, the average size and distribution in the pore wall widths may still be improved after the post-etch pore wall thinning treatment. In this treatment, the cap layer that was not uniformly porous, was carefully removed and discarded whilst the porous layer was retained. The pore wall thinning method consist of 2 main steps: 1) dry oxidation at 1100°C, with O_2 flow rate of 100 sccm and 2) subsequent oxide removal by etching in HF/ethanol for 5 minutes with a subsequent rinse in ethanol.

(a)

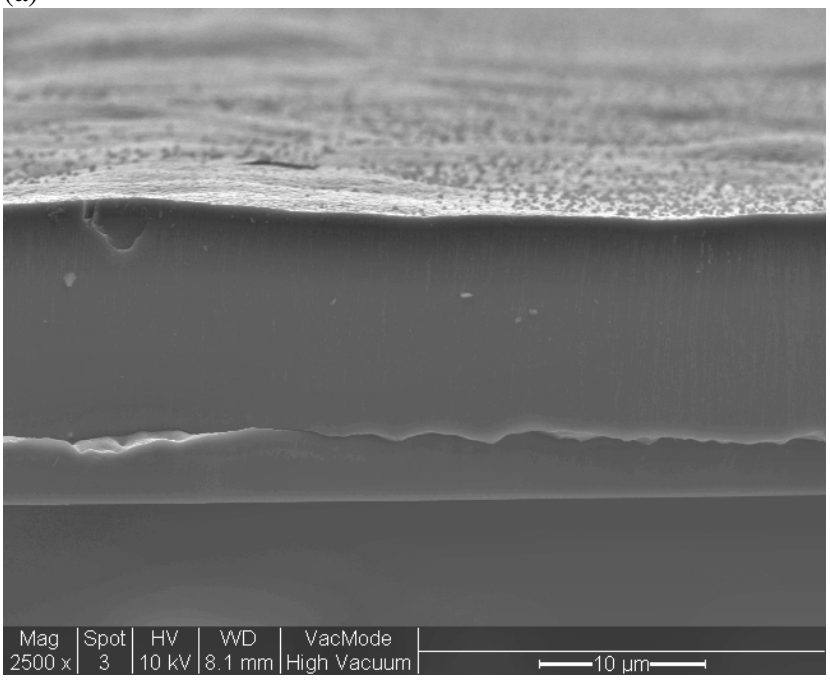

(b)

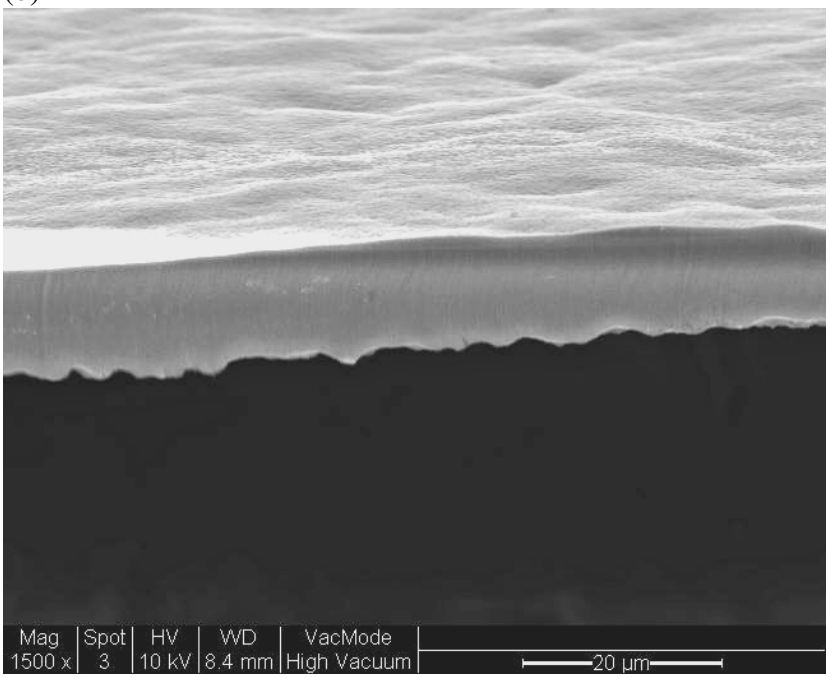

Figure 5.4: Cross-sectional SEM image of D-Por-SiC (a) before pore wall thinning and (b) after pore wall thinning (without cap layer) employing 3 hours oxidation at 1100°C followed by 5 minutes HF/ethanol dip). Slight deformation was observed whereby the edge was curved possibly due to combined effects from the high temperature treatment and the subsequent handling and cleaving steps.

5.2.2.1 Cross Sectional SEM

Figure 5.4(a) shows D-Por-SiC before the treatment and removal of the cap layer. Fig. 5.4(b) shows the D-Por-SiC (without cap layer) after 3 hours of oxidation at 1100°C followed by 5 minutes HF/ethanol dip and rinse in ethanol. There was a discernible curvature on the edge where the cross section was made, showing the porous channels conforming to the deformation. This was likely a result of the high temperature treatment and the subsequent cleaving step.

Fig. 5.5(a) shows a cross-sectional SEM image of as-etched D-Por-SiC. For a set of 20 data points the average interpore width was (27.1±5.0) nm (5.0 nm being the standard deviation). With 1 hour oxidation and subsequent oxide etch in HF, the average interpore width reduced to (20.5±2.8) nm as shown in Fig. 5.5(b). A 3 hour oxidation treatment resulted in further reduction of the average width to (18.2±2.9) nm for the sample shown in Fig. 5.6(a). A 6 hour oxidation treatment resulted in an average pore width of 17.0±1.8 nm (Fig. 5.6(b)).

A significant deformation was observed for this sample at the top portion (surface) which may be due to the high temperature thermal oxidation and subsequent cleaving step. Figure 5.7(a) shows a cross section through a D-Por-SiC layer after 9 hours of thermal oxidation. The average pore wall thickness was 15.9±1.4 nm. The data in Fig. 5.7(b) show the trends for the pore wall thickness as a function of oxidation time. It can be observed that the rate at which the pore wall thickness reduces was highest in the first hour of oxidation (6.6 nm/hour) and this reduces for longer oxidation times (1.2 nm/hour for 9 hours). The oxidation of SiC is similar to that observed for bulk Si, in that it occurs at the interface between the oxide film and the underlying semiconductor, where SiC is the source of Si to form SiO_2. The observed reduction in oxidation rate may be influenced by the increasing distance that oxygen need to diffuse through SiO_2 and reach the SiO_2/SiC interface as oxidation progresses (diffusion rate limited) or reaction rate limited oxidation at the SiO_2/SiC interface itself. The in-diffusion of the oxidant and out-diffusion of CO through SiO_2 is likely the rate limiting step.

The proposed oxidation reaction for SiC is as below [165],

(a)

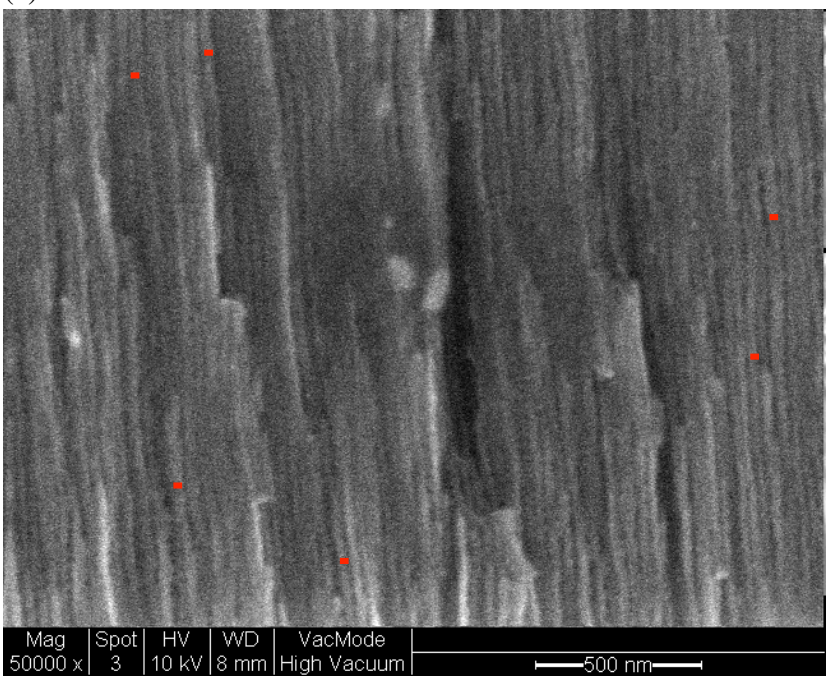

(b)

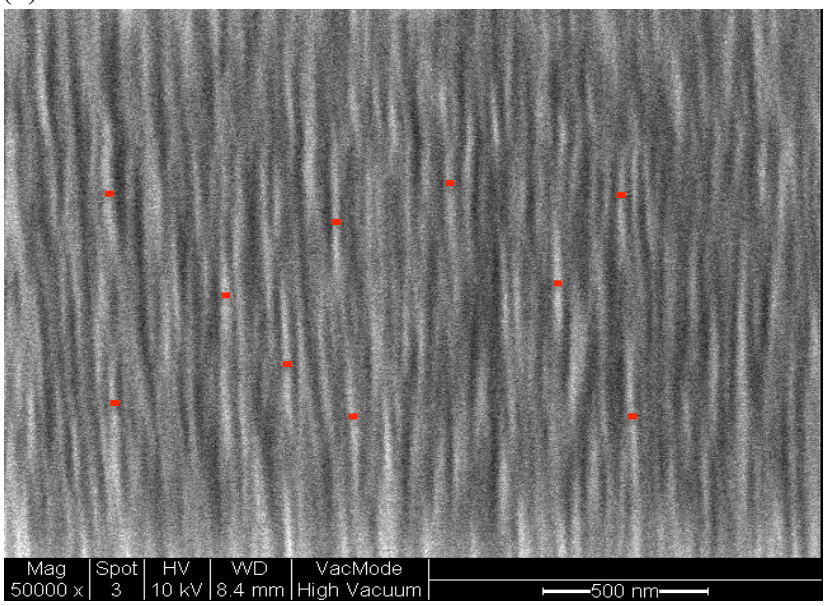

Figure 5.5: Cross-sectional SEM image showing the representative porous morphologies and indicated lateral widths of pore walls for (a) as etched D-Por-SiC and (b) D-Por-SiC after pore wall thinning with 1 hour oxidation at 1100°C followed by 5 minutes HF/ethanol dip.

$$SiC + 1.5O_2 \rightarrow SiO_2 + CO \tag{5.1}$$

Oxidation of porous materials generally exhibit a larger oxidation rate than the bulk

(a)

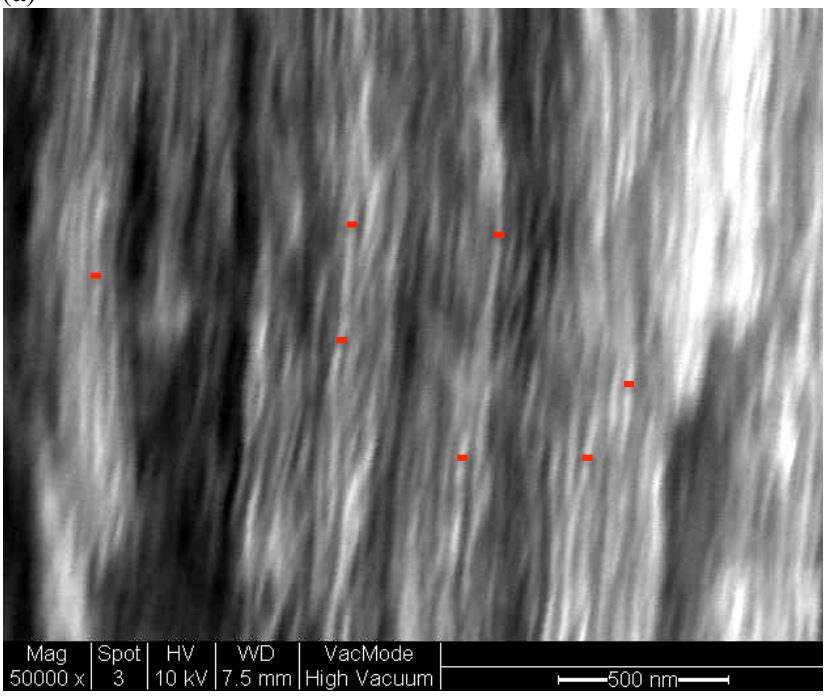

(b)

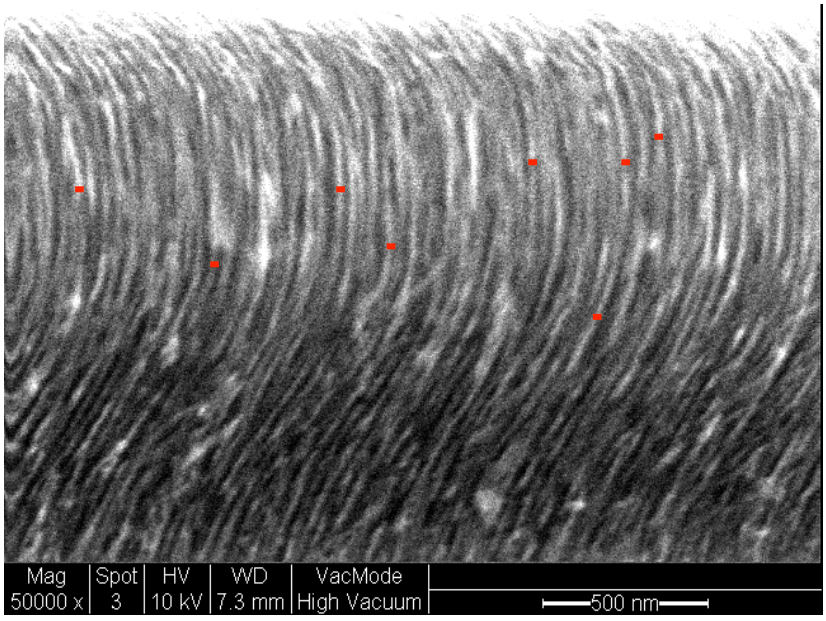

Figure 5.6: Cross-sectional SEM image showing the representative porous morphologies and indicated lateral widths of pore walls for (a) D-Por-SiC after pore wall thinning with 3 hours oxidation at 1100°C followed by 5 minutes HF/ethanol dip and (b) D-Por-SiC after pore wall thinning with 6 hours oxidation at 1100°C.

due to larger exposed surface area [166, 167]. In bulk SiC, the crystal face plays a significant role: oxidation of the Si face has been shown to be slower than the C-face, which is ascribed to the formation of an oxycarbide layer ($Si_4C_{4-x}O_2$) on the surface,

(a)

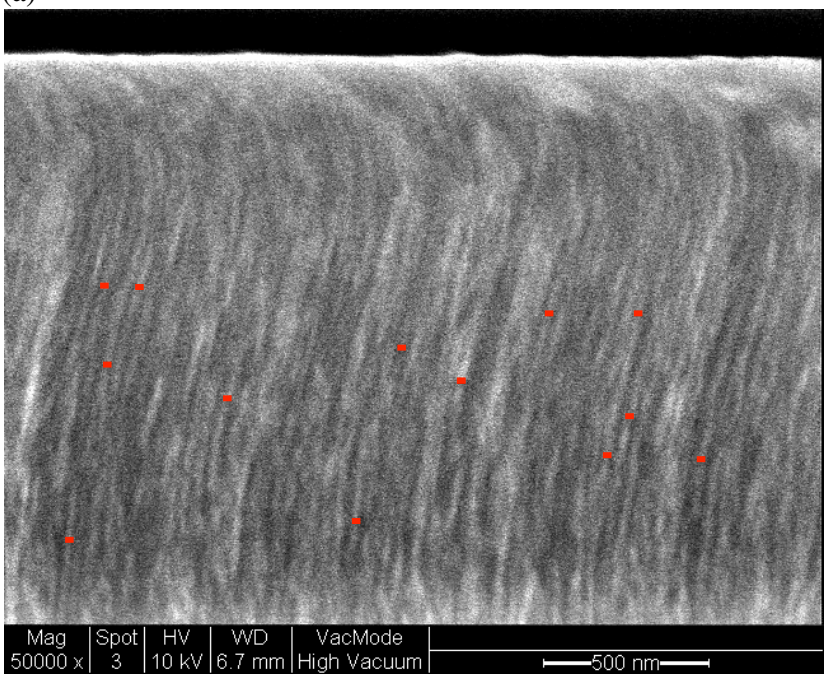

(b)

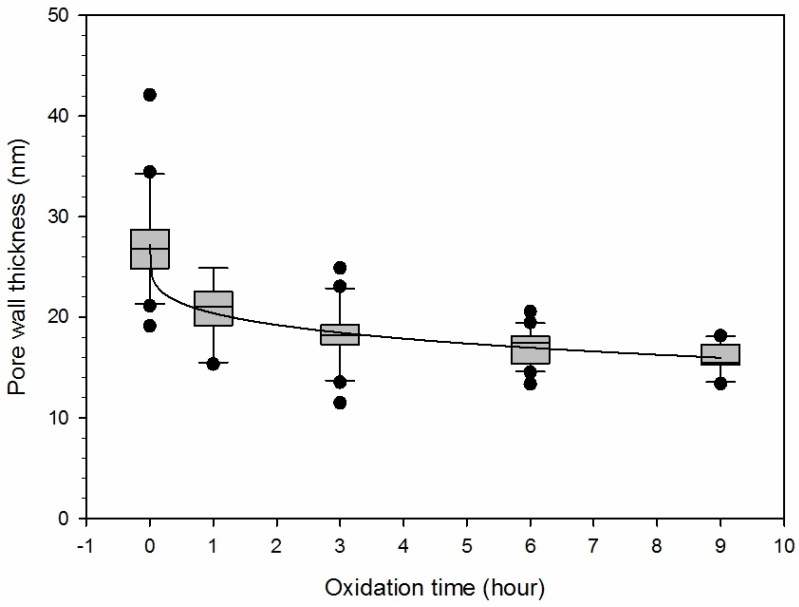

Figure 5.7: Cross-sectional SEM image showing the representative porous morphologies and indicated lateral widths of pore walls for (a) D-Por-SiC after pore wall thinning with 9 hours oxidation at 1100°C followed by 5 minutes HF/ethanol dip and (b) the mean and size distribution of D-Por-SiC pore wall thickness with respect to oxidation time. The data consists of 20 data points for each oxidation time).

impeding the oxidation process [168]. The exact nature of the etched SiC surface in this work is not ascertained, however previous work indicate that electrochemically etched SiC surface is likely to show Si depletion and be C-rich [169, 170].

This layer may not be similar to the crystalline face of the bulk as the formation of an amorphous layer between crystalline SiC and pore has been reported [170], the formation of which was linked to the etching conditions.

In this work it was observed from XPS data that an amorphous layer of approximately 1 nm thick exist on the etched surface surrounding the pore in D-Por-SiC. Peaks related to silicon oxycarbide and SiO_2 was observed from XPS spectra as shown by the data in section 4.3.2 and these may be attributed to the existence of an amorphous layer as observed in TEM (Fig. 4.8 (d)). This layer would be expected to play a significant role in the oxidation of D-Por-SiC.

5.2.2.2 Deal-Grove Relationship

The pore wall thinning data under is summarised in Table 5.1 for 20 data points for each oxidation time (N=20). In order to target the desired pore wall thickness, a prediction of the oxide growth rate is required. The thickness of the oxide layer on the pore wall can be inferred from the width of the pore wall after the oxide film has been removed. As the removed oxide covers two surfaces of the pore walls, the value is halved to represent oxide thickness on a pore wall, as shown in Table 5.1.

Table 5.1: Thicknesses after pore wall thinning of D-Por-SiC.

Oxidation time (hour)	Average pore wall thickness (nm)	Standard deviation (nm)	Pore wall thickness with standard error N=20 (nm)	Pore wall thinning rate (nm/hour)	Removed oxide thickness with standard error N=20 (nm)	Oxide thickness on pore wall with standard error N=20 (nm)
0	27.1	5.0	27.1 ± 1.1			
1	20.5	2.8	20.5 ± 0.6	6.6	6.6 ± 1.3	3.3 ± 0.7
3	18.2	2.9	18.2 ± 0.6	3.0	8.9 ± 1.3	4.5 ± 0.7
6	17.0	1.8	17.0 ± 0.4	1.7	10.1 ± 1.2	5.1 ± 0.6
9	15.9	1.4	15.9 ± 0.3	1.2	11.2 ± 1.2	5.6 ± 0.6

The Deal-Grove relationship is a widely used model for predicting the thermal

oxidation process for Si [171] especially for wet oxidation. The derived general relationship for thermal oxidation is a quadratic equation for the oxide thickness, x_o:

$$x_o{}^2 + Ax_o = B(t + \tau) \tag{5.2}$$

where B is the parabolic rate constant, B/A is the linear rate constant and τ is the time shift to correct for the initial oxide thickness prior to oxidation.

Solving the quadratic equation for x_o, yields,

$$x_o\,(t) = \frac{-A + \sqrt{A^2 + 4(B)(t + \tau)}}{2} \tag{5.3}$$

Figure 5.8(a) shows the averaged oxide thickness on the pore wall as a function of oxidation time. There is a non-zero oxide thickness when extrapolated to *t=0* which is characteristic of dry oxidation, as is generally observed for dry oxidation of Si [171]. Unlike wet oxidation that extrapolates to zero at *t=0*, dry oxidation of Si gives an oxide thickness of about 20 nm for all experimental temperatures attributed to a different oxidation mechanism for thicknesses less than 30 nm [171] and was not due to a pre-existing oxide.

In earlier work [171], the initial thickness was related to the diffusing species being ionic for dry oxygen compared to water. A space charge region within the growing oxide was induced by negatively charged $O_2{}^-$ that in turn increases the oxidation rate for the initial 150$\mathring{A}$, which is considered to be the extent of the space charge region. In a later work, fast initial oxidation rates have been accounted for in a modified Deal-Grove model by incorporating a term that exponentially decays with thickness [172]. A similar approach was taken for SiC oxidation [164] and additionally took into account Si and C emission into the oxide from the substrate interface. The out-diffusion of CO from SiC during oxidation was considered in greater detail [165] and it was also shown that the crystal face plays a significant role, where a higher C density at the surface in comparison to the density of Si results in an increased oxidation rate. In this work, as the longer oxidation time is of interest to thin down the pore wall dimension, models to describe for initial high oxidation rate were not utilised and the conventional Deal-Grove model was used.

(a)

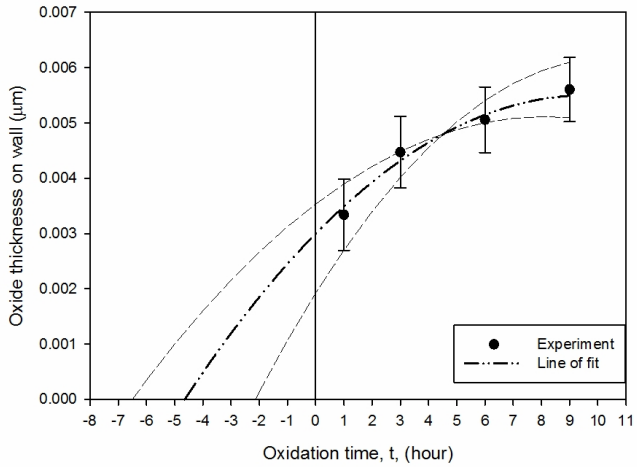

(b)

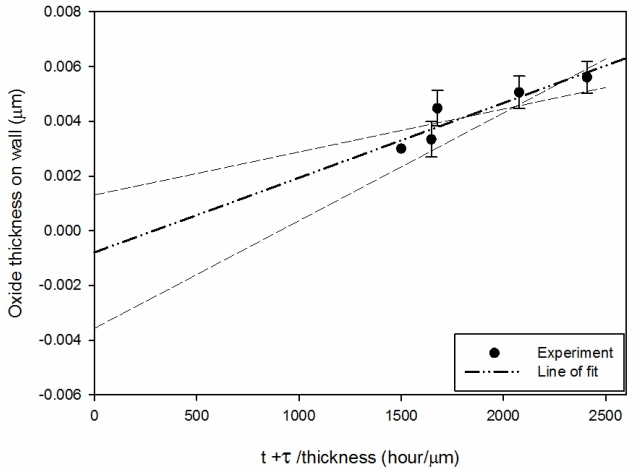

(c)

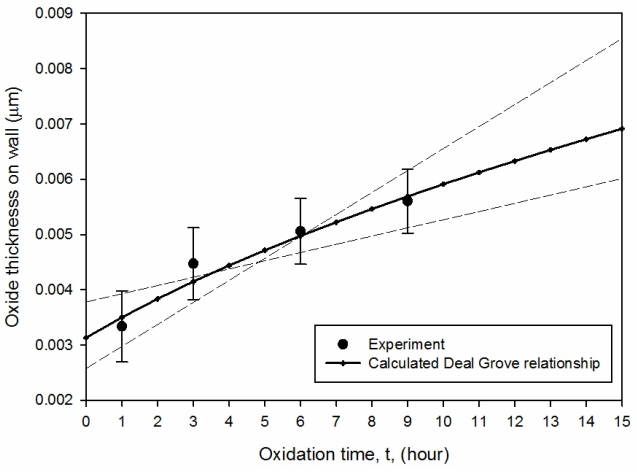

Figure 5.8: (a) Shows a plot of the averaged oxide thickness on the pore wall as a function of thermal oxidation time for the duration of 1 to 9 hours, (b) shows a plot of oxide thickness as a function of the inverse of oxidation time to determine rate constants B and A, and (c) calculated oxide thickness as a function of oxidation time, based on equation 5.4. The error bars represent the standard error of the data (N=20).

As shown by the data in Fig. 5.8(a), the initial oxide thickness extrapolated to *t=0* is approximately 3 nm. The corrective time parameter, τ, being the approximate shift in the time coordinate to correct for the initial 3 nm oxide thickness can be determined by extrapolating the curve back through *t=0* and finding the value of the intercept at the x-axis, resulting in a value of (4.5±2.2) hours.

Figure 5.8(b) shows a plot of oxide thickness as a function of the inverse oxidation rate. Note that the data point at 1500 hour/μm of the x-axis is to account for the initial thickness of 3 nm at *t=0*. The slope of the line of best fit and the intercept at y-axis represent the rate constants B and -A [171], which are determined to be (2.7±1.2)$\times 10^{-6}$ μm^2/hour and (-7.9±24.0)$\times 10^{-4}$ μm respectively. It is noted that the uncertainty for rate constant -A is large in the present work. The uncertainty can be reduced with more experiments for different oxidation times in future work. The linear rate constant B/A is then (0.003±0.009) μm/hour. The extracted rate constants from the experiment is summarised in Table 5.2. The parabolic constant, B, is linked to the in-diffusion of oxygen in the oxide whereas the linear rate, B/A, depends on the reaction rate at the SiC/SiO_2 interface.

Table 5.2: Rate constants for oxidation of D-Por-SiC in dry oxygen.

Oxidation temperature (˚C)	A (μm)	B (μm^2/hour)	B/A (μm/hour)	τ (hour)
1100	(7.9 ± 24) x10^{-4}	(2.7 ± 1.2) x10^{-6}	0.003 ± 0.009	4.5 ± 2.2

The obtained parabolic rate constant, B, at (2.7±1.2)$\times 10^{-6}$ μm^2/hour is smaller than that reported for parabolic rate constant for C face (0.010 μm^2/hour) and Si face (1.9$\times 10^{-4}$ μm^2/hour) oxidation of 4H-SiC at 1100°C in dry oxygen [165]. Similarly, the linear rate constant B/A, (0.003±0.009) μm/hour, for D-Por-SiC is smaller compared to the reported 0.11 μm for C face and 0.029 μm for Si face at 1100°C. Both results indicate that D-Por-SiC is highly resistive towards oxidation compared to the 4H-SiC bulk. The general relationship for the thermal oxidation of D-Por-SiC according to the linear-parabolic relationship by Deal and Grove can be expressed as,

$$x_o{}^2 + 7.9\times10^{-4}x_o = 2.7\times10^{-6}\ (\mathrm{t} + 4.5) \tag{5.4}$$

The calculated oxide thickness with respect to oxidation time, based on equation 5.4 is shown in Fig. 5.8(c). As discussed, the Deal-Grove model can well describe the oxide growth, particularly for longer oxidation times, as exhibited by the agreement within the experimental error, between the calculated oxide thickness with experimental data throughout the 9 hour oxidation period. In this work, the oxide thickness on the pore wall after 1 hour oxidation at 1100°C is approximately 3.3 nm. As the data for the oxidation of nanostructures in 4H-SiC is lacking, 3C-SiC is compared. The growth rate is slower in comparison to 15 nm obtained for 3C-SiC whiskers (diameters 100-140 nm) oxidised for 1 hour at 1100°C [173]. Reasons for the discrepancy may be related to the different surface morphology of the porous structure studied here in contrast to free-standing SiC nanowires and the existence of an amorphous layer on the surface of D-Por-SiC, which is absent for the SiC nanowires. The nature of the porous network and existing amorphous surface layer in D-Por-SiC may have reduced the in-diffusion of oxygen and out-diffusion of CO resulting in a slower oxidation rate. The conformity of the experimental oxide thickness trend with the conventional Deal-Grove model in Fig. 5.8(c) supports the hypotheses that diffusion through the SiO_2 is the rate limiting step.

The projected oxide thickness based on equation 5.4 is used to predict the thickness of the pore wall beyond the experimental 9 hours of oxidation, as shown by the data in Fig. 5.9. Experimentally, majority of the pore wall thickness reduction occurred during the first hour, where the thinning rate was 6.7 nm/hour (not predicted by Deal-Grove in this regime) which then reduced over time. Over the first 3 hour period the thinning rate reduced to an average of 3 nm/hour. The rate further reduced to approximately 1.2 nm/hour over the 9 hour period. It is projected to within the experimental error that the pore wall thickness would reduce to 13.3 nm after 15 hours of oxidation. More experiments for longer times are required for prediction beyond 15 hours.

The trend suggest a retarded oxidation for prolonged oxidations times. Retarded oxidaton and self-limited oxidation has been observed for Si nanowires, where the thinning of the Si core [174, 175] is dependent upon the curvature which increases

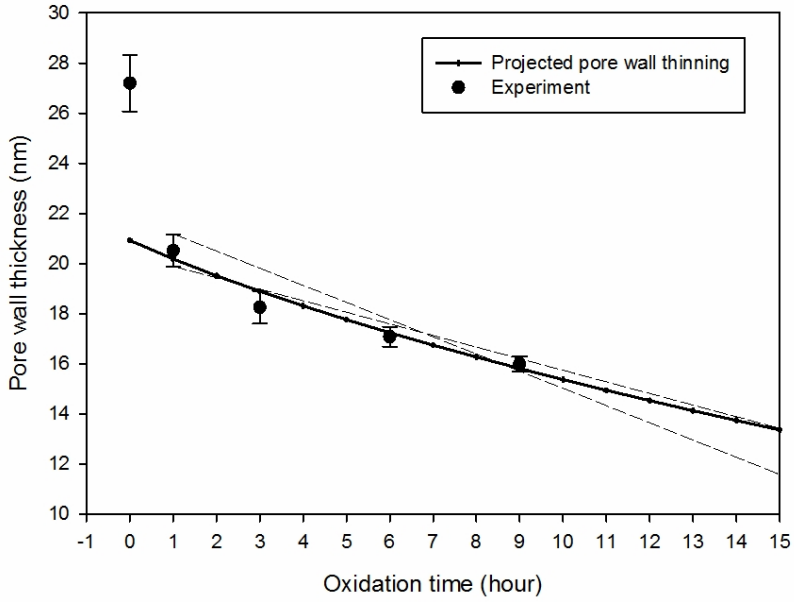

Figure 5.9: Projected pore wall thinning of D-Por-SiC by thermal oxidation, based on the removed oxide calculated from equation 5.4. The error bars represent the standard error of the data (N=20).

with reduced diameters and oxidation temperature. The data in Fig. 5.10 show the reduction in the Si nanowire core size with respect to oxidation time from a diameter of 30 nm at oxidation temperatures of 800°C and 850°C respectively [174]. The data points represent the experimental data, whilst the solid lines are predicted using a modified Deal-Grove model [174, 176]. The modified Deal-Grove model incorporated a cylindrical model with a finite reactive region sandwiched in between the outer SiO_2 and the Si nanowire core underneath. The finite reactive region represents a suboxide layer which is thought to be highly compressive and impedes the oxidation process. The smaller the nanowire, the larger the curvature resulting in an increased compressive stress within the suboxide layer. Thus, a reduced oxidation rate results. The model describes the diffusivity of the oxidant as decaying exponentially within the finite reactive region.

In this work the pore wall thinning of D-Por-SiC is retarded, but does not exhibit the self-limiting trend within the investigated oxidation duration or projection using the Deal-Grove model. It is highly likely that as the pore wall is not cylindrical in shape like the nanowire and exists as part of a larger porous network, that stress generated

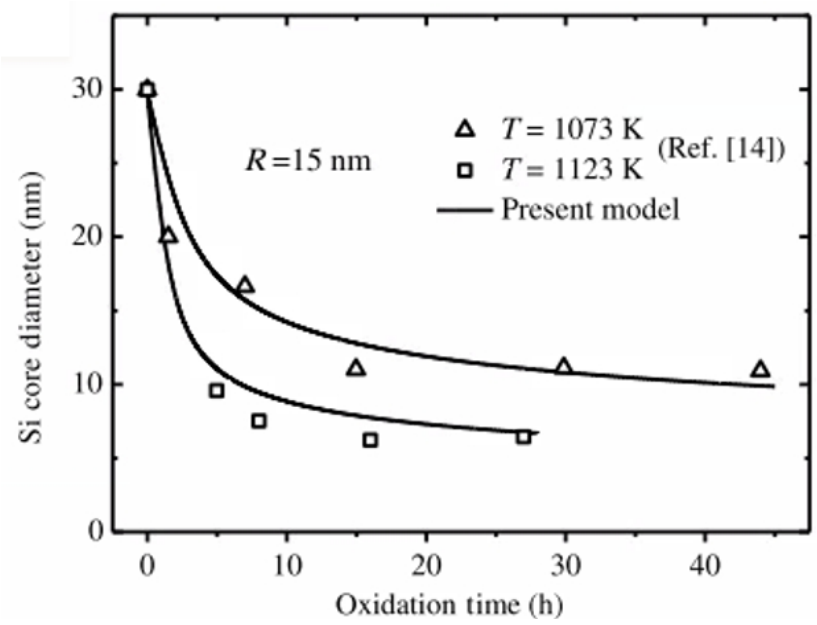

Figure 5.10: Experimental and theoretical data on the thinning of Si nanowire core size with respect to oxidation time from a diameter of 30 nm at oxidation temperatures 800°C and 850°C, exhibiting self-limited oxidation .

during the oxidation is relieved over a larger area, as can be observed from the slight deformation of D-Por-SiC shown in Fig. 5.4. Additionally, for SiC nanowires, it was reported that a 100 nm diameter nanowire can be fully oxidised within 12 hours at 1200°C [173] whilst in [177], 20-70 nm diameter SiC nanowires were fully oxidised at 1000°C within 2 hours. Though the different process conditions and experimental setups may have resulted in different oxidation rates, the results suggest that self-limited oxidation due to stress effects do not affect SiC nanowires as it does for Si nanowires. The retarded oxidation rate of D-Por-SiC in comparison to bulk 4H-SiC and SiC nanowires is likely to be related to the pre-existing surface amorphous layer (silicon oxycarbide and SiO_2 as identified in XPS spectra) the formation of which was dependent on the etch conditions. This condition poses a likely diffusion limited oxidation for D-Por-SiC. Hence, the calculated and projected pore wall thickness shown in Fig. 5.9 may serve as a guide to thin down the dimensions of as-prepared D-Por-SiC by way of thermal oxidation and subsequent HF etch.

5.2.3 Optical Characterisation of Pore Wall Thinned Mesoporous 4H-SiC

Following the pore wall thinning treatment, D-Por-SiC was characterised by Raman scattering spectroscopy to observe effects in terms of the LO peak red-shift and asymmetric broadening to lower wavenumbers. Thereafter, the D-Por-SiC film was sonicated for 30 minutes and dispersed in ethanol, prior to characterisation by photoluminescence (PL) and photoluminescence excitation (PLE), to observe for potential blue-shift in emission and absorption.

5.2.3.1 Raman Scattering

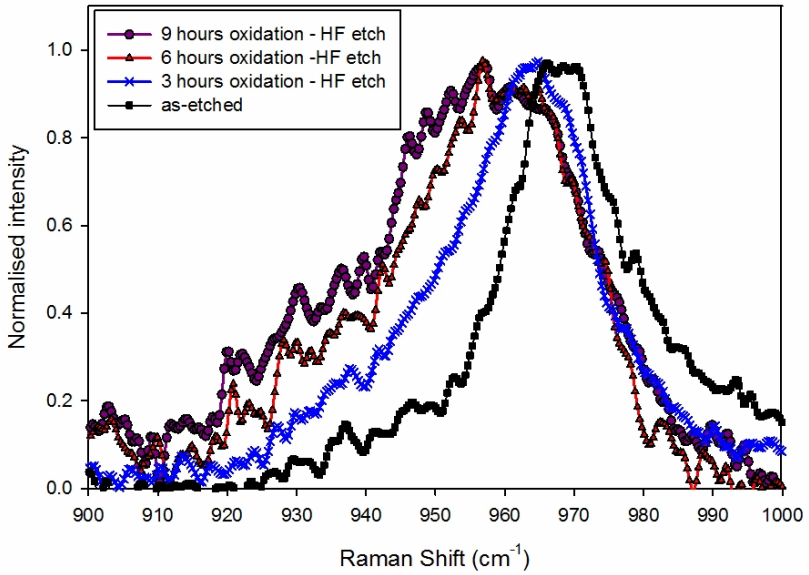

Figure 5.11: Raman spectra for D-Por-SiC oxidised for 3, 6 and 9 hours at 1100°C and HF/ethanol dipped for 5 minutes.

The data in Fig. 5.11 show the Raman spectra of the LO mode, for D-Por-SiC after pore wall thinning treatment for 3, 6 and 9 hour oxidation at 1100°C. The effect of pore wall thinning on the Raman spectra is evident in the LO mode. With the increase in oxidation time, the LO mode peak frequency becomes red-shifted and was accompanied by an asymmetric lineshape broadening to lower wavenumbers. The as-etched LO mode showed a peak frequency at 968 cm^{-1} which is red-shifted by approximately 12 cm^{-1} from the bulk (980.3 cm^{-1}). This red-shift, being relatively large was likely due to free carrier depletion (from 5×10^{18} cm^{-3} to 3×10^{18} cm^{-3}

[90]) at the surface of the porous structures as discussed in section 4.3.1. After 3 hours of oxidation, the peak was further red-shifted by 2 cm^{-1} from 968 cm^{-1} to 966 cm^{-1} (from 3×10^{18} cm^{-3} to 1×10^{18} cm^{-3}) and additionally, the LO mode lineshape asymmetrically broadened to the lower frequency side. The spectra for both 6 and 9 hours of oxidation showed a similar red-shift in the peak position, by another 2 cm^{-1} from 966 cm^{-1} to 964 cm^{-1} (indicating a doping reduction from 1×10^{18} cm^{-3} to 9×10^{17} cm^{-3}). 9 hour data exhibit a similar red-shift in the peak position coupled with slightly larger asymmetric broadening. An alternative explanation for the red-shift is that the overall size reduction with increasing oxidation time could be generating smaller structures within the porous layer resulting in phonon confinement (quantum size effects) to occur.

The origins of the LO mode asymmetric broadening at lower wavenumbers may arise from surface modes and/or transitions of confined phonons with $\Delta q \neq 0$. Surface modes which are also known as Fröhlich modes, appear in polar semiconductors for particles with dimensions lower than the wavelength of the exciting laser light inside the particle. In this work, the wavelength of the exciting beam was 514.5 nm. Fröhlich modes have been observed in porous GaAs and GaN structures with diameters of 60 nm and 50 nm respectively [178]. Phonon confinement on the other hand arise from quantum size effects and relaxation of selection rules due to the breaking of the translational symmetry of the periodic lattice. The size scales for the latter effect are close to the Bohr diameter. The broadening observed for porous Si, whilst initially debated, has been accepted to be due to quantum confinement as deduced from the phonon confinement model (PCM) [151]. Thus, for polar semiconductors, depending on the distribution of sizes, there may be mixed contributions from surface modes and confined phonons giving rise to the observed frequencies between the TO and LO peaks. Fröhlich modes have been widely reported as the dominant feature in the asymmetric broadening of the LO lineshape for porous polar semiconductors such as InP [178] and SiC [27] that were prepared by electrochemical etching. The average dimensions of 16-27 nm verified by cross-sectional SEM in this work support the hypotheses that Fröhlich modes are the primary contributor to the broadening observed in the LO lineshape rather than quantum confinement.

In terms of the red-shift in the LO peak frequency, free carrier depletion has been

observed in porous InP prepared by anodic electrochemical etching [178]. The free carrier concentration was found to decrease as the wall thickness of the semiconducting skeleton decreases. The charge carrier concentration profile across the wall between two pores was calculated as shown in Fig. 5.12 [178]. The surface of the porous walls are depleted as depicted by the vertical dashed lines, which form the boundaries of the surface depletion layer. As the pore wall thickness decreases, from 100 nm to 30 nm, the mean carrier concentration depicted by the gaussian curve reduces accordingly, as the effective area of the depletion layer within the wall increases. When the wall thickness is sufficiently small, the wall may become fully depleted as the depletion layers from the opposing sides intersect. In relation to this work, the free carrier depletion effect is in qualitative agreement with the observed red-shifting of the LO peak position, commensurate with the reducing pore wall thickness as measured using cross sectional SEM imaging.

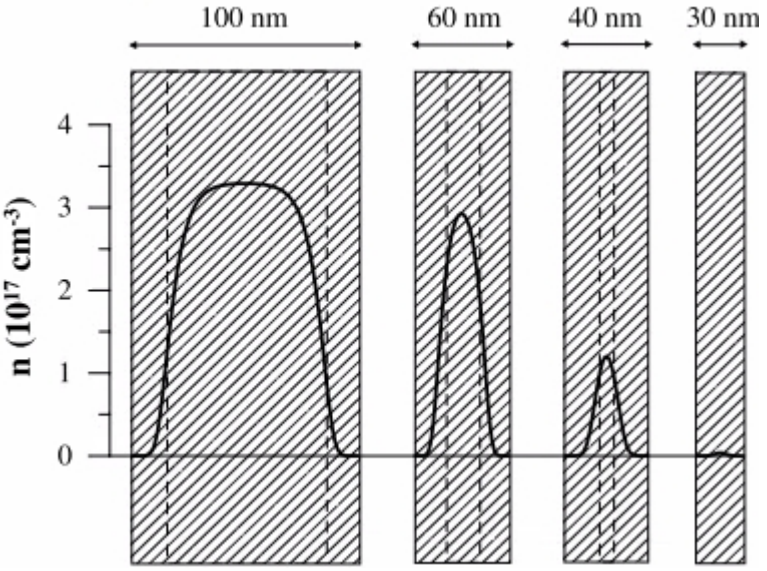

Figure 5.12: Calculated charge carrier concentration profile across the wall between two pores for porous InP. Dashed lines indicate depletion region at the wall's surfaces

.

The data in Fig. 5.13 show the trends for the peak position in frequency and full width at half of maximum (FWHM) of the LO mode for bulk and D-Por-SiC oxidised for different durations. The n-type 4H-SiC bulk was highly doped and therefore the LO phonons were highly coupled to the free carriers, resulting in a peak at a large wavenumber of 980.3 cm^{-1}. The correspondingly large FWHM of 36.5 cm^{-1}

for the bulk was due to asymmetric broadening to higher wavenumbers which is a characteristic of high doping effects [90]. After the electrochemical etch process, the as-etched D-Por-SiC exhibited a significant red-shift in the LO mode peak and reduction in the FWHM due to free carrier depletion in the surface of the newly formed columnar walls. At this point the behaviour of the peak broadening changed from the higher wavenumber side of the peak after the short duration oxidation towards the lower wavenumbers, related to Fröhlich modes. With subsequent pore wall thinning via thermal oxidation, the LO mode peak position continues to drop as the mean carrier concentration reduces until saturating at approximately 964 cm^{-1}. With longer oxidation times the peak FWHM increases significantly due to the stronger asymmetric broadening towards lower wavenumbers, from as-etched at 20.8 cm^{-1}, to 23.3 cm^{-1}, 32.9 cm^{-1} and 37.3 cm^{-1} for 3, 6 and 9 hours respectively. The significant increase in broadening for oxidation times beyond 6 hours indicates that further reduction in dimension or increase in disorder in the crystal was enhancing the Fröhlich modes and possibly phonon confinement respectively. For the Fröhlich modes, the shape of the pore walls may enhance these surface modes as the aspect ratio (length-to-width) increases with decreasing pore wall thickness, resulting in the appearance of modes in between the TO and LO peaks [106]. As for the phonon confinement case, at nanometric length scales within a mesoporous structure, there are possibilities in breakage in the translational symmetry of the crystal that may enhance phonon confinement and broadening of the LO mode peak [51, 52, 92].

The effective surface depletion region increases when the columnar wall dimensions are reduced. Thus, reduction in mean carrier concentration correlate with reducing columnar pore wall dimensions. The observed red-shift in the LO mode peak following oxidation and HF dip in this work strongly suggest that the mean carrier concentration reduced as a result of further reduction in the pore wall dimensions. Furthermore, the enhanced Fröhlich modes-related asymmetric broadening to lower wavenumbers resulted in the significant increase of the peak FWHM, as a function of oxidation time. The red-shift and asymmetric broadening to low wavenumbers of the LO mode both support the hypotheses that the oxidation and HF dip processes further reduce the pore wall dimensions. The pore wall thinning via thermal oxidation and oxide removal is a viable post-treatment for anodic electrochemical etching and nanostructuring of

4H-SiC.

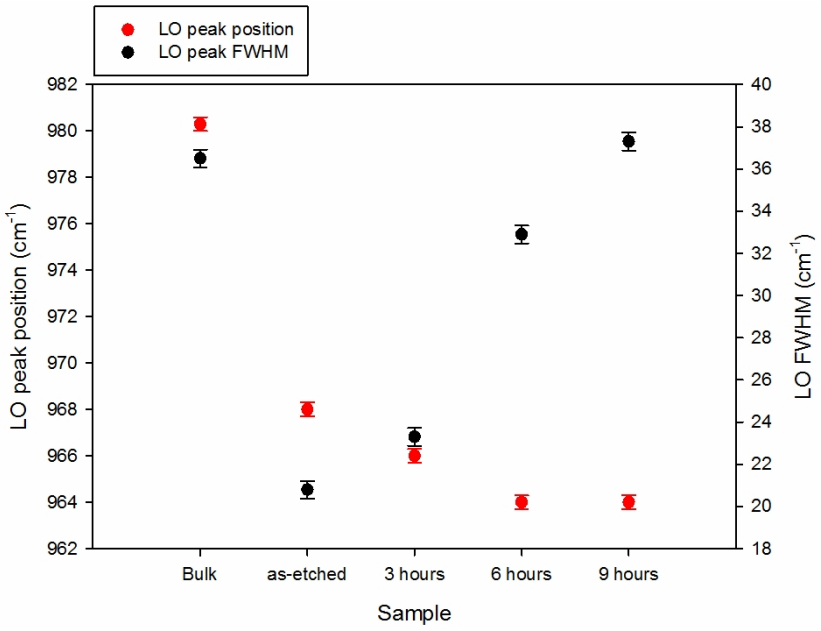

Figure 5.13: Trends in the LO mode peak position and the respective full width at half maximum (FWHM) for the conditions studied. The error bar is based on the spectral resolution of the Raman spectrometer.

5.2.3.2 Photoluminescence and Photoluminescence Excitation Spectroscopy

According to quantum confinement theory, the energy gap widens with decreasing size for length scales near to the Bohr diameter of the semiconductor [11]. Provided that the surface chemistry or surface defects do not introduce states within the bulk bandgap that may obscure the size dependent properties [157], the effects of quantum confinement may be observed in the blue-shift in energy (reduced wavelength) of its photoluminescence (PL) spectra. The absorption process that results in the radiative recombination shown by the PL may be inferred from the photoluminescence excitation spectra (PLE).

In this work, after pore wall thinning which comprised of 9 hours of thermal oxidation and 5 minutes HF/ethanol dip for oxide removal, the D-Por-SiC was sonicated for 30 minutes and dispersed in ethanol (forming S-Por-SiC). For comparison, S-Por-SiC with pore wall thinning is referred to as S-Por-SiC-PWT whilst without pore wall thinning is referred to as S-Por-SiC. The PL spectra for S-Por-SiC-PWT and S-Por-SiC are shown by the data in Figs. 5.14(a) and (b) respectively. Two significant

differences can be observed in the PL spectra. Firstly, for excitation wavelengths from 220 nm to 360 nm, two distinct PL emission bands can be observed for S-Por-SiC (Fig. 5.14(b)) consisting of above (emission band (i)) and below bulk bandgap emission (emission band (iii)). In contrast, only one emission band is observed for S-Por-SiC-PWT (Fig. 5.14(a)), which originates from above bulk bandgap transitions. The removal of the sub bandgap emission band from the PL spectra is significant in this work as it indicates that surface states in the energy gap have been suppressed. As sacrificial oxidation only consumes the top surface of the porous layer, the removal of the sub bandgap emission confirms the hypothesis that it originates at the surface rather than in the bulk (polytype). It also suggests that sacrificial oxidation is a highly promising route to address the dual-feature PL and sub bandgap emission in 4H-SiC nanostructures.

The emission intensity for S-Por-SiC-PWT is significantly reduced in comparison to that shown in Fig. 5.14(b) and so the sharp Raman scattering peaks of ethanol can be observed in the spectra (marked with asterisks). The Raman peaks of ethanol shifted systematically with a Stokes shift of approximately 20-30 nm from the excitation wavelength.

The blue-shifted, above bulk bandgap emission for S-Por-SiC-PWT is centred around 325 nm (3.8 eV) with FWHM of approximately 100 nm. For S-Por-SiC the above bulk bandgap emission was centred at 303 nm (4.0 eV) with FWHM of approximately 50 nm. This indicates that the S-Por-SiC sample contained small crystallites that are restricted in size distribution resulting in the narrow peak, most likely originating from the edges of the pore walls observed in TEM images in section 4.3.1. In contrast, the S-Por-SiC-PWT contained particles with a wider distribution of sizes, resulting in the larger FWHM. The data indicate that the particles in the S-Por-SiC-PWT sample lie within the desirable and targeted size range, being small enough for quantum confinement effects to occur, as evidenced by the blue-shifted, above bandgap emissions. The S-Por-SiC-PWT spectra share a similarity with those from the S-Por-SiC, in that the above gap PL peaks did not red-shift with increasing excitation wavelengths, indicating excitation wavelength-independent emissions that originate from a defect/surface state outside of the bulk energy gap. This is depicted as region A in Fig. 5.15. The formation of these defects has been previously associated with

(a)

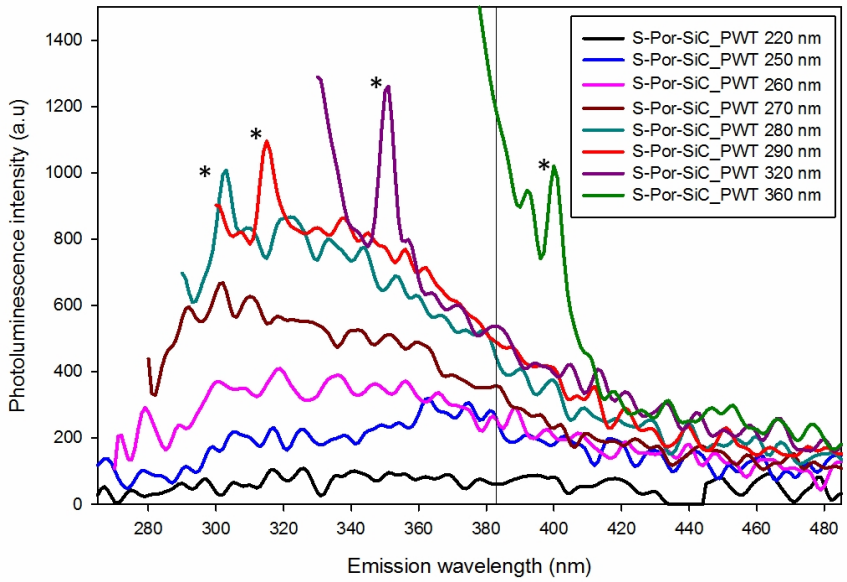

(b)

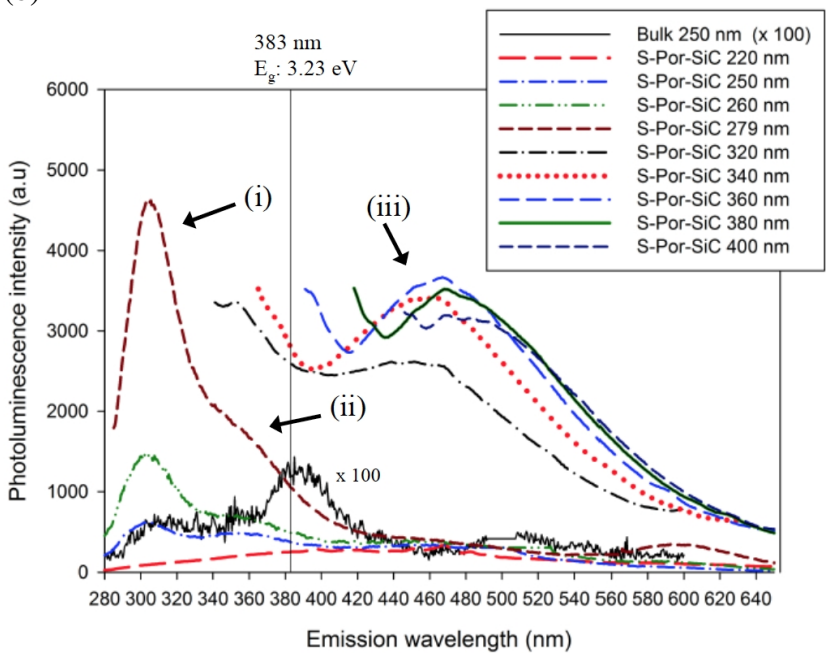

Figure 5.14: PL spectra of S-Por-SiC dispersed in ethanol with different excitation wavelengths (a) with pore wall thinning (PWT) and (b) without pore wall thinning. Vertical dashed lines indicate 4H-SiC bulk bandgap. As a result of sacrificial oxidation in the PWT procedure, the below bandgap emssion near 450-460 nm is removed in (a) in comparison to without pore wall thinning in (b).

-F termination of the surface originating from the used HF during etch process, as outlined in section 4.3.6.

The absorption process that lead to the observed PL spectra for S-Por-SiC-PWT can be inferred from the PLE data shown in Fig. 5.16(a). The excitation wavelength was varied whilst monitoring at fixed emission wavelengths of 310 nm, 340 nm and 360 nm. All three emission wavelengths of S-Por-SiC-PWT share a common absorption band centred at approximately 290 nm (4.28 eV). This absorption band is close to the 280 nm (4.42 eV) absorption band denoted by (i) in Fig. 5.16(b) that gave rise to above bandgap emission peak (i) at approximately 303 nm in Fig. 5.14(b)) for S-Por-SiC. The sharp peaks (marked with asterisks) in Fig. 5.16(a) which appear near the monitored emission wavelengths, are due to Raman scattering from ethanol that are red-shifted by approximately 20-30 nm from the excitation wavelengths. It is evident that after the pore wall thinning treatment, the sub bandgap emission centred at 455 nm (iii) in Fig. 5.14(b), associated with the absorption band (iii) centred at 353 nm (Fig. 5.16(b)) has been suppressed. The suppression may be due to removal or passivation of the defects located within the bandgap depicted as the horizontal dotted red line in Fig. 5.15.

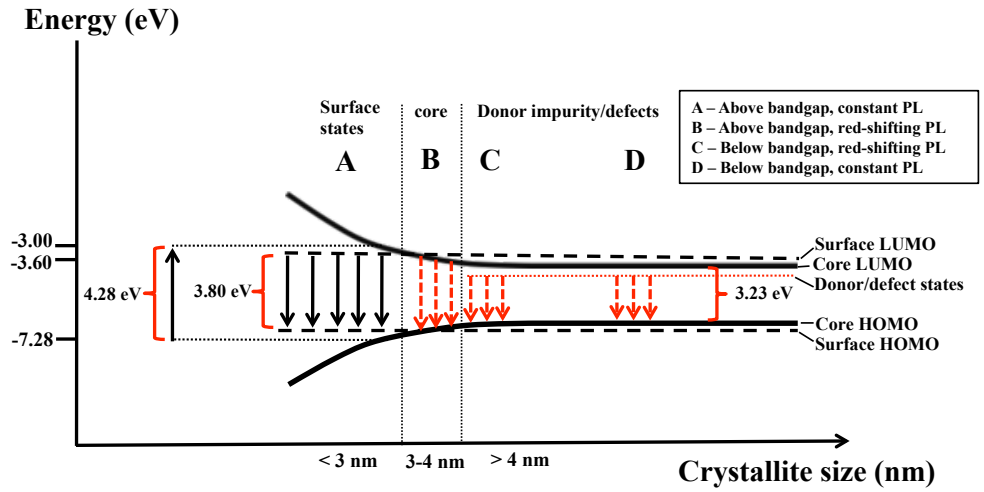

Figure 5.15: Removal or passivation of within energy gap defect state (dotted horizontal red line) after the pore wall thinning treatment.

It is very likely that the removal or passivation of the defect states within the bandgap occurred during thermal oxidation. In section 4.3.6, these states were ascribed to oxygen related defects in C=O/COOH bonds [34], N doping [28] or possibly the $Z_{1/2}$ defect centre [146] as potential contributors. It is also noted that an amorphous layer at the surface formed during the etch process as observed in the TEM images in

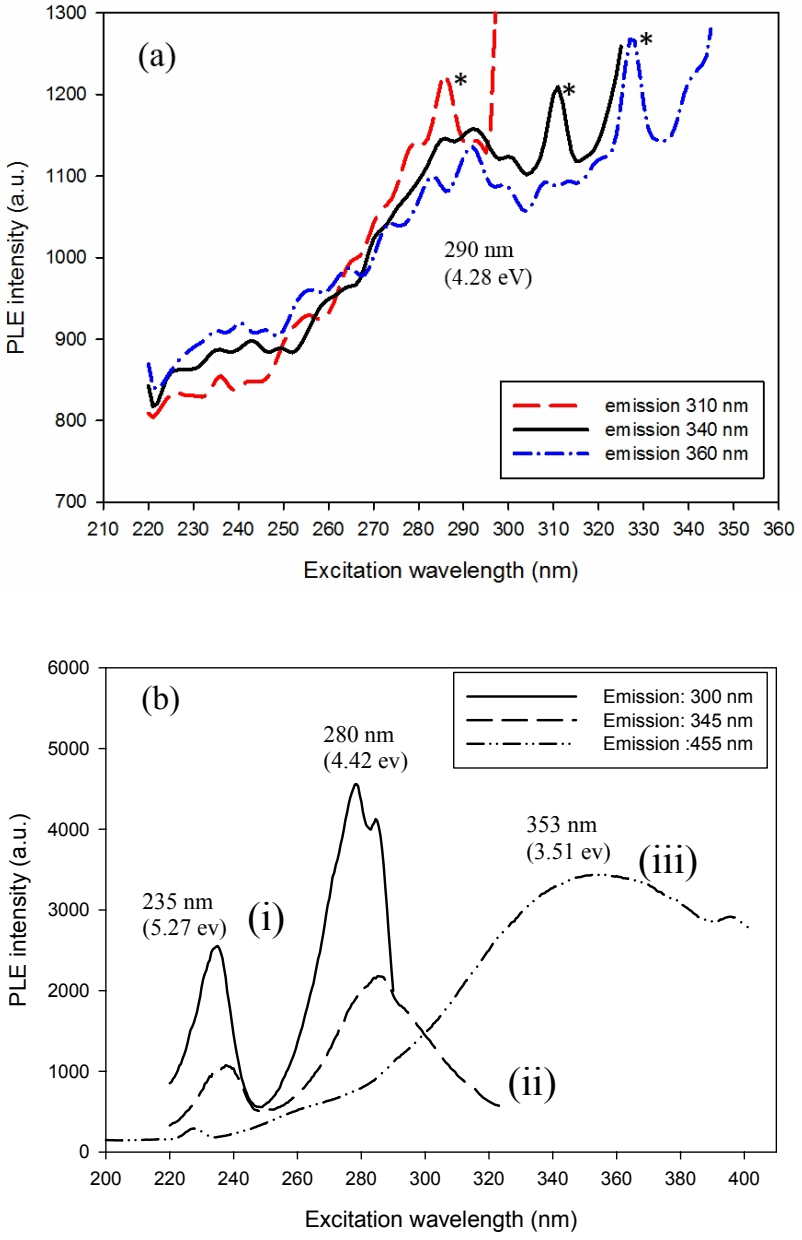

Figure 5.16: Photoluminescence excitation spectra for (a) S-Por-SiC-PWT and (b) S-Por-SiC to probe the absorption transition corresponding to the selected emission wavelengths.

Fig. 4.8(d) may contain defects that would have been removed in the sacrificial oxide during the pore wall thinning treatment. Surface passivation by thermal oxidation has been reported in [179], as shown by the data in Fig. 5.17, where the characteristics of 3C-SiC nanopowder prepared by electrochemical etching shows almost complete passivation of the sub bandgap states upon oxidation. A blue-shifted and reduced

emission intensity was observed in the data in [179], which was attributed to quantum confinement (resulting from the SiC core) and contribution from the grown oxide was ruled out, as the PL spectra were similar after the oxide removal. As for the reduced emission intensity, it was reasoned that the oxidation process may have also introduced non-radiative recombination channels, resulting in a reduction in PL intensity.

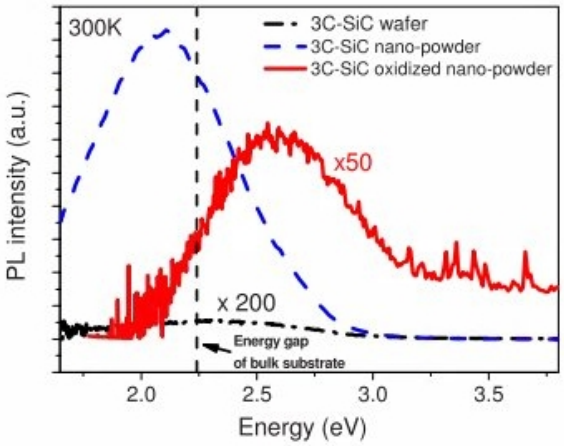

Figure 5.17: PL spectra of dry as-prepared 3C-SiC nanopowder and oxidised nanopowder .

Previous studies of PL on porous SiC substrates [180] showed that, despite the difference in bulk bandgaps, almost identical PL spectra for several SiC polytypes were obtained, that were centred at 2.5 eV (496 nm), as shown by the data in Fig. 5.18(a). It was suggested that the origin of the PL was related to defect states located at the etched surface. Recent work [7] with 4H-SiC quantum dots (dissolved in water) derived from sonicated, electrochemically etched 4H-SiC substrates showed sub bandgap emission centred near 450 nm (2.75 eV) as shown in Fig. 5.18(b). The PLE associated with this emission exhibited similar absorption centre at 365 nm for 3C, 6H and 4H-SiC polytypes, as shown by the data in Fig. 5.18(c) and was attributed to polytype transformation from 6H and 4H into 3C during the sonication process. Previous study [153] has shown that high temperatures in excess of 800°C and highly doped n-type ($\sim 10^{17}$ to 10^{19} cm^{-3}) are required to cause stacking faults or polytype transformation. This indicates that polytypic transformation require a large amount of energy.

In this work, x-ray diffraction (XRD) analysis did not show evidence of a polytypic transformation upon sonication. In section 4.3.5, the XRD data for ground S-Por-

SiC in Fig. 4.17, exhibit peaks near 2θ Bragg angle of 33°, 35°, 36° and 38° which correspond to the $(10\bar{1}0)$, $(10\bar{1}1)$, (0004) and $(10\bar{1}2)$ planes of 4H-SiC. Though the XRD peak for (111) plane for 3C-SiC overlap with the (0004) plane for 4H-SiC near 2θ Bragg angle of 36°, the rest of the peaks are not related to 3C-SiC. Additionally, the interplanar spacing of 0.267 nm for S-Por-SiC as measured from the transmission electron microscopy (TEM) imaging (Fig. 4.8 (d)) is associated with the $(10\bar{1}0)$ plane of 4H-SiC. The XRD patterns for before and after ultrasonication were consistent, indicating that polytypic transformation did not occur in this work [25]. It is suggested then that the sub bandgap emission centred around ∼450 nm that are widely reported in the literature [7, 17, 21, 24] and this work is the result of defects at the etched surface.

The removal of a known defect centre in bulk 4H-SiC by thermal oxidation has been reported previously [181], where the concentration of the $Z_{1/2}$ defect located at E_C-0.65 eV was studied by deep level transient spectroscopy (DLTS) and found to be reduced after thermal oxidation at 1150-1300°C. The $Z_{1/2}$ defect ascribed to C vacancy was said to be reduced during oxidation as C generated at SiO_2-SiC interface forms interstitials that then diffuse into the bulk before recombining with C vacancies.

Surface defects and surface passivation have been critical factors in determining the optical properties of semiconductor nanostrucures. II-VI compound semiconductors and Si based nanostructures are sensitive to oxidation in the ambient air and aqueous environment. Various approaches such as surface capping with a larger bandgap material or organic ligands have been employed [182, 183]. Although SiC is renowned as oxidation resistant and photostable in comparison to other semiconductors, the optical properties are still affected by surface termination or surface defects. These defects introduces states within the energy gap and obscures quantum confinement effects as discussed in section 3.3.3. The sub bandgap emission in 4H-SiC QDs and 'dual-feature' in the reported PL spectra of SiC QDs are highly likely linked to surface states. These common observations indicate possible surface defects forming during the electrochemical etch process. In this work, the pore wall thinning by oxidation and subsequent oxide removal in HF dip offer two advantages. Firstly, a reduction in pore wall dimension of the mesoporous SiC was apparent from SEM imaging where average size reduction from 27 nm to 16 nm can be observed. Secondly, as can be observed from the PL spectra, the pore wall thinning process resulted in sub bandgap emission

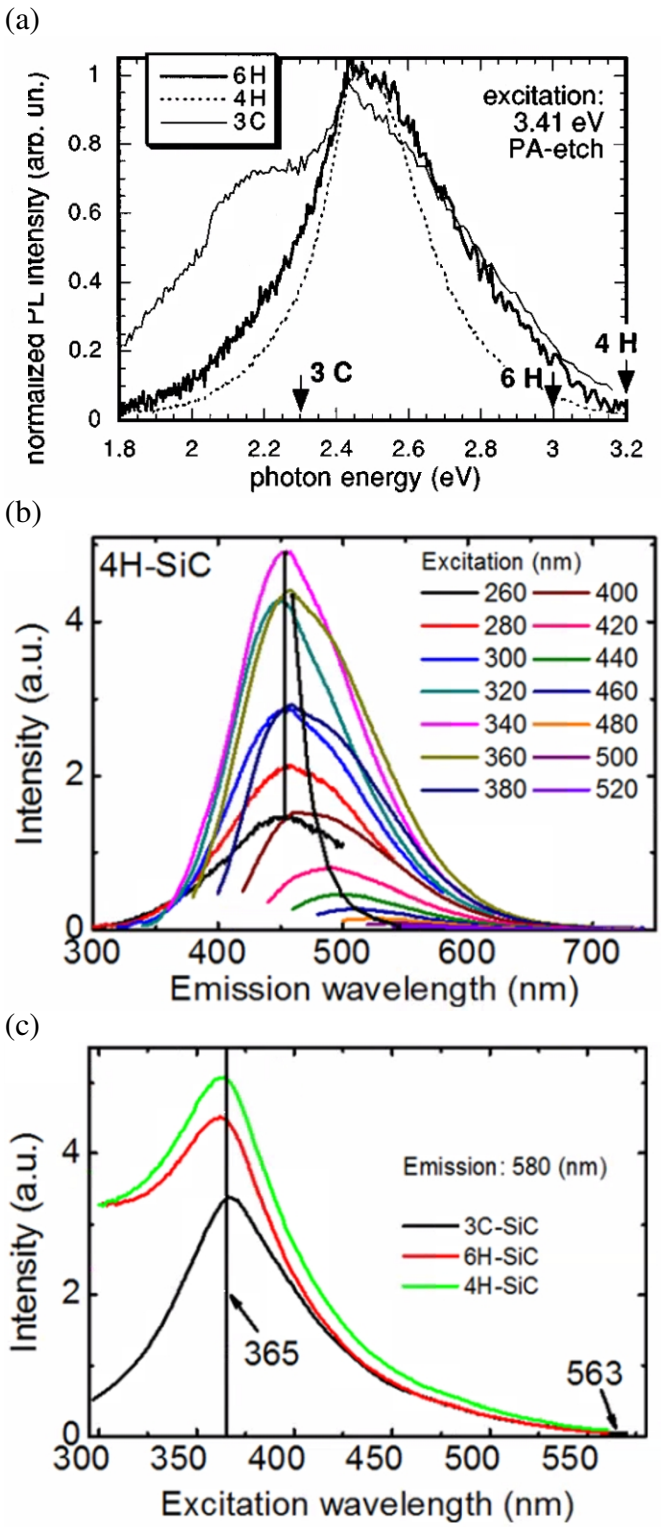

Figure 5.18: (a) Reported PL spectra that are almost identical for porous SiC substrates of different polytypes centred at 2.5 eV (496 nm) , (b) 4H-SiC quantum dots dispersed in water showing sub bandgap PL emission centred near 450 nm and (c) PLE showing similar absorption centre at 365 nm for 3C, 6H and 4H-SiC .

suppression, allowing for UV emission to dominate and better conforming to the expected quantum confinement effects. Data indicating defect removal [181], surface passivation [180], and blue-shift in the PL spectra [179], upon thermal oxidation of SiC has been reported. To date the process has not been incorporated as part of the nanostructuring of SiC after etch for further size reduction. The pore wall thinning technique by thermal oxidation has been applied for porous Si [158] but yet to be fully exploited for porous SiC. It is proposed herein, that further size reduction can be achieved and the sub bandgap emission can be suppressed, in etched SiC nanostructures by a post-etch pore wall thinning treatment by thermal oxidation.

5.3 Conclusions

In this work, nanostructuring of bulk 4H-SiC by a top-down electrochemical etch at 20V bias was employed, resulting in mesoporous 4H-SiC (D-Por-SiC) with nanocolumnar walls. The average interpore width was 27.1$\pm$5.0 nm as verified by cross-sectional SEM. Direct sonication of this material and subsequent dispersion in ethanol produces S-Por-SiC with dimensions ranging from 16.9$\pm$5.5 nm to 2.9$\pm$1.0 nm as verified by TEM images and described in section 4.3.1. The resulting PL exhibited two main emission bands, one being above bulk bandgap (303 nm) and was independent of excitation wavelength whilst the other was sub bandgap (455 nm) and showed a distinct dependence on excitation wavelength.

A pore wall thinning technique was undertaken in order to further reduce the dimensions of as-etched D-Por-SiC. The treatment consisted of thermal oxidation at 1100°C, in a flow of 100 sccm O_2 for durations of 1, 3, 6 and 9 hours followed by subsequent oxide removal in a 5 minutes HF/ethanol dip, to produce D-Por-SiC-PWT. Cross sectional SEM analysis showed reductions in average pore wall thickness to 20.5$\pm$2.8 nm, 18.2$\pm$2.9 nm, 17.0$\pm$1.8 nm and 15.9$\pm$1.4 nm for 1, 3, 6 and 9 hours respectively. The corresponding average oxide thickness on the pore wall was analysed using the conventional Deal-Grove model and it was found that oxidation of D-Por-SiC was retarded, most likely due to a pre-existing amorphous layer of approximately 1 nm in thickness comprising of silicon oxycarbide and SiO_2. This layer could be observed in the XPS characteristics and TEM imaging, which is attributed to the electrochemical

etch process. In order to further reduce dimensions to below 13 nm, an oxidation time exceeding 15 hours is expected, based on the extrapolation of the experimental data.

Raman scattering of pore wall thinned D-Por-SiC-PWT (9 hours) showed (in comparison to as-etched D-Por-SiC), a significant red-shift of the LO mode peak frequency (from 968 to 964 cm^{-1}) and enhanced asymmetric broadening to lower wavenumbers (FWHM from 20.8 to 37.3 cm^{-1}) due to free carrier depletion in the former and to increased contribution from Fröhlich modes in the latter. The observed trends in these optical measurements indicate size reduction at the nanometric length scales with increase in oxidation time. The trends are in qualitative agreement with the thinning of the pore walls when oxidation time was increased, as observed in the SEM images.

D-Por-SiC-PWT was subsequently sonicated for 30 minutes and dispersed in ethanol producing S-Por-SiC-PWT. PL spectra of S-Por-SiC-PWT exhibited an emission band that was blue-shifted, above bandgap and centred at 325 nm (3.82 eV). This emission band is independent of the excitation wavelength, indicative of surface state related energy levels that are not located within the bulk bandgap. The associated absorption for this 325 nm emission was centred at 290 nm (4.28 eV). In contrast, the normally observed sub bandgap emission centred at 455 nm, associated with absorption centre at 353 nm in S-Por-SiC was suppressed in the oxidised sample. The suppression of this sub bandgap emission can be attributed to the removal or passivation of surface defects at the etched surface during thermal oxidation in the pore wall thinning treatment.

Finally, it is identified that electrochemically etched 4H-SiC in ethanoic HF is applicable to produce nanostructures emitting in the visible or UV wavelengths. S-Por-SiC (as-etched, without pore wall thinning), may find applications where emission in the visible with a distinct peak at $\sim$455 nm is required. The emission is excitation wavelength-dependent with absorption ranging from 320 to 400 nm. In contrast, for applications requiring UV emission, S-Por-SiC-PWT (after pore wall thinning by thermal oxidation) is extremely promising. Excitation in the range 270-300 nm would result in excitation wavelength-independent PL emission centred at $\sim$325 nm. In comparison to wide bandgap ZnO nanowires and nanorods, absorption in the UV range of 254 to 390 nm have been reported, whilst SnO_2 nanowires absorb at 325 nm

[184] which lies within the range shown by the mesoporous 4H-SiC in this work. The benefit afforded by the choice of either UV or visible emission by employing thermal oxidation or otherwise may pose porous SiC as a versatile material in wide ranging applications from non-toxic biomarkers to photodetectors.

Chapter 6

Conclusions and Future Research Suggestions

6.1 Conclusions

It is widely reported that SiC nanostructures of various polytypes: 3C-, 4H- and 6H-SiC exhibit dual-feature in the PL spectra. Secondly, these polytypes show similar PL emission with wavelength around 450 nm which is above bandgap for 3C-SiC but unexpectedly below bandgap for 4H-SiC and 6H-SiC. The dual-feature and below bandgap emissions are counterintuitive to quantum confinement and warrant further investigation. 4H-SiC is a suitable polytype to study these effects. The objectives of this study were to understand through density functional theory (DFT) simulation, the effect of surface chemistry on the optical properties of 4H-SiC QDs in the range of sizes relevant to experiment (deviation from quantum confinement for sizes less than 3 nm) and describe the origin of the dual-feature PL spectra; manufacture mesoporous 4H-SiC via anodic electrochemical etching and ultrasonication processes followed by structural and optical characterisations; and evaluate a new post etch treatment by sacrificial oxidation that resulted in pore wall thinning and surface removal of mesoporous 4H-SiC. In this thesis, a new model to explain the dual-feature PL as observed in the experiments has been presented. It was found that the interplay between both quantum confinement and surface states played a role to dictate the optical properties of 4H-SiC nanostructures as has been shown by the DFT simulations and verified in the experimental work for mesoporous 4H-SiC. The rarely reported above bandgap emissions for 4H-SiC nanostructure were identified in this work. Additionally, sacrificial oxidation that resulted in the reduction of the pore wall thickness and suppression of the below bandgap emission has been demonstrated. The removal of the below bandgap PL correspond to surface removal of defects during thermal oxidation and subsequent oxide etch. These findings strongly indicate that the dual-feature PL and below bandgap emission in 4H-SiC seen in experiments originate

from surface defects rather than from polytypic transformation or mixed polytypes within the core. DFT calculations and experimental evidence in this thesis form the basis of a model to explain the observed optical properties of 4H-SiC nanostructures.

Density functional calculations were performed for OH-, F- and H-terminated 4H-SiC, 10-20 Å diameter clusters. The selected surface termination species and size range relate to the chemistry involved using HF/ethanol electrolyte in SiC QD preparation and the reported deviation from quantum confinement for sizes smaller than 3 nm. H-termination resulted in a pronounced size-dependent quantum confinement in the absorption, whereas F- and OH-terminations exhibited much reduced size dependent absorption due to the higher number of surface states. Surface reconstruction and surface composition have impact but smaller than the choice of surface terminations (-OH, -F, -H). Surface states (surface HOMO/LUMO) were projected to dominate QDs with diameters less than 25 Å whilst the QD core atoms' related states (Core HOMO/LUMO) dominated the larger sized QDs (larger than $\sim$27 Å). The interplay between quantum confined core states and surface states have resulted in the dual-feature PL observed in experiments. This finding provides insight to experimental works in terms of the possibilities to tune the optical properties. If it is desired to have absorption over a wide wavelength range, surface states must be avoided so that quantum confinement effects dominate in SiC nanostructures particularly for 4H- and 6H-SiC. This analysis indicated that for SiC nanostructures, H-termination is favourable in order to preserve quantum confinement effects. If absorption and emission with wavelengths only weakly dependent on size is desirable, then the size independence of the absorption due to surface states (-OH, -F) may be exploited. A new model to explain the dual-feature PL as observed in the experiments was developed in chapter 3.

Mesoporous 4H-SiC was prepared by anodic electrochemical etching in ethanoic HF electrolyte. The average crystallite size inferred from Raman scattering spectroscopy and XRD was approximately 13 nm, whilst AFM imaging showed 40 nm. The discrepancy was most likely due to the lateral width broadening influenced by the AFM tip shape. After sonication and dispersion in ethanol, HRTEM imaging showed mesoporous structures with average pore diameter of (30.5$\pm$6.3) nm and average interpore spacings of (16.9$\pm$5.5) nm down to (2.9$\pm$1.0) nm. Dimensions below 3

nm was promising in supporting quantum confinement effects.

Analysis of the I-V characteristics without considering surface states showed that employing asymmetric metallisation (Ni-Al) may result in carrier injection by internal photoemission from metal contacts. Consideration of surface states in the back-to-back Schottky diode model showed that the barrier height for Ni in particular was lower than expected, indicative of influence from surface states at the Ni-por-SiC interface. Ionisation from surface states may have resulted in increased photocurrent by an order of magnitude. An increase of 5 to 6 orders of magnitude in photocurrent is required for applications in photodetectors.

PL and PLE measurements showed three PL bands: with absorption/emission centres of (i) 235/300 nm, (ii) 280/345 nm and (iii) 353/455 nm. The first two PL bands were above bandgap, rarely reported and strong indications of quantum confinement but were related to surface states as indicated by the independence on excitation wavelength. The third PL band was below bandgap and most likely to be impurity/defect related. Interestingly, the below bandgap PL emission peaks red-shifted with increasing excitation wavelengths, indicative of quantum confinement effects. Indeed, the below bandgap emission centred at 455 nm is in agreement with the commonly reported PL emission for SiC nanostructures, regardless of the polytype. The rarely reported above bandgap emissions centred at 300 nm and 345 nm in this work provided evidence that 4H-SiC nanostructure has the potential for quantum confined emission. A model was developed as a continuation from the findings in chapter 3 to explain this observation. The model suggest that the optical transitions between either of the core HOMO or LUMO with a defect related energy level within the bulk bandgap resulted in a red-shifting and below bandgap emission. As for the above bandgap and excitation wavelength-independent emissions, a defect or surface state outside the bulk bandgap dominate the effective HOMO-LUMO gap when the particle sizes are sufficiently small. The observed red-shifting and below bandgap emission was a result of the interplay between quantum confinement effects and surface states within the energy gap as depicted in the model in chapter 4.

Pore wall thinning and surface removal of the as-etched D-Por-SiC was performed by thermal oxidation in dry oxygen (flow rate of 100 sccm) at 1100°C for durations

of 1, 3, 6 and 9 hours followed by oxide removal in HF/ethanol. The pore wall thickness reduced from (27.1±5.0) nm for as-etched to (20.5±2.8) nm, (18.2±2.9) nm, (17.0±1.8) nm and (15.9±1.4) nm for the durations of 1, 3, 6 and 9 hours respectively. The oxide thickness was inferred from the reduced pore wall thicknesses and analysed using the conventional Deal-Grove model, which suggested a diffusion limited oxidation process. Raman scattering showed a significant red-shift in the LO mode peak position from 968 cm^{-1} for as-etched to 964 cm^{-1} for 9 hours oxidation indicating reduced mean carrier concentration of the porous layers. The LO mode peak red-shifts were accompanied by asymmetric broadening to the low frequency side, which exhibited an increased FWHM from 20.8 cm^{-1} to 37.3 cm^{-1}. The data from Raman scattering were in qualitative agreement with the trend in reducing dimensions shown by the data in SEM imaging and in support that pore wall thinning occurred during the oxidation process. The PL and PLE characterisation showed absorption/emission band centred at 290/325 nm which was above bandgap and not dependent on the excitation wavelengths. The usually observed below bandgap emission centred at 455 nm was removed and is a significant finding in this thesis as the evidence supports one of the hypotheses to explain the deviation from quantum confinement. The data strongly suggest that the 455 nm emission originated from the surface of the nanostructure in the form of defects (as shown in XPS data). Upon thermal oxidation and oxide removal in HF, the residuals or defects on the surface left by the anodic electrochemical etching would be removed together. The removal of surface defects suppresses the below bandgap emission at 455 nm allowing the above bandgap emission at 325 nm to dominate. The finding is in strong support of the hypothesis that the dual-feature and below bandgap emission that obscure quantum confinement in 4H-SiC originate from surface states rather than the mixed phases of polytypes resulting from ultrasonication.

The finding for 4H-SiC imply that a similar effect can be expected in other polytypes to demonstrate above bandgap emission as predicted by quantum confinement. Apart from H-termination to passivate the surface, an alternative route is to thermally oxidise and remove the oxide and defects to suppress surface states. For mesoporous 4H-SiC, emission in the blue (455 nm) can be accessed with excitation wavelengths in the range of 320 to 400 nm, whilst emission in the UV (300 and 345 nm) can be accessed

with excitation wavelengths from 230 to 300 nm. If it is desirable to suppress the below bandgap PL band centred at 455 nm, a thermal oxidation treatment followed by HF/ethanol dip after the electrochemical etching process is viable. The resulting emission would be centred at 325 nm and can be excited in the wavelength range of 260 to 320 nm.

6.2 Future Research Suggestions

Suppression of the PL emission centred at 455 nm by sacrificial oxidation is highly promising for application to other polytypes such as 6H-SiC. As the other polytypes have smaller bandgaps in comparison to 4H-SiC, their blue-shifted PL emission as a result of quantum confinement can be expected to overlap with emissions related to surface states within the energy gap, obscuring the quantum confinement effects. The current model serve as the basis to cater for other cases of surface terminations, defects and polytypes. With continuous refinements, the model may be used as a tool to understand and predict the optical properties of SiC nanostructures. In future sacrificial oxidations studies, the shift of the PL peak at 455 nm with oxidation time can be investigated by PL measurements taken between shorter time intervals, in order to identify the period at which the defects are eliminated. XPS measurements taken to monitor the changes in the spectra as oxidation progresses may reveal important information regarding the bonds that play the major role in this defect. Findings may be simulated with DFT for understanding at the molecular level. The sacrificial oxidation process may also be employed on SiC powders for comparative study.

For biomedical applications, 4H-SiC nanostructures can be employed as biomarkers capable of emission either in the UV (325 nm) or near 450 nm when required by manipulating the respective excitation wavelength range. With optimisations, nanostructured 4H-SiC may be applied in novel optoelectronic and engineering applications. The 4H-SiC nanostructured material can be incorporated on the surface of Si photovoltaic devices as a light down-shifting (LDS) layer to transform high-energy photons into lower-energy photons for the underlying Si to absorb. Additionally, nanostructured 4H-SiC may be employed in a metal-semiconductor-metal structure, having a low dark current, applicable for UV detection.

Bibliography

[1] P. Walter, E. Welcomme, P. Hallégot, N. J. Zaluzec, C. Deeb, J. Castaing, P. Veyssiére, R. Bréniaux, J.-L. Lévêque and G. Tsoucaris, *Nano Letters*, 2006, **6**, 2215–2219.

[2] A. I. Ekimov and A. A. Onushchenko, *Jetp Lett*, 1981, **34**, 345–349.

[3] A. L. Efros and A. L. Efros, *Soviet Physics Semiconductors-Ussr*, 1982, **16**, 772–775.

[4] R. Rossetti, J. L. Ellison, J. M. Gibson and L. E. Brus, *The Journal of Chemical Physics*, 1984, **80**, 4464–4469.

[5] X. Lan, S. Masala and E. H. Sargent, *Nat. Mater*, 2014, **13**, 233–240.

[6] H. T. Grahn, *Introduction To Semiconductor Physics*, World Scientific Publishing Co Inc, 1999.

[7] J. Fan, H. Li, J. Wang and M. Xiao, *Applied Physics Letters*, 2012, **101**, 131906.

[8] S. J. Rosenthal, J. McBride, S. J. Pennycook and L. C. Feldman, *Surface Science Reports*, 2007, **62**, 111–157.

[9] M. C. Roco, R. S. Williams and P. Alivisatos, *Nanotechnology Research Directions: IWGN Workshop Report: Vision for Nanotechnology in the Next Decade*, Springer Science Business Media, 2000.

[10] M. C. Roco, *Journal of Nanoparticle Research*, 2011, **13**, 427–445.

[11] G. Konstantatos and E. H. Sargent, *Colloidal Quantum Dot Optoelectronics and Photovoltaics*, Cambridge University Press, New York, 2013.

[12] A. M. Derfus, W. C. W. Chan and S. N. Bhatia, *Nano Letters*, 2004, **4**, 11–18.

[13] A. Shiohara, A. Hoshino, K. Hanaki, K. Suzuki and K. Yamamoto, *Microbiology and Immunology*, 2004, **48**, 669–675.

[14] J. Fan, H. Li, J. Jiang, L. K. Y. So, Y. W. Lam and P. K. Chu, *Small*, 2008, **4**, 1058–1062.

[15] J. Y. Fan, X. L. Wu, H. X. Li, H. W. Liu, G. G. Siu and P. K. Chu, *Applied Physics Letters*, 2006, **88**, 041909.

[16] M. E. Levinshtein, S. L. Rumyantsev and M. S. Shur, in *Silicon Carbide (SiC)*, John Wiley & Sons, 2001, book section 5, p. 96.

[17] X. Guo, D. Dai, B. Fan and J. Fan, *Applied Physics Letters*, 2014, **105**, 193110.

[18] J. Zhu, S. Hu, W. W. Xia, T. H. Li, L. Fan and H. T. Chen, *Materials Letters*, 2014, **132**, 210–213.

[19] D. Beke, T. Z. Jànosi, B. Somogyi, D. A. Major, Z. Szekrènyes, J. Erostyàk, K. Kamaràs and A. Gali, *The Journal of Physical Chemistry C*, 2015, **120**, 685–691.

[20] S. Yang, B. Kiraly, W. Y. Wang, S. Shang, B. Cao, H. Zeng, Y. Zhao, W. Li, Z.-K. Liu, W. Cai and T. J. Huang, *Advanced Materials*, 2012, **24**, 5598–5603.

[21] D. Dai, X. Guo and J. Fan, *Applied Physics Letters*, 2015, **106**, 053115.

[22] X. L. Wu, S. J. Xiong, J. Zhu, J. Wang, J. C. Shen and P. K. Chu, *Nano Letters*, 2009, **9**, 4053–4060.

[23] X. L. Wu, J. Y. Fan, T. Qiu, X. Yang, G. G. Siu and P. K. Chu, *Physical Review Letters*, 2005, **94**, 026102.

[24] D. Beke, Z. Szekrènyes, I. Balogh, Z. Czigàny, K. Kamaràs and A. Gali, *Nanoscale*, 2015, **7**, 10982–10988.

[25] M. Rashid, B. R. Horrocks, N. Healy, J. P. Goss and A. B. Horsfall, *Journal of Applied Physics*, 2016, **120**, 194303.

[26] X. Guo, X. Chen, B. Fan, Y. Zhang and J. Fan, *Applied Physics Letters*, 2016, **109**, 013104.

[27] T. L. Rittenhouse, P. W. Bohn, T. K. Hossain, I. Adesida, J. Lindesay and A. Marcus, *Journal of Applied Physics*, 2004, **95**, 490–496.

[28] J. Botsoa, J. M. Bluet, V. Lysenko, L. Sfaxi, Y. Zakharko, O. Marty and G. Guillot, *Physical Review B*, 2009, **80**, 155317.

[29] B. Xiao, X. L. Wu, W. Xu and P. K. Chu, *Applied Physics Letters*, 2012, **101**, 123110.

[30] J. Wang, S. J. Xiong, X. L. Wu, T. H. Li and P. K. Chu, *Nano Letters*, 2010, **10**, 1466–1471.

[31] X. H. Peng, S. K. Nayak, A. Alizadeh, K. K. Varanasi, N. Bhate, L. B. Rowland and S. K. Kumar, *Journal of Applied Physics*, 2007, **102**, 024304.

[32] M. Vörös, P. Deák, T. Frauenheim and A. Gali, *Applied Physics Letters*, 2010, **96**, 051909.

[33] A. Miranda and L. A. Prez, *Computational Materials Science*, 2016, **111**, 294–300.

[34] M. Vörös, P. Deák, T. Frauenheim and A. Gali, *The Journal of Chemical Physics*, 2010, **133**, 064705.

[35] F. A. Reboredo, L. Pizzagalli and G. Galli, *Nano Letters*, 2004, **4**, 801–804.

[36] S. Saha and P. Sarkar, *Chemical Physics Letters*, 2012, **536**, 118–122.

[37] A. Kassiba, M. Makowska-Janusik, J. Boucl, J. F. Bardeau, A. Bulou and N. Herlin-Boime, *Physical Review B*, 2002, **66**, 155317.

[38] N. P. Rao, N. Tymiak, J. Blum, A. Neuman, H. J. Lee, S. L. Girshick, P. H. McMurry and J. Heberlein, *Journal of Aerosol Science*, 1998, **29**, 707–720.

[39] T. Rajagopalan, X. Wang, B. Lahlouh, C. Ramkumar, P. Dutta and S. Gangopadhyay, *Journal of Applied Physics*, 2003, **94**, 5252–5260.

[40] J. Q. Hu, Q. Y. Lu, K. B. Tang, Y. T. Qian, G. E. Zhou, X. M. Liu and J. X. Wu, *Chemistry of Materials*, 1999, **11**, 2369–2371.

[41] S. Yang, W. Cai, H. Zeng and X. Xu, *Journal of Materials Chemistry*, 2009, **19**, 7119–7123.

[42] J. Zhu, Z. Liu, X. L. Wu, L. L. Xu, W. C. Zhang and K. C. Paul, *Nanotechnology*, 2007, **18**, 365603.

[43] J. S. Shor, I. Grimberg, B. Z. Weiss and A. D. Kurtz, *Applied Physics Letters*, 1993, **62**, 2836–2838.

[44] Y. Ke, R. P. Devaty and W. J. Choyke, *Physica Status Solidi (b)*, 2008, **245**, 1396–1403.

[45] U. Starke, J. Schardt and M. Franke, *Applied Physics A: Materials Science Processing*, 1997, **65**, 587–596.

[46] U. Starke, *Physica Status Solidi (b)*, 2009, **246**, 1569–1579.

[47] J. E. Huheey, E. A. Keiter, R. L. Keiter and O. K. Medhi, *Inorganic Chemistry: Principles of Structure and Reactivity*, Pearson Education India, 2006.

[48] N. G. Wright and A. B. Horsfall, *Journal of Physics D: Applied Physics*, 2007, **40**, 6345.

[49] J. P. Wolfe, *Physics Today*, 1982, **35**, 46–54.

[50] N. O Farrell, A. Houlton and B. R. Horrocks, *International Journal of Nanomedicine*, 2006, **1**, 451–472.

[51] E. G. Barbagiovanni, D. J. Lockwood, P. J. Simpson and L. V. Goncharova, *Applied Physics Reviews*, 2014, **1**, 011302.

[52] L. Brus, *The Journal of Physical Chemistry*, 1994, **98**, 3575–3581.

[53] M. S. Hybertsen, *Physical Review Letters*, 1994, **72**, 1514–1517.

[54] P. R. Briddon and R. Jones, *Physica Status Solidi (b)*, 2000, **217**, 131–171.

[55] J. P. Goss, M. J. Shaw and P. R. Briddon, in *Marker-method Calculations for Electrical Levels Using Gaussian-orbital Basis Sets*, ed. D. A. Drabold and S. K. Estreicher, 2007, vol. 104, pp. 69–93.

[56] M. J. Rayson and P. R. Briddon, *Physical Review B*, 2009, **80**, 205104.

[57] W. Kohn and L. J. Sham, *Physical Review*, 1965, **140**, A1133–A1138.

[58] J. P. Perdew and Y. Wang, *Physical Review B*, 1992, **45**, 13244.

[59] B. Somogyi, V. Zölyomi and A. Gali, *Nanoscale*, 2012, **4**, 7720–7726.

[60] H. J. Monkhorst and J. D. Pack, *Physical Review B*, 1976, **13**, 5188.

[61] Y. Xi, M. Zhao, X. Wang, S. Li, X. He, Z. Wang and H. Bu, *The Journal of Physical Chemistry C*, 2011, **115**, 17743–17749.

[62] M. E. Ahmed, J. P. Goss, R. J. Eyre, P. R. Briddon and M. A. Taylforth, Journal of Physics: Conference Series, p. 012046.

[63] C. Hartwigsen, S. Goedecker and J. Hutter, *Physical Review B*, 1998, **58**, 3641–3662.

[64] U. Bangert, A. J. Harvey, R. Jones, C. J. Fall, A. T. Blumenau, R. Briddon, M. Schreck and F. Hörmann, *New Journal of Physics*, 2004, **6**, 184.

[65] C. J. Fall, A. T. Blumenau, R. Jones, P. R. Briddon, T. Frauenheim, A. Gutirrez-Sosa, U. Bangert, A. E. Mora, J. W. Steeds and J. E. Butler, *Physical Review B*, 2002, **65**, 205206.

[66] E. Polak, *Computational Methods in Optimization: A Unified Approach*, Academic Press, 1971, vol. 77.

[67] F. Buda, J. Kohanoff and M. Parrinello, *Physical Review Letters*, 1992, **69**, 1272.

[68] J. M. Rondinelli and E. Kioupakis, *Annual Review of Materials Research*, 2015, **45**, 491–518.

[69] Y. Ke, Y. Shishkin, R. P. Devaty and W. J. Choyke, in *Porous SiC Preparation, Characterization and Morphology*, ed. R. M. Feenstra and C. Wood, John Wiley & Sons, Ltd, 2008, pp. 1–29.

[70] B. R. Horrocks, in *Photoluminescent Nanoparticle Derivatization Via Porous Silicon*, Springer, 2014, pp. 671–681.

[71] L. H. Lie, M. Duerdin, E. M. Tuite, A. Houlton and B. R. Horrocks, *Journal of Electroanalytical Chemistry*, 2002, **538**, 183–190.

[72] H. Harima, *Microelectronic Engineering*, 2006, **83**, 126–129.

[73] D. W. Feldman, J. H. Parker, W. J. Choyke and L. Patrick, *Physical Review*, 1968, **173**, 787–793.

[74] J. A. Freitas Jr and W. J. Moore, *Brazilian Journal of Physics*, 1998, **28**, 12–18.

[75] S. I. Nakashima and H. Harima, *Physica Status Solidi (A)*, 1997, **162**, 39–64.

[76] G. Gouadec and P. Colomban, *Progress in Crystal Growth and Characterization of Materials*, 2007, **53**, 1–56.

[77] J. I. Langford and A. J. C. Wilson, *Journal of Applied Crystallography*, 1978, **11**, 102–113.

[78] D. R. Lide, *Handbook of Chemistry and Physics, vol. 87, CRC*, 2006.

[79] S. J. Lim, M. U. Zahid, P. Le, L. Ma, D. Entenberg, A. S. Harney, J. Condeelis and A. M. Smith, *Nature Communications*, 2015, **6**, 8210.

[80] Z. Zhang, Y. Dai, L. Yu, M. Guo, B. Huang and M.-H. Whangbo, *Nanoscale*, 2012, **4**, 1592–1597.

[81] A. Trejo, M. Calvino and M. Cruz-Irisson, *International Journal of Quantum Chemistry*, 2010, **110**, 2455–2461.

[82] A. Puzder, A. J. Williamson, J. C. Grossman and G. Galli, *Physical Review Letters*, 2002, **88**, 097401.

[83] B. Ghosh and N. Shirahata, *Science and Technology of Advanced Materials*, 2016.

[84] S. Yang, B. Kiraly, W. Y. Wang, S. Shang, B. Cao, H. Zeng, Y. Zhao, W. Li, Z.-K. Liu, W. Cai and T. J. Huang, *Advanced Materials*, 2012, **24**, 5598–5603.

[85] L. E. Brus, *The Journal of Chemical Physics*, 1983, **79**, 5566–5571.

[86] S. Thomas, *Journal of Physics: Condensed Matter*, 2004, **16**, S1755.

[87] C. Coletti, C. L. Frewin, A. M. Hoff and S. E. Saddow, *Electrochemical and Solid-State Letters*, 2008, **11**, H285–H287.

[88] M. Chafai, A. Jaouhari, A. Torres, R. Antòn, E. Martin, J. Jiménez and W. C. Mitchel, *Journal of Applied Physics*, 2001, **90**, 5211–5215.

[89] H. Harima, S. Nakashima and T. Uemura, *Journal of Applied Physics*, 1995, **78**, 1996–2005.

[90] J. C. Burton, L. Sun, M. Pophristic, S. J. Lukacs, F. H. Long, Z. C. Feng and I. T. Ferguson, *Journal of Applied Physics*, 1998, **84**, 6268–6273.

[91] S. Nakashima, T. Mitani, J. Senzaki, H. Okumura and T. Yamamoto, *Journal of Applied Physics*, 2005, **97**, 123507.

[92] H. Richter, Z. P. Wang and L. Ley, *Solid State Communications*, 1981, **39**, 625–629.

[93] G. Polisski, D. Kovalev, G. Dollinger, T. Sulima and F. Koch, *Physica B: Condensed Matter*, 1999, **273**, 951–954.

[94] P. T. B. Shaffer, *Acta Crystallographica Section B: Structural Crystallography and Crystal Chemistry*, 1969, **25**, 477–488.

[95] N. Begum, A. S. Bhatti, F. Jabeen, S. Rubini and F. Martelli, *Journal of Applied Physics*, 2009, **106**, 114317.

[96] I. H. Campbell and P. M. Fauchet, *Solid State Communications*, 1986, **58**, 739–741.

[97] T. Matsumoto, J. Takahashi, T. Tamaki, T. Futagi, H. Mimura and Y. Kanemitsu, *Applied Physics Letters*, 1994, **64**, 226–228.

[98] T. V. Torchynska, A. V. Hernandez, A. D. Cano, S. Jimnez-Sandoval, S. Ostapenko and M. Mynbaeva, *Journal of Applied Physics*, 2005, **97**, 33507–33507.

[99] G. Polupan and T. V. Torchynska, *Thin Solid Films*, 2010, **518**, S208–S211.

[100] T. V. Torchynska, A. D. Cano, S. J. Sandoval, M. Dybic, S. Ostapenko and M. Mynbaeva, *Microelectronics Journal*, 2005, **36**, 536–538.

[101] S. Zangooie, J. A. Woollam and H. Arwin, *Journal of Materials Research*, 2000, **15**, 1860–1863.

[102] O. Bisi, S. Ossicini and L. Pavesi, *Surface Science Reports*, 2000, **38**, 1–126.

[103] D. Tranchida, S. Piccarolo and R. A. C. Deblieck, *Measurement Science and Technology*, 2006, **17**, 2630.

[104] C. A. Schneider, W. S. Rasband and K. W. Eliceiri, *Nature Methods*, 2012, **9**, 671.

[105] M. D. Abràmoff, P. J. Magalhães and S. J. Ram, *Biophotonics International*, 2004, **11**, 36–42.

[106] G. D. Mahan, R. Gupta, Q. Xiong, C. K. Adu and P. C. Eklund, *Physical Review B*, 2003, **68**, 073402.

[107] T. Taguchi, T. Miyazaki, S. Iikubo and K. Yamaguchi, *Materials Science and Engineering: C*, 2014, **34**, 29–34.

[108] S. Schelz and P. Oelhafen, *Surface Science*, 1992, **279**, 137–148.

[109] K. Shimoda, J.-S. Park, T. Hinoki and A. Kohyama, *Applied Surface Science*, 2007, **253**, 9450–9456.

[110] R. Alfonsetti, L. Lozzi, M. Passacantando, P. Picozzi and S. Santucci, *Applied Surface Science*, 1993, **70**, 222–225.

[111] Y.-C. Yen, S.-C. Chao, H.-C. Wu and N.-L. Wu, *Journal of The Electrochemical Society*, 2009, **156**, A95–A102.

[112] C. Das, M. Tallarida and D. Schmeisser, *Nanoscale*, 2015, **7**, 7726–7733.

[113] T. Takahagi and A. Ishitani, *Carbon*, 1984, **22**, 43–46.

[114] D. C. Marcano, D. V. Kosynkin, J. M. Berlin, A. Sinitskii, Z. Sun, A. Slesarev, L. B. Alemany, W. Lu and J. M. Tour, *ACS Nano*, 2010, **4**, 4806–4814.

[115] Y. Ma, H. Yang, J. Guo, C. Sathe, A. Agui and J. Nordgren, *Applied Physics Letters*, 1998, **72**, 3353–3355.

[116] Y. Shishkin, W. J. Choyke and R. P. Devaty, *Journal of Applied Physics*, 2004, **96**, 2311–2322.

[117] G. Gautier, J. Biscarrat, D. Valente, T. Defforge, A. Gary and F. Cayrel, *Journal of The Electrochemical Society*, 2013, **160**, D372–D379.

[118] J. Bateman, R. Eagling, B. Horrocks and D. Worrall, *Chemical Communications*, 1997, **23**, 2275–2276.

[119] D. Beke, Z. Szekrényes, I. Balogh, M. Veres, E. Fazakas, L. K. Varga, K. Kamarás, Z. Czigány and A. Gali, *Applied Physics Letters*, 2011, **99**, 213108.

[120] M. Fontana, T. Deppe, A. K. Boyd, M. Rinzan, A. Y. Liu, M. Paranjape and P. Barbara, *Scientific Reports*, 2013, **3**, 1634.

[121] A. Pospischil, M. M. Furchi and T. Mueller, *Nature Nanotechnology*, 2014, **9**, 257–261.

[122] Q. Zhang, J. Jie, S. Diao, Z. Shao, Q. Zhang, L. Wang, W. Deng, W. Hu, H. Xia, X. Yuan and S.-T. Lee, *ACS Nano*, 2015, **9**, 1561–1570.

[123] I. Mora-Sero, L. Bertoluzzi, V. Gonzalez-Pedro, S. Gimenez, F. Fabregat-Santiago, K. W. Kemp, E. H. Sargent and J. Bisquert, *Nature Communications*, 2013, **4**, 2272.

[124] J. P. Clifford, K. W. Johnston, L. Levina and E. H. Sargent, *Applied Physics Letters*, 2007, **91**, 253117.

[125] M. Casalino, M. Iodice, L. Sirleto, I. Rendina and G. Coppola, *Optics Express*, 2013, **21**, 28072–28082.

[126] H. B. Michaelson, *Journal of Applied Physics*, 1977, **48**, 4729–4733.

[127] M. Wiets, M. Weinelt and T. Fauster, *Physical Review B*, 2003, **68**, 125321.

[128] Z. Alaie, S. Mohammad Nejad and M. H. Yousefi, *Materials Science in Semiconductor Processing*, 2015, **29**, 16–55.

[129] L. Peng, L. Hu and X. Fang, *Advanced Materials*, 2013, **25**, 5321–5328.

[130] S. M. Sze, D. J. Coleman and A. Loya, *Solid-State Electronics*, 1971, **14**, 1209–1218.

[131] A. Itoh and H. Matsunami, *Physica Status Solidi (a)*, 1997, **162**, 389–408.

[132] J. Kohlscheen, Y. N. Emirov, M. M. Beerbom, J. T. Wolan, S. E. Saddow, G. Chung, M. F. MacMillan and R. Schlaf, *Journal of Applied Physics*, 2003, **94**, 3931–3938.

[133] A. J. Chiquito, C. A. Amorim, O. M. Berengue, L. S. Araujo, E. P. Bernardo and E. R. Leite, *Journal of Physics: Condensed Matter*, 2012, **24**, 225303.

[134] Z. Zhang, K. Yao, Y. Liu, C. Jin, X. Liang, Q. Chen and L. Peng, *Advanced Functional Materials*, 2007, **17**, 2478–2489.

[135] S. Sinha, S. Kumar Chatterjee, J. Ghosh and A. Kumar Meikap, *Journal of Applied Physics*, 2013, **113**, 123704.

[136] H. Mimura, T. Matsumoto and Y. Kanemitsu, *Applied Physics Letters*, 1994, **65**, 3350–3352.

[137] N. Naderi and M. R. Hashim, *Materials Research Bulletin*, 2013, **48**, 2406–2408.

[138] E. H. Rhoderick and R. H. Williams, *Metal-Semiconductor Contacts*, Clarendon Press Oxford, 1978.

[139] E. H. Rhoderick, *IEE Proceedings I-Solid-State and Electron Devices*, 1982, **129**, 1.

[140] D. J. Ewing, L. M. Porter, Q. Wahab, X. Ma, T. S. Sudharshan, S. Tumakha, M. Gao and L. J. Brillson, *Journal of Applied Physics*, 2007, **101**, 114514.

[141] W. Mönch, *Journal of Vacuum Science Technology B: Microelectronics and Nanometer Structures Processing, Measurement, and Phenomena*, 1999, **17**, 1867–1876.

[142] S. N. Das, J.-H. Choi, J. P. Kar, K.-J. Moon, T. I. Lee and J.-M. Myoung, *Applied Physics Letters*, 2010, **96**, 092111.

[143] S. Limpijumnong, W. R. L. Lambrecht, S. N. Rashkeev and B. Segall, *Physical Review B*, 1999, **59**, 12890–12899.

[144] E. Biedermann, *Solid State Communications*, 1965, **3**, 343–346.

[145] S. Zollner, J. G. Chen, E. Duda, T. Wetteroth, S. R. Wilson and J. N. Hilfiker, *Journal of Applied Physics*, 1999, **85**, 8353–8361.

[146] T. Dalibor, G. Pensl, H. Matsunami, T. Kimoto, W. J. Choyke, A. Schner and N. Nordell, *Physica Status Solidi (a)*, 1997, **162**, 199–225.

[147] N. G. Wright, A. B. Horsfall and K. Vassilevski, *Materials Today*, 2008, **11**, 16–21.

[148] C. Persson and U. Lindefelt, *Journal of Applied Physics*, 1997, **82**, 5496–5508.

[149] J. Zhu, Z. Liu, X. L. Wu, L. L. Xu, W. C. Zhang and K. C. Paul, *Nanotechnology*, 2007, **18**, 365603.

[150] D. Dai, N. Zhang, W. Zhang and J. Fan, *Nanoscale*, 2012, **4**, 3044–3046.

[151] A. G. Cullis, L. T. Canham and P. D. J. Calcott, *Journal of Applied Physics*, 1997, **82**, 909–965.

[152] O. Jessensky, F. Müller and U. Gösele, *Thin Solid Films*, 1997, **297**, 224–228.

[153] L. J. Brillson, S. Tumakha, G. H. Jessen, R. S. Okojie, M. Zhang and P. Pirouz, *Applied Physics Letters*, 2002, **81**, 2785–2787.

[154] Z. Szekrényes, B. Somogyi, D. Beke, G. Károlyházy, I. Balogh, K. Kamarás and A. Gali, *The Journal of Physical Chemistry C*, 2014, **118**, 19995–20001.

[155] M. Rashid, A. K. Tiwari, N. Wood, P. Briddon, J. P. Goss, M. J. Rayson, N. Wright and A. B. Horsfall, Materials Science Forum, pp. 375–378.

[156] M. V. Wolkin, J. Jorne, P. M. Fauchet, G. Allan and C. Delerue, *Physical Review Letters*, 1999, **82**, 197–200.

[157] M. Rashid, A. K. Tiwari, J. P. Goss, M. J. Rayson, P. R. Briddon and A. B. Horsfall, *Physical Chemistry Chemical Physics*, 2016, **18**, 21676–21685.

[158] E. Secret, C. Leonard, S. J. Kelly, A. Uhl, C. Cozzan and J. S. Andrew, *Langmuir*, 2016, **32**, 1166–1170.

[159] L. Zhang, V. Belova, H. Wang, W. Dong and H. Mohwald, *Chemistry of Materials*, 2014, **26**, 2244–2248.

[160] Y. Ke, R. P. Devaty and W. J. Choyke, *Electrochemical and Solid-State Letters*, 2007, **10**, K24–K27.

[161] A. A. Sagüès, J. T. Wolan, A. De Fex and T. J. Fawcett, *Electrochimica Acta*, 2006, **51**, 1656–1663.

[162] A. Tanaka and H. Katsuno, *Japanese Journal of Applied Physics*, 2009, **48**, 120217.

[163] A. Sagar, C. D. Lee, R. M. Feenstra, C. K. Inoki and T. S. Kuan, *Journal of Applied Physics*, 2002, **92**, 4070–4074.

[164] Y. Hijikata, H. Yaguchi and S. Yoshida, *Applied Physics Express*, 2009, **2**, 021203.

[165] Y. Song, S. Dhar, L. C. Feldman, G. Chung and J. R. Williams, *Journal of Applied Physics*, 2004, **95**, 4953–4957.

[166] T. Ito and A. Hiraki, *Journal of Luminescence*, 1993, **57**, 331–339.

[167] J. S. Shor and A. D. Kurtz, *Journal of the Electrochemical Society*, 1994, **141**, 778–781.

[168] B. Hornetz, H. J. Michel and J. Halbritter, *Journal of Materials Research*, 1994, **9**, 3088–3094.

[169] J. S. Shor, X. G. Zhang and R. M. Osgood, *Journal of The Electrochemical Society*, 1992, **139**, 1213–1216.

[170] S. Zangooie, P. O. A. Persson, J. N. Hilfiker, L. Hultman and H. Arwin, *Journal of Applied Physics*, 2000, **87**, 8497–8503.

[171] B. E. Deal and A. S. Grove, *Journal of Applied Physics*, 1965, **36**, 3770–3778.

[172] H. Z. Massoud, J. D. Plummer and E. A. Irene, *Journal of the Electrochemical Society*, 1985, **132**, 2685–2693.

[173] J. Kuang and W. Cao, *Journal of the American Ceramic Society*, 2014, **97**, 2698–2701.

[174] M. Liu, P. Jin, Z. Xu, D. A. H. Hanaor, Y. Gan and C. Q. Chen, *Theoretical and Applied Mechanics Letters*, 2016, **6**, 195–199.

[175] X.-L. Han, G. Larrieu and C. Krzeminski, *Nanotechnology*, 2013, **24**, 495301.

[176] D. B. Kao, J. P. McVittie, W. D. Nix and K. C. Saraswat, *IEEE Transactions on Electron Devices*, 1988, **35**, 25–37.

[177] C. Tang and Y. Bando, *Applied Physics Letters*, 2003, **83**, 659–661.

[178] G. Irmer, *Journal of Raman Spectroscopy*, 2007, **38**, 634–646.

[179] Y. Zakharko, J. Botsoa, S. Alekseev, V. Lysenko, J. M. Bluet, O. Marty, V. A. Skryshevsky and G. Guillot, *Journal of Applied Physics*, 2010, **107**, 013503.

[180] A. O. Konstantinov, A. Henry, C. I. Harris and E. Janzn, *Applied Physics Letters*, 1995, **66**, 2250–2252.

[181] T. Hiyoshi and T. Kimoto, *Applied Physics Express*, 2009, **2**, 091101.

[182] C. Kirchner, T. Liedl, S. Kudera, T. Pellegrino, A. Muñoz Javier, H. E. Gaub, S. Stölzle, N. Fertig and W. J. Parak, *Nano Letters*, 2005, **5**, 331–338.

[183] F. Hua, F. Erogbogbo, M. T. Swihart and E. Ruckenstein, *Langmuir*, 2006, **22**, 4363–4370.

[184] L. Peng, L. Hu and X. Fang, *Advanced Materials*, 2013, **25**, 5321–5328.